Development, Characterization, and Application of a Charged Particle Microbeam for Radiobiological Research

by

Michael R. Folkert

S.B. and S.M., Nuclear Engineering (1998)
Massachusetts Institute of Technology

SUBMITTED TO THE DEPARTMENT OF NUCLEAR SCIENCE AND ENGINEERING AND THE HARVARD-MIT DIVISION OF HEALTH SCIENCES AND TECHNOLOGY ON AUGUST 25, 2005 IN PARTIAL FULFILLMENT OF THE REQUIREMENTS FOR THE DEGREE OF

DOCTOR OF PHILOSOPHY IN RADIOLOGICAL SCIENCES
AT THE
MASSACHUSETTS INSTITUTE OF TECHNOLOGY

SEPTEMBER 2005

Signature of Author: _____
Department of Nuclear Science and Engineering and the
Harvard-MIT Division of Health Sciences and Technology, Radiological Sciences Joint Program
August 25, 2005

Certified by: _____
Jacquelyn Yanch
Professor of Nuclear Science and Engineering
Thesis Supervisor

Certified by: _____
Richard Lanza
Senior Research Scientist, Nuclear Science and Engineering
Thesis Reader

Accepted by: _____
Jeffrey Coderre
Associate Professor of Nuclear Science and Engineering
Chairman, Department Committee on Graduate Students

This page intentionally left blank.

Development, Characterization, and Application of a Charged Particle Microbeam for Radiobiological Research

by

Michael R. Folkert

Submitted to the Department of Nuclear Science and Engineering
and
the Harvard/MIT Division of Health Sciences and Technology
on August 25, 2005 in Partial Fulfillment of the
Requirements for the Degree of Doctor of Philosophy in
Radiological Sciences

ABSTRACT

The goal of this work is to develop a charged-particle microbeam for use in radiobiological research at the MIT Laboratory for Accelerator Beam Applications (LABA). The purpose of this device is to precisely explore the radiation response of biological systems on a cellular and subcellular level, particularly in the area of temporal and spatial effects of radiation on in vitro systems. An accelerator-based 750 keV proton source was characterized and integrated into a laboratory-scale device that includes a deflection/gating system, single-particle detection system, imaging and positioning system, and a collimation system with two designed modes: a "charged-particle microslit" for delivering a ~3 micron by 1 mm dose profile; and a pinhole aperture for delivering a ~3 micron diameter pattern of radiation. The entire device measures less than 4 m, requires minimal radiation shielding, and utilizes a dedicated ion source.

The charged particle microslit has been fully characterized and used to deliver a radiation pattern to a series of mammalian fibroblast cell monolayers that have subsequently been assayed for direct and indirect chemical effects of radiation, double-stranded DNA damage, and DNA repair protein localization. These studies will contribute to the understanding of the radiation-induced bystander effect, which is generally defined as the induction of biological effects in cells that are not directly traversed by ionizing radiation. Analysis of the range of assays performed on the microbeam-irradiated cells demonstrates that even though the physical radiation dose is confined to a subnuclear width (< 5 microns), in many cases the biological effects of the radiation extend for many cell widths (> 40 microns) and show dependence on the initial radiation dose delivered to the directly irradiated cells.

As an experimental system, the LABA Microbeam was designed to be practically turn-key, and most applications require only one operator to perform. The LABA Microbeam represents a significant step towards a cost-effective and easily operated charged-particle microbeam appropriate for use as a standard laboratory research tool. Further work remains in automation of the microbeam subsystems and optimization/characterization of the pinhole-aperture collimator, as well as expanding the scope of the radiobiological assays performed using the charged-particle microslit.

Thesis Supervisor:
Jacquelyn Yanch, Ph.D.
Professor of Nuclear Science and Engineering, Massachusetts Institute of Technology

This page intentionally left blank.

Acknowledgements

First and foremost, I would like to thank my family, who have been so incredibly supportive and encouraging all my life and especially while I've been here at MIT. My mother and father have been wonderful role models for me in my somewhat pathological quest for knowledge, while my brothers and sister have helped to keep me grounded. I'd also definitely like to thank my patient and loving girlfriend Meredith for putting up with me through the harrowing final years of my doctorate – hopefully she can endure the next couple of years towards my medical degree with the same fortitude!

I would like to thank my advisor, Jackie Yanch, for patiently guiding me all of these years. I've known her since I was a sophomore in 1994, brand new to the MIT Nuclear Engineering Department, and in the decade since then she has been a constant and trusted teacher, supporter, and friend. Working with her has been an education in and of itself, but she's managed to keep it fun as well – I only wish that every graduate student at MIT could be as fortunate in finding an advisor as I was.

I would also like to thank Jeff Coderre, Kathy Held, and Dick Lanza of my thesis committee, who've been exacting editors and generous contributors of technical assistance and advice. I known many excellent professors and researchers in this department over my many years at MIT, so many that it would be difficult to list them all here (but I'll try!) David Cory, John Bernard, Neil Todreas, Mujid Kazimi, Ian Hutchinson, Lisa Porter, Kim Molvig, Sidney Yip, Gordon Kohse, Joanne O'Meara, Ken Czerwinski, and Bruce Rosen have all contributed a great deal to my academic and personal growth.

I am deeply indebted to Andrew Dart, Bob Ledoux, and all the rest of the folks at Pyramid Technical Consultants for their assistance with machining, electronics, and programming for the microbeam, as well as Bob Klinkowstein, Ruth Shefer, and Tom Doucette from Newton Scientific, Inc. for all their help with the accelerator. My fellow graduate student Ray Albritton helped me tremendously with the microbeam hardware and software, and I wish him the best in all his future endeavours. Over at MGH, I'd like to acknowledge Chunmei Luo for her help with the hMRE11 and gamma-H2A.X assays and Simon Powell for radiobiological insight, and back at MIT in the BE Department, I'd like to thank Bevin Engleward and Dominika Wiktor for their assistance with the ROS assay and with their pithy observations about our other microbeam experiments.

I've worked with a number of wonderful UROP students over the years, and in particular I'd like to acknowledge Paige Hopewell, Gheorghe Chistol, and Jen Lobo for their help with cell culture, experiments, analysis, and sanity maintenance. All my fellow graduate buddies who helped keep things lively will be fondly remembered in the years to come – Whitney Raas, Peter Yarsky, Pete Cochran, Craig Gerardi, Michelle Ledesma, Antonio Damato, Brad Schuller, Rong Wang, Jingli Kiger, Marco Pravia, Victoria Anderson, Lisa Treat, Caroline Boudoux, Heather Maclean, Brandon Blackburn, Hongyu Jiang, and so many more…

During the course of my graduate studies at MIT, I was supported by the United States Department of Energy (DOE) Nuclear Engineering/Health Physics Fellowship and by other DOE research grants, as well as by a number of internal MIT fellowships and teaching assistantships.

Contents

List of Figures

Chapter 1. Introduction and Overview

1.1 The LABA Microbeam Project

The goal of this work is the development and characterization of an economical and compact charged-particle microbeam system capable of delivering a subnuclear distribution of radiation dose. Application of such a device will increase understanding of radiobiology and radiation interactions with biological systems on a cellular and subcellular level, permitting precise quantitative investigations of the cellular response to radiation, particularly in the area of temporal and spatial effects on in vitro systems. For the purposes of this thesis, a microbeam is defined as a focused or collimated radiation source capable of delivering a localized dose distribution to an area with micron-level resolution.

The Laboratory for Accelerator Beam Applications (LABA) has been investigating a possible design for a charged-particle radiobiological microbeam since the Fall of 2000.[109] With two small charged-particle accelerator options available, each with sufficient energy to penetrate a monolayer of cells on a simple cell dish, the possibility of a charged-particle microbeam of sufficiently compact design and low cost that it would be reasonable for regular hospital, commercial, or industrial use was viewed as a realizable goal.

1.2 Thesis Overview

This thesis will detail the process of the design, development, and characterization of a compact and inexpensive charged-particle microbeam for use in radiobiological research, as well the initial application of the device to the study of the cellular response to radiation.

- **Chapter 1** introduces the LABA Microbeam project, its goals, accomplishments, and future applications.
- **Chapter 2** provides background on the history of microbeams in radiobiology and the basis of microbeam techniques, and describes existing microbeam projects all over the world.
- **Chapter 3** describes the hardware and software used to generate and deliver a vertically-oriented charged-particle beam to the experimental endstation of the LABA Microbeam.

- **Chapter 4** describes the subsystems comprising the biological endstation and discusses the experimental methodology used to characterize the operation of each system.
- **Chapter 5** describes the biological target holder design and development, and details how the methodologies for performing a range of radiobiological studies with the LABA charged-particle microbeam were developed and applied.
- **Chapter 6** presents general conclusions about the LABA Microbeam, and describes the future work needed to improve upon the system so that it may meet its full potential as a standard research tool.
- Lastly, the **Appendix** provides greater detail on the LABA Microbeam control systems and detection electronics, the methods used to predict the operations of the deflection and bending magnet subsystems, the radiobiological assays performed on microbeam-irradiated cells, and the post-processing image analysis techniques used.

1.3 The LABA Charged-Particle Microbeam

Despite progress in microbeam development and its proven usefulness as a tool for radiobiological research, availability of machines with which research may be performed has presented a major barrier to microbeam techniques becoming standard research tools.[10] Most microbeams currently in operation or under development utilize very large accelerators and ancillary facilities. Additionally, in many cases the beam time is shared with other projects, and maintenance of the accelerator and associated apparatus requires a large staff of well-trained physicists and engineers to operate. On the other hand, the entire MIT LABA charged-particle microbeam, measuring less than 4 m and costing in its entirety < $2 million (in 2002 US dollars), utilizes a dedicated ion source and can be placed in an existing room due to the fact that the radiation background it creates is low enough that the operators may sit in the room while it is energized. (**Figure 1.1**) The system is designed to be practically "turn-key," and most experiments require only one operator to conduct (although two operators are required at all times by MIT Radiation Protection Office (RPO) guidelines).

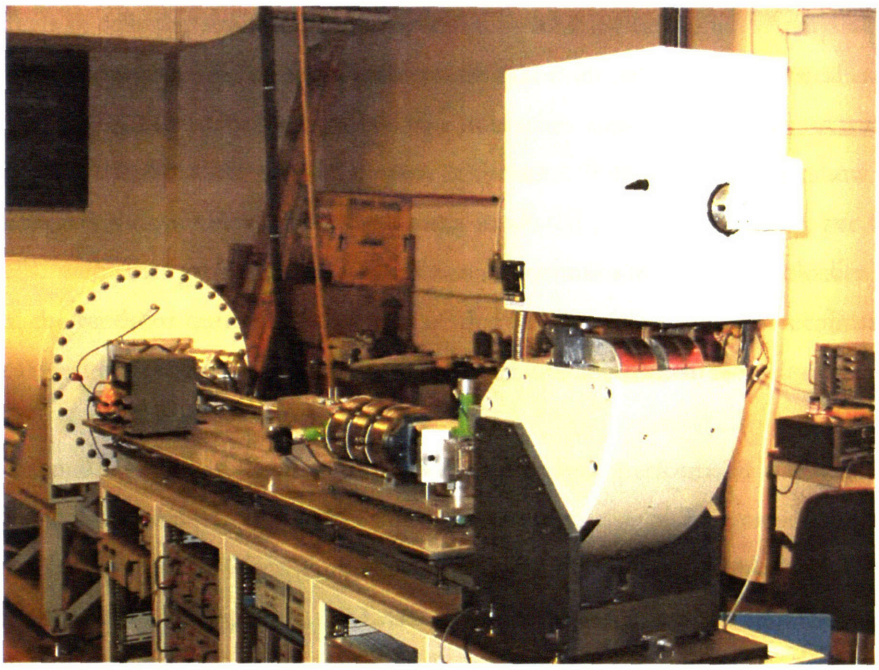

Figure 1.1 The LABA Charged-Particle Microbeam.

The microbeam apparatus includes an electrostatic accelerator that provides a horizontal beam, an electrostatic deflection system capable of gating the beam, a 90^0 bending magnet to redirect the charged-particle beam vertically, and a dedicated endstation for biological irradiations consisting of a light source, imaging camera, micron-resolution stage, single-particle counter, and beam collimation assembly. The He^{++} or H^{+} charged-particle beam is delimited using either a slit or a pinhole collimator assembly. Particle counting is performed upstream of the cell dish using an organic plastic scintillator in combination with two photomultiplier tubes (PMTs) in coincidence mode that are used both for dose measurement and as the control signal for shuttering the beam with the electrostatic deflection system. Control software, developed in-house, manipulates all aspects of the hardware including the accelerator, beam line components, vacuum systems and all subsystems of the biological endstation.

1.4 Accomplishments

The charged particle microslit has been fully characterized and used to deliver a radiation pattern to a series of cell monolayers that have subsequently been assayed for direct and indirect chemical effects of irradiation, double-stranded DNA damage, and DNA repair protein localization. These studies will contribute to the understanding of the cellular response to radiation, and more specifically, to the characterization of the radiation-induced bystander effect (generally defined as the induction of

biological effects in cells that are not directly traversed by ionizing radiation). Analysis of the assays performed on microbeam-irradiated cells demonstrates that even through the physical radiation dose delivered by the LABA Microbeam is confined to a subnuclear size (< 5 microns), in many cases the biological effects of the radiation extend for many cell widths (> 40 microns), and show dependence on the initial radiation dose delivered to the directly irradiated cells. Additionally, pre-treatment of irradiated cells with the gap-junction intercellular communication (GJIC) blocker *lindane* has demonstrated the mode of transmission of two of these biologically-mediated secondary effects of radiation are at least in part due to GJIC-mediated cellular interactions.

As an experimental system, the LABA Microbeam successfully performs as a device that can be operated by biologists and physicians, instead of a team of physicists and engineers. Due to its small size, simple and easy-to-use interface, limited radiation shielding requirements, and applicability to a wide range of workplace environments, the LABA Microbeam represents a significant step towards a cost-effective and easy-to-operate charged-particle microbeam appropriate for use as a standard laboratory research tool. Further work remains in extending the automation of the microbeam subsystems and optimization/characterization of the pinhole-aperture collimator, as well as expanding the scope of the radiobiological assays performed using the charged-particle microslit.

Chapter 2. Background

2.1 LABA Charged-Particle Microbeam

The Laboratory for Accelerator Beam Applications (LABA) has been investigating the design and implementation of a charged-particle microbeam for radiobiological research since 2000.[109] With two small charged-particle accelerators available with sufficient energy to penetrate a thin tissue-approximating layer of cells on a simple dish at her disposal, one of which had been developed by Pyramid Technical Consultants (Waltham, MA USA) to serve as a small, inexpensive laboratory-size tool, Professor Jacquelyn Yanch proposed the possibility of a microbeam of sufficiently compact design and low cost that it would be reasonable for hospital/commercial/industrial use.

Most microbeams currently in operation or under development utilize large and complex accelerators and ancillary facilities. Availability presents a major problem, as most microbeams share beam time with other projects, and maintenance of the accelerator and associated apparatus requires a staff of well-trained physicists and engineers. The LABA Microbeam was designed to overcome these barriers of cost and complexity in order to allow microbeam techniques to serve as standard research tools. Compared to other microbeam accelerators currently operating and under development, the LABA Microbeam has a number of advantages and disadvantages. The small size of the system allows for portability and ease of maintenance. The dose equivalent rate at the operator position during an irradiation is generally < 0.5 mrem/hr, so the LABA Microbeam requires little or no additional radiation shielding. The centralized control system permits a single operator to manage almost all aspects of the microbeam operation, and the dedicated accelerator allows for flexible irradiation scheduling. On the other hand, the accelerator is only capable of generating a very limited range of energies, and the maximum energy for singly-charged ions that the accelerator can safely generate at the present time is approximately 800 keV.

2.2 Review of Microbeams

2.2.1 History

Charged particle microbeams have a surprisingly lengthy history, given the complexity of the apparatus; however, only recently have biological advances provided the tools required to take full advantage of their use. The primary operational microbeams today are located at Columbia

University's Radiological Research Accelerator Facility (RARAF), and at the UK-based Gray Cancer Institute. A number of other microbeams are under construction or are at some level of characterization.

The use of radiation as a general cellular probe was reviewed by Zirkle in 1947,[115] with the specific application of partial irradiation of cells described in 1953,[116] but a rigorous description of the use of microbeams as an analytical probe was first provided in 1987.[104] It was observed that targeted irradiation of portions of individual cells would be of interest to biological research for two reasons – first, because it would allow investigators to gain information about how radiation induces damage in living systems; and second, because it would aid in the analysis of the normal functions of various cellular components by selectively and specifically altering them.[116]

Zirkle and Bloom accomplished this by directing a beam of charged particles (2 MeV protons produced by a vertical Van de Graaff electrostatic generator, with a range of 73 μm in tissue) through one of two collimators – one, type "G," consists of two parallel plates pressed together, one of which had a microscopic groove cut or scored into it (**Figure 2.1**), creating a triangular aperture; and type "XS," which consisted of two crossed slits, each of which could be adjusted to a desired width (**Figure 2.2**), creating a variable size rectangular aperture.

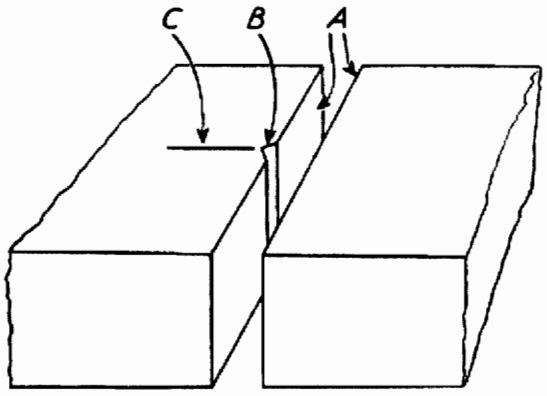

"G"

Figure 2.1 "G" Type Collimator, consisting of a pair of parallel plates, one of which has a "notch" cut into the opposing face.[116]

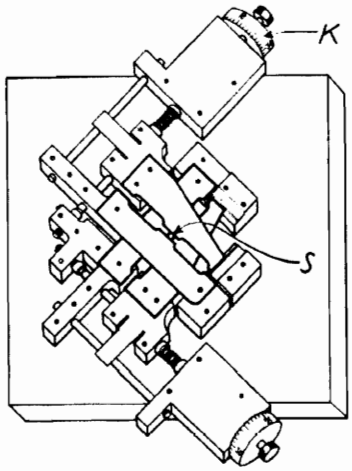

"XS"

Figure 2.2 "XS" Type Collimator, consisting of two crossed slits, each of which could be adjusted to a desired width.[116]

The particles had to traverse two mica windows with a stopping power equivalent of 25-30 μm in tissue (about 5 μm thick). While this methodology did provide a highly-collimated beam (over 95% of transmitted particles within a 5 μm diameter spot for their optimal "G" type collimator design),

there was no precise control over the number of particles transmitted, and vacuum control was very poor, leading to a high degree of energy straggle. Poor particle energy control from straggle and accelerator "wobble" led to poor dosimetry, which in turn introduced a degree of error (>5%) unacceptable for a true dose-effect study with the precision and accuracy desired today.

A host of other inadequacies plagued initial microbeam development. Visualization and targeting of cells was limited by the lack of efficient electronic imaging systems, and without computerization, automated identification and logging of cell and/or nuclear location was not possible. Machining of mechanical components to micron-level tolerances was prohibitively expensive, and achieving precise stage motion to accuracies greater then 10-100 microns was prohibitively difficult, which introduced mechanical errors large enough to overwhelm targeting precision and prevented reliable targeting of structures on the order of a cell or smaller. The biological techniques available between 1950 and the early 1980's were highly limited, especially in the areas of advanced cell culture and cell signaling.[27, 104]

Technical advances in physics, electronics, biology, and engineering were required to provide the microbeam desired. By 1987, Watt and Grime had described the fundamental requirements for the use of heavy charged ions as analytical probes, including advances in delimiting techniques (both physical collimation and focusing methods) as well as and targeting technology. The timeline shown **Figure 2.3** illustrates the advances in precision and beamspot size through the late 1980's for microbeams developed for in-vacuum sample analysis.[104]

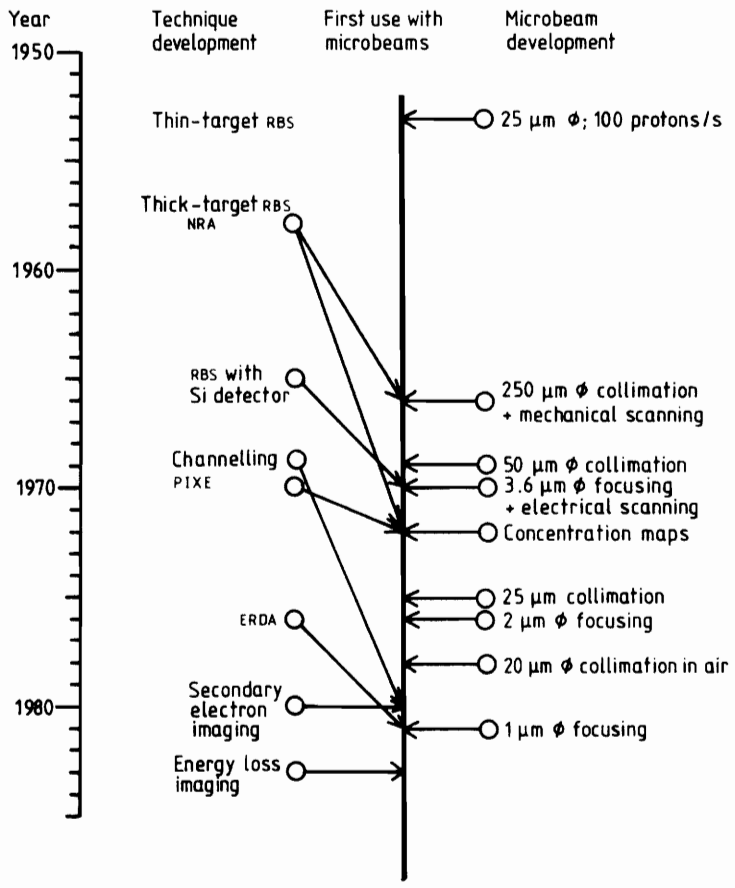

Figure 2.3 An illustration of the time-scale of development of in-vacuum charged-particle analytical microbeams.[104]

The last two decades have seen the biological developments needed to make the charged-particle microbeam truly useful as a radiobiological research tool. As of 2005, six international workshops on the use of microbeam probes for investigation of cellular radiation response have been held as biological advances have enlarged the potential areas of microbeam research.[1, 2, 3] Direct utilization of an accelerator-based microprobe for biological research began to occur in the early 90's. At that point, laboratories in the USA,[34] UK,[31, 32, 33] and Japan began developing charged-particle microprobes for irradiation of cells *in vitro*.[3, 11] In the past 10 years there has been a rapid increase in the number of centers developing or planning to develop charged-particle and x-ray microbeams. Initial studies focused on the use of collimated or focused charged-particle beams to study low dose/single particle effects;[65] to selectively irradiate a specific subset of cells in a homogeneous or heterogeneous cell culture population;[80] or to selectively irradiate specific sub-cellular portions of individual cells, generally the cytoplasm or the nucleus.[65, 106] The potential for reliable subnuclear dose deposition made the possibility of investigating spatial and temporal distribution of DNA damage repair proteins a reality.[76]

There are currently approximately 14 microbeams at some level of operation worldwide, primarily studying low-dose effects and "non-targeted" responses such as bystander effects, genomic instability and adaptive responses.[3]

2.2.2 Significance of Microbeam Techniques

The precision that microbeam irradiation provides is of key importance to radiobiological studies for a number of reasons:[27, 31, 81, 104]

1) it allows the experimenter to precisely control the amount of radiation deposited in a given cell or defined subpopulation of cells, as well as permitting the targeting of a specific subset of cells from a larger population
2) it allows investigation into the distribution of radiosensitivity across a cell or nucleus, in that micron resolution and single particle control permits the deposition of varying levels of radiation intensity across the cell or subcellular structures
3) defined subnuclear distribution of radiation dose allows visualization of damage repair protein localization and the time evolution of DNA damage resolution
4) it allows targeting of specific cellular regions and the ability to return to those regions to permit direct visualization of radiation effects over time (such as for membrane damage studies).

The most important aspect of microbeam irradiation is the role it can play in improving the statistical nature of dose determination. Traditional broad-beam irradiations of cell cultures rely on probabilistic "average" numbers of particle traversals – for example, a traditional "broad beam" irradiation follows Poisson statistics, such that an irradiation designed to deliver an average of one particle per nucleus (a "hit") would result in 37% of the irradiated cells receiving no "hits," 37% of the irradiated cells receiving a single "hit," and 26% of the irradiated cells receiving 2 or more hits.[65] While the average dose is the same for a Poisson-distributed mean number of charged-particle irradiations in a broad-beam irradiation as it is for a set of uniformly targeted, single-hit irradiations in a microbeam irradiation, the true dose distribution on the cellular level is completely different. With the precision and accuracy of a properly designed microbeam, the statistical and heterogeneous nature of broad-beam irradiations is overcome and replaced by the relative certainty and uniformity of targeted irradiation.

Precise spatial targeting allows the operator to selectively irradiate the nucleus directly, or spare the nucleus and irradiate only the cytoplasm, permitting study of the relative contribution of the passage of a charged particle to a range of biological damage endpoints. Irradiation of a specific cell type (using fluorescently tagged surface markers, for example) in a heterogeneous cell population would allow the study of a range of cell-specific secondary biological effects. An understanding of these reactions on the cellular level could contribute a great deal towards "personalized therapy," in which a radiotherapeutic regimen could be optimized *in vitro* to an individual patient's needs in order to maximize therapeutic benefit.

2.2.3 Characteristics of a Microbeam

As previously mentioned, a microbeam is a device capable of delivering a precisely controlled amount of radiation to a specified target of micron dimensions. In its simplest form, radiation must be generated, directed towards a target, and regulated spatially and temporally in such a way that a specified dose may be deposited in that target or targets. In developing such a device, certain specific subsystems are needed:

1) a **radiation source**,
2) a **collimating/focusing system** for generating a micron-scale beam spot,
3) a **detection system,** used to precisely control the number of particles within the micron-scale beam spot, and
4) a **targeting/positioning system**, used to align the beam relative to the target (or vice versa).

There are many possible ways to design these subsystems – a brief overview of each follows, although point 3) is broken into 2 general categories: a detection system and a shuttering system.

A **radiation source** is defined as the means by which the radiation used by the microbeam apparatus is produced. This may be a source of charged particles, such as protons, alphas or electrons; or it could be a source of x- or gamma rays. A charged-particle source could range from a simple radionuclide-based source such as Americium-241 (^{241}Am), which has the advantages of highly flexible size requirements and low expense, but is limited to specific energies and charged-particle types (alphas, electrons, and positrons); to an accelerator-based source such as a Van de Graaff, Cockcroft-Walton, or cyclotron, all of which are significantly larger than any radionuclide source as well as orders of magnitude more expensive, but provide a much greater range of possible energies,

intensities, and particle types for use in biological irradiations. An x- or gamma ray beam can also be provided in a wide range of energies through a number of cathode-ray, radionuclide, or synchrotron sources.

A **collimating/focusing system** is the most crucial defining component of a "micro"-beam, in that it is the means by which the beam spot produced by the **radiation source** may be collimated to a precise, micron-scale cross-sectional area. Physical collimation methods, in which a physical barrier is imposed in the path of the beam to reduce the cross-sectional area of the beam to a micron-scale spot, are probably the simplest way to control the profile of a radiation beam as well as reduce the beam intensity, although they may be considered a "brute force" method. This method is appropriate for both charged-particle sources and x- or gamma ray sources, but in the latter cases scattering effects may cause difficulties in obtaining a small spot in which the majority of all particles fall. "Focusing" methods may also be used on both classes of radiation. In the case of charged particles, electrostatic or magnetic focusing elements may be employed; in the case of uncharged particles such as x- or gamma rays, diffractive and/or reflective elements may be used. Focusing methods do not generally reduce the initial beam intensity significantly, which would make higher-intensity radiation sources more difficult to control; the higher the beam current, the more difficult it is to limit the number of transmitted particles delivered to the target.

A **detection system** generally consists of two components; a detection system that verifies that the target has been hit and by how many particles, and a gating system that "shutters" the beam, allowing a single or specified number of particles to hit the target.

1) **particle detection system**: a system capable of detecting precise amounts of radiation dose or single particles. A number of methods exist, including transmission detectors, in which the radiation must have sufficient penetrating power to traverse the transmission detector, with enough remaining to irradiate the cell; and termination detectors, including surface barrier and thin-window proportional counters, in which case the radiation used must have sufficient energy to penetrate the entire target and any other intervening material before it reaches the detector face. Generally, the particle detection system also provides the signal to the gating system.
2) **gating system**: a means by which to limit the number of particles, usually coordinated with the single-particle detection system. The gating system could employ a physical barrier (mechanical shuttering) or use electrostatic or magnetic means to divert the beam away from the target (electromagnetic shuttering).

Last, a **targeting/positioning system** is crucial to the use of a microbeam as an analytical or biological probe. Such a system requires both a visualization methodology that permits visualization of cells and/or subcellular components that should be able to log the locations of cells or landmarks on the cells for irradiation, and a means by which to either place the target in the path of the beam (such as an x-y automated stage) or to direct the beam to the target (such as electrostatic or electromagnetic beam positioning). Stage-based targeting is generally used for physically collimated beam methods, whereas electrostatic/electromagnetic based targeting methods are generally coupled with focused beam methods due to the fact that the hardware to direct the beam is already present.

2.2.4 Existing Microbeams

As of 2004, there are approximately 14 microbeams at some level of operation worldwide.[3] Many of these microbeams are at the most embryonic of stages, while a few, notably the Gray Cancer Institute and Columbia RARAF microbeams, are highly developed and fully operational. Countries engaged in microbeam research include the US (3 – Columbia RARAF (charged-particle and x-ray), MIT LABA, and Texas A&M), UK (GCI (charged-particle and x-ray), Japan (3 - JAERI, Tsukuba (x-ray only), SPICE/Chiba), China (Chinese Academy of Science in Hefei), Germany (4 - GSI, PTB, Munich and LIPSION/Leipzig), France (CENBG) and Italy (INFN-LNL). Other facilities are also exploring the option of developing microbeams – for example, in the US, the Advanced Light Source at Berkeley has also been used to produce x-rays for microbeam irradiation.[1, 2, 3, 7]

An overview of the many microbeams and their operating characteristics is provided in **Table 2.1** below. The two longest-established microbeams at the Gray Cancer Institute in the UK and the RARAF Microbeam in the USA will be discussed in more detail.

Country	Laboratory	Microbeam	ion source	ions used	accelerator	collimator	usable spot size
UK	*Gray Lab*	charged-particle	RF	H, He	4 MeV Van de Graaff	capillary	~2 um
		x-ray	carbon x-ray	n/a	n/a	diffraction focusing	~0.5 um
USA	*Columbia RARAF*	charged-particle	duoplasmotron	H, He	4.2 MeV Van de Graaff	dual aperture	~5 um
		(proposed)	laser	H, He	4.2 MeV Van de Graaff	electrostatic lens	0.6 um
							~2 um (proposed) or 2.5
	MIT LABA	charged-particle	RF	H, He	1.5 MeV Cockroft-Walton	capillary or slit	um x 1mm
						two sets of micro-adjustable x-y knife-edge collimators, followed by a 5 micron	
	Texas A&M	charged-particle	n/a	H, He	2 MeV positive-ion Tandem Van de Graaff	aperature	3 um
		electron	n/a	e-	100 keV electron microbeam	short length of 5 micron capillary tube	3-5 um
	Berkeley ALS	x-ray	synchrotron	n/a	Advanced Light Source Synchrotron	n/a	n/a
Japan	*JAERI*	charged-particle	n/a	Ne, Ar	vertical beam from AVF Cyclotron	microaperture	5 um
	Tsukuba	x-ray	5.35 keV x-rays	n/a	n/a	Kirkpatrik Baez (K-B) mirror system	possibly 1 um
	SPICE/NIRS	charged-particle	duoplasmotron	H, He	3.4 MeV Tandetron (tandem, single-ended)	magnetic quadrupole lens (triplet)	possibly 2 um
China	*CAS Hefei*	charged-particle	n/a	H, He	3.5 MeV Van de Graaff	microaperture	10 um
Germany	*GSI*	charged-particle	n/a	any	GSI UNILAC	magnetic quadrupole lens	0.5 um
	PTB	charged-particle	n/a	n/a	3.75 MeV Van de Graaff + 20 MeV Cyclotron	magnetic quadrupole lens	1.5-3.0 um
	SNAKE/Munich	charged-particle	n/a	H, He	14 MeV Tandem accelerator	superconducting multipole lens	1 um x 260 nm
	LIPSION/Leipzig	charged-particle	n/a	H, He	Ultrastable single-ended 3.5 MeV Singletron	magnetic quadrupole lens	~50 nm
						5 µm circular object collimator and a 10 µm circular diaphragm, 6 m away from the collimator; then magnetic focusing w/ four	
France	*CENBG*	charged-particle	n/a	H, He	3.5 MeV Van de Graaff	magnetic quadrupoles	~5 um
Italy	*INFN-LNL*	charged-particle	n/a	H, He	7 MeV Van de Graaff CN accelerator	microaperture and slit	2-3 um

Country	Laboratory	Microbeam	shutter	single-particle detection	stage/scanner	References
UK	*Gray Lab*	charged-particle	mechanical, electrostatic?	transmission scintillator, single PMT above	x-y stage	[Folkard 1997a,b; GCL website]
		x-ray	n/a	n/a	x-y stage	[GCL website]
USA	*Columbia RARAF*	charged-particle	electrostatic	P10 gas-filled pulsed ion counter	x-y stage	[Randers-Pehrson 2000, 2001]
		(proposed)	electrostatic	P10 gas-filled pulsed ion counter	x-y stage	[Dymnikov 2000]
	MIT LABA	charged-particle	electrostatic	transmission scintillator, dual PMT coincidence	x-y stage	[Folkert 2005]
	Texas A&M	charged-particle	n/a	n/a	n/a	[Texas A&M site]
		electron	n/a	n/a	n/a	[Texas A&M site]
	Berkeley ALS	x-ray	n/a	n/a	x-y stage and beam scanner	www-als.lbl.gov
Japan	*JAERI*	charged-particle	"beam shutter"	scintillator+PMT above	x-y stage	[Kobayashi 2000]
	Tsukuba	x-ray				[Tsukuba website]
	SPICE/NIRS	charged-particle	electrostatic	scintillator+PMT above	x-y stage	[Yamaguchi 2004]
China	*CAS Hefei*	charged-particle	incomplete	incomplete	incomplete	[Hu 2002]
Germany	*GSI*	charged-particle	electrostatic	channeltron (detects electron cloud from hits on vacuum window)	x-y stage+electrostatic scanner	[Fischer 1988]
	PTB	charged-particle	?	transmission scintillator, single PMT above	x-y stage	[Greif 2004]
	SNAKE/Munich	charged-particle	electrostatic	detector above	electrostatic scanner	[Hauptner 2004]
	LIPSION/Leipzig	charged-particle		STIM/Si3N4 detector	electrostatic scanner	[Butz 2000]
France	*CENBG*	charged-particle		transmission through 3.5 mm long isobutane proportional counter prior to target		[Michelet 2002, Moretto 2001]
Italy	*INFN-LNL*	charged-particle		silicon detector above	x-y stage	[Cherubini 2002]

Table 2.1. Microbeams in operation and under development in research labs around the world.

2.2.4.1 Gray Cancer Institute Microbeam

The Gray Cancer Institute (GCI) Microbeam, part of the Gray Cancer Research Trust in the UK, is one of the oldest established microbeams, having been in routine operation since 1996. Specifically, the microbeam utilizes the Gray Cancer Institute's 4 MeV Van de Graaff accelerator, which provides either singly- or doubly-charged particles (generally protons, He-3 and He-4) with an RF ion source. The layout of the GCI facility is shown in **Figure 2.4** below.

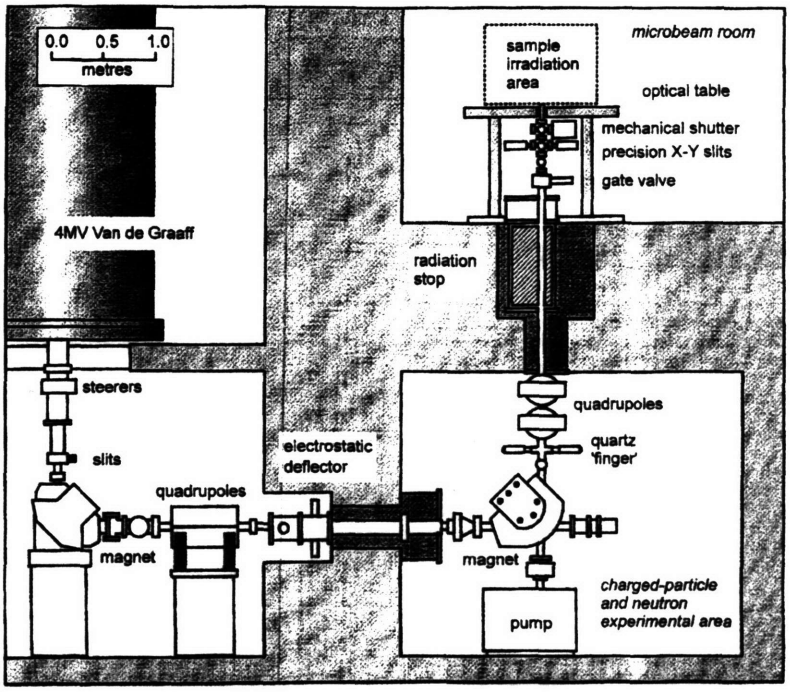

Figure 2.4 The Gray Cancer Institute Van de Graaff beamline.[32]

These ions are directed through a ~10 m beamline using a number of bending magnets, focusing/steering magnets, deflectors, and slits, and then collimated via a glass capillary tube with possible inner bore diameter of 5, 1.5, or 1 μm. Ions passing through the collimator traverse an 18μm-thick scintillating film, which allows determination of particle fluence by a photomultiplier tube positioned above the cell dish. The signal from the PMT-based detection system may be used to trigger a shuttering system that mechanically blocks the beam.[32, 33] The collimator/deflector block used in the GCI Microbeam is shown in **Figure 2.5**.

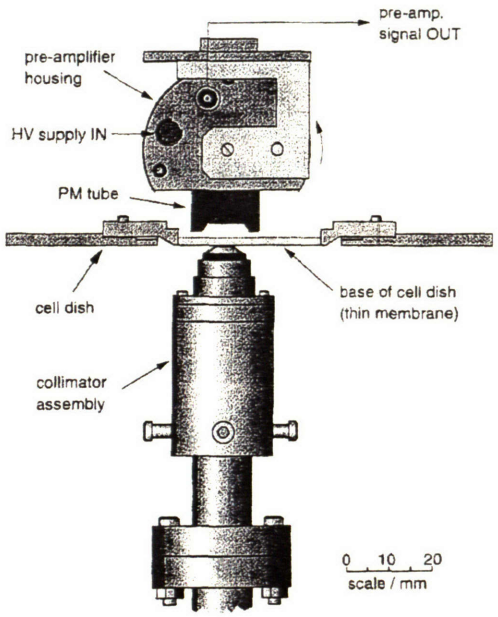

Figure 2.5 The GCI Microbeam collimator-detector assemblies and cell dish.[33]

The individual subsystems of the GCI Microbeam are summarized in **Table 2.1** above. The subsystems work together as shown in **Figure 2.6**:

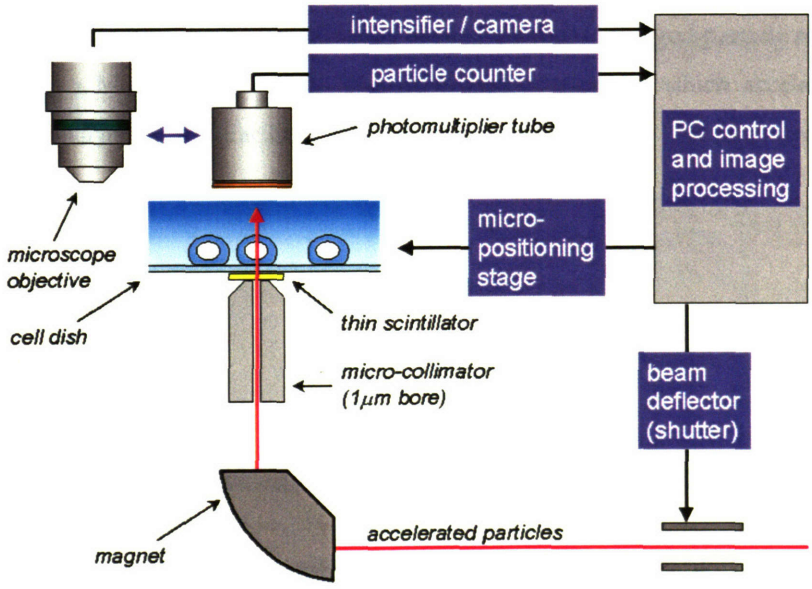

Figure 2.6 An illustration of the GCI Microbeam subsystems.[38]

Characterization of the collimated beam shows that the GCI Microbeam is able to deliver >90% of transmitted particles within a 2 μm diameter area of the center of the target, with the remainder falling within a 5 μm diameter area. The GCI Microbeam has demonstrated that it is capable of

performing single-particle irradiations of the nucleus and/or cytoplasm of specific, individual cells. The maximum throughput of the system is over 15,000 cells/hr.

In addition, the Gray Lab has been developing an x-ray microbeam. Rather that accelerating charged particles, the Ultrasoft X-Ray Microbeam uses diffracted 278 eV carbon K-shell x-rays focused to a sub-micron spot size. The purpose of such a device is to look at clustered DNA damage, which generally takes the form of a number of DNA base and/or backbone chemical modifications and DNA single strand breaks in close proximity to one another, rather than the DNA double strand break (DSB) damage induced by heavy charged particles.[92] This is possible because low-LET radiation such as gamma and x-rays has a "sparsely ionizing" pattern of radiation damage, in which damage manifests in a range of chemical modifications to DNA bases and/or the DNA backbone. When a number of these chemical modifications occur in close proximity to each other, they form a "cluster," which may cause damage to DNA that can overwhelm the afflicted cells' ability to repair themselves, or inadvertently cause greater damage in the repair process.[37, 95, 103]

2.2.4.2 RARAF Microbeam

The Radiological Research Accelerator Facility (RARAF), at Columbia University's Center for Radiological Research in New York, lays claim to the second major charged-particle microbeam. The microbeam utilizes a Model D1 4.2 MeV Van de Graaff accelerator, which accelerates helium or hydrogen ions produced by the Facility's duoplasmatron ion source. The layout of the facility is shown in **Figure 2.7**.

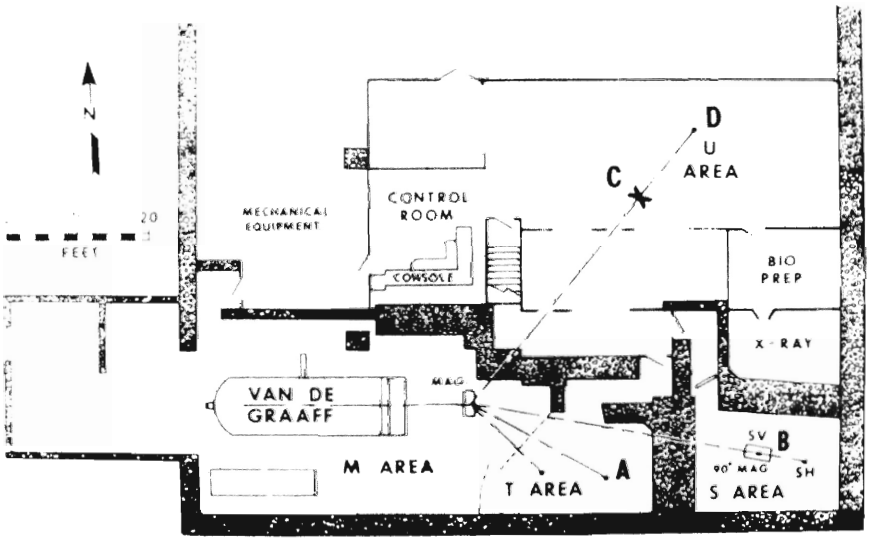

Figure 2.7 Layout of the ground floor of the RARAF microbeam facility. A 90^0 bending magnet is located at "C," directing a vertical beam to the second-floor irradiation area.[34]

Charged particles travel ~2 m to a horizontal bending magnet, and then travel ~10 m to a vertical 90^0 bending magnet that redirects the beam to an irradiation area on the next floor above.

Collimation is accomplished with a set of laser-drilled apertures consisting of two 12.5 μm -thick stainless steel foils with 5 μm and 6 μm holes separated by a 300μm spacer (constructed by Lenox Laser, Glen Arm MD, USA). Cells are plated on a custom cell dish in which the base is composed of a 4 μm-thick polypropylene film. Single-particle detection is accomplished using a P10 gas-filled pulsed ion counter placed above the cells, which requires that the cell medium be removed during irradiation. The counting signal may be used to trigger a set of electrostatic deflection plates that is capable of gating the beam.

RARAF is currently implementing modifications to its microbeam that will improve the spatial resolution of the beam from ± 3.5 μm to ± 0.3 μm by incorporating an electrostatic focusing lens instead of physical collimation, and allow the use of a wider range of charged particles using a laser ion source.[3, 25]

The individual subsystems of the RARAF Microbeam are summarized in **Table 2.1** above. The subsystems work together as shown in **Figure 2.8**.

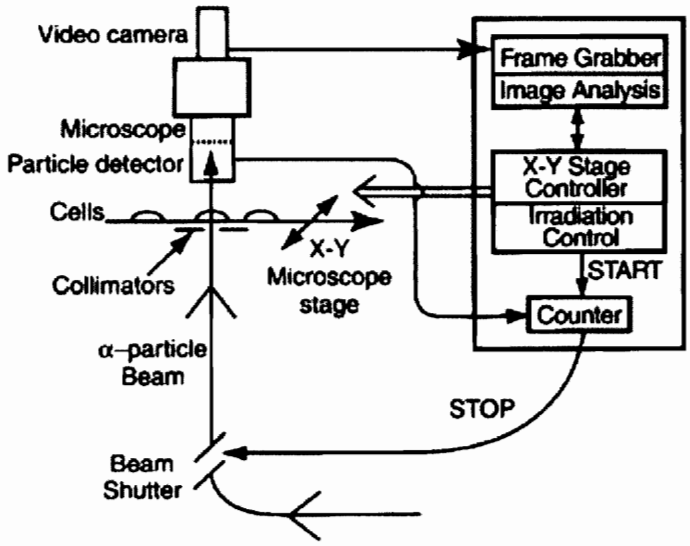

Figure 2.8 An illustration of the coordination of the RARAF Microbeam subsystems.[84]

Using physical collimation methods, the RARAF Microbeam is capable of generating a beamspot in which approximately 91% of transmitted particles lie within a 5 μm diameter area, 7% fall within an 8 μm diameter "halo" region about the center of the target, and the remaining 2% are scattered about a > 8 μm diameter area. The electrostatic deflection plate gating system has a rise and fall time such that there is a 0.04% chance of an extra particle being delivered to the target during an irradiation. The RARAF microbeam is capable of performing single-particle irradiations of the nucleus and/or cytoplasm of specific, individual cells. The throughput of the system is over 10,000 cells/hr.[35, 82]

2.2.5 Applications

Charged-particle microbeams are research tools with a wide range of biological applications. With a very precise microbeam, capable of generating a < 5 μm beamspot, exploration of the temporal and spatial distribution of DNA damage repair processes in response to a subnuclear distribution of radiation becomes possible.[33, 76] The ability to precisely target the number and type of cells allows for well-controlled investigations into the radiation-induced bystander effect and its mechanisms. Additionally, it permits the investigation of how tissue organization affects the type and extent of radiation response. Registration of the location of a charged-particle "hit" may allow visualization of changes in membrane permeability and/or structure integrity. Further details regarding particularly interesting applications of microbeams follow.

2.2.5.1 Radiation-Induced Bystander Effect Studies

The radiation-induced bystander effect is generally defined as the induction of biological effects in cells that are not directly traversed by ionizing radiation.[58, 72]

2.2.5.1.1 Radiation-Induced Bystander Effect Background

According to the currently accepted model,[48] radiation interacts with DNA (defined by Hall to be the "critical target for biological damage"[42]) through two mechanisms:

- "direct" interaction with the critical target, in which the DNA strand itself is structurally altered or disrupted; and
- "indirect" action via free radical damage, in which case free radicals are produced by radiation interactions in sufficiently close proximity to a DNA strand that they are able to reach and chemically interact with the critical target.

Both of these effects happen on a very short timescale, as ion radicals have lifetimes on the order of 10^{-10} seconds, and free radicals survive about 10^{-5} seconds.[42] However, studies over the last decade and a half have demonstrated that the "indirect" effects of radiation may be far more complex than the relatively simple interaction of free radicals with DNA, in that radiation damage on the cellular level seems to result in a cascade of biological processes that impact not only the directly irradiated cells, but cells that are in close contact or continuous with the medium that the irradiated cells are bathed in as well. [58, 72, 74, 80]

It may be necessary to reclassify "indirect" radiation damage into two distinct forms: the "proximal indirect," which encompasses the chemical damage induced by ion and free radicals in close contact with the DNA strand; and "distal indirect," which includes the potentially far-reaching biological effects that are induced by radiation damage and may result in additional damage to the injured cell as well as to other cells in the area. This "distal indirect" form of radiobiological action, known as the radiation-induced bystander effect, was first characterized by Nagasawa and Little in 1992.[74] Using a simple benchtop α-particle irradiator,[62] chinese hamster ovary (CHO) cells were exposed to 0.03-0.25 cGy of α-particles. While only 0.07-0.6% of cell nuclei should have been physically traversed by the α-particles at these doses, 30-45% of the cells in the population were shown to have an increased frequency of sister chromatid exchanges over background.

As the classic radiation effects on DNA described by Hall were insufficient to explain this result, a biologically-mediated secondary pathway must exist by which the cells not "hit" by radiation could still experience observable damage endpoints similar to those induced by radiation.[43, 59, 72, 74, 91, 112] Other recent studies using charged-particle microbeams have shown that the magnitude of this effect can be much greater than expected – studies using the Gray Lab microbeam have shown that targeting as few as four cells (primary human fibroblasts) in a population of several thousand with one or more alpha particles results in apoptosis and micronuclei formation in 25 to 40 times as many nearby cells, with the increase in micronuclei formation corresponding most closely to increased dose.[80]

The radiation-induced bystander effect is generally defined as the induction of biological effects in cells that are not directly traversed by ionizing radiation. A wide range of data exists describing this radiation-induced bystander effect, falling into two general categories: broad beam studies with medium transfer, in which the medium from broad beam irradiated cells triggers an observable biological effect in unirradiated cells;[69, 71] and microbeam studies, in which a controlled amount of

ionizing radiation (specified numbers of charged particles, or discrete amounts of gamma/x-ray radiation) are directed at specific cells or portions of specified cells, with observation of biological effects in neighboring cells.[83]

Medium transfer experiments have demonstrated a range of bystander effects, including induction of apoptosis,[59] chromosomal aberrations, cell cycle delay, and cell lethality.[69, 70, 71] In these experiments, it has been observed that the choice of cell type (epithelial vs. fibroblast, for example) appears to have a significant effect on the biological outcome. Many experiments suggest that the observed effect is initiated by a molecule or set of molecules secreted by irradiated cells. This secreted component must be capable of transferring damage (or inducing pathways that result in damage) to neighboring and distant cells.[69, 70, 72, 73]

Bystander experiments using single-particle irradiations with charged-particle microbeams have demonstrated an equally wide range of bystander effects, including mutation,[110] oncogenic transformation,[90] chromosomal aberrations,[43] and cell lethality.[91] When cells are in close contact, allowing gap junction intercellular communication (GJIC), the bystander effect has been observed to be of a much larger magnitude than the phenomenon demonstrated in medium transfer experiments, and this contact enhancement can be reduced by the use of GJIC inhibitors such as lindane.[4] Microbeam studies performed with non-confluent cultures have also demonstrated transmission of biological effects consistent with mediation by diffusion completely independent of GJIC.[80] This supports the conclusion that there is more than one biological mediator of the radiation-induced biological effect, and that the mechanisms of bystander damage transfer differ between the secreted and GJIC forms of transmission. In addition, the cell type and environment as well as the type of radiation used may play a significant role in how the radiation-induced bystander effect is manifested.

2.2.5.1.2 Implications of the Radiation-Induced Bystander Effect

In general, bystander effects have been demonstrated for both high- and low-LET radiations but tend to be of greater magnitude for densely ionizing radiation such as alpha particles. Evidence exists for a comparable bystander effect in three-dimensional normal tissue,[51, 73, 107] and models have been developed to investigate how such an effect would impact such a system.[8, 9] Bystander studies imply that the "target" for the biological effects of radiation may be much larger than that actually experiencing direct radiation damage, which could have serious consequences for treatment planning and dose control.

2.2.5.1.2.1 Radiation Protection

The most serious implications for radiation protection are demonstrated by the bystander studies of Zhou et al.,[110, 111] which have investigated low dose effects on mutation frequency. A non-linear increase in mutation frequency in the zero to one alpha traversal range suggests that a simple linear extrapolation of radiation risks from high to low dose may be invalid (see **Figure 2.9** and **2.10** below).[110, 111]

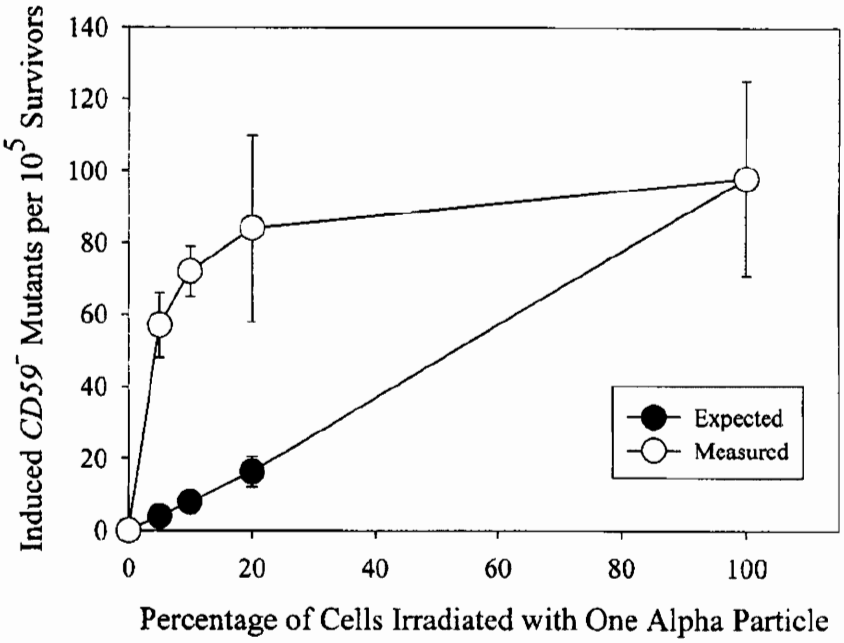

Figure 2.9 Induced *CD59* mutant fractions per 10^5 survivors obtained from populations of AL cells in which 0, 5, 10, 20, or 100% had been irradiated with exactly one α particle through its nucleus using the RARAF Microbeam. Induced mutant fraction = total mutant fraction minus background incidence, which was 46+/-10 mutants per 10^5 clonogenic survivors in A_L cells used in these experiments. Data are pooled from three to seven independent experiments. Error bars represent +/- SD. The calculated curve deviates slightly from a straight line fitting because of the slight cytotoxic effect of single particle traversal among the irradiated cells.[111]

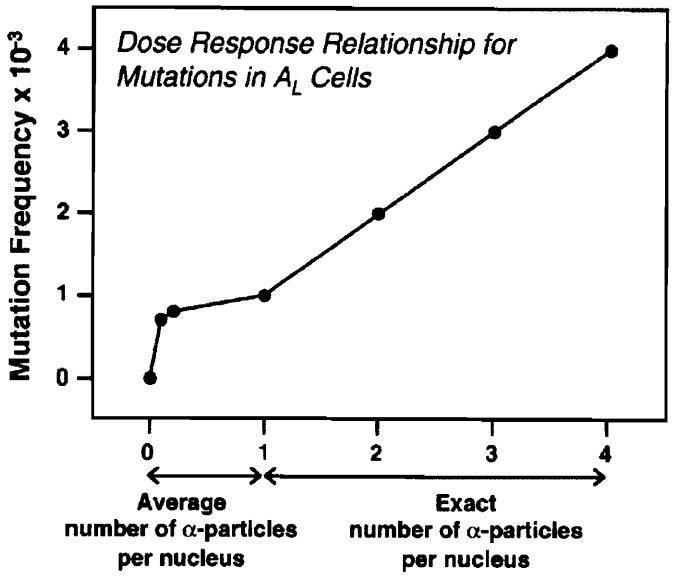

Figure 2.10 Mutation frequency as a function of the number of alpha particles traversing cell nuclei. [from Hall 2003, based on data of Zhou et al. 2000, 2001][43,110,111]

Current risk estimates are based on extrapolating high-dose cancer induction data (Uranium miners and Hiroshima/Nagasaki bombing survivors) in a linear manner to low doses.[12] If a low-dose supralinear effect exists (as suggested in **Figure 2.10)**, these estimates could be much lower than they should be for an accurate assessment of cancer risk due to increased mutation frequency. While a direct relation between mutation frequency and cancer induction has not yet been established, increased mutation frequency is indicative of genomic instability, which many studies link directly to cancer formation (hypermutation is a key contributor to malignancy).[6, 112] Various extrapolation models are shown below in **Figure 2.11**.

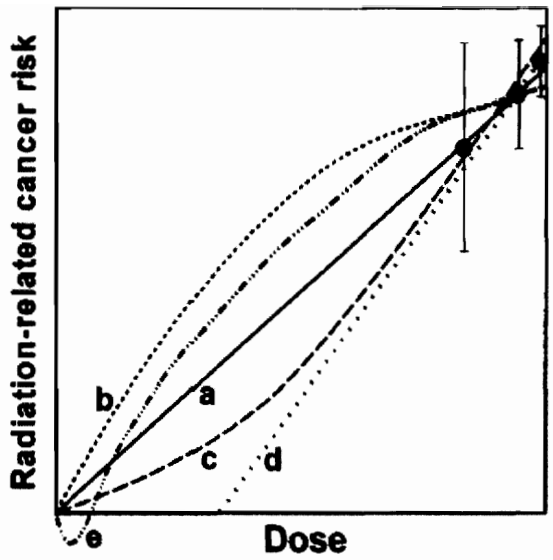

Figure 2.11 Schematic representation of different possible extrapolations of measured radiation risks down to very low doses, all of which could, in principle, be consistent with higher-dose epidemiological data. Curve **a**, linear extrapolation; curve **b**, downwardly curving (decreasing slope), curve **c**, upwardly curving (increasing slope); curve **d**, threshold; curve **e**, hormetic.[12]

In addition to a possible supralinear effect (curve **b** in **Figure 2.11**), there is also a possibility that risk estimates overestimate the dose, as a host of mechanisms have been proposed to justify a hormetic or adaptive response.[12] In the former of these two scenarios, a certain amount of low-dose radiation exposure may theoretically upregulate radiation-related DNA repair mechanisms and/or immune responses. In the latter case, a brief low-dose exposure stimulates the DNA repair machinery of the exposed cells for an extended period, so that they may more effectively cope with a later insult.

2.2.5.1.2.2 Radiation Therapy

The radiation-induced bystander effect poses some concern for radiation therapy, as it could possibly affect the theoretical benefits achieved by precisely targeted therapies, in either a negative or positive manner. It is possible that the secondary biological effects could enlarge the effective field and induce unexpected and/or uncontrolled abscopal ("out-of-field") effects, characterized as responses that follow irradiation but occur outside of the zone of actual radiation absorption. This could result in a loss of therapeutic control at the edges of the exposed field, as the biological response of the irradiated tissue may not correlate with the spatial distribution of radiation dose. Much of current clinical radiation therapy is based on "broad field" irradiations of relatively high dose (1.5-2.0 Gy daily). With such a large uniformly irradiated volume, it is possible that bystander effects only contribute to heightened "dose" at the edges of the field, in the cells that are in closest contact with

the irradiated cells. Several "targeted" therapies are in development or at the early stages of clinical application, including:

- Radioimmunotherapy (RIT), whose target specificity is based on antibody affinity to specific cellular targets, and incorporates radionuclides to deliver therapeutic radiation dose;
- Radionuclide-labeled receptors or growth factors that are specific to a target tissue (generally a tumor);
- Neutron Capture Therapy (NCT), a bimodal therapy in which a patient is given a highly neutron-absorbing isotope (any isotope with a large neutron absorption cross-section, such as Boron-10) incorporated into a compound that is selectively absorbed by tumor tissue, coupled with exposure to a neutron beam. The resulting neutron/isotope interaction is intended to occur preferentially in tumor tissue, resulting in a highly specific deposition of energy that selectively destroys tumor tissue;
- Charged-Particle Therapy, (including hadron therapies such as proton beam therapy) that use highly focused beams of charged particles in conjunction with a delivery system capable of directing the beam at a precisely located tumor mass from multiple angles (many degrees of freedom), allowing for millimeter or submillimeter deposition of therapeutic radiation dose.

Any of these therapy methodologies can create small, non-uniform distributions of energy such that many irradiated cells will be in close proximity to neighboring, un-irradiated cells. If proximity to irradiated cells is sufficient for transmission of the radiation-induced bystander effect, and proportional to the magnitude of the observed biological outcomes (which seems to be the case with studies that look at the role of gap-junction intercellular communication (GJIC)), this could result in a significant increase in net abscopal effect where the mass of tissue affected by radiation-induced biological damage is as large or larger than the mass of tissue to which the radiation dose was administered.[8, 9]

To illustrate this point, assume a tumor volume, approximated as a sphere, 5 cm in radius **r**.

$$\text{Surface Area (SA)} = 4\pi r^2 = 314 \text{ cm}^2;$$

$$\text{Volume (V)} = \frac{4}{3}\pi r^3 = 524 \text{ cm}^3$$

Following irradiation of this volume, and assuming that the radiation-induced bystander effect "biological mediator" is able to diffuse a distance $\mathbf{x_d}$ of 0.2 mm (a conservative estimate based on LABA studies), the bystander-affected volume $\mathbf{V_b}$ is now that contained within radius $\mathbf{r_b}$, where:

$$r_b = r + x_d \qquad \textbf{Equation 2.1}$$

The difference between the irradiated tumor volume **V** and the bystander biological mediator-affected volume $\mathbf{V_b}$ is then given by **Equation 2.2**:

$$V_b = \frac{4}{3}\pi(r_b)^3 = 530 \text{ cm}^3$$

$$V_b\text{-}V = V_a \qquad \textbf{Equation 2.2}$$

Based on these assumptions, the bystander abscopal volume ($\mathbf{V_a}$) would be 6 cm^3, or approximately 1% of the total tumor volume.

It is possible to take the same tumor volume **V** (524 cm^3) defined above and distribute the total volume among a number of smaller tumors (number of sites **n**). Then, solving for the radius of the individual tumor site $\mathbf{r_n}$:

$$r_n = \sqrt[3]{\left(\frac{3}{4\pi}V/n\right)} \qquad \textbf{Equation 2.3}$$

The resulting total bystander biological mediator-affected volume $\mathbf{V_{b,n}}$ for **n** irradiated tumor sites is given by **Equation 2.4**:

$$V_{b,n} = n(\frac{4}{3}\pi(r_n + x_d)^3) \qquad \textbf{Equation 2.4}$$

and the total bystander abscopal volume **Va,n** for **n** irradiated tumor sites is given by **Equation 2.5**:

$$V_{b,n}\text{-}V = V_{a,n} \qquad \textbf{Equation 2.5}$$

The resulting increases in surface area and bystander abscopal volume $\mathbf{V_{a,n}}$, (assuming none of the bystander biological mediator-affected volumes overlap), is illustrated in **Table 2.2.**

# of Tumor Sites (n)	Tumor Surface Area (cm^2)	Abscopal Volume (cm^3)	Abscopal Volume (% tumor volume)
1	314	6	1%
10	677	14	3%
100	1,458	30	6%
1,000	3,141	65	12%
10,000	6,768	147	28%
100,000	14,582	349	67%
1,000,000	31,416	913	174%

Table 2.2 Size of the "abscopal" bystander-affected volume ($\mathbf{V_{a,n}}$) with the number of distributed irradiated sites in a nonuniformly-irradiated field. (For a fixed total tumor volume of 524 cm^3 and effective "biological mediator" diffusion distance of 0.2 mm).

Given that a 70 kg male has a total body volume of approximately 70,000 cm^3, there is obviously a limit to the size of the abscopal volume. While this is a very simple approximation, the concern remains - with RIT, NCT, and the other labeled-protein techniques, the number of irradiated sites could be in the tens or hundreds of thousands, possibly even in the millions. It has been demonstrated that the radiation-induced bystander effect plays a biologically-relevant role in the response of *in vivo* normal and tumor tissue to radiation,[51, 73, 107] and cell-cell contact and/or proximity has been suggested to play a role in the magnitude of the response.[107] The potential for a corresponding geometric increase in bystander-affected volume and the possible negative impact on the benefits of increasingly-targeted therapies makes the need to understand and, if possible, control this effect highly critical for the future of radiation therapy.

2.3 Chapter Summary

The resulting aim is to develop a proof-of-principle prototype for a laboratory-size microbeam suitable for hospital or industrial installation. As many of the radiobiological research options presented by charged-particle microbeams have direct application to clinical research, a design that is safe and appropriate for hospital use is essential. A description of the accelerator and beamline components will be provided in **Chapter 3**, and the methods by which each beamline component was characterized will be discussed.

Chapter 3. LABA Accelerator and Beamline

This chapter will discuss the design and characterization of the components of the LABA Microbeam that are responsible for generating and delivering a vertically-oriented charged particle beam to the experimental endstation. A diagram of the major components that make up the LABA Microbeam is shown in **Figure 3.1**, including the accelerator itself, the integrated Faraday cup, the electrostatic deflector system, the quadrupole triplet, the 90^0 bending magnet, and the experimental endstation. The relevant components to be discussed in this chapter are surrounded by the blue dashed box.

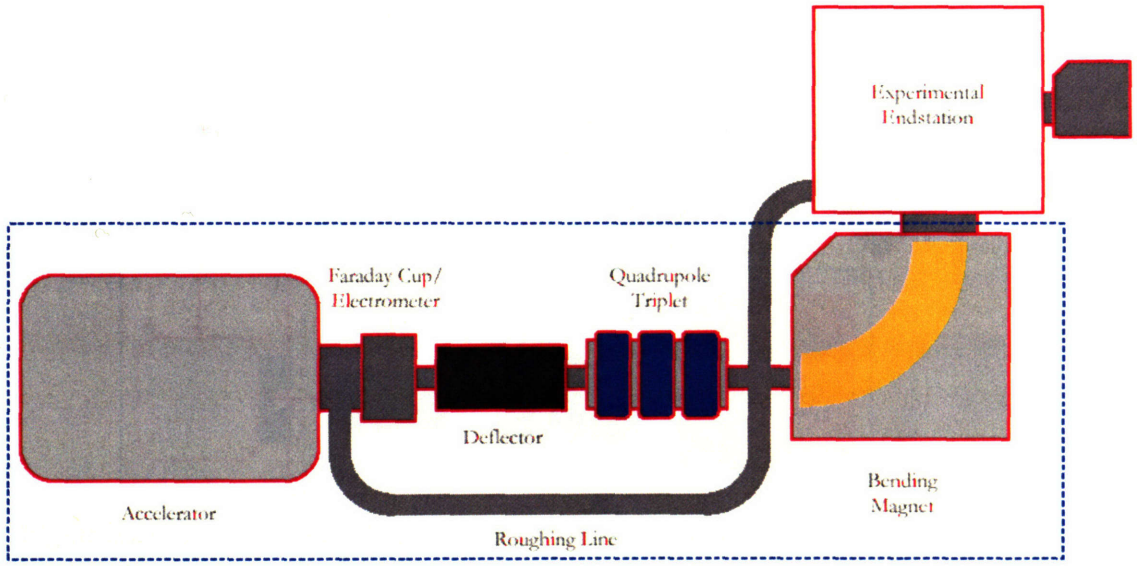

Figure 3.1 Overview diagram of the LABA Microbeam accelerator, beamline, and experimental endstation. Relevant components discussed in this chapter are surrounded by the blue dashed box.

The Laboratory for Accelerator Beam Applications charged-particle microbeam accelerator is a multi-stage linear accelerator, of the type first built by J. D. Cockcroft and E. T. S. Walton in 1932.[18, 19] The accelerator is capable of accelerating protons, deuterons, and alphas (He-3 and He-4), although its primary use to this point has been to generate beams of protons. The original application of the device was for proton-induced x-ray emission (PIXE) surface analysis, and the accelerator is well suited for use in microbeam techniques due to the stability (energy and positioning) and relatively low intensity of the generated beam current, precise voltage regulation, as well as the small size of the in-lab device.[10]

Control of the various beamline subsystems is managed on the "Vacuum," "Accelerator Control," and "Facilities" screens of the central computer-based control system, discussed in detail in **Section 3.3** later in this Chapter. These screens control the components marked **b**, **d**, **e**, and **f** on **Figure 3.2** (surrounded by a blue dashed box), corresponding to the accelerator, deflector, quadrupole triplet, and bending magnet, respectively.

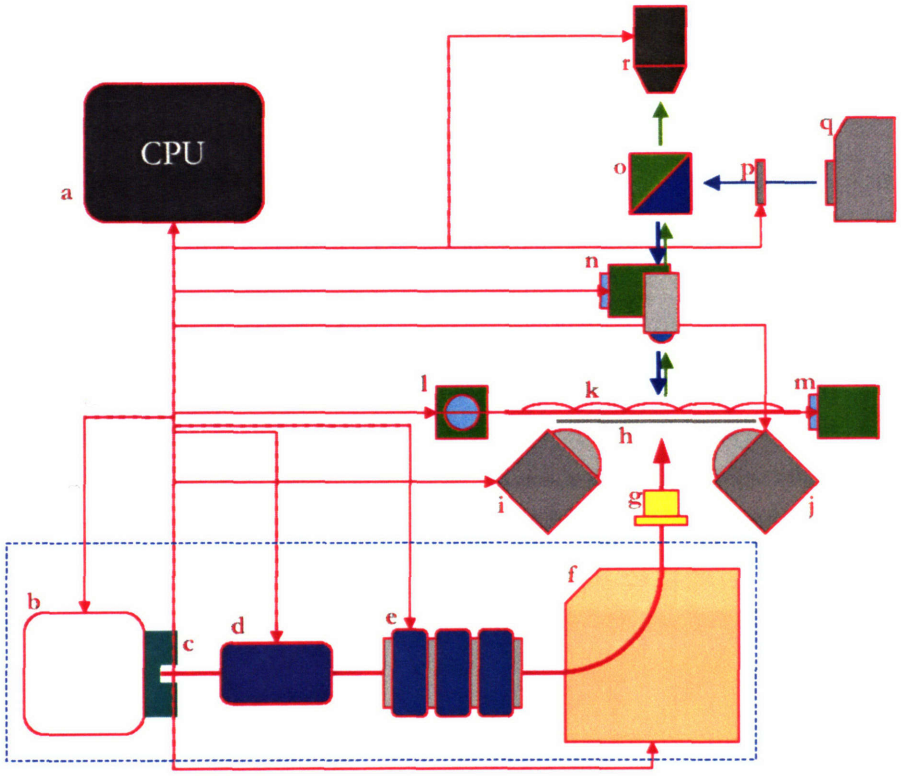

Figure 3.2 Control diagram (Chapter 3 components surrounded by blue dashed box). a) CPU, b) Accelerator, c) Faraday cup, d) Deflector, e) Quadrupole Triplet, f) Bending Magnet, g) Collimator assembly, h) Scintillating plastic, i) PMT 1, j) PMT 2, k) Cells on cell dish, l) X-direction stage motor, m) Y-direction stage motor, n) Objective on motorized focus, o) Dichroic mirror, p) Light shutter, q) Light (UV) source, r) CCD camera.

3.1 Accelerator Components

The accelerator, shown in **Figures 3.3** and **3.4**, was designed and constructed by Newton Scientific, Inc. (NSI, Cambridge MA, USA) and the beamline and initial versions of the components between the accelerator and before the bending magnet were designed and constructed by Pyramid Technical Consultants (PTC, Waltham MA, USA), including the Faraday cup, a set of deflector plates, and the quadrupole triplet. Prior to coming on-line the accelerator and beam tube were donated to MIT, at which point the elements "upstream" of the LABA Microbeam experimental endstation that are

responsible for producing the charged-particle beam prior to collimation and delivery to a biological target were designed, constructed, and/or characterized.

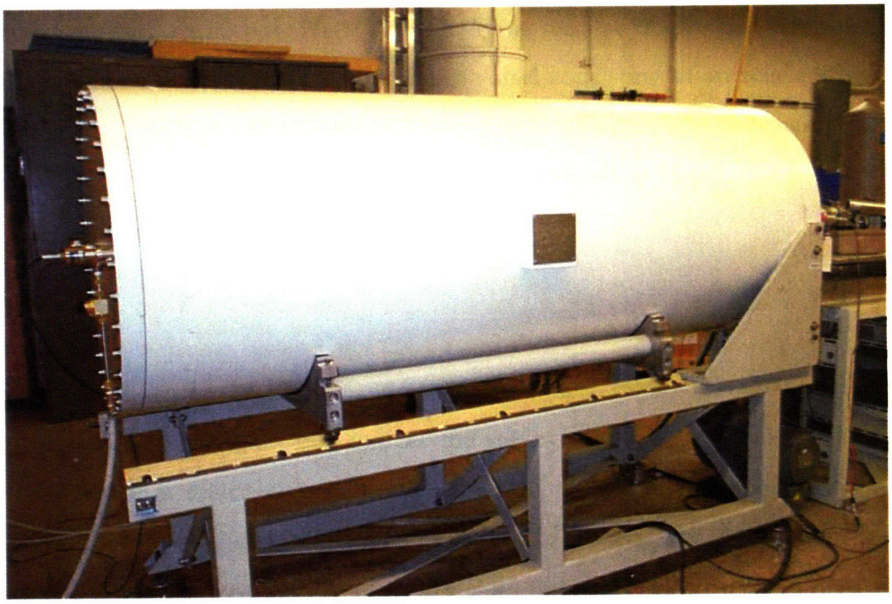

Figure 3.3 The LABA single stage electrostatic accelerator, with the vessel sealed for operation. The pressure vessel is approximately 1.8 meters long, and is normally pressurized to 95 psi with SF_6.

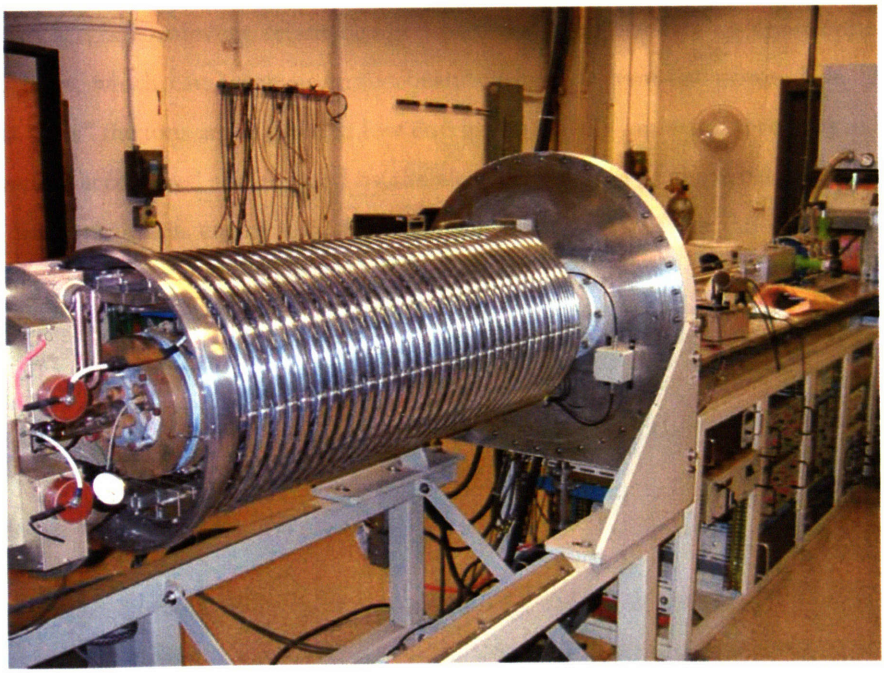

Figure 3.4 The LABA single-stage electrostatic accelerator, with the pressure vessel opened to expose the accelerating column and terminal.

3.1.1 Ion Source/Accelerator

The LABA Microbeam makes use of a 1.5 MeV single-stage electrostatic accelerator, shown in Figures 3.3 and 3.4. This accelerator is capable of ionizing and accelerating a number of particle types (generally protons, deuterons, He-3, and He-4), as well as singly- and doubly-charged states. The accelerator column is housed within a pressure vessel consisting of an accelerating tube, a high-voltage power supply, the high voltage terminal assembly, ion source, and associated electronics. The pressure vessel contains SF_6, an insulating gas, usually pressurized to 95 psi.

3.1.1.1 Design

The ion source (see **Figures 3.5** and **3.6**) located in the high voltage terminal consists of a quartz chamber in which an RF oscillator coil ionizes the gas by stripping it of electrons. The resulting plasma is stabilized by a set of electrostatic field plates. The ionized gas is forced towards the Cockcroft-Walton accelerating elements by an extraction probe that can be functionally considered a point charge; as a result, the ions are extracted in the 2π direction towards the beamline. A focusing element, acting as a lens, is located immediately outside of the quartz ionization chamber and is always at power in order to generate a relatively forward-biased beam of charged particles. Focusing the beam also serves to prevent errant charged-particles from discharging against the electrostatic accelerating rings, which can result in erratic beam current or transient power loss. After passing through this "lens" the ions are injected at low energy (15-30 keV) into the acceleration stack and the resulting beam is accelerated and focused by the electrostatic field of the accelerating tube (designed to attain a final maximum energy of 1.5 MeV (singly-charged ions) or 3.0 MeV (doubly-charged ions)).[52, 109]

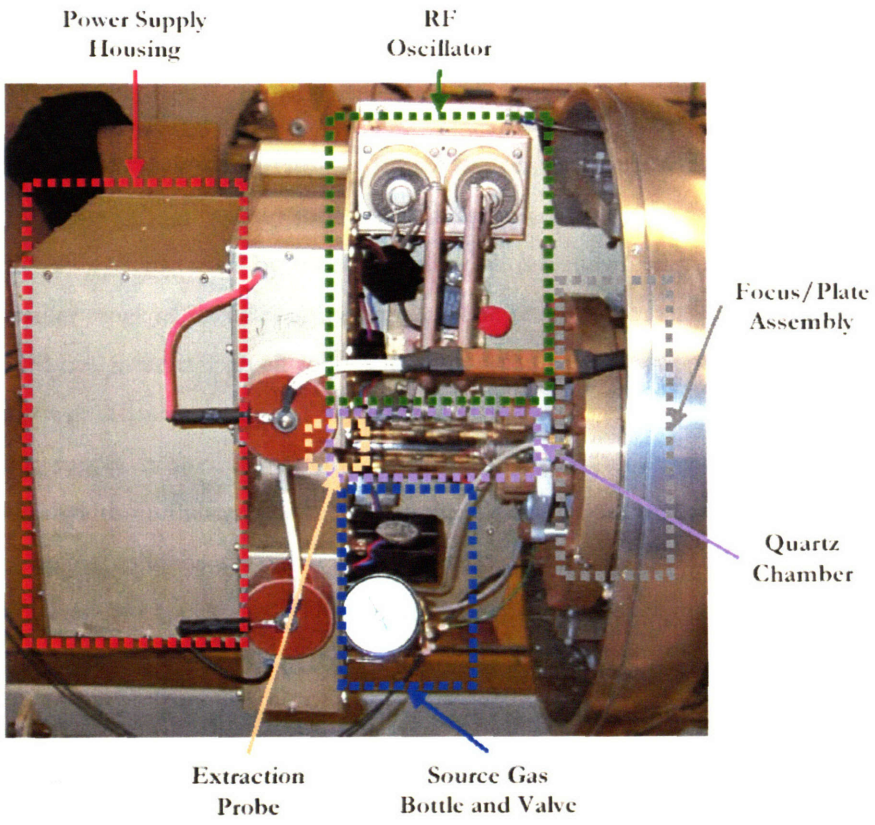

Figure 3.5 LABA Microbeam terminal components exposed.

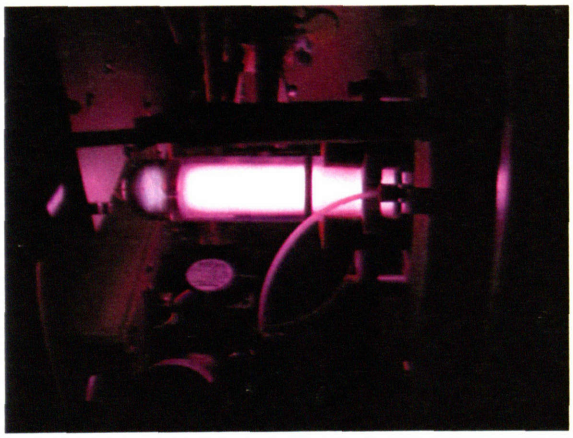

Figure 3.6 Quartz ionization chamber containing the hydrogen plasma generated by the RF oscillator coils.

In addition to housing the ion source for the charged-particle accelerator, the high voltage terminal also contains the source gas in a pressurized bottle. While this is necessary due to the design of the accelerator, it may be inconvenient when the source gas runs out or if one wishes to use an alternate accelerant. Accessing the accelerant in order to change or refill the gas requires the removal of SF_6 from the tank, after which the vessel must be brought up to atmospheric pressure and the tank and

terminal housing removed. Gas flow is regulated by a needle valve controlled from the central control system.

The LABA charged-particle accelerator is much smaller (approximately 1.8 m long, 0.77 m in diameter and weighing about 500 kg) and more manageable than the Van de Graaff,[32, 34] Pelletron,[45, 46] and Cyclotron[54] systems used by other microbeams (as shown in **Table 2.1, Chapter 2**), but produces a smaller range of particles and energies. The reduction in size and complexity is possible because the NSI design utilizes an all-solid-state high voltage power supply that is significantly more compact and power efficient than other hardware designs. A 30-stage symmetrical series-fed cascade rectifier power supply is used to supply continuous current to the 1.5 MV terminal. A high frequency, pulse-width modulated converter supplies power to the multiplier stack through two AC coupling capacitator columns that charge each of the power supply stages. The AC voltage is rectified and filtered and appears as a DC voltage on the high voltage terminal. With this series-fed design, excellent voltage regulation ($\Delta V/V < 0.005\%$) is achieved without the need for the "tank liner" voltage stabilizer that is required to achieve efficient voltage regulation in mechanically charged systems.[52, 109] Voltage regulation will be critical for studies requiring precise knowledge of particle energy and hence particle LET.

3.1.1.2 Characterization Methods

An understanding of the shape and intensity of the charged-particle beam at several stages along the beamline is critical to the proper characterization of the beam. A number of methods are available for this analysis, including:

- Faraday cup
- Quartz window
- Track etch techniques (CR39, LR115)
- Radiochromic film techniques (MD55, HD-810)

To measure the current of the charged-particle beam generated by the accelerator up to the beginning of the beamline, an integrating Faraday cup that can be inserted into the beam path without breaking vacuum was used. This Faraday cup, shown in **Figures 3.7a** and **b**, was attached to a Keithley analog electrometer. (Keithley Model 602, Keithley Instruments Inc., Cleveland, OH USA) This allowed for measurement of beam current prior to manipulation by beamline components. Under pressure conditions that permit safe operation of the accelerator (typically,

stable tank pressures less than $5x10^{-5}$ Torr), beam currents range from a few nanoamperes to several microamperes (10^{-9} – 10^{-6} A), depending primarily on tank pressure and extraction voltage.

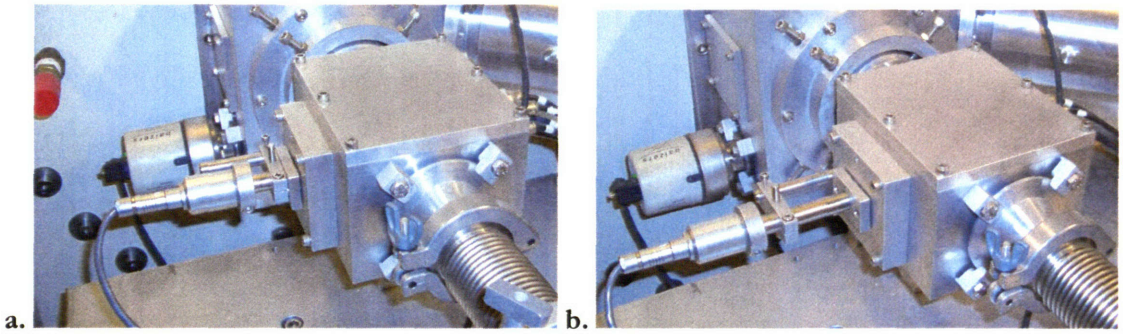

Figure 3.7 Faraday cup current measurement system at the accelerator exit, **a)** Probe in beam path allowing for current measurement, **b)** Probe out, beamline open.

Verification of beam throughput, position, and general profile at the end of the beamline immediately prior to collimation in the experimental endstation is easily accomplished through the use of a quartz window. When charged particles interact with the quartz, the resulting excitations/ionizations create a luminescence that, provided the charged particle beam is of sufficient intensity, is visible to the naked eye. This allows for very rapid verification of the location and general profile of the incident beam at the window. The setup for quartz window irradiation in the experimental endstation is shown in **Figure 3.8**.

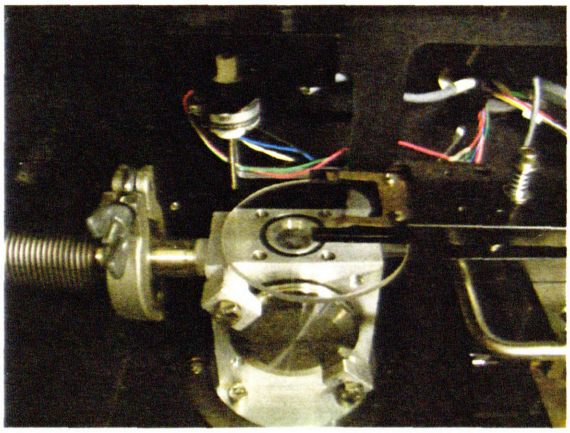

Figure 3.8 Quartz window irradiation setup in the experimental endstation. The collimator assembly is removed to allow the vertically-oriented beam to strike the quartz window.

Both track-etch and radiochromic techniques are based on radiation-induced chemical reactions, which generate a semi-permanent record of the spatial delivery of radiation dose. In order to

determine the dimensions of the resulting image, the track-etch plastic or radiochromic film is compared to a standard, or "graticle," as shown in **Figure 3.9**.

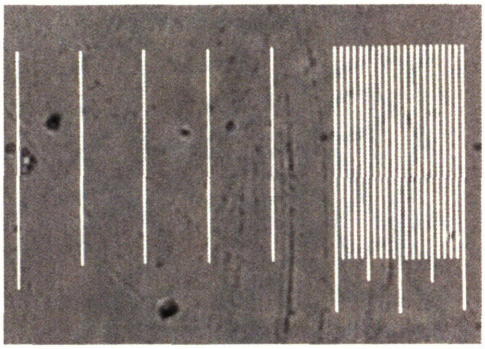

Figure 3.9 Microscopic standard, or "graticle," at 10x magnification. Spacing between the closely packed lines is 10 μm.

The graticle itself is mounted on a microscope slide, and a set of images of the graticle at 5x, 10x, 40x, 63x, and 100x magnification was taken using a SPOT CCD camera (Diagnostic Instruments, Sterling Heights, MI USA) attached to a Zeiss Axioplan 2 microscope (Zeiss Inc., Oberkochen Germany). These images were used as sizing standards to determine the dimensions of all images taken in the course of the characterization of the LABA microbeam.

Track etch techniques are based on the effects of ionizing radiation passing through a polymer-based material. Radiation interactions result in excitation, de-excitation, and polymer chain breaks along the track. These interactions produce regions where chemically reactive sites are formed. (Shown in **Figure 3.10**)

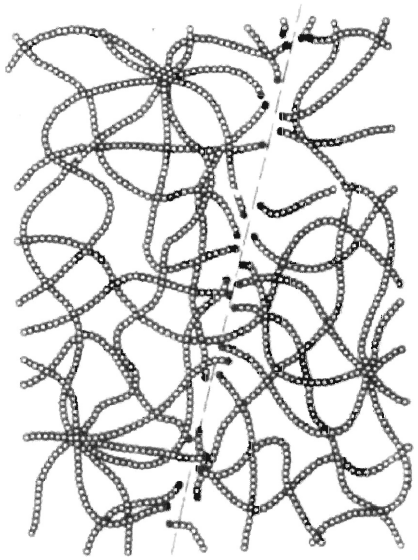

Figure 3.10 Effect of the passage of a charged particle through a polymer.[30]

Treating chemically reactive sites with a strong base such as NaOH results in degradation of the polymer about the site, creating an etched pit that can be visualized with a microscope. Two types of track-etch film were used in our verification processes – Type I LR115 film and CR39 plastic.

Type I LR115, produced by the DosiRad Corporation (Lognes, France), consists of a 6 μm red cellulose nitrate ($C_6H_8O_9N_2$) layer on a 100 μm clear polyester base. It is highly sensitive, detecting charged particles including low-energy protons.[30] While LR115 has several disadvantages, including high sensitivity to abrasion, temperature, oxidation, and a range of chemical actions, with careful handling the following properties make Type I LR115 very useful for frequent beam verification:[5, 30]

- High image contrast (white pits on a red background)
- Relatively fast etching time (less than 1 hour)

Type I LR115 development parameters in the literature suggest the use of 2.5N NaOH in a 60°C bath for 25-40 minutes,[5, 22] but optimization to the LABA microbeam irradiation suggests that etching the exposed film in 60°C 1N NaOH for ~40 min provides the most defined and reproducible pits. A representative image of a charged-particle slit irradiation is shown in **Figure 3.11**.

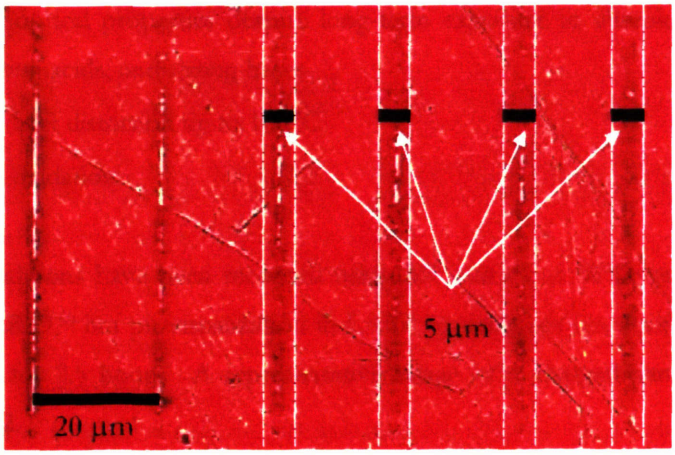

Figure 3.11 Example LR115 image of a 200 Gy charged-particle irradiation through a ~1.5 μm x 1mm slit. Spacing between stripes = 20 μm. All tracks within 5 μm field demarcated by white lines, average track profile width = 3.2 μm (10x magnification, color adjusted)

CR39 (Columbia Resin #39) plastic is made by polymerization of the dietilenglycol bis allylcarbonate (also known as allyl diglycol carbonate, or ADC). The monomer is an allyl resin containing the functional group **[CH_2=CH-CH_2-].** The monomer itself contains two of these functional groups and has the following structure:

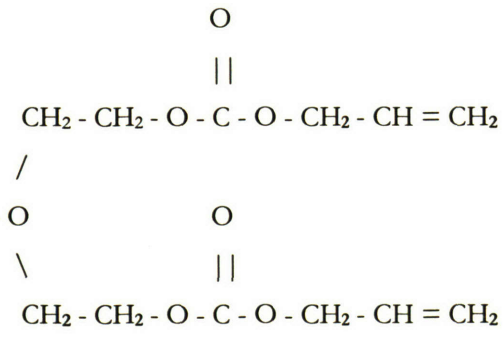

Because of the presence of the two allyl functional groups, the monomer can not only polymerize but also cross-link which results in an optically clear, amorphous, thermoset plastic with a high uniformity of response (<1% variation) and high sensitivity to protons in the energy range produced by the LABA accelerator (~1 MeV).[15] CR39 is a sound choice for producing archival verification images that will be kept for extended periods and for generating very precise pits because of the following properties:[16]

- high abrasion resistance
- high-quality optical properties (allowing for detailed imaging of fine pit/beamspot structure

- retention of optical properties despite long-term exposure to chemicals such as solvents, highly oxidizing acids, and strong bases
- resistance to heat distortion up to 100°C
- resistance to oxidation

Optimal etching conditions have been recorded using 6N NaOH at 70°C, generating the steepest response curve for CR39,[39] but pit visualization in LABA applications seems best accomplished with 5N NaOH at 60°C for 2.5 hours. A representative image of a charged-particle slit irradiation is shown in **Figure 3.12**.

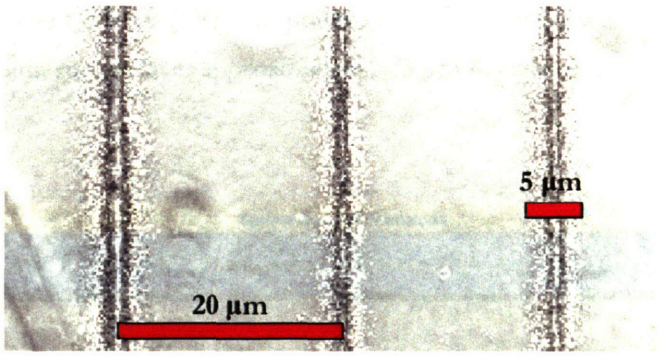

Figure 3.12 Example CR39 image of a series of ~300, 100, and 200 Gy charged-particle irradiations through a ~1.5 µm x 1mm slit. (20x magnification)

Radiochromic techniques are similar to track-etch techniques in that radiation interactions with the target material result in chemical changes, but these chemical changes directly cause the radiochromic target material to observably change color. For radiochromic beam verification experiments, a modified version of the Gafchromic MD55 film (International Specialty Products) was used. This film consists of a radiation-sensitive gel active layer, approximately 16 µm thick, on clear, transparent 2.6 mil (~67 µm) polyester. Normally two pieces of this film are then laminated together with two layers of two-sided adhesive tape, each approximately 1 mil (~25 µm) thick, surrounding a 1 mil thick clear, transparent polyester base, as shown in **Figure 3.13a**. However, the charged particles produced by the LABA accelerator do not have sufficient range to penetrate the clear polyester base, so a modified version of the MD55 film was obtained prior to lamination, as shown in **Figure 3.13b**.

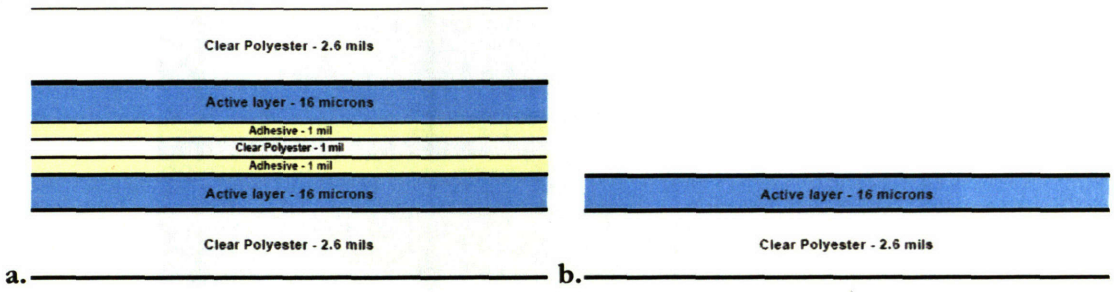

Figure 3.13 a) Standard MD55 film configuration, **b)** Modified MD55 film configuration, suitable for low-energy charged-particle irradiation. (GafChromic, International Specialty Products)

A standardized form of the "modified" MD55 radiochromic film has more recently become available as HD-810 film. This film consists of a radiation-sensitive gel active layer, approximately 6.5 μm thick, on clear, transparent 3.8 mil (~97 μm) polyester. The active layer is protected from oxidation and abrasion by a gelatin surface layer approximately 0.75 μm thick, as shown in **Figure 3.14**.

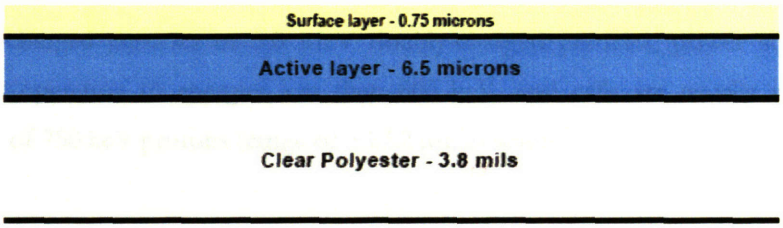

Figure 3.14 HD-810 film configuration. (GafChromic, International Specialty Products)

In both of these radiochromic film types, the active layer is a radiation sensitive monomer. Upon exposure to radiation, the active component polymerizes to form a dye polymer that causes the irradiated portion of the film to turn blue. (The reaction has an incubation period of at least 1 μsecond, and the polymerization proceeds with first order kinetics and a rate constant of ~10^3 sec^{-1} for the first few minutes after exposure.[61] These film types were particularly useful for beam throughput verification due to instantaneous response of the film to radiation exposure. A representative image of a charged-particle slit irradiation is shown in **Figure 3.15**.

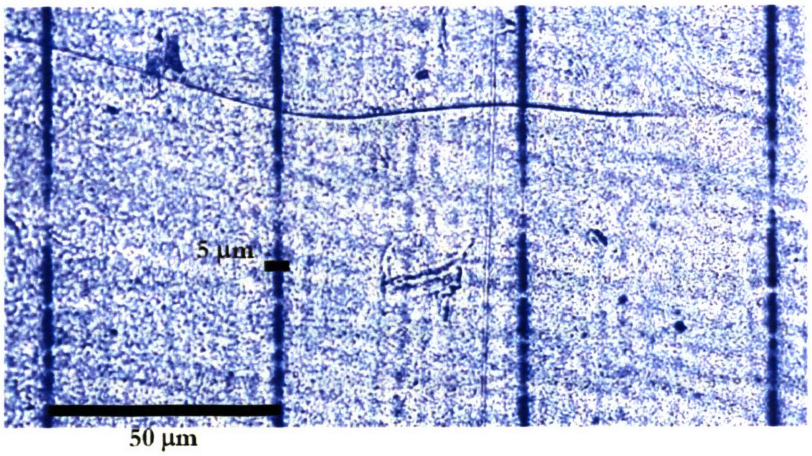

Figure 3.15 Example MD55 (modified) image of a series of 100 Gy charged-particle irradiations through a ~1.5-18 µm x 1mm slit. (5x magnification, color adjusted)

3.1.1.3 Ion Source Characterization

While the LABA Microbeam accelerating column was originally designed for the generation of up to 1.5 MeV singly-charged particles or 3.0 MeV doubly-charged particles, power supply limitations generally restrict operation to energies less than 800 keV, and cells are usually irradiated with a collimated beam of 750 keV protons (range of ~17.2 µm in water).

In developing a microbeam for precisely controlled radiobiological studies, it is important for the radiation source to be well-characterized in terms of fluence as well as energy. The beam current must be manageable so that the end goal of limiting the irradiation of a target to a single particle is possible. For the LABA Microbeam, this degree of control cannot be obtained at the level of the accelerator, as the lowest achievable current is on the order of nanoamperes, or 6.3 billion (6.3×10^9) protons/second. As the existing electronics used in deflecting and "gating" the beam operate at best on the order of microseconds (more often on the millisecond scale), a 10^3-10^6 order or magnitude reduction in beam current will still be necessary at some point along the beamline.

The Faraday cup was used to characterize the charged-particle beam generated by the accelerator up to the beginning of the beamline (at the exit of the accelerator). This allowed for measurement of beam current prior to manipulation by beamline components. The first step of accelerator beam characterization required an understanding of the intensity of the charged-particle beam as it exits the accelerator, and determining the operating state that provided the most stable beam. This intensity can be affected by a number of operating conditions, including:

- previous operating state

- the amount of source gas introduced into the accelerator
- the terminal voltage (typically 750 kV)
- the voltage applied to the focus electrode (ranging from 6 – 12 kV)
- the voltage applied to the extraction electrode (ranging from 0 – 5kV)

By varying each condition in turn, it was found that the extraction voltage was the single most important factor contributing to the intensity of the beam, as indicated by the current measured on the Faraday cup. All other factors were kept as consistent as possible during biological irradiations. A relationship between extraction voltage and the current measured on the electrometer is shown in **Figure 3.16**, with the extraction voltage region between 0.4 kV and 1.0 kV showing the most linear relationship, and the extraction voltage region between 0.3 kV and 0.6 kV showing the least degree of deviation. For experimental irradiations, knowledge of the current at the Faraday cup is not as useful as an accurate assessment of the actual particle fluence at the target, but it is important to ensure that a stable beam current is delivered. Thus, based on these observations, subsequent biological experiments were performed primarily at extraction voltages around 0.5 kV.

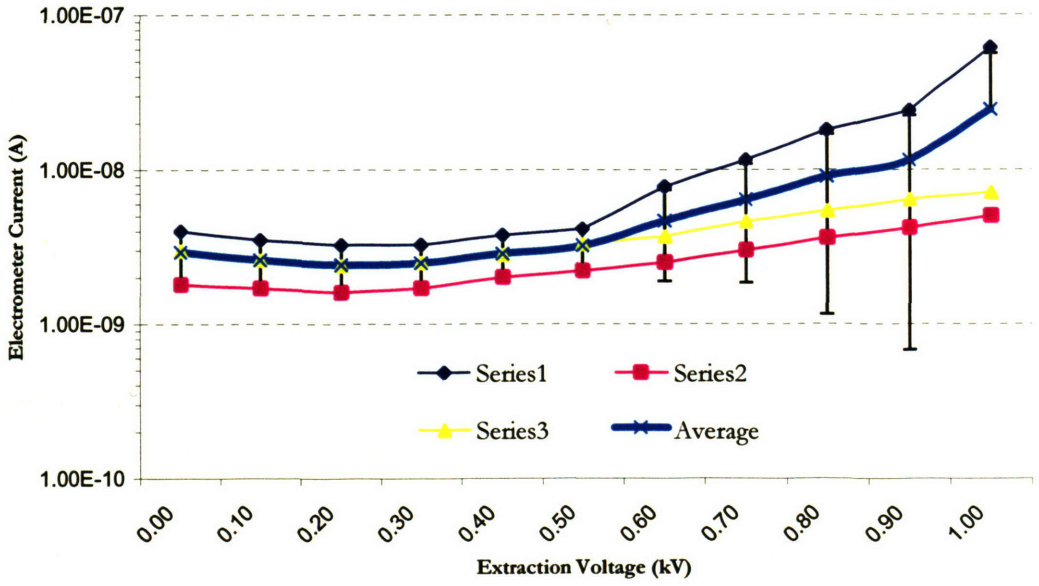

Figure 3.16 Microbeam current at the Faraday cup as a function of the applied extraction voltage.

While stability of beam current is of crucial importance in the operation of the LABA Microbeam, the most critical current measurement is that made at the exit of the collimator in the experimental endstation (discussed in detail in **Chapter 4**), as it bears the most direct relationship to the dose

delivered to the biological target. Current measurements exiting the collimator were performed by a combination of single particle detection and track-etch methods, and were used to determine the final charged-particle fluence on the target. These investigations will be described in detail in **Chapter 4**.

3.1.1.4 Safety Interlocks

Underneath the graphical control interface is a network of safety interlocks, implemented to ensure the safety of components within the high-voltage terminal. Incorporation of automated interlocks is necessary to provide a sufficient level of protection for the accelerator since user response times are not rapid enough to prevent catastrophic "arcing" (short circuit across a gap due to insulation breakdown) made possible by increased pressures in the accelerator tank. For example, if pressures within the accelerator exceed safe values, safety interlocks programmed into the control software immediately respond by setting the terminal voltage to 0, thus avoiding an arc that could seriously damage or destroy the digital electronics housed within the high-voltage terminal. All electronics housed outside of the terminal are optically isolated from the rest of the system, adding an additional level of passive protection. Similarly, critical gate valves in the beam line cannot be opened unless required settings for the vacuum pumps meet specific conditions.

3.1.1.4.1 Electronic Interlocks

A number of software interlocks have been developed to protect the accelerator against an uninformed user or to prevent a transient operating condition from damaging the accelerator. On the "Accelerator Control" screen (refer to **Section 3.3.1**), these consist of a number of programmed limitations on the magnitude and manner of terminal voltage increases, constant monitoring of tank pressures to shut off power in the case of a pressure spike, and limitations on the amount and rate at which source gas may be introduced into the accelerator.

On the "Vacuum" screen (refer to **Section 3.3.2**), software interlocks prevent the unsafe opening of gate valves or operation of the turbopumps. On the "Facilities" screen (refer to **Section 3.3.3**), the only software interlocks implemented pertain to the controls for the bending magnet power supply. As sudden increases in current may damage the bending magnet coils (due to the threat of significant inductive heating) any user-requested increase in current is automatically made in small (0.1 A) incremental steps.

3.1.1.4.2 Physical Interlocks

In addition to the range of software interlocks integrated directly into the control system, a number of physical interlocks have been implemented to protect the accelerator hardware and associated electronics.

The accelerator terminal power supply, located outside of the accelerator vessel, consists of a high voltage driver and a generating voltage meter (GVM). The GVM checks the high voltage driver voltage against the voltage specified by the operator, which would otherwise steadily increase. As precise voltage control is necessary for the intended experimental applications of the microbeam, and excessively high voltages (> 900 kV at the present time for the LABA Microbeam Accelerator) could damage the accelerator terminal electronics and the high voltage driver, the driver power supply is interlocked to a fuse box that will not allow it to be turned on without the GVM activated to modulate it. The fuse box is located underneath the accelerator tank, as shown in **Figure 3.17**.

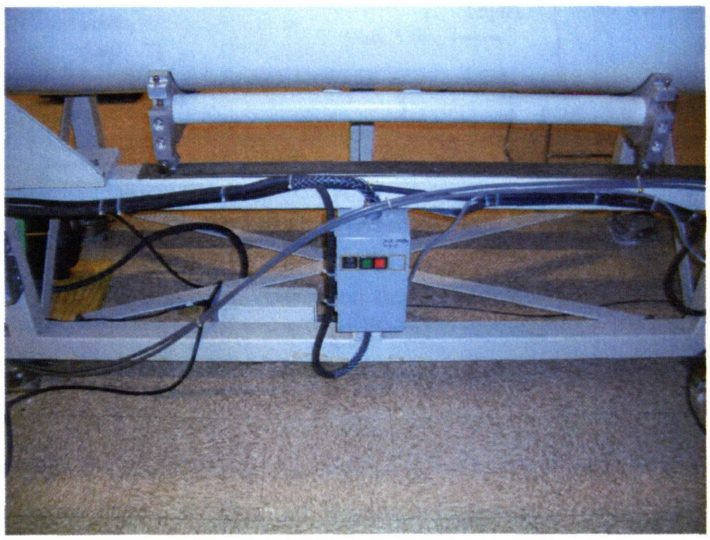

Figure 3.17 Fuse box that prevents terminal power supply from being activated without the GVM voltage regulator engaged.

In the event of an "arc," the control electronics would be vulnerable to disruption by the discharge. All control electronics are optically isolated from the accelerator to limit the likelihood of such an occurrence.

3.2 Beamline Components/Optics

Once the particle beam leaves the accelerator it travels down a 1.2 m beam tube. This beamline houses a number of control elements (shown schematically in **Figure 3.18**), including a set of x-y steering plates for beam deflection that serves as an electrostatic shutter for beam gating, and a magnetic quadrupole triplet. The quadrupole triplet could be used for later studies in which a focused, high intensity beam is desired (the original configuration of the microbeam was a horizontal set-up designed to provide a highly focused (1 μm) beam spot in vacuum for use in proton-induced x-ray emission (PIXE) studies or other surface analysis techniques) or for defocusing the beam to reduce its intensity through the collimation system in the experimental endstation. Vacuum is maintained in the beamline using a two-stage vacuum system, in which high vacuum (10^{-7} Torr) is maintained by a Varian V250 and Varian V550 Turbopump (Varian Inc. Vacuum Technologies, Lexington, MA USA) in parallel with the beamline. The pair of turbopumps are backed by a Varian TriScroll 300 roughing pump, which maintains low vacuum (10^{-2} Torr) and vents to atmosphere. The turbopumps, quadrupole triplet, and the bending magnet are cooled by a chilled water system.

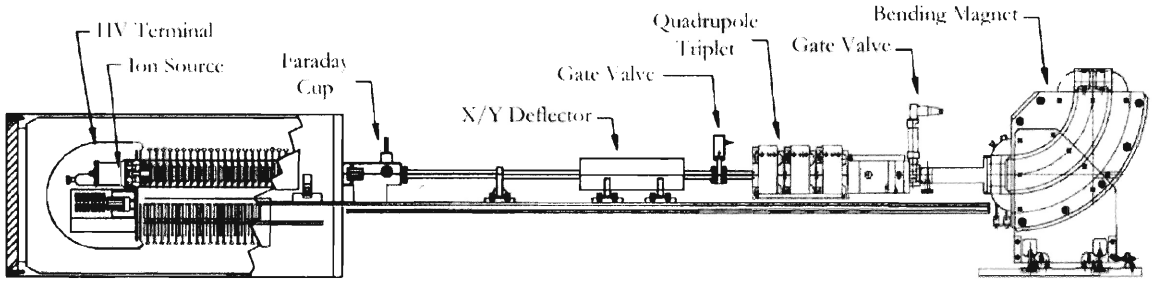

Figure 3.18 LABA beamline schematic. (based on drawings from Andrew Dart, Pyramid Technical Consultants)

3.2.1 X/Y Deflectors/Shutter

The beamline, constructed in part by Pyramid Technical Consultants (PTC), Waltham, MA, includes an X/Y deflector plate system that is used to electrostatically deflect the beam. The deflector system plays a number of roles in the operation of the LABA Microbeam, including dose control during experiments, beam gating for particle counting, and general shuttering of the beam.

3.2.1.1 Deflector Design

The X/Y deflectors are powered by two "kickers," which are robust power supplies with very rapid voltage rise times (KEPCO bipolar operational power supply/amplifier model BDP 1000M (+/- 1000 VDC, +/- 40 mADC)). (**Figure 3.19a** and **b**)

a. 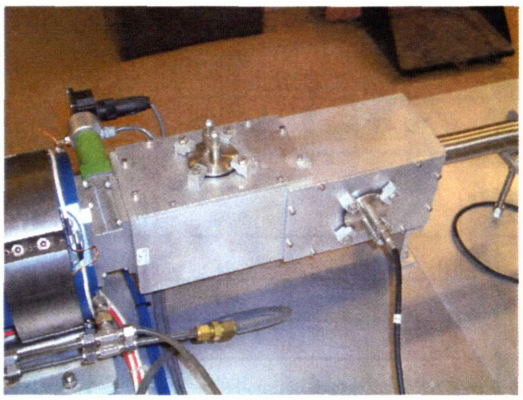 b. 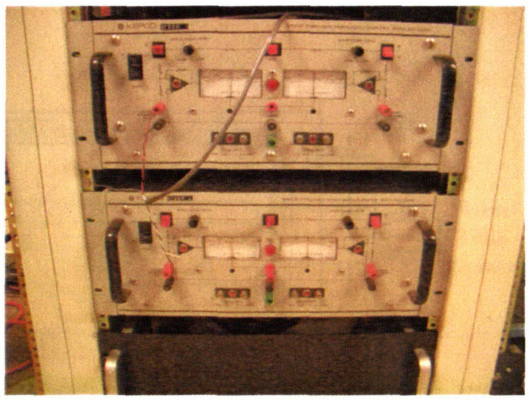

Figure 3.19 a) LABA Microbeam deflector assembly, **b)** Deflector power supplies.

Control of the deflectors will be explained in more detail in **Section 3.3.3** of this Chapter. To be useful, the deflectors must be able to divert the beam sufficiently so that no accelerated charged particles make it through the collimator when the deflection plates are engaged. Testing the deflection system to determine if it meets this requirement was accomplished with a series of methods, including beam on the quartz window, radiochromic film, and track-etch detection. As only track-etch methods are capable of registering a single "hit," they served as the "gold standard" for this study.

3.2.1.2 X/Y Deflector Characterization

In the characterization of the charged-particle beam deflector, the first step is to establish an understanding of the forces involved in electrostatic deflection. To allow the deflector system to absolutely prevent any of the beam from being directed upon the biological target in the experimental endstation, it is necessary to ensure that none of the original beam enters the bending magnet. As an additional failsafe, the bending magnet itself may be utilized to filter the beam to some degree, in that the magnet is "tuned" to allow only a beam of a particular energy and orientation to undergo the 90^0 bend for vertical beam alignment.

The deflector itself is ~0.15 m in length, the diameter of the beam tube is ~0.012 m, and the total distance between the deflector and the beginning of the bending magnet is ~1 m. The direction of the beam is defined as "z," and "x" and "y" are defined as the horizontal transverse and vertical transverse directions, respectively. This arrangement is shown in **Figure 3.20**.

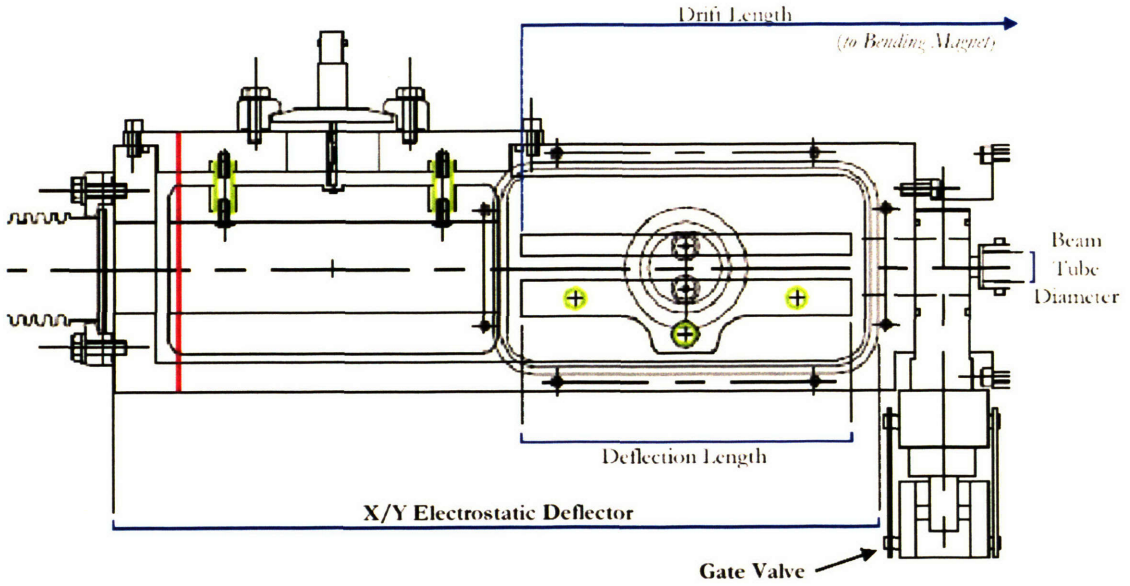

Figure 3.20 A diagrammatic representation of the LABA x/y electrostatic deflector. The beam tube diameter and deflection length are labeled. (*Courtesy Andrew Dart, Pyramid Technical Consultants*)

Following the methods of Larson at the Brookhaven National Laboratory,[55] a reasonable estimate for the y-displacement necessary to "dump" the charged-particle beam on the beam tube wall prior to entering the bending magnet based on the geometry of the LABA Microbeam beamline would be $y_{deflect} = 0.006$ m at 1 m, equivalent to a deflection angle (α) of 5.6 steradians. This would place the termination of the beam on the beam tube wall beyond the quadrupole triplet and before the bending magnet. Moreover, the beam should be deflected vertically "up," which results in the bending magnet "overdeflecting" the beam, rather than creating a situation where the bending magnet may accidentally compensate for the electrostatic deflection and "undeflect" the beam.

The full derivation of the required electrostatic field strength is provided in **Appendix C, Section C.1**. It was shown that a 560 V/cm electrostatic field ($\mathbf{E_y}$) was required to sufficiently deflect a beam of 750 KeV protons. Given the 1.2 cm plate gap (**d**) built into the LABA deflection system, the necessary applied voltage $V = E_y d = (560)(1.2) = 670V$. Thus, deflection of a 750 keV proton beam is within the operating parameters of the existing +/- 1000 VDC power supplies. The general equation for the deflector voltage required to completely terminate the beam as a function of the charged-particle energy using the LABA Microbeam deflection system is given by **Equation 3.1**:

$$V = E_y d = \frac{\alpha \gamma m_p \beta^2 c^2}{e\lambda} d \qquad \textbf{Equation 3.1}$$

where E_y = electric field in the vertical (y) direction

α = deflection angle (~ 5.6 steradians)

λ = length of deflection field (~0.15 m)

$e = q_p$ = charge of a proton (1.6022×10^{-19} C).

m_p = mass of a proton (1.6726×10^{-27} kg)

d = plate gap (1.2 cm)

A plot of charged-particle energy (MeV) vs. the deflector voltage (V) required to completely terminate the beam using the LABA Microbeam deflection system is shown in **Figure 3.21**.

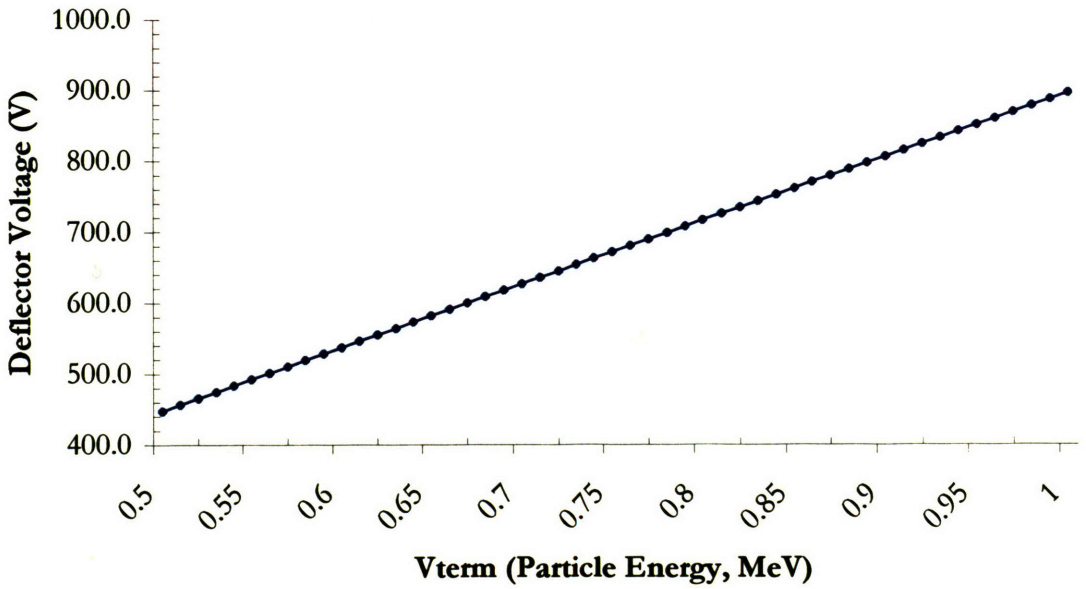

Figure 3.21 Plot of deflection voltage required to completely terminate the charged-particle beam vs. the terminal voltage using the LABA Microbeam deflection system.

It was found experimentally that a minimal field of 600 V in the "y" direction was sufficient to completely deflect the beam, generating no "pits" in the LR115 track-etch film. An example of a deflector verification experiment is shown in **Figure 3.22**. In this example, the charged-particle microslit was scanned across the film, with the deflectors engaged while the stage was in motion between the two slit images, but disengaged to the right of the second slit. Between the two slits, only the normal background for the LR115 is noted (from prior abrasion or other damage to the film surface), but after the second slit a large number of pits may be observed.

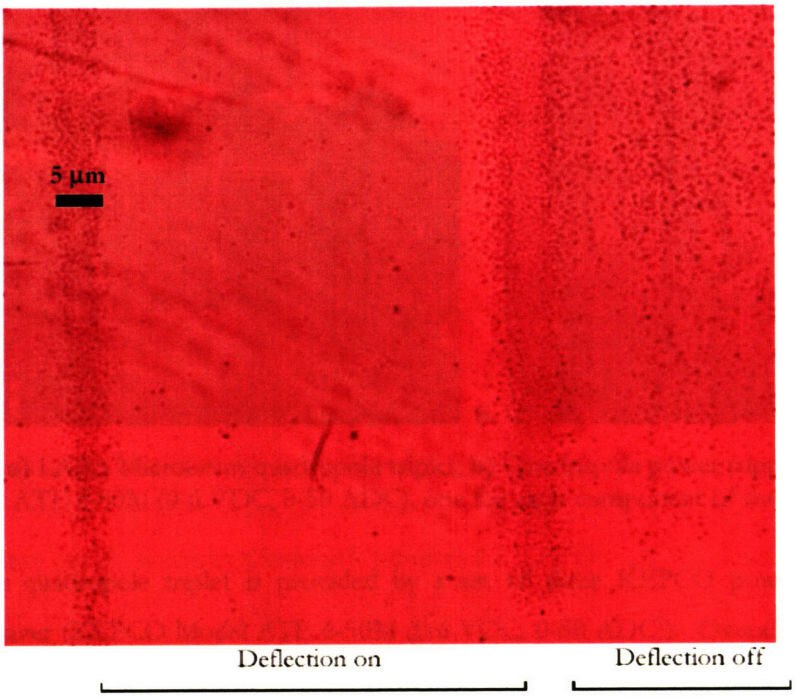

Figure 3.22 LR115 image of charged-particle microslit showing on/off deflection pattern. The deflectors were engaged while the stage was in motion between the two slit images, but disengaged to the right of the second slit. (10x magnification, color adjusted)

The single-particle detection system (discussed in greater detail in **Chapter 4**), will be used to provide the signal that prompts shuttering of the beam, as well as managing the dose delivered to the biological target during the microslit irradiation experiments. Characterization of the deflector system in conjunction with the single-particle detection system and the collimators used in the experimental endstation will be described more fully in **Chapter 4, Section 4.3.4**.

3.2.2 Quadrupole Triplet

Any alteration in the shape of the cross-sectional profile of the charged-particle beam prior to the horizontal beam entering the bending magnet may be accomplished through the use of the quadrupole magnet triplet. (**Figure 3.23a** and **b**) The quadrupole triplet is located after the deflector and before the bending magnet, and is controlled by executables on the "Facilities" screen of the control system graphical interface.

a. 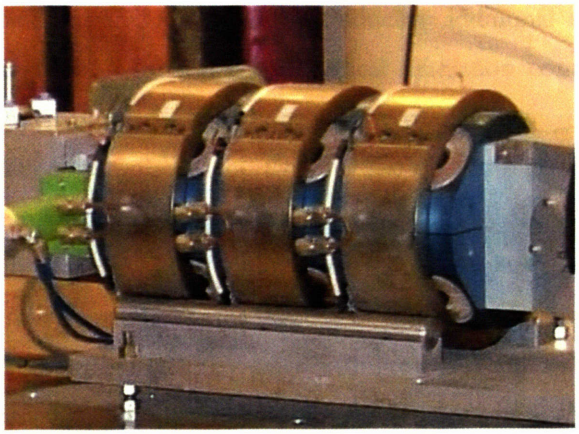 b. 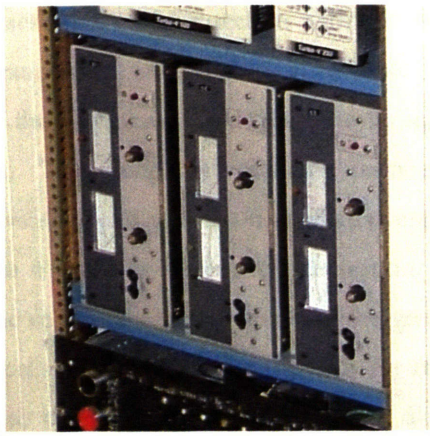

Figure 3.23 a) LABA Microbeam quadrupole triplet, **b)** Quadrupole power supplies, KEPCO Model ATE 6-50M (0-6 VDC, 0-50 ADC), one for each component of the triplet.

Current for the quadrupole triplet is provided by a set of three KEPCO power supplies with automatic crossover (KEPCO Model ATE 6-50M (0-6 VDC, 0-50 ADC)). Overall, the quadropole has little relevance to the final output of the microbeam, as the effect of the collimation system on the final beam profile is dominant and obliterates any "shape" that the beam may have had previously. As a result, it was not used very often in our experiments, although it may be used to somewhat focus or defocus the charged-particle beam prior to its entry into a 90° bending magnet, adding an additional level of control over the final beam intensity on target.

3.2.3 Bending Magnet

The accelerator used for the LABA charged-particle microbeam was originally designed for the purpose of surface analysis studies using proton-induced x-ray emission (PIXE) and other techniques, and the charged-particle beam was aligned horizontally (parallel to the floor). A 90^0 bending magnet was incorporated into the beamline to produce a vertical beam.

3.2.3.1 Bending Magnet Design

A vertically aligned beam was obtained by adding a 90^0 bending magnet (designed by Pyramid Technical Consultants of Waltham, MA USA and constructed by Buckley Systems Ltd. of New Zealand), allowing the irradiation of horizontally-placed cell dishes. This major conversion had two purposes – the first for its benefit to biological studies, as it simplifies the irradiation and allows the growth medium to remain on the cells in a conformation that also allows the medium to be exposed to air (allowing oxygen to diffuse to the cells). This is crucial for experiments requiring long-

irradiation times, and avoids introducing additional stresses that could interfere with biological observations. Horizontal and vertical irradiation configurations are shown in **Figure 3.24**. The horizontal beam configuration was the original design for the microbeam, in which the biological endstation was placed shortly after the quadrupole triplet. This design introduced a number of concerns in the biological management of the cells, as it was difficult to keep the cells covered in growth medium while at the same time exposing them to a uniform oxygen concentration. As shown in **Figure 3.24**, the placement of the vent allows the cells at the top of the dish the greatest access to air, but poor coverage with growth medium; the cells at the bottom of the dish are amply covered with growth medium but starved for oxygen due to the long distance that it must diffuse through the covering medium in order to reach the cells. The vertical beam configuration addressed this concern, allowing for uniform growth medium coverage and oxygen exposure. Cell dish design will be discussed in greater detain in **Chapter 5, Section 5.2.**

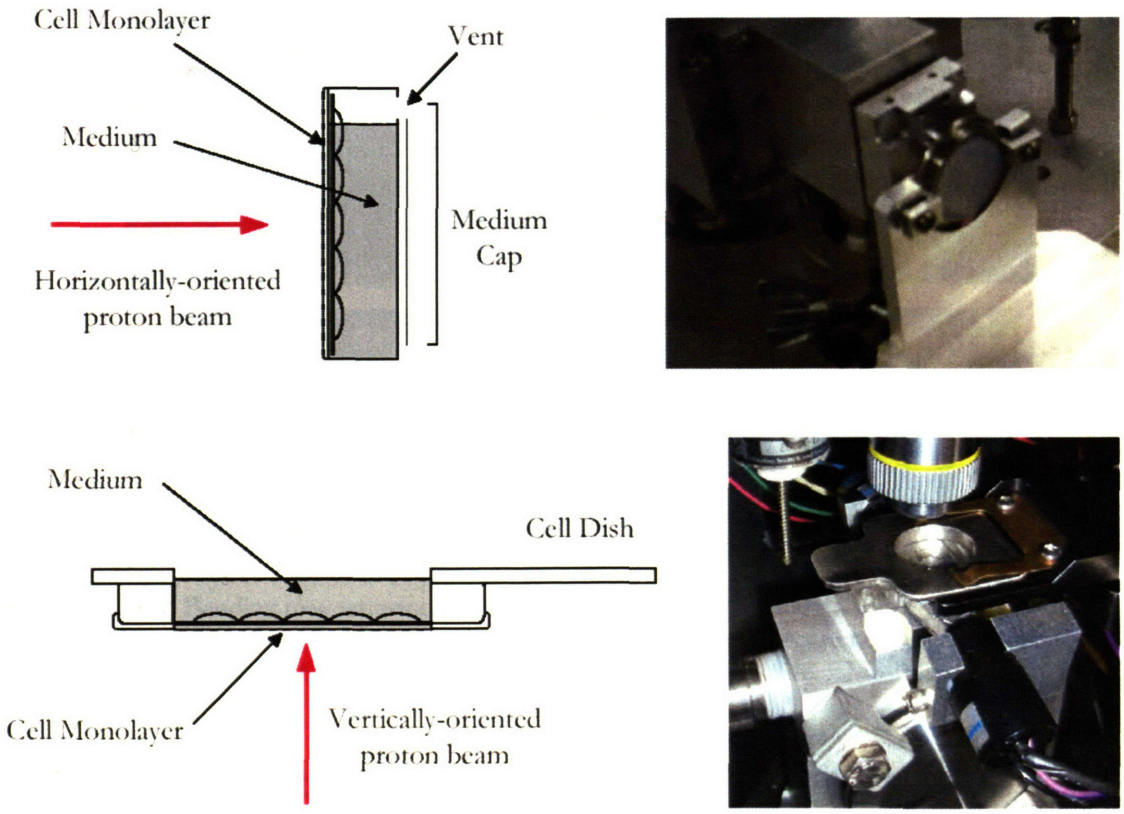

Figure 3.24 Horizontal and vertical target irradiation configurations, cut away side views and images. The top images depict the horizontal irradiation configuration, used before the installation of the bending magnet. The lower images depict the vertical irradiation configuration, used in the LABA Microbeam experimental endstation.

The second major benefit of the bending magnet is that it acts as an energy filter. Because the bending of an ion's path in a magnetic field is a function of the charge on the ions and the ion energy (kinetic), the magnet selectively transports the ions of choice into the vertical orientation (those of inappropriate energy/charge are over- or under-bent, and are grounded out on the beam tube prior to the target). For example, if the operator wishes to irradiate a biological target with a doubly-charged helium beam (He-3 or He-4), the beam may be contaminated with singly-charged ions of the same isotope, with only half the energy of the desired particle. The bending magnet would filter out these ions, depositing them on the wall of the waveguide.

The bending magnet and power supply are shown in **Figure 3.25a**, **b**, and **c**.

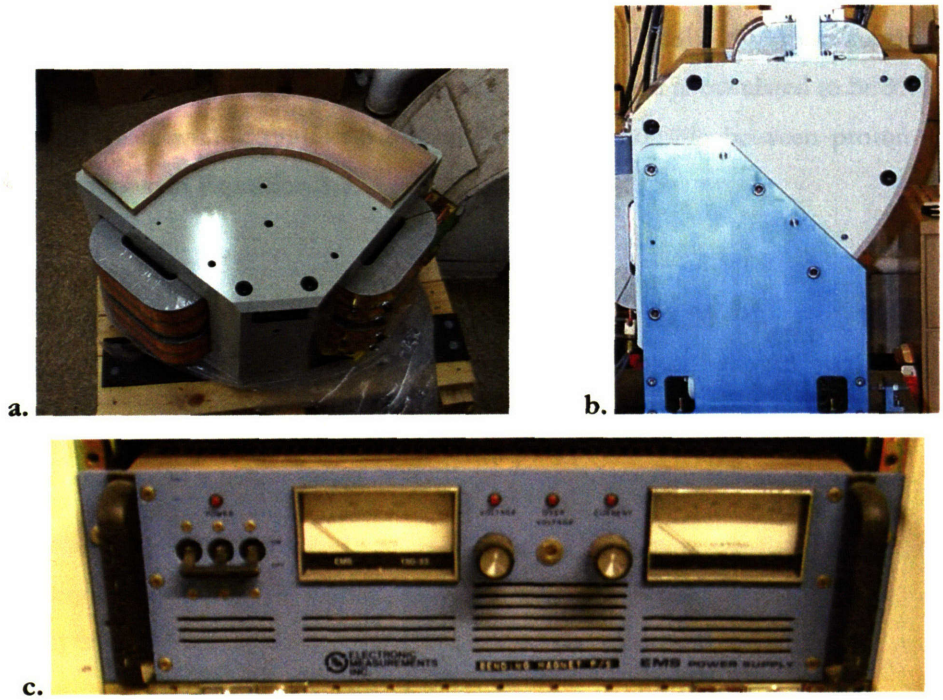

Figure 3.25 a) Bending magnet prior to installation with the high-vacuum waveguide lying on top, **b)** Bending magnet installed in the beamline, waveguide inside and connected to high-vacuum system, **c)** Bending magnet power supply, Electronic Measurements Inc. EMS Power Supply Model EMS 150-33 (0-150 VDC, 0-33 ADC).

3.2.3.2 Bending Magnet Characterization

In order to characterize the bending magnet, a relationship between proton energy and magnetic field was needed. The full derivation of the required magnetic field strength is provided in **Appendix C**, **Section C.2**. It was shown that the relation for the magnetic field required to produce a 90^0 bend in the charged-particle beam produced by the LABA accelerator is provided by **Equation 3.2**:

$$B = \frac{1}{Rq_p}\sqrt{2m_p q_p V_{term}} \qquad \textbf{Equation 3.2}$$

where R= radius of curvature of bending magnet (0.280 m)

q_p = charge of a proton (1.6022 x 10^{-19} C)

m_p = mass of a proton (1.6726 x 10^{-27} kg)

V_{term} = accelerator terminal voltage (V)

Equation 3.2 provides a relationship between magnetic field strength and the kinetic energy of the proton. However, missing is a factor relating the bending magnet current to the strength of the resulting magnetic field. A plot of magnet current vs. central magnetic field, as displayed in **Figure 3.26,** supplies this last relationship. From the figure, a slope of 0.2812 kG/A can be inferred. Thus, the needed relationship between magnet current and magnetic field is calculated to be 35.56 A/Tesla. Combining this value with **Equation 3.2** results in the relationship between proton energy and magnet current shown in **Equation 3.3**:

$$BendingMagnetCurrent(A) = \left(\frac{1}{Rq_p}\sqrt{2m_p q_p V_{term}}\right) \cdot 35.56\,{}^{A}\!/_{Tesla} \qquad \textbf{Equation 3.3}$$

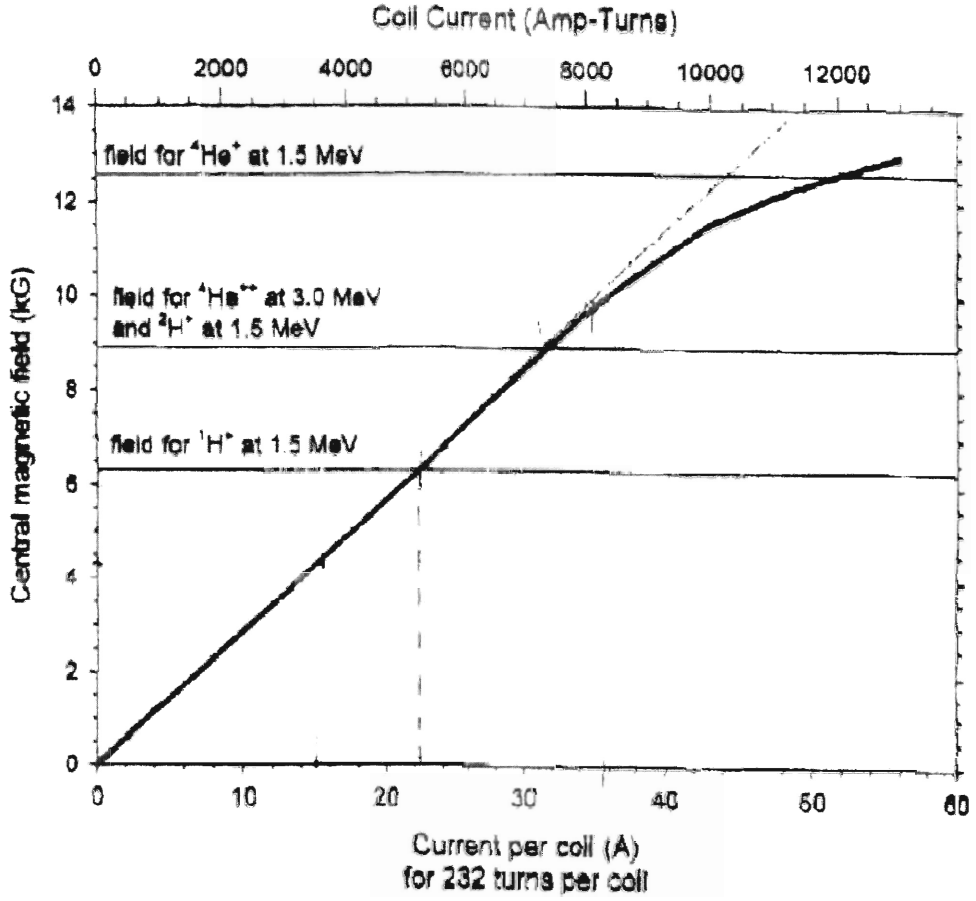

Figure 3.26 Relationship between magnet current and the resulting magnetic field (*provided by Pyramid Technical Consultants*)[56]

Using this relationship, experimental characterization of the bending magnet subsystem (composed of the bending magnet itself, the bending magnet power supply, and the control system) was then performed by a series of experiments in which protons of various energies were passed through the bending magnet, and the magnet current was adjusted via the CPU until the proton beam was centered on the quartz window placed in the target position within the experimental endstation. The setup for quartz window irradiation was shown above in **Figure 3.8**, and Figures **3.27a** and **b** below show the irradiation of the quartz window with the beam properly centered.

a. 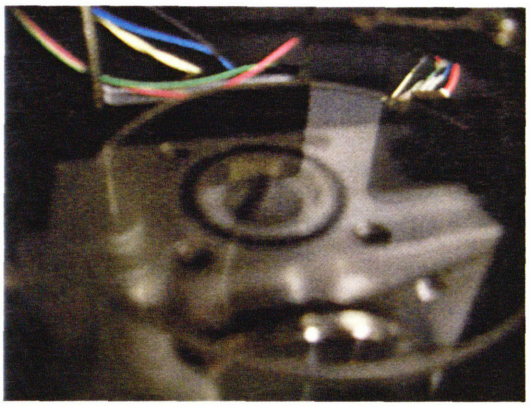 b. 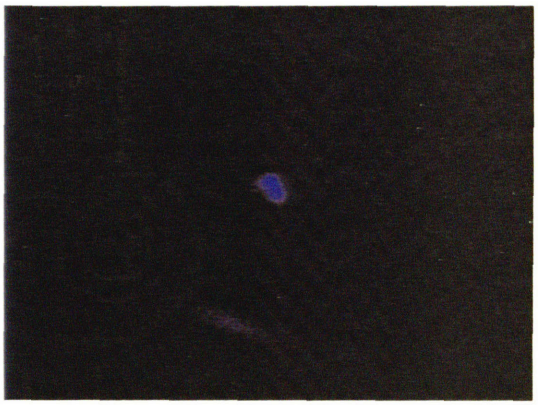

Figures 3.27 a) Closeup view of the quartz window with room lights on, **b)** Image of the centered beamspot on the quartz window with the room lights off.

Once the beam was centered on the quartz window, thus indicating that the correct magnetic field had been produced, the CPU magnet current was recorded for that proton energy along with the voltage applied across the programming terminals of the magnet power supply. The measured programming voltages were used to calculate the actual bending magnet currents, which were compared to those requested by the CPU. The results of this experiment are displayed graphically in **Figure 3.28**. The magnetic field, and thus the magnet current, should vary as (proton energy)$^{1/2}$; the relationship in **Figure 3.28** only appears linear due to the small range of proton energies plotted.

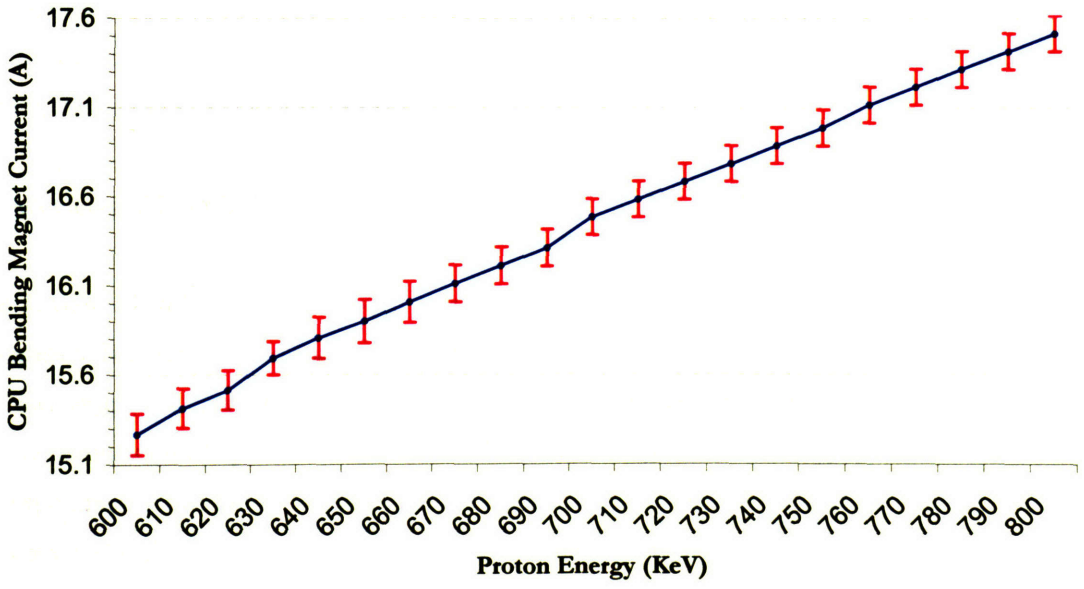

Figure 3.28 Plot of bending magnet current vs. proton energy required for a 90° bend (verified by quartz window irradiation). Error bars represent the standard deviation of three sets of experimental measurements.

Magnet currents calculated by **Equation 3.3** were compared to the experimental magnet currents that produced a beam spot on the quartz window, and a correction ratio of 1.061 was calculated for 750 keV protons and could be a result of a number of different sources of error (possibly the 35.57 A/Tesla slope determined from **Figure 3.26**). The 1.061 correction ratio at 750 keV appears consistent over the range of proton energies most likely to be used for radiobiological studies as determined by SRIM calculations and within the limitations of the LABA Microbeam accelerator, so it was incorporated into **Equation 3.3** to correct the calculated magnet currents. **Equation 3.4** is the result (37.74 A/Tesla = 35.57 A/Tesla * 1.061).

$$BendingMagnetCurrent(A) = \left(\frac{1}{Rq_p} \sqrt{2m_p q_p V_{term}} \right) \cdot 37.74 \, {}^{A}\!/_{Tesla} \qquad \textbf{Equation 3.4}$$

3.2.3.3 Safety Interlocks

The bending magnet power supply is passively interlocked by its voltage regulation and by a fuse system. Voltage regulation is performed by a circuit that prevents the control voltage from the OptoElectronics (capable of ranging from 0-5 V) from exceeding a voltage of 50 mV to the control inputs of the bending magnet power supply. This prevents the power supply from applying excessive current to the magnetic coils of the bending magnet. Additionally, because excessive current can cause heating in the magnetic coils sufficient to overwhelm the chilled water cooling system, the circuit is tied to a 30 A fuse.

3.3 Accelerator Control Systems

The LABA Microbeam is controlled primarily by a graphical interface, which is written in a proprietary language developed by Pyramid Technical Consultants (Waltham, MA USA).[56] This interface simplifies operation of the accelerator and the various subsystems and provides a platform for the automation of specific tasks. For the beamline components (leading up to but not including the experimental endstation), automation is responsible for a limited number of tasks, including: 1) emergency shutdown of all critical accelerator systems, 2) "soft" startup of the accelerator vacuum systems after a shutdown or power failure, 3) "priming" of the plasma to generate an accelerated beam, and 4) the tuning of the bending magnet current to the energy of the charged particles so that it produces the exact magnetic field required to direct the horizontal particle beam vertically through

the beam collimator. These automated tasks will be described more fully in the sections specific to the applicable control system, and full descriptions of all executables on the control screens are provided in Appendix A.

The three screens discussed in this Chapter that are used in the basic operation of the LABA Microbeam are the Vacuum Screen (**Figure 3.30**), the Accelerator Control Screen (**Figure 3.31**), and the Facilities Screen (**Figure 3.32**). The Acquire and Image Screens will be discussed in detail in **Chapter 4**. All screens have a common border that allows the operator to run experiments, monitor the integrity of the vacuum system, rapidly turn off critical systems, and switch between the various system interfaces. **Figure 3.29** shows this common border with the variable interface removed.

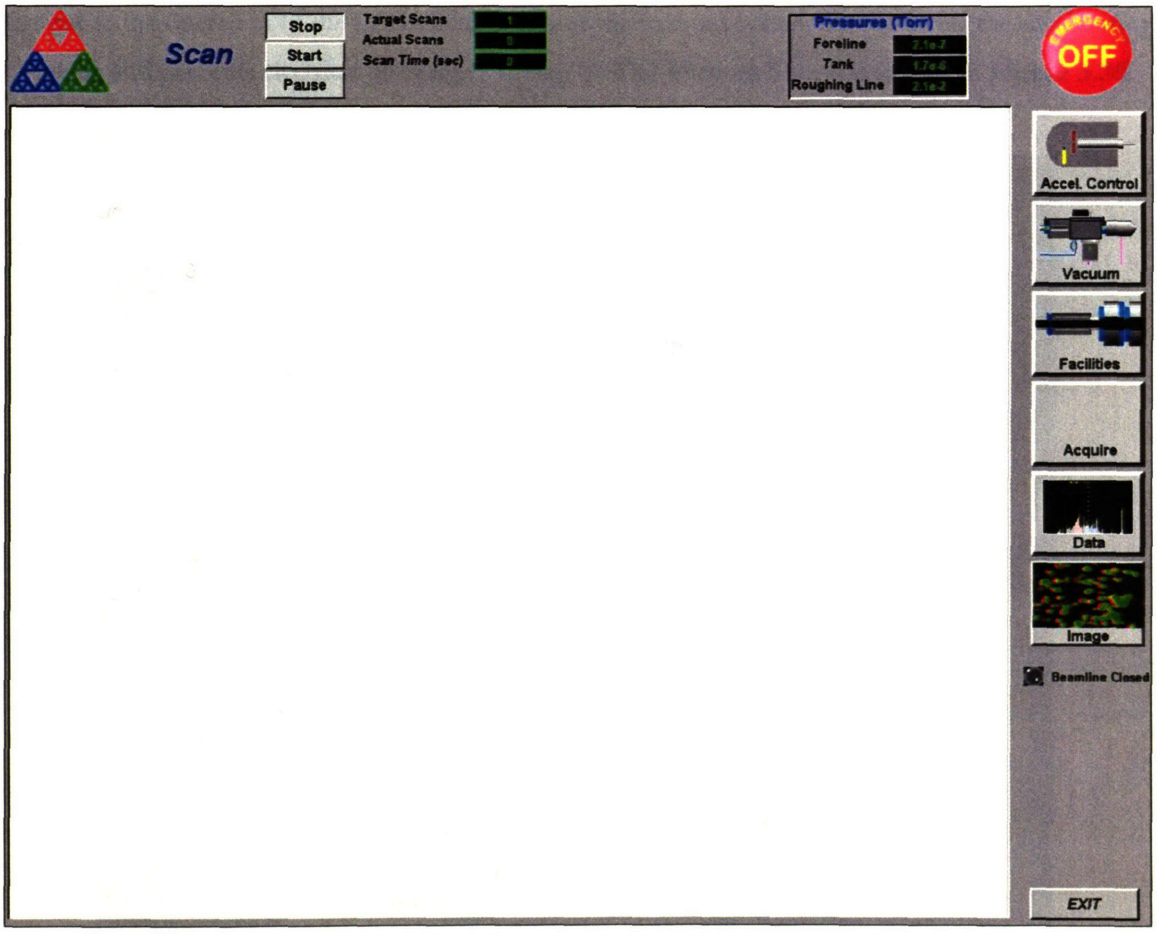

Figure 3.29 The "Common Border," present on all graphical interface screens.

The Scan buttons allow the operator to start, pause, and stop a pre-defined experiment, as specified on the "Acquire" screen (to be explained in detail in **Chapter 4** and **Appendix A**). The displays indicate the number of scans performed and the total duration of an individual scan. The **Pressures**

readback indicates vacuum pressures in the foreline, tank, and roughing line and allows the operator to quickly and continuously assess the integrity of the system.

Other options on the "common border" include the **Emergency Off** and **Exit** buttons, which disable the machine in a way that turns off critical components first in the case of the former, or in an orderly fashion suitable for quickly restarting the machine later in the case of the latter. The "common border" also has a set of Screen Selection buttons that permit the operator to rapidly switch between control screens (Accelerator Control, Vacuum, Facilities, Acquire, Data, and Image).

3.3.1 Vacuum Control

Crucial to the operation of the LABA Microbeam is the vacuum system that insulates the accelerating elements and prevents electrical discharge ("arcing"). The Vacuum Screen is shown in **Figure 3.30**.

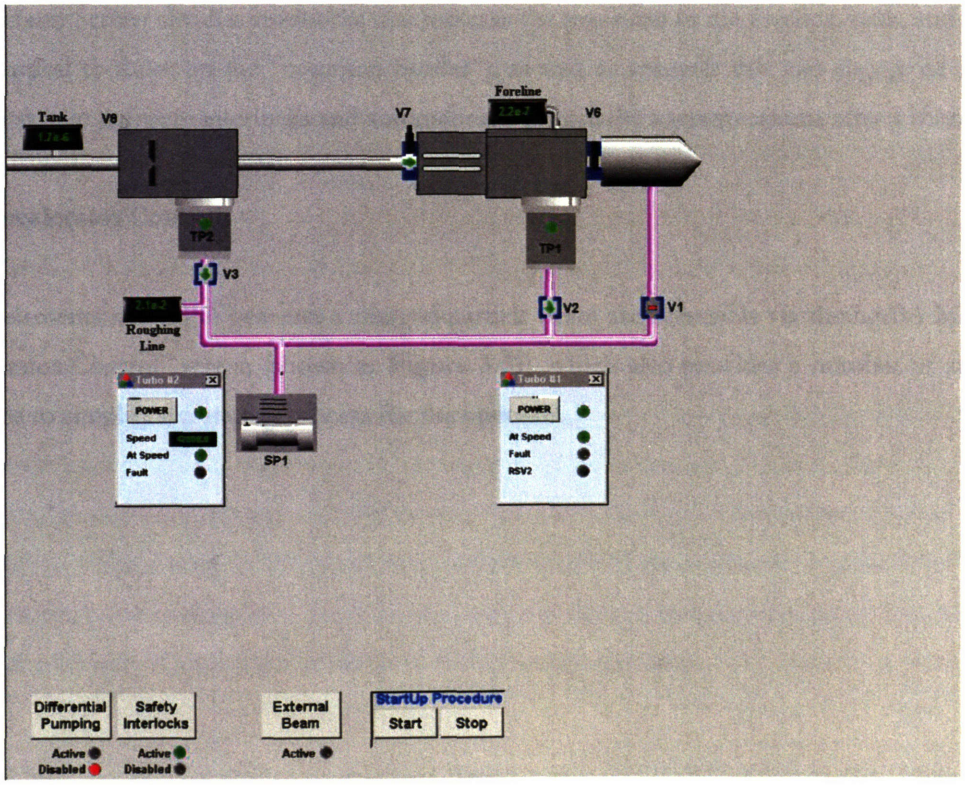

Figure 3.30 The "Vacuum Screen" graphical interface, which allows the operator to control the LABA Microbeam vacuum subsystems and open/close the beamline (common border removed).

At various points on the vacuum system diagram are the turbopump icons (TP1 and TP2) that allow the operator to change the operating characteristics of the vacuum system turbopumps, and the gate

valve icons (V1, V2, V3, V6, and V7) that allow the operator to open or close the gate valves that are used to isolate portions of the system.

TP1 or "Turbo #1" is a Varian V250 Turbopump (Varian Inc. Vacuum Technologies, Lexington, MA USA) with an operating speed of 56 krpm. It provides high vacuum (on the order of 10^{-7} torr for a closed beamline, 10^{-5} torr with the microslit collimator in place on an open beamline, and 10^{-6} torr with the pinhole collimator in place on an open beamline) for the microbeam foreline. It is physically mounted after the deflectors and quadrupole magnets, between the V7 and V1 gate valves prior to the bending magnet. TP2 or "Turbo #2" is a Varian V550, with an operating speed of 42 krpm. It provides high vacuum (on the order of 10^{-7} Torr for a closed beamline and 10^{-6} Torr while generating beam) for the microbeam accelerator tank. It is located immediately at the exit of the accelerator tank. SP1 indicates the "roughing pump," a Varian Triscroll 300 that maintains the low vacuum ($<5x10^{-2}$ torr) required for the operation of the Turbopumps.

The Vacuum Screen also has readbacks that indicate the pressures in the foreline, tank, and roughing line (identical to those on the "common border"), as well as controls that can engage or disengage vacuum system software interlocks and automatically restore the vacuum system after a shutdown.

3.3.2 Accelerator Control

All the elements needed to generate a charged-particle beam are accessible via the LABA Microbeam "Accelerator Control" screen (shown in **Figure 3.31**), which also provides a number of automated functions to simplify the startup process for the operator.

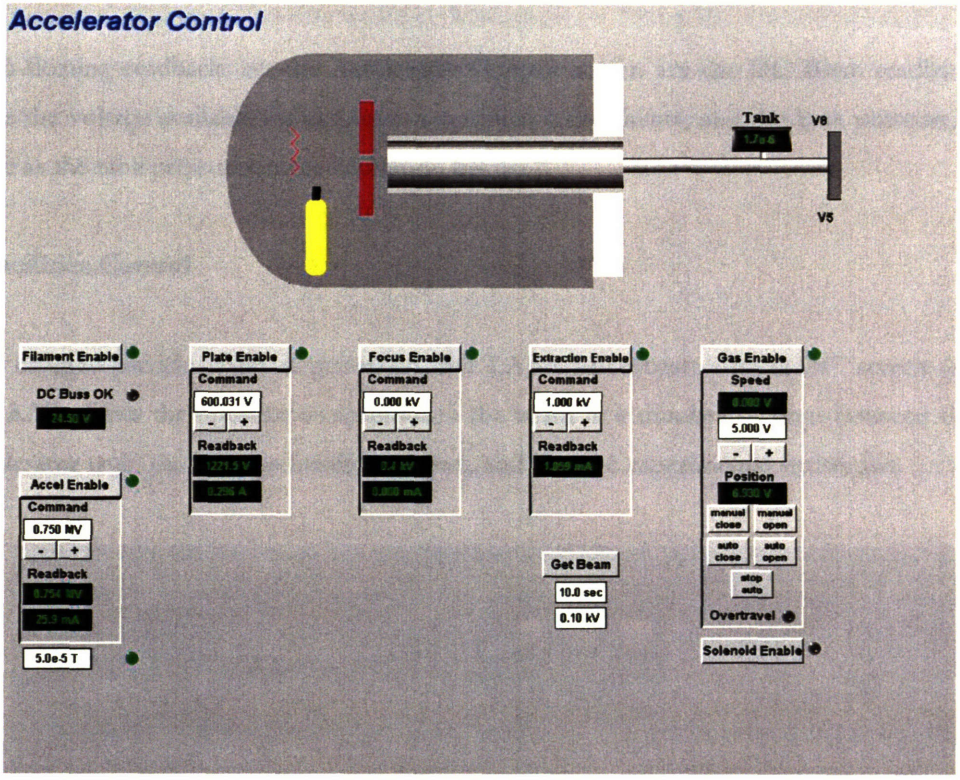

Figure 3.31 "Accelerator Control" Screen, which allows the user to regulate the accelerator components: terminal voltage, filament, oscillator plate, focusing element, extraction probe, gas valve, and priming solenoid (common border removed).

The controls on the Accelerator Control Screen have the most direct effect on charged-particle beam generation and intensity. The **Accel Enable** controls set the terminal voltage and the resulting particle energy. The critical pressure setting (usually defined as 5.0×10^{-5} Torr) is located directly beneath the **Accel Enable** controls, and is used to specify a tank pressure which, if exceeded, will result in an automatic shut down of the accelerator. The **Filament Enable**, **Plate Enable**, and **Focus Enable** are not generally adjusted by the operator during use. **Extraction Enable** activates the extraction voltage controls that allow the operator to adjust the extraction voltage, which directly affects the bean current intensity. **Gas Enable** activates the gas bottle needle valve controls, which regulate the amount of source gas available to ionize and accelerate.

One of the automated functions is the **Get Beam** command, which triggers the solenoid for a specified number of seconds, after which it turns off the solenoid and switches the Extraction voltage to the specified value. The solenoid is used to "prime" the plasma by preventing it from leaving the quartz ionization chamber, which creates a pressure load. Releasing the solenoid allows a burst of plasma to escape, which eventually initiates the generation of a stable charged-particle beam.

The two floating readbacks on the Accelerator Control Screen are the **DC Buss** readback, which indicates the voltage available for the various terminal components, and the tank pressure, which is the same as the tank pressure on the "common border."

3.3.3 Facilities Control

Once a charged-particle beam is generated, the LABA Microbeam "Facilities" screen (shown in **Figure 3.32**) allows the operator to manipulate the beam in a number of ways between the exit of the accelerator tank, through the bending magnet, and into the experimental endstation.

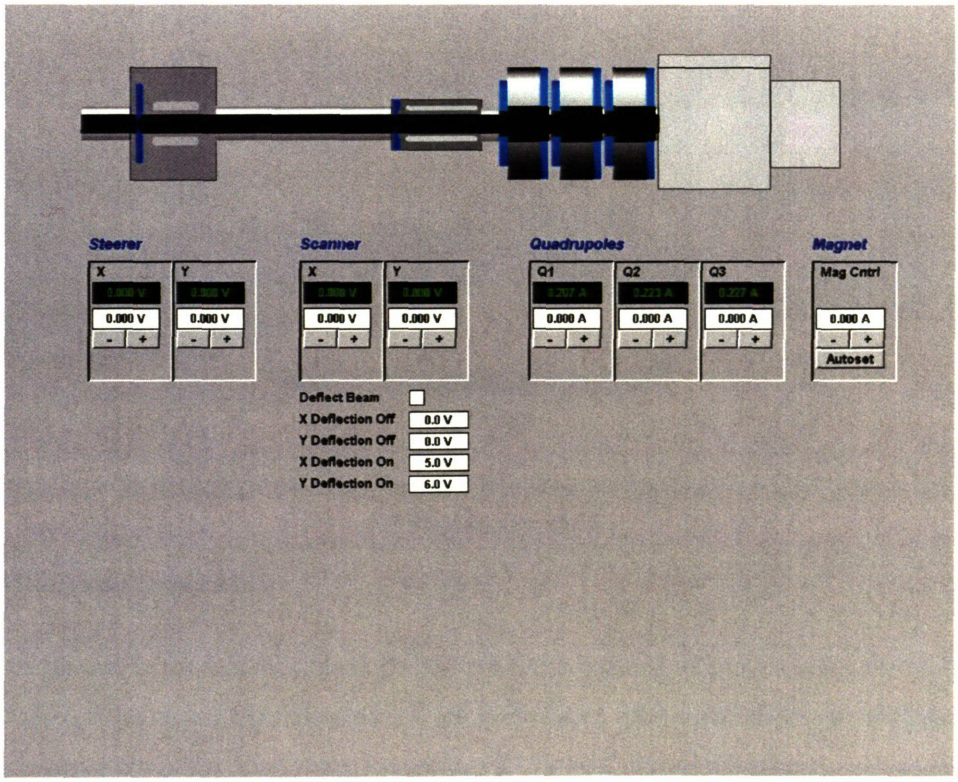

Figure 3.32 The "Facilities Screen" graphical interface, which allows the operator to control the LABA Microbeam beamline subsystems and deflect the beam (common border removed).

The three functional groups on the Facilities control Screen are the **Scanner**, the **Quadrupoles**, and the **Magnet**. The **Scanner** controls determine the deflection of the beam in two dimensions perpendicular to the beamline. The presets specifically allow the operator to define "resting" and "active" deflection during the course of an irradiation – these presets are engaged while the experimental stage (to be described in detail in Chapter 4) is in motion, and disengaged when the

stage is at rest. The **Quadrupoles** controls independently adjust the current applied to each the magnets in the quadrupole triplet, allowing the operator to alter the beam profile to varying degrees. The **Magnet** control is used to set the current applied to the bending magnet, in order to generate a vertically-oriented beam.

3.4 Chapter Summary

In this chapter, the hardware and software used to generate and deliver a vertically-oriented charged-particle beam to the experimental endstation of the LABA Microbeam was described. In **Chapter 4**, the subsystems comprising the biological endstation will be described and experiments performed to characterize the operation of each system will be discussed.

4. LABA Microbeam Experimental System

In **Chapter 3**, the hardware and software used to generate and deliver a vertically-oriented charged-particle beam to the experimental endstation was described. The LABA microbeam experimental endstation is housed within a light-tight box mounted above the bending magnet, as shown in **Figure 4.1**. In this chapter, the subsystems comprising the biological endstation are described and experiments performed to characterize the operation of each system are discussed.

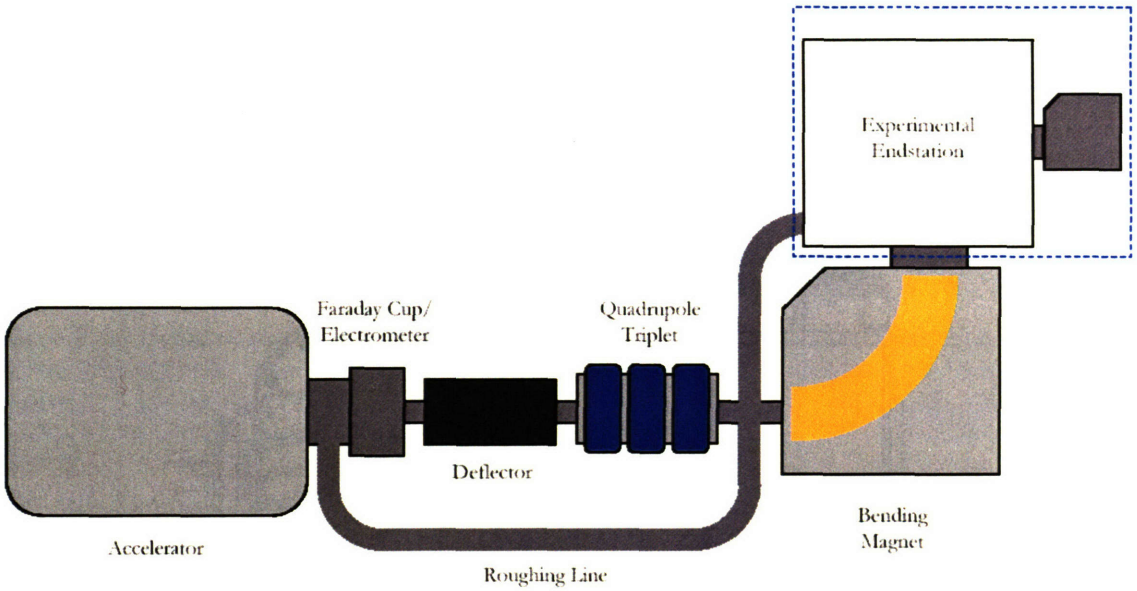

Figure 4.1 Schematic diagram showing the main components of the LABA Microbeam beamline components, with the components pertinent to this Chapter marked by a dashed blue box. (Note: drawing not to scale).

4.1 Experimental Endstation

Every component in the beamline prior to the endstation has served to produce a vertically-directed beam of charged particles, approximately 1.5 cm in diameter, with minimal energy straggle. The low degree of energy straggle is a key point in the overall "quality" of the microbeam, accomplished both at the level of the accelerator itself and then refined by the bending magnet, which selects for the "correct" energy by being tuned for a particular terminal voltage – particles of other energies are "over-" or "under-bent" and collide with the wall of the beam tube.

The elements of the endstation shape the final beam profile, providing the actual microbeam to be directed onto a target, as well as monitoring the current on the target (with the goal of limiting to single particles by interacting with the shuttering system), and imaging/positioning the target with respect to the beamspot.

Located immediately above the 90° bending magnet, the experimental endstation consists of the following subsystems (illustrated in **Figures 4.2** and **4.3)**:

- a collimator or slit to delimit the beam,
- a 2-dimensional motorized stage with micron-scale precision,
- a plastic scintillator, light guide and two photomultiplier tubes (PMTs) for particle counting,
- a specially designed cell dish,
- a light source (visible and UV range) with shuttering mechanism,
- a visible/UV light objective with motorized z-motion focusing, dichroic mirror, and a CCD camera with image intensifier for cell visualization.

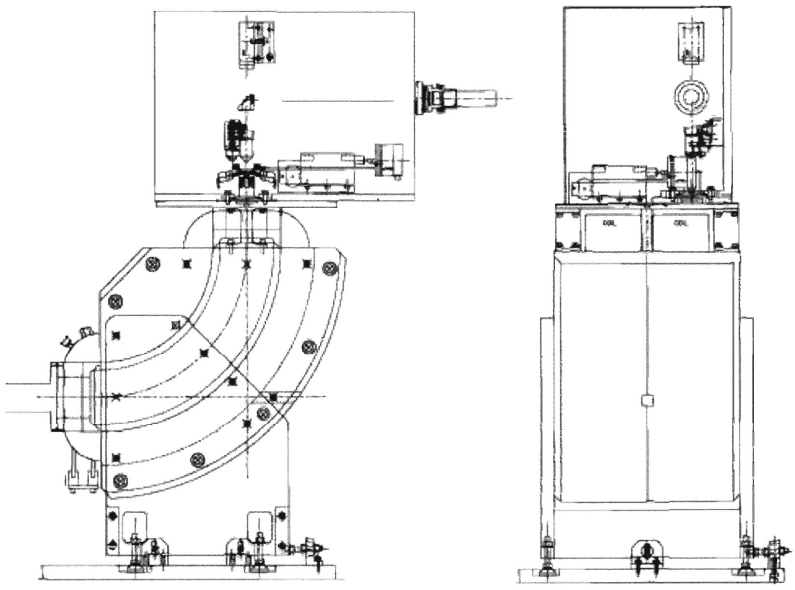

Figure 4.2 A CAD drawing of downstream portion of the microbeam showing the position of the light-tight cell-irradiation experimental endstation above the bending magnet. (A larger view of the endstation, with labels, can be seen in **Figure 4.3**). The endstation is located approximately 4.5 ft above floor-level; a 2.5 ft-high stand is used to access the endstation. (*courtesy of Andrew Dart, Pyramid Technical Consultants*)

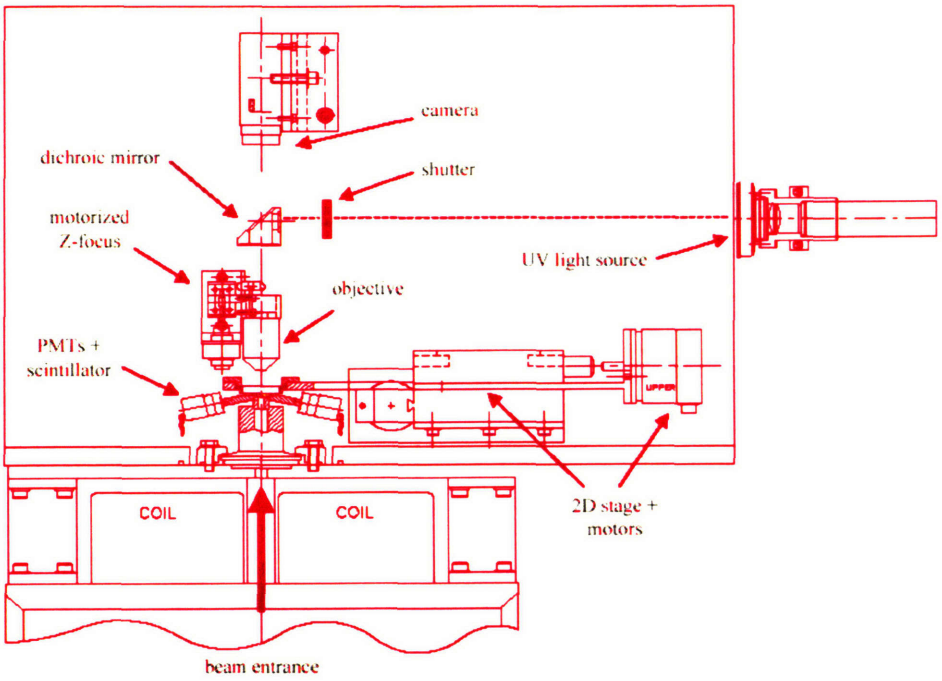

Figure 4.3 Experimental Endstation components. The UV light source is mounted on the outside of the light-tight box to minimize light contamination, and all other components (x/y stage, imaging system, UV light shutter, collimation and particle detection system) are housed inside. (*courtesy Andrew Dart, Pyramid Technical Consultants*)

The deflection plates, motorized stage, PMTs, light source and CCD camera are interfaced with the control PC for management of all aspects of cell irradiation, as shown in **Figure 4.4**. Control of the various beamline subsystems is managed on the "Image" and "Acquire" screens of the central control system, discussed in detail in **Section 4.5** later in this Chapter. Specifically, these screens control the components marked **g-r** on **Figure 4.4** (surrounded by a blue dashed box), corresponding to the collimation, single-particle detection, stage, and imaging systems.

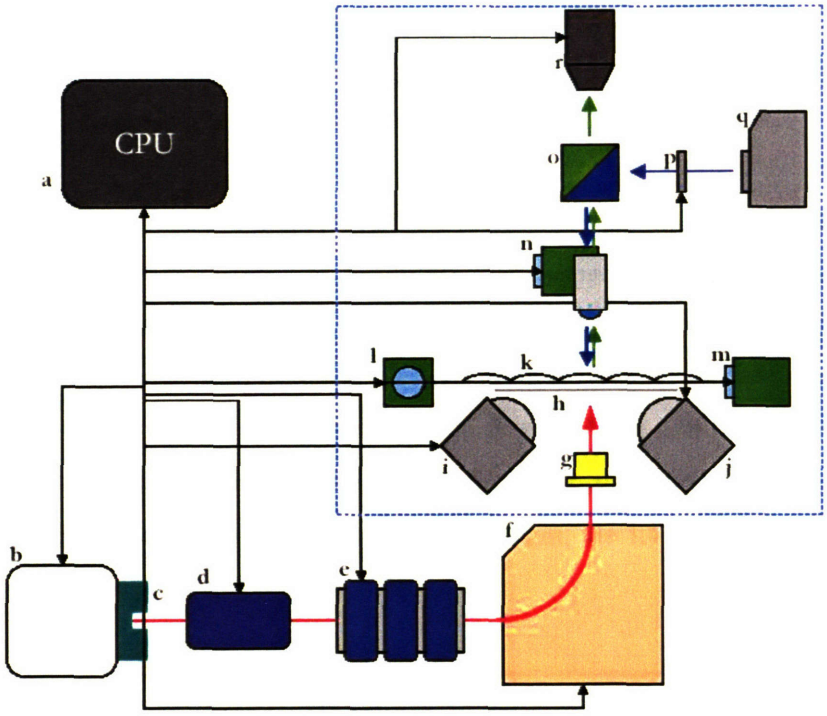

Figure 4.4 Control diagram (Chapter 4 components surrounded by blue dashed box). **a)** CPU, **b)** Accelerator, **c)** Faraday cup, **d)** Deflector, **e)** Quadrupole Triplet, **f)** Bending Magnet, **g)** Collimator assembly, **h)** Scintillating plastic, **i)** PMT 1, **j)** PMT 2, **k)** Cells on cell dish, **l)** X-direction stage motor, **m)** Y-direction stage motor, **n)** Objective on motorized focus, **o)** Dichroic mirror, **p)** Light shutter, **q)** Light (UV) source, **r)** CCD camera.

Irradiations are performed with a collimated beam of protons or alpha particles. The collimation is accomplished either through the use of an approximately 1.5 μm x 1mm laser-drilled slit or a 1.5 or 5 μm pinhole aperture consisting of a 1 mm section of capillary tube with a 1.5 or 5 μm inner diameter channel held by a positionable mount. (Discussed in greater detail in **Section 4.4**)

4.2 Calculations and Design Considerations

The LABA Microbeam accelerating column was designed for the generation of up to 1.5 MeV singly-charged particles (usually protons, which at 1.5 MeV have a range of 45.6 mm in air or 49.8 μm in water) or 3.0 MeV doubly-charged particles (usually He^{++} ions, which at 3.0 MeV have a range of 17 mm in air or 18.4 μm in water). However, at the present time power supply limitations generally restrict operation to energies less than 800 keV, and cells are usually irradiated with a collimated beam of 750 keV protons. The 750 keV protons that can be routinely generated by the LABA accelerator have a range of 15.3 mm in air or 17.2 μm in water, calculated using a simple air- or water-target model in SRIM 2003.[94, 113] Assuming a 6 μm cell thickness (typical for the fibroblasts used for preliminary radiobiological experiments,[99] to be discussed in greater detail in **Chapter 5**),

that allows for only ~11 μm of water-equivalent range that may be occupied by the vacuum window, the scintillating material (discussed in **Section 4.3**) and the material that is used for the cell dish (be discussed in greater detail in **Chapter 5**).

SRIM 2003 was used to simulate a beam of 750 keV protons passing through a number of different collimator/cell target models in order to test whether the experimental design was suitable. As shown in **Figures 4.5a** and **b**, this range is sufficient for the charged-particle microslit collimator system, in which the protons must penetrate the 1.4 μm Mylar vacuum window, the 1.4 μm Mylar cell dish, and the entire effective thickness of the cell (**Figure 4.5a**), and for the pinhole aperture collimator system, in which the protons must penetrate the 1.4 μm Mylar vacuum window, the 5.0 μm scintillating plastic for the single-particle detection system, the 1.4 μm Mylar cell dish, and the entire effective thickness of the cell (**Figure 4.5b**).

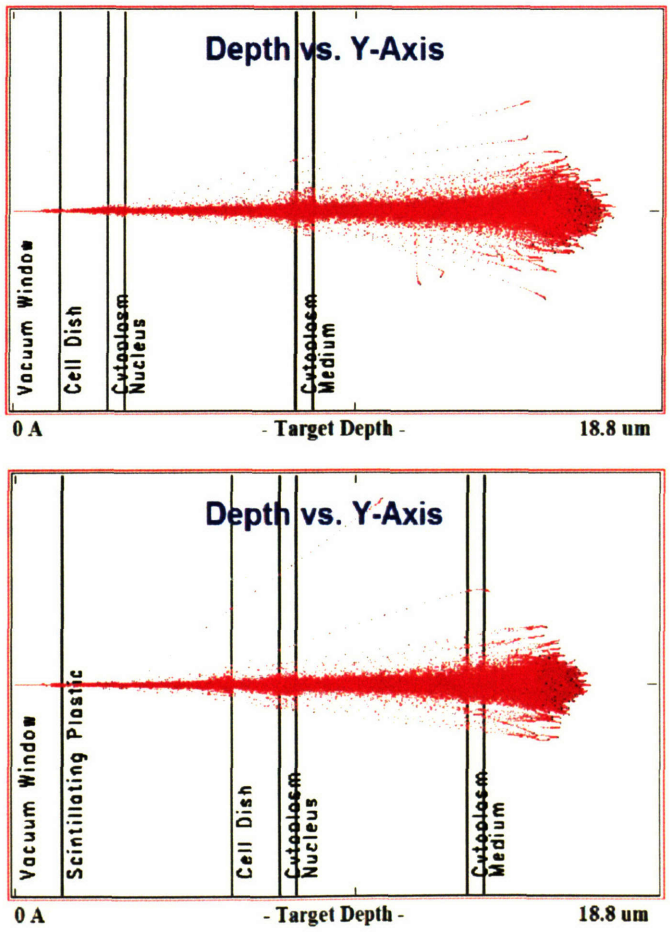

Figure 4.5 a) SRIM 2003 calculation for the charged-particle microslit, in which a 750 keV proton beam traverses the 1.4 μm Mylar vacuum window, the 1.4 μm Mylar cell dish, 6 μm of cell thickness (cytoplasm and nucleus), and terminates in medium, **b)** SRIM 2003 calculation for the pinhole

aperture collimator, in which a 750 keV proton beam traverses the 1.4 μm Mylar vacuum window, 5 μm of scintillating plastic, the 1.4 μm Mylar cell dish, 6 μm of cell thickness (cytoplasm and nucleus), and terminates in medium.[94]

4.3 Single Particle Detection System

In the design of a single-particle irradiation system, a reliable and accurate method of detecting single particles is required, as well as a method of using that signal to activate the shuttering system for the beam to limit the delivered radiation dose to a single particle or specified number of particles. The deflector system components are described in detail in **Chapter 3**, and its use as a shuttering system is described below in **Section 4.3.4**.

4.3.1 Background/Options

Single-particle detection has been handled in a number of ways for charged-particle microbeams. Particles may be detected immediately after exiting the collimator and before traversing the cells ("pre-target detection"), or after traversing the cell dish material and cell targets ("post-target detection"). The two primary means of single-particle detection are with a "pre-target" transmission scintillator, and with a "post-target" ionization chamber.

The GCI Microbeam at the Gray Cancer Institute in England uses the transmission scintillator technique. Placing a series of three thin (each 6 μm thick) pieces of organic scintillating plastic (total thickness of 18 μm) between the collimator and the cell dish allows for the production of a measurable number of photons during a charged-particle traversal. These photons are detected by a photo-multiplier tube (PMT), housed in one of the positions on the observation microscope turret (as shown in **Figure 4.6**). Because the observation microscope objective must be moved aside to engage the detector assembly, continuous observation of the cells during irradiation is not possible.[33]

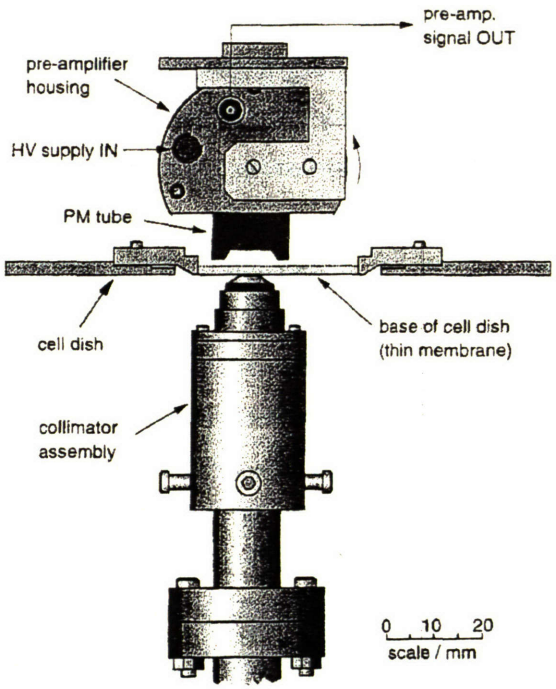

Figure 4.6 GCI Microbeam collimator and single particle detection apparatus.[33]

The RARAF Microbeam at Columbia University detects charged particles either before or after they pass through the cell, using either a solid-state detector for pre-target detection or a gas-filled ionization chamber mounted on the 40x objective of the observation microscope above the cell dish for post-target detection. The latter method requires the removal of practically all the medium from above the irradiated cells so that transmitted particles of sufficient energy are still present for detection, but confers the advantage of continuous observation of the cells during an irradiation. This arrangement is shown in **Figure 4.7**.[82]

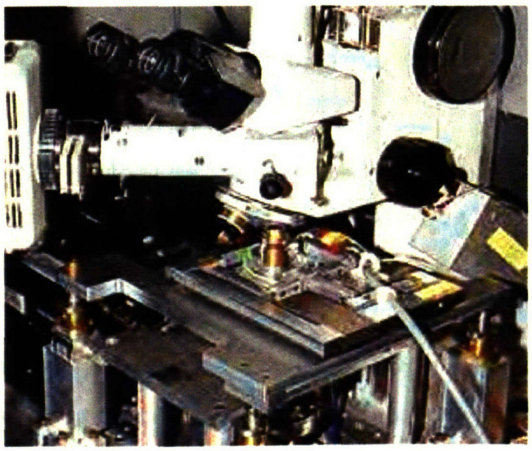

Figure 4.7 RARAF Microbeam observation microscope, with gas-filled ionization chamber mounted on 40x objective.[84]

A scintillator method similar to the one used in the GCI Microbeam was chosen for the LABA Microbeam, primarily to optimize for a wide range of radiobiological research given the limited range of the 750 keV protons that may be routinely generated by the LABA accelerator. The requirement of medium removal for use of "post-target" methods that directly detect particles after passing through the cell target was viewed as overly problematic for radiobiological studies, as it precluded long irradiation times during which the cells could potentially dry out. Altering the cells' environment in this manner introduces the possibility of "biological error" from a wide range of cellular responses to the perceived environmental insult. While the RARAF Microbeam partially addresses this problem by maintaining a moist atmosphere over the cells, it doesn't address altered biological variables such as oxygen tension, nutrient concentration, and waste diffusion, so the environment is still significantly changed. The LABA design was also modified to address the issue facing the GCI microbeam, in that the GCI detection system does not allow for continuous observation and monitoring of the irradiated cells while the detector assembly is in position.

4.3.2 LABA Design, Coincidence Techniques

For the LABA Microbeam, a system by which the passage of a single charged particle may be detected as the cell is irradiated, originally devised by O'Meara et al. in 2002[77] has been designed and implemented. This method uses a ~5 μm thick film of scintillating plastic (Bicron BC-400 organic scintillator, Saint-Gobain Crystals and Detectors, Paris France), a light guide to which the scintillating plastic is attached with optical cement (Bicron BC-600 optical cement), and two photomultiplier tubes (Hamamatsu R7400U series) operating in coincidence mode. The signal produced by the detection system will be used to trigger the electrostatic deflector, in order to shutter the beam immediately after a particle or specified number of particles traverses the scintillator. A diagram of this apparatus is shown in **Figure 4.8**.

The scintillating plastic was chosen because it is readily available in thin sheets of ~5 μm thickness, has high conversion efficiency and allows for a very short resolving time (rise time of ~0.9 ns, decay time of ~2.4 ns). (Saint-Gobain Crystals and Detectors, Paris France) This compares well to typical resolving times for plastic scintillators and silicon charged-particle detectors, which are generally on the order of a few nanoseconds for the energy range of 0.1 to 1 MeV.[14, 53] The light guide was included because it collects a greater fraction of the light emitted when the charged particle traverses the scintillating plastic, effectively increasing the solid angle subtended by the PMTs and improving the signal available to the detectors.

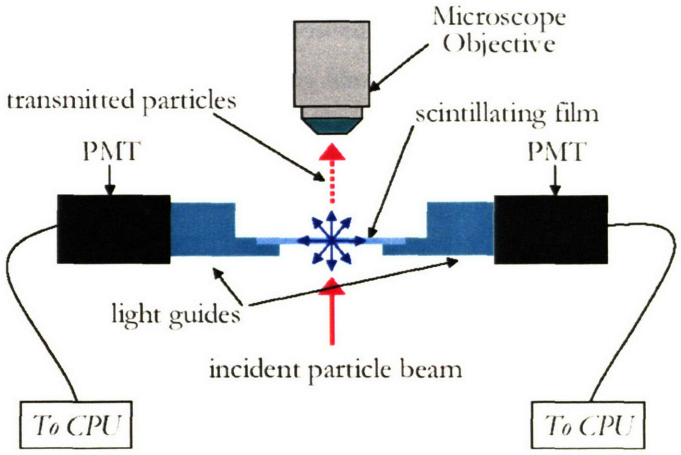

Figure 4.8 Diagram of the LABA Microbeam single-particle detection system, including the scintillating film, light guides, and photomultiplier tubes.

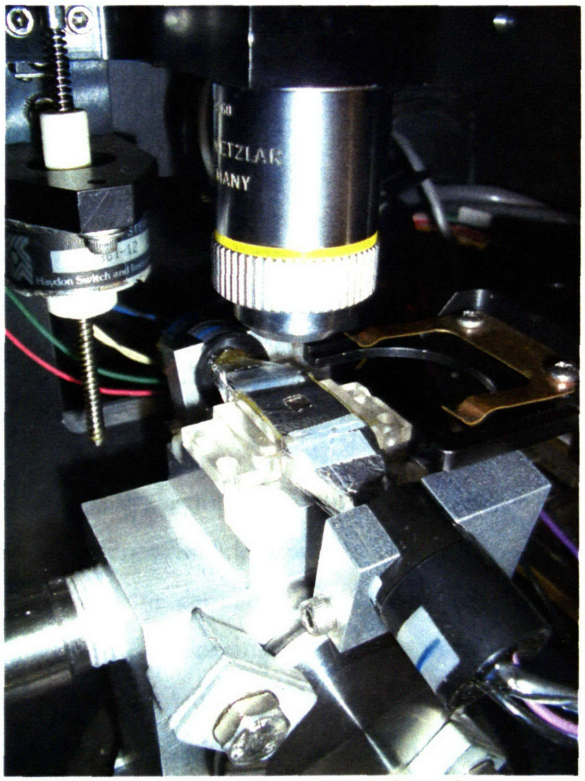

Figure 4.9 LABA single-particle detection system, consisting of two PMTs mounted via a yoke to the collimator assembly, with light guide and scintillating plastic in place over the collimator aperture.

Coincidence measurement, or the measurement of events that occur in two separate detectors within a given time interval, was chosen because it reduces the error associated with random detection pulses in the photomultiplier tubes. A simple coincidence circuit accomplishes this by summing the voltage "height" of two input pulses occurring within a pre-defined interval, passing the resultant sum pulse through a discriminator level that is greater than the "height" of a single pulse, and only

generating an output pulse when the two overlapping input pulses exceed this level. (illustrated in **Figure 4.10**) The uniformity of the energy deposited by the 750 keV protons generated by the LABA accelerator as they pass through the scintillating film is such that the output pulses are highly similar in amplitude.

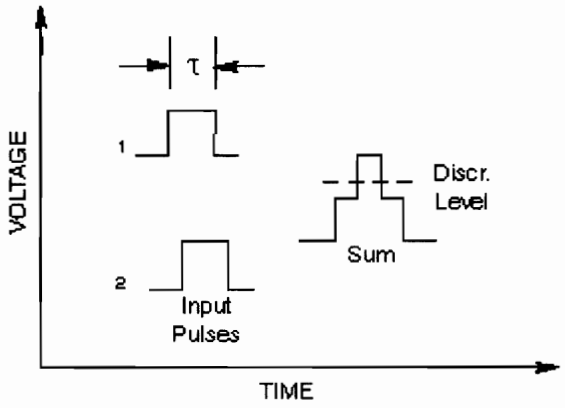

Figure 4.10 Pulse height discrimination for a simple coincidence circuit.[14]

The period during which the two input pulses can be accepted is defined as the resolving time, which is determined by the width of an individual pulse, τ, such that the ideal resolving time is equal to 2τ. However, in practice the actual resolving time may be greater than 2τ due to electronics delay and timing jitter.

However, use of a coincidence analyzer improves upon this scheme by allowing for the analysis of several input signals. The coincidence module produces a logic pulse output when the input pulses, on the active inputs, occur within the defined resolving time window (usually selected by a front panel control on the module itself). Specification of the resolving time window is of utmost importance, since, as noted previously, detector events may occur at random times. These can create "accidental" coincidences between two pulses which result in background counts in the coincidence counting. The rate of "accidental" or random coincidences is given by **Equation 4.1**:

$$\mathbf{N}_{acc} = \mathbf{N}_1\mathbf{N}_2(2\tau) \qquad \textbf{Equation 4.1}$$

Where:

$\mathbf{N}_1$ = Count rate in detector number 1

$\mathbf{N}_2$ = Count rate in detector number 2

N_τ = resolving time of the coincidence circuit = 2τ

From **Equation 4.1**, it seems that the simplest way to reduce the number of "accidental" coincidences is to make the resolving time as small as possible. However, the number of counts in the detectors is dependent upon the experiment parameters and the type of detector used, and the resolving time cannot be reduced below the amount of time jitter in the detector pulses without losing true coincident events. Thus, the type of detector determines the minimum possible resolving time.

The LABA coincidence detection electronics setup, using two PMT-based detectors, is shown in **Figure 4.11**. The unipolar pulse from the amplifier is processed by a constant-fraction timing SCA to produce a standard NIM logic pulse for the coincidence unit. Either an alpha-emitting radionuclide or a pulse generator may be used to test operation, but the latter also allows the operator to test delays.

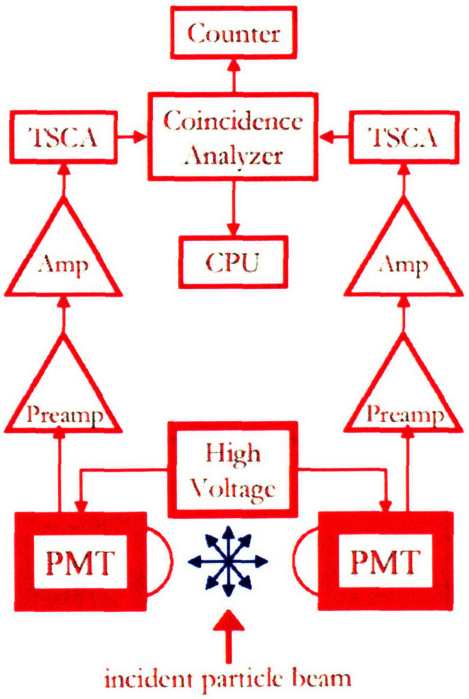

Figure 4.11 LABA Microbeam coincidence detection system electronics (Amp=spectroscopy amplifier, TSCA=timing single-channel analyzer).

Table 4.1 lists the electronics used in the LABA Microbeam single particle detection system.

Component Type	Model
Detector	2 Hamamatsu R7400U series PMTs
Preamplifer	2 Hamamatsu C5781 Socket Assemblies, attached to a +/- 15 V power supply
High Voltage Power Supply	2 Canberra 3105 HV power supplies (1-5000 V)
Amplifier	1 Ortec 471 Spectroscopy Amplifier 1 Aptec 6300 Spectroscopy Amplifier
Timing Single Channel Analyzer	2 Canberra 2037A Edge/Crossover TSCAs
Coincidence Analyzer	1 Canberra 2040 Coincidence Analyzer
Counter	1 Ortec 770 Counter
Computer Interface	1 Canberra 8715ADC

Table 4.1 Electronics used for the PMT-based LABA Microbeam single-particle detection system.

In order to properly operate the LABA Microbeam coincidence detection system a timing curve was obtained in which coincidences are measured as a function of the time interval between the start input (from one PMT/TSCA) and the stop input (from the other PMT/TSCA). In the ideal case of no time jitter in either detector, the solid curve in **Figure 4.12a** is obtained. Real detectors such as the photomultiplier-based system used in the LABA Microbeam will produce the dashed curve shown in **Figure 4.12a**, and the minimum resolving time setting is the width of the flat region (above which all true coincidences are collected).[14, 53] **Figure 4.12b** shows the resolving time curve for the LABA Microbeam coincidence detection system.

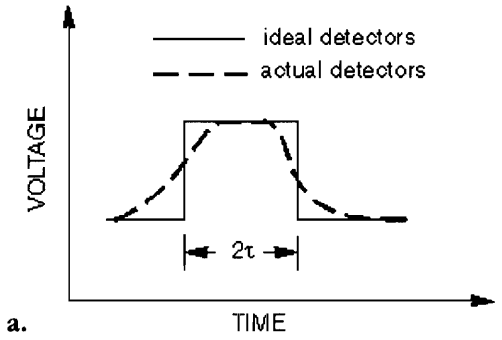

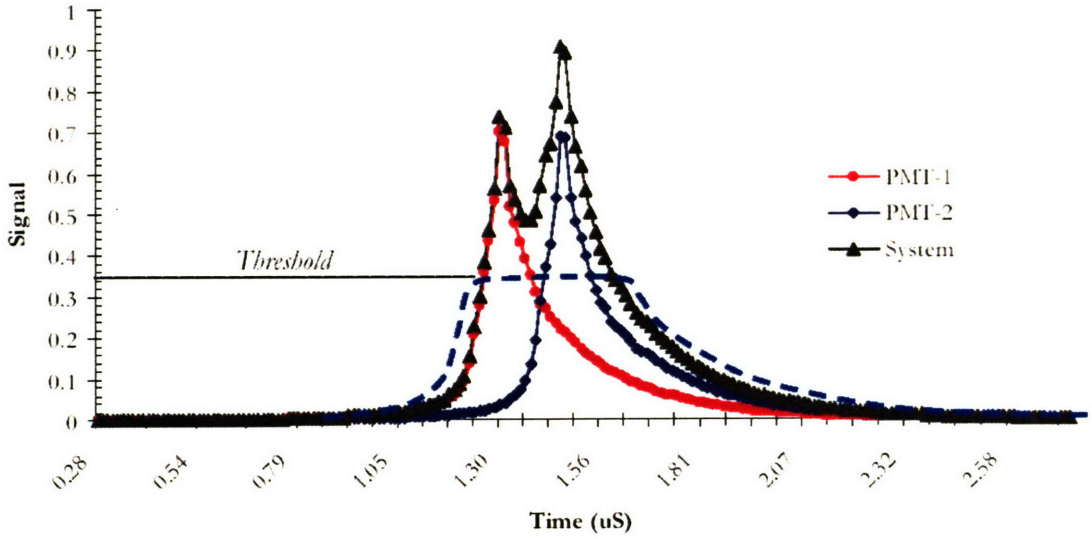

b.

Figure 4.12 a) Typical resolving time curve[14], **b)** LABA Microbeam coincidence detection system resolving time curve shown as a light blue dashed line, superimposed over TAC output data from the two PMTs. Signal is normalized to 1.

The full-width half-maximum (FWHM) of the system is ~0.268 μsec, and because the shape of the curve is roughly Gaussian, FWHM=2.35*σ.[53] The resulting value for σ is then 0.114 μsec, and in order to reduce the probability of false coincidences to < 1%, a 10*σ spread (1.14 μsec) was determined. Using these values, it can be stated the coincidence system should be able to reliably detect single-particle transmissions whose intensity is < 0.8 particles/μsec with > 99% accuracy. As the highest intensity through the charged-particle microslit is approximately 0.11 particles/μsec and the highest theoretical intensity through the proposed pinhole aperture is approximately 0.165 particles/msec, both collimation systems are within the detection limits of the LABA single-particle detection system.

4.3.3 Verification

In practice, it is difficult if not impossible to analyze coincidence events with 100% confidence due to the statistical uncertainties inherent to the nature of the electronic processes. Some of these errors include statistical timing errors from the detection process and uncertainties in the electronics resulting from timing jitter, amplitude walk and noise, which lead to statistically variable time delays between processed events. Despite these issues, coincidence detection techniques seem to be the most appropriate method of determining the fluence of the charged-particle microbeam entering from the collimating apparatus in the LABA experimental endstation, given the restrictions created

by the limited amount of light production in the thin scintillators required by the low energy of the proton beam that may be generated by the LABA accelerator.

For the LABA Microbeam, the proposed coincidence detection method of using a thin film of scintillating plastic (~5um) coupled to a light guide with Bicron BC-600 optical cement and two photomultiplier tubes was evaluated with respect to detection efficiency and its physical effect on the quality of the beam with respect to energy and radial straggle. High detection efficiency (on the order of 99%) is required for precise control of radiation delivery, and the physical effect of the detection system must have a minimal impact on the quality of the beam so as not to compromise spatial and energy resolution. Data from simulation and from experiments using a test assembly and an Am-241 alpha particle source will be used in this discussion.

A test assembly was constructed that would allow for the two PMT detectors in coincidence to be compared with a silicon surface barrier detector (which operates at ~100% detection efficiency).[56] A diagram of this arrangement and the actual test assembly are shown in **Figures 4.13** and **4.14a,b.**

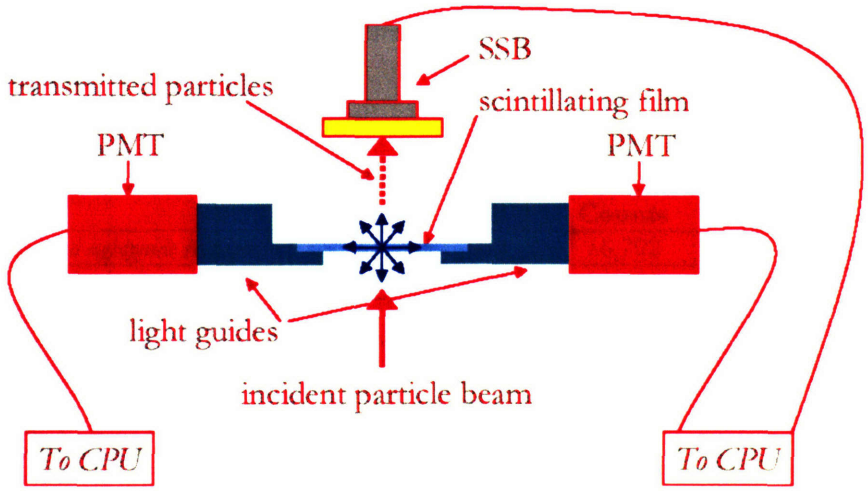

Figure 4.13 Coincidence detection test assembly diagram.

In addition to the electronics listed above in **Table 4.1**, the following electronics were used for the silicon surface barrier (SSB) detector (**Table 4.2**).

Component Type	**Model**
Detector	Silicon Surface Barrier, 10 μm silicon on gold substrate
Preamplifer	1 Ortec 142IH Preamplifier

High Voltage Power Supply	1 Harshaw NV-25A HV power supply (0-2000 V)
Amplifier	1 Canberra 816 Amplifier
Timing Single Channel Analyzer	1 Ortec 553 TSCA

Table 4.2 Electronics used for the silicon surface barrier (SSB) detector.

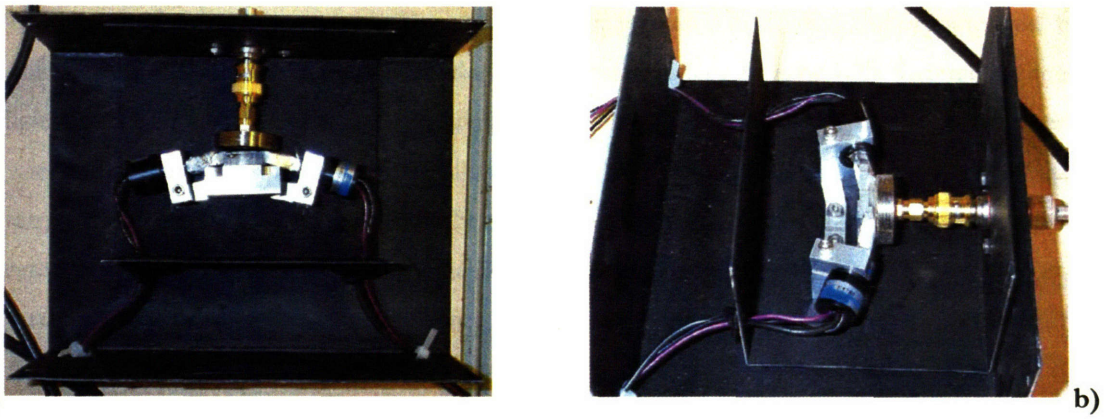

a) **b)**

Figure 4.14 Coincidence detection test assembly, **a)** top and **b)** side views.

In **Table 4.3**, the manipulations performed on the single-particle detection system to increase detection efficiency are shown. The experiments were performed using a 0.3 μCi ^{241}Am source ($T_{1/2}$ = 432 years), counting for 100 seconds unless otherwise noted. The silicon surface barrier (SSB) detector high voltage was set to 100 V, and the two photomultiplier (PMT) detectors in coincidence mode were set to 800 V.

Manipulation	SSB Counts	PMT(1,2) Counts	Detection Efficiency
Baseline, unwrapped lightguide in place	20,204	16,792	***83.1%***
Timing SCA lower level raised to 3.0 V	16,281	14,383	***88.3%***
Bicron optical coupling grease added to PMTs (Bicron BC-630)	9,241	8,322	***90.1%***
Light guide cleaned and arms wrapped in reflective foil	9,180	8,584	***93.5%***
Timing SCA lower level raised to 3.5 V	15,768	14,978	***95.0%***
Foil added to top of scintillator	13,410	13,127	***97.9%***
Light guide cleaned again w/ toothpaste, arms re-wrapped in reflective foil	12,994	12,801	***98.5%***
Redo previous, 20 minute count	156,211	153,111	***98.0%***

Table 4.3 Progression of manipulations used to improve the detection efficiency of the two photomultiplier (PMT) detectors in coincidence mode with respect to the silicon surface barrier (SSB) detector. All errors calculated to be <1%.

Efforts made to further improve the detection efficiency of the PMT-based coincidence detector system met with mixed results; no manipulation of the system was successful at increasing the detection efficiency to 99% or more.

4.3.4 Shutter Application

As described in **Chapter 3, Section 3.2.1.2**, the deflector system is capable of gating the beam "on" or "off" as specified by the operator. The gating signal is provided by feeding the output signal from the coincidence analyzer in the single-particle detection system (see **Figure 4.11**) through an analog-to-digital converter (ADC). The resulting digital signal is then sent to the CPU, where the operator can specify the number of particles that is allowed to pass before the deflector is engaged. When the operator-specified number of particles has been delivered to the target, the deflector is electronically activated and remains activated until particle delivery is again desired. **Figure 4.15** shows an on/off pattern of film irradiation using the deflector system. In this particular application, the default for the deflector is "on," preventing protons from reaching the target – in this case, a piece of LR115 track-etch film pressed onto a cell dish. The stage was set to move in 20 μm steps, and dwell for 0.1 seconds between each step. The deflectors disengage for the length of the dwell time, allowing particles to reach the film, and then re-engage while the stage is moving.

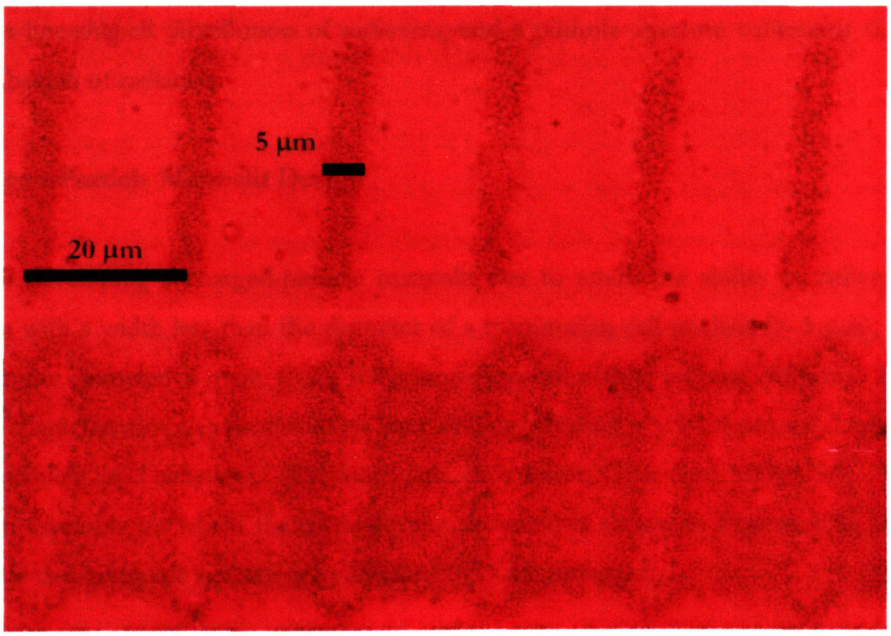

Figure 4.15 Testing of "on/off" deflector pattern with LR115, using X=500V, Y=600V deflector parameters. Comparison of charged-particle microslit irradiations with the deflection enabled between dwells on the top, and with the deflection disabled on the bottom. (20 μm spacing between dwells, color adjusted, 10x magnification)

4.4 Collimation/Target Design and Verification

Designing the collimator that delimits the charged-particle beam is a challenging task – several considerations come into play:

- Aspect Ratio: The aspect ratio is defined as the ratio between the length of the collimator and the width of the aperture. A small aspect ratio allows more of a penumbra effect from charged particles that are not in line with the desired beam, while a large aspect ratio is more likely to occlude the beam if not oriented properly.
- Photon Production/"Contamination": Some materials interact with charged particles to produce x-rays; for example, PIXE, or proton-induced x-ray emission, may produce a significant x-ray background. This could result in a "dirty" or "contaminated" beam, where a non-negligible dose is distributed outside of the targeted region and low-LET radiation is delivered along with the charged particles within the targeted region. This confounds the desired precision of a microbeam.
- Space/Design Limitations: For the LABA microbeam, while the light-tight experimental endstation box is sizeable, there is a lot of other equipment limiting the available space.

Two classes of collimator have been designed – a slit-type collimator (the "microslit") capable of delivering a line-shaped distribution of radiation, and a pinhole aperture collimator that delivers a point distribution of radiation.

4.4.1 Charged-Particle Microslit Design

The aim in developing a charged-particle microslit was to attain the ability to deliver a radiation distribution with a width less than the diameter of a mammalian cell nucleus (< 5 μm), and a length greater than the diameter of many (>20) full mammalian cell widths (at least 200 μm). A custom slit with these characteristics was produced by laser drilling, creating a 1.5-1.8 μm x 1.1 mm slit in a 40 μm thick stainless steel substrate. (Produced by Lenox Laser, Glen Arm MD, USA) A diagram of the vacuum assembly on which the microslit was mounted is shown in **Figure 4.16**, indicating the points where the lightguide and the yoke for the PMTs are mounted.

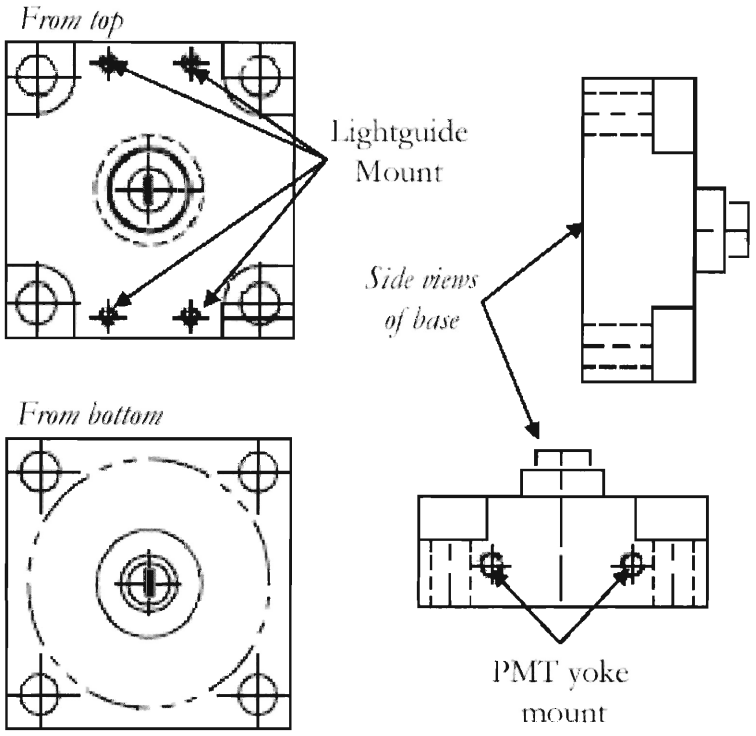

Figure 4.16 Microslit collimator base assembly schematic, showing the points where the lightguide for the single-particle detection system and the yoke that holds the two photomultiplier tubes in place are located. *(Courtesy Andrew Dart, Pyramid Technical Consultants)*

Theoretical beamspot dimensions produced by the charged-particle microslit were determined by extrapolating the aspect ratio of the slit (25:1) through to the biological target and adding the contribution from radial straggle caused by interactions with the intervening material (1.4 μm of mylar, 5 μm of scintillating material from the single-particle detection system, an additional 1.4 μm of mylar (the base of the cell dish, to be discussed further in **Chapter 5, Section 5.2**) as modeled by the SRIM 2003 code.[94, 113] The calculated beam profile was determined to be 2.2 ± 0.15 μm, subsequently verified by irradiation of LR115 track-etch film (**Section 4.4.3**).

The microslit assembly is covered with a 1.4 μm layer of mylar to help maintain vacuum and prevent dust from occluding the slit over time. **Figure 4.17** shows the charged-particle microslit assembly in place in the LABA Microbeam experimental endstation, with the single-particle detection system removed. (The fully assembled system with the single-particle detection system in place was previously shown in **Figure 4.9**.)

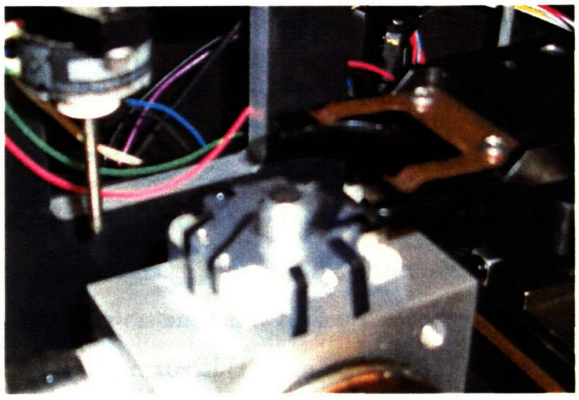

Figure 4.17 The charged-particle microslit assembly in place in the LABA Microbeam experimental endstation, with the single-particle detection system removed.

4.4.2 Charged-Particle Pinhole Aperture Design

The aim in developing a charged-particle pinhole aperture was to attain the ability to deliver a point radiation distribution with a diameter of < 3 μm. As discussed in **Chapter 2** (**Section 2.1.3**), there are many means by which the charged particle beam generated by the LABA Microbeam accelerator could be collimated or focused to a micron-scale size. The GCI Microbeam (**Section 2.1.4.1**), for example, uses a glass capillary tube to physically collimate their beam down to < 3 μm. The RARAF Microbeam (**Section 2.1.4.2**), on the other hand, uses a set of 5 μm and 6 μm apertures laser-drilled in 12.5 μm thick stainless steel discs separated by a 300 μm spacer to produce a roughly 5-8 μm beamspot. It was determined that physical collimation with a glass capillary tube (O.D. 250 μm, I.D. 1.5 μm) would be the method used for the LABA charged-particle pinhole aperture.

The pinhole aperture consists of a 1 mm piece of glass capillary tubing mounted in a positionable vacuum assembly. (**Figure 4.18a,b**)

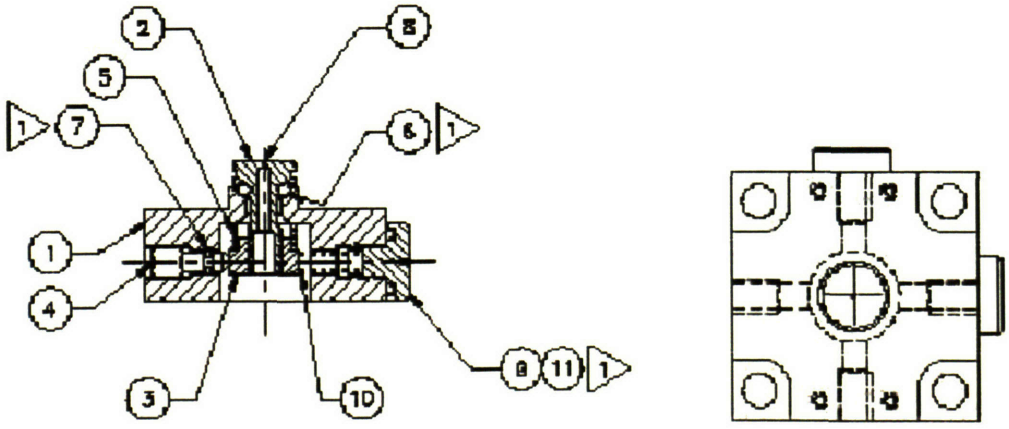

a) **b)**

Figure 4.18 Pinhole aperture collimator assembly, **a)** side view and **b)** top view. On side view diagram: **(1)** Collimator Block, **(2)** Collimator Shaft, **(3)** Shaft Nut, **(4)** Adjuster Screw, **(5)** Compression Spring for Shaft (Lee Spring LC-026E-1), **(6)** O-Ring (Viton #007), **(7)** O-Ring (Viton #002), **(8)** Collimator Tube (1 μm I.D., glass capillary), **(9)** Spring Retainer Screw, **(10)** Compression Spring (Lee Spring LC-024A-4), **(11)** O-Ring (Viton #010)

Theoretical beamspot dimensions produced by the charged-particle pinhole aperture were determined by extrapolating the aspect ratio of the inner diameter of the glass capillary tube (1100:1.5) through the intervening distance and adding the contribution from radial straggle caused by interactions with the intervening material (1.4 μm of mylar, 5 μm of scintillating material from the single-particle detection system, and an additional 1.4 μm of mylar (the base of the cell dish, to be discussed further in **Chapter 5, Section 5.2**) as modeled by the SRIM 2003 code.[94, 113] The calculated beam profile was determined to be a circle with a diameter of 1.8 ± 0.2 μm, although this has not yet been physically demonstrated by irradiation of LR115 track-etch film (**Section 4.4.3**). A comparison of SRIM 2003 calculations for the aperture collimators used in the GCI, RARAF, and LABA Microbeams is shown in **Table 4.4**.

Microbeam	Particle Type	Collimator Type	Intervening Material	Calculated Beamspot Size
Gray Lab (GCI)	4 MeV protons	1.5 μm by 1 mm glass capillary	3.0 μm mylar, 18 μm scintillating plastic, 4.0 μm polypropylene	2.3 ± 0.3 μm
Columbia (RARAF)	5.3 MeV α particles	5 μm and 6 μm discs separated by 300 μm	1.4 μm mylar, 3.8 μm polypropylene	6.2 ± 0.02 μm
MIT (LABA)	0.75 MeV protons	1.5 μm by 1 mm glass capillary	2.8 μm mylar, 5 μm scintillating plastic	1.8 ± 0.2 μm

Table 4.4 A comparison of SRIM 2003 calculations for the aperture collimators used in the GCI, RARAF, and LABA Microbeams.

The design shown in **Figure 4.18** was finalized by Pyramid Technical Consultants (Waltham MA, USA) and was constructed by Machine Technology (Beverly MA, USA). The collimator itself is actually a 1 mm long piece of glass capillary tubing (fused silica tubing, OSGE) with a 1.5 μm inner diameter and 250 μm outer diameter. The shaft in which the capillary tubing is held (**#2** in **Figure 4.18a**) may be "tuned" with respect to the beam direction using the orthogonal x/y "adjuster screws" (**#4** in **Figure 4.18a**), which are opposed by a set of springs (**#10** in **Figure 4.18a**). The pinhole collimator assembly is covered with a 1.4 μm layer of mylar to help maintain vacuum and prevent dust from occluding the capillary tube over time.

Generating appropriate lengths of capillary tubing required the construction of a custom tube cutter, shown in **Figures 4.19a** and **b**. The motor turns a diamond saw that is used to nick the tubing; a

Starrett micrometer allows the operator to advance the stock capillary tubing forward so that an exact length may be cut.

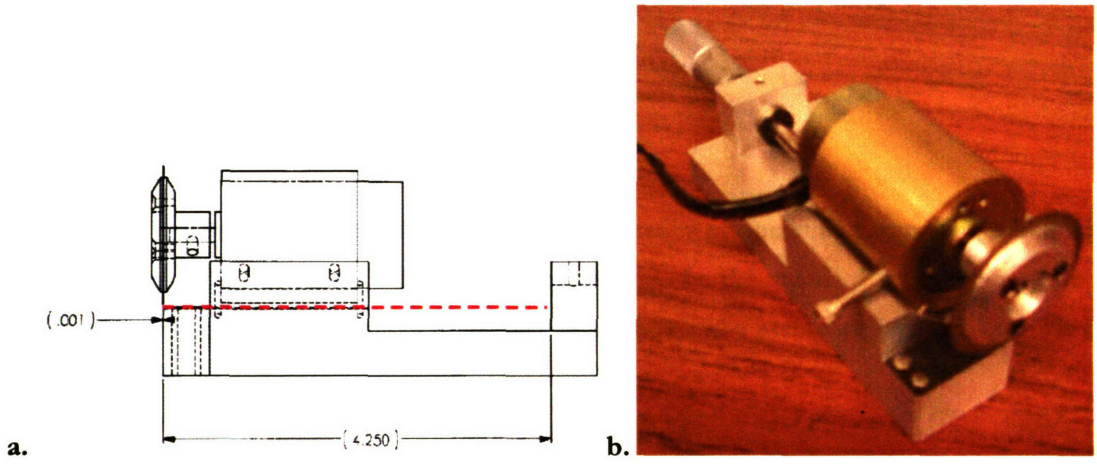

Figure 4.19 a) Schematic of collimator cutter, side view. The red dashed line indicates the channel in which the collimator stock is placed. **b)** Image of actual collimator cutter. The blade is diamond edged, motor turns at constant speed. The Starrett micrometer is used to determine length of capillary tube to be cut.

Images of the capillary and the pinhole aperture assembly glass capillary tube in place are shown in **Figures 4.20a** and **b**.

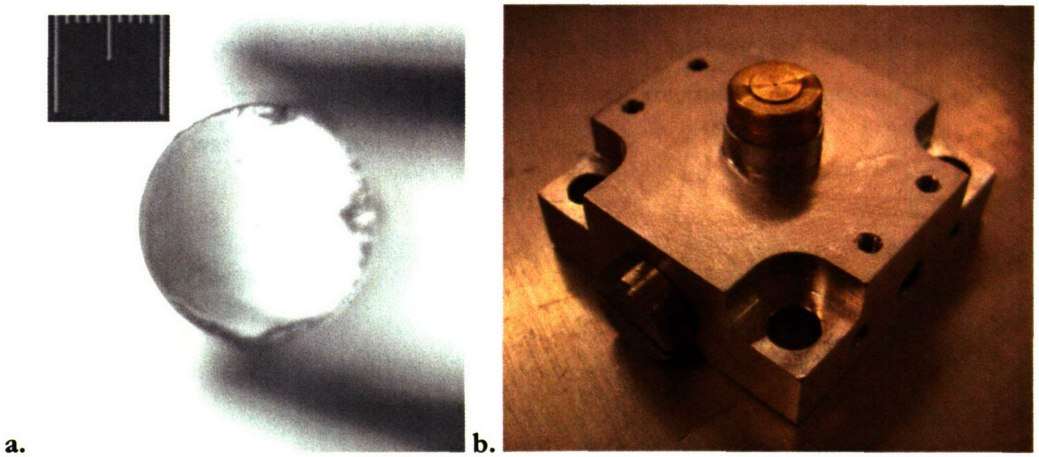

Figure 4.20 a) Image of glass capillary tube with scale; large ticks separation = 100 μm, small tick separation = 10 μm, measured capillary outer diameter = 227 μm, inner diameter = 1.5 μm; **b)** Pinhole aperture assembly with glass capillary tube in place.

4.4.3 Verification Methods and Design Assessment

The methods available for verifying microbeam beamspot characteristics were introduced in **Chapter 3, Section 3.1.1.2**. The subset of these techniques used in beamspot characterization at the endstation includes:

- Faraday cup
- Track etch techniques (CR39, LR115)
- Radiochromic film techniques (MD55, HD-810)

The Faraday cup was used primarily to maintain consistency of operating parameters at the level of the accelerator. Track etch techniques are considered to be the standard for providing the most useful data with respect to the true beam profile, as they show the exact distribution of particle tracks that result from the collimated beamspot.

4.4.3.1 Charged Particle Microslit Verification

The beam profile generated by the charged-particle microslit was verified using both radiochromic and track-etch techniques. While both of these methods are capable of generating a physical representation of the beamspot dimensions at the target, the "gold standard" for beam profiling is the image on a track-etch film because of its ability to show individual particle hits. The beam profile for the charged-particle microslit is shown in **Figure 4.21**, obtained from a charged-particle microslit irradiations of ~300, 100, and 200 Gy in 20 μm steps on CR39 track-etch plastic. The black bar indicates 10 μm. Comparison of the track-etch images to the microscopic standard verified that the width of the beam profile generated by the charged-particle microslit under the conditions used for biological irradiation was 2.5-3.0 μm.

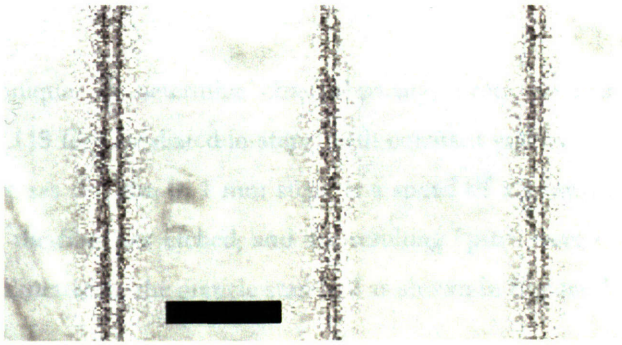

Figure 4.21 Beam profile of the LABA microslit, ~300, 100, and 200 Gy charged-particle irradiations separated by 20 μm steps on CR39 track-etch plastic. The black bar indicates 10 μm. (20x magnification)

In **Figure 4.22**, modified MD55 radiochromic films were irradiated for different dwell times, demonstrating the dependency of beam profile width on delivered dose. It should be noted that the radiochromic film characterization method is useful for demonstrating inhomogeneities in dose distribution – the gaps evident in **Figure 4.22** are due to occlusion of the laser-drilled slit by dust after extended operation, underscoring the importance of protecting the slit with a thin layer of mylar.

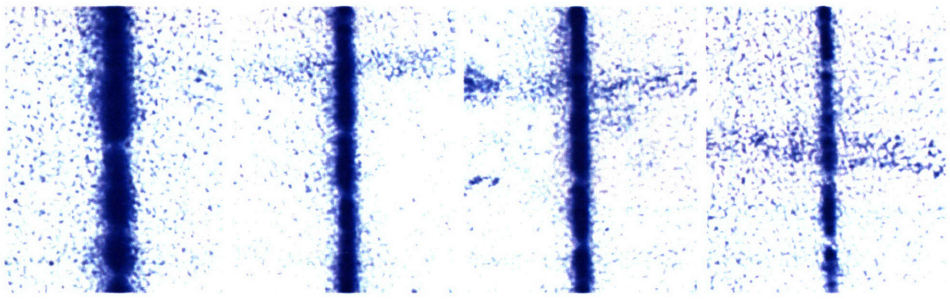

10 seconds (approx. 11 microns wide)	5 seconds (approx. 6 microns wide)	2 seconds (approx. 5 microns wide)	<1 second (approx. 2.5 microns wide)

Figure 4.22 Slit aspect width on modified MD55 film with variation in irradiation time. (color adjusted)

In addition to determining the beam profile, track-etch techniques are well suited for measuring the current at the exit of the charged-particle microslit. Total beam current is primarily a function of the extraction voltage applied to the plasma, which is measured using a Faraday cup and electrometer at the exit of the accelerator. Dose delivered to the biological target, however, is solely a function of the number of particles delivered through the slit. Thus, the relationship between the total beam current and the corresponding dose delivered by the collimated current at the target position must be determined.

Using track etch techniques to determine charged-particle beam intensity at the target position required the use of LR115 film irradiated in steps, with constant velocity sweep between short dwell times. The beam traverses the film in 1 mm steps at a speed of 1.5 mm/sec, with 1 second dwells each step, after which the film was etched, and the resulting "pits" were counted using an eyepiece grid with square size calibrated to the graticle standard as shown in **Figure 4.23**.

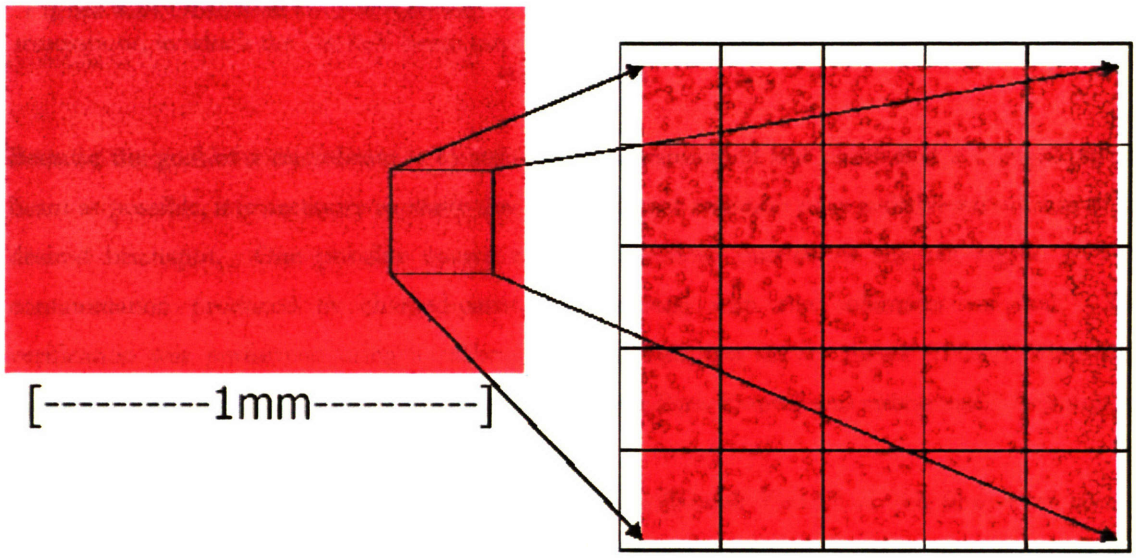

Figure 4.23 "Pits" in LR115 film used to determine intensity of the beam through the microslit assembly (color adjusted).

For example, a 0.02 μA beam on the Faraday cup results in a beam intensity of 2.2×10^4 particles/sec. For most charged-particle microslit irradiations, the single-particle detection system is not used. From SRIM 2003 calculations, it can be determined that after traversing the 1.4 μm of Mylar that serves as the vacuum window and an additional 1.4 μm of Mylar that serves as the base of the cell dish, a beam of 750 keV protons will deliver 275 keV/particle to the cell (assuming 7 μm cell thickness). Energy is deposited in a very small volume of unit density, 2.5 μm wide by 1mm long by 7 μm deep, for a total irradiated mass of 1.26×10^{-11} kg. Thus, by varying the extraction voltage and dwell time, we can vary the dose distributed to the cells through the microslit over a range from tens to hundreds of Gy, as shown in **Figure 4.24**.

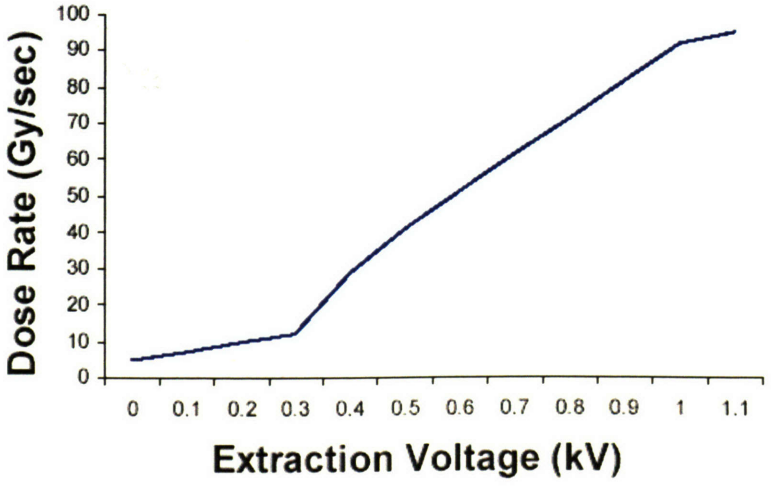

Figure 4.24 Dose Rate to Cells (Gy/sec) vs. Extraction Voltage (kV) for charged-particle microslit irradiations, in which the 750 keV beam traverses a total of 2.8 μm of Mylar prior to interacting with the cell target.

Because the goal of a microbeam is to attain as uncontaminated and controlled a charged-particle beam as possible, it is necessary to verify that no significant radiation dose is delivered outside of the desired beamspot. One possible source of radiation dose outside of the slit region is x-ray contamination produced by charged-particle interactions with the collimator material. This verification was performed using a calibrated μRem radiation survey meter (Bicron Micro-Rem Radiation Monitor, Saint-Gobain Crystals and Detectors, Paris France) and radiographic techniques.

In **Figure 4.25a,b**, sheets of standard radiographic film (Kodak T-MAT G/RA film) were used to determine if a significant amount of x-ray contamination was produced by the protons terminating in the collimator material (i.e., not passing through the microslit). The film was placed within a light-tight sleeve of cardboard of sufficient thickness to fully attenuate any protons, but scarcely attenuate the low-energy x-rays that may be produced by the proton-induced x-ray emission in the collimator material.

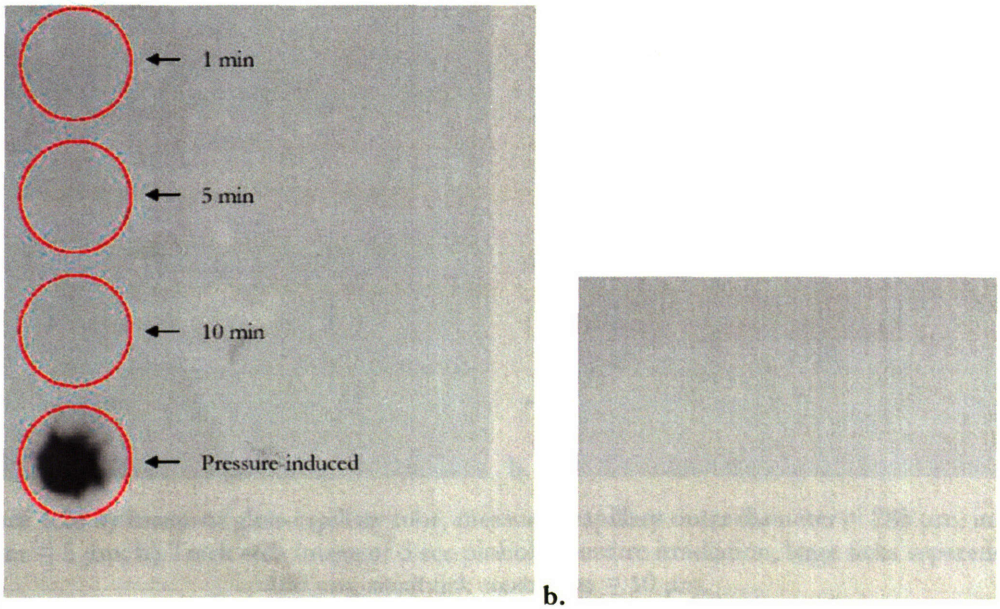

Figure 4.25 a) Irradiated film with rings indicating the position of 1, 5, and 10 minute irradiations, as well as the pressure-induced exposure from slit top, **b)** baseline film exposure. Width of rings = 2 cm.

While the x-ray film is sensitive to just a few mrem, the only darkening of the film was noted when it was pressed vigorously against the slit itself. This suggests that proton-induced x-ray emission

(PIXE) does not significantly contribute to the dose delivered to the cells by the charged-particle microslit.

4.4.3.1 Charged Particle Pinhole Aperture Verification

The beam profile generated by the charged-particle pinhole aperture was analyzed primarily through track-etch techniques, as the small size of the intended beamspot would be difficult to detect using radiochromic methods. **Figure 4.20a** showed a light-microscopy image of a glass capillary tube with a measured capillary outer diameter (OD) of 227 μm and an inner diameter (ID) of 1.5 μm. For initial testing purposes, a glass capillary tube with a measured capillary outer diameter (OD) of 285 μm and an inner diameter (ID) of 5 μm was used, as it was deemed simpler to initially visualize a larger beamspot. An image of the glass capillary tube in place within the pinhole aperture assembly and an example of the beamspot generated by the charged-particle pinhole aperture are shown in **Figures 4.26a** and **b**, the latter obtained from a series of five second charged-particle pinhole aperture irradiations of LR115 track-etch plastic.

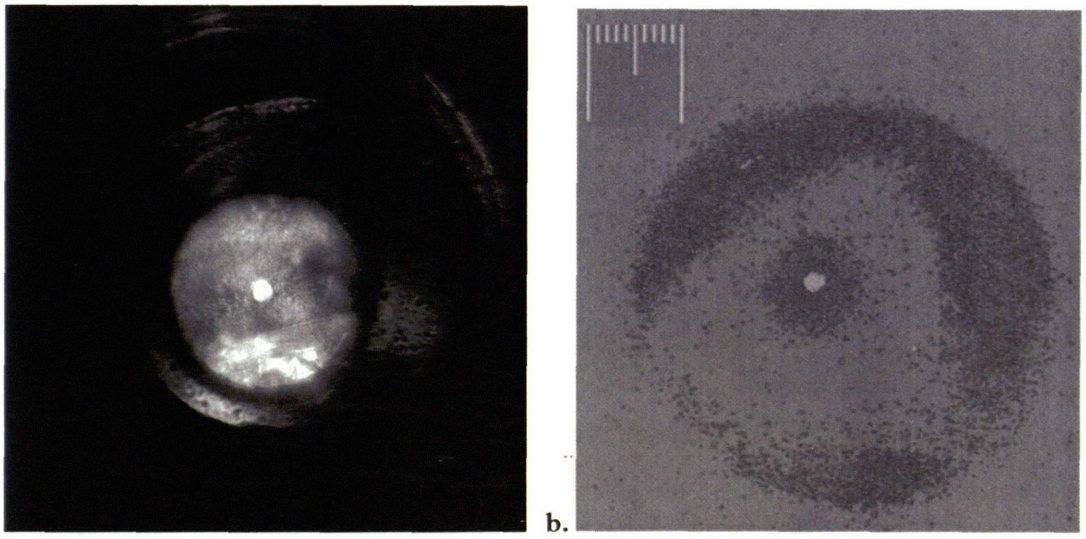

Figure 4.26 a) Image of glass capillary tube, measured capillary outer diameter = 285 μm, inner diameter = 5 μm; **b)** Track etch image of 5 sec pinhole aperture irradiation, large ticks separation = 100 μm, small tick separation = 10 μm.

As can be seen in **Figure 4.26b**, the pinhole aperture collimator did not generate a < 10 μm beamspot on the track-etch film; instead, a nearly 100 μm penumbra around a ~15 μm central spot resulted, surrounded by a secondary penumbra over 400 μm in diameter. It is hypothesized that the secondary 400 μm penumbra is the result of protons streaming around the outside glass capillary tube, but it is not understood how the inner 100 μm penumbra could have arisen. Further work will

be necessary to eliminate the penumbra effect and reduce the size of the pinhole aperture beamspot to a subnuclear size.

One important consideration in the future use of the pinhole aperture is that the slightest deviation from proper alignment will completely block the charged-particle beam from getting through. For example, the capillary tubing used in the pinhole aperture collimator is 1mm in length with a 1.5 μm inner diameter, resulting in a 1:667 aspect ratio for transmission through the inner channel. Such a large aspect ratio means that a deviation of as little as 0.086^0 would be sufficient to completely block transmission of the vertical beam. Thus, it was determined that the development of a simple and rapid method of tuning the beam was necessary to ensure proper alignment.

A simple tuning unit using a photomultiplier tube optically coupled to a light guide upon which a 50 μm piece of scintillating plastic was mounted was designed and built. **Figures 4.27a** and **b** depict the photomultiplier tube (PMT) based detection system used to verify that the pinhole aperture collimator is properly aligned.

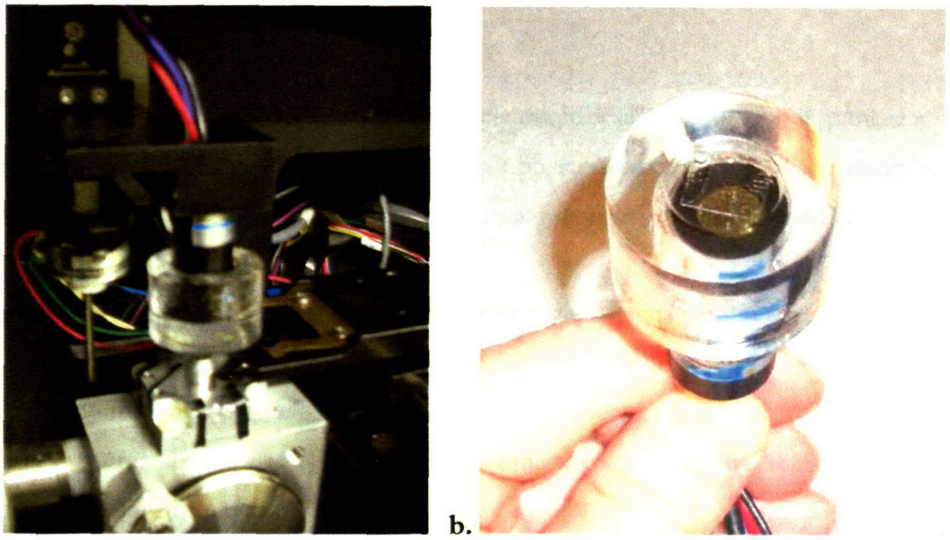

Figure 4.27 a) PMT-based tuning system, mounted in place of the 10x objective in the z-directional focusing stage, **b)** Face of PMT-based tuning system, showing coupling of 50 μm scintillating film on light guide to the PMT via BC-630 optical grease.

The PMT-based tuning system output is currently a simple counting system, with an electronics setup similar to that seen in **Figure 4.11** (although for only one photomultiplier detector). **Table 4.5** lists the electronic components used in the tuning system.

Component Type	Model
Detector	1 Hamamatsu R7400U series PMT
Preamplifer	1 Hamamatsu C5781 Socket Assembly, attached to a +/- 15 V power supply
High Voltage Power Supply	1 Harshaw NV-25A HV power supply (0-2000 V)
Amplifier	1 Canberra 816 Amplifier
Timing Single Channel Analyzer	1 Ortec 553 TSCA
Counter	1 Ortec 770 Counter
Computer Interface (not yet used)	1 Canberra 8715 ADC

Table 4.5 Electronics used for the PMT-based tuning system.

Once the characterization of the pinhole aperture assembly is complete, the tuning system will be integrated fully into the CPU-based control system using the Canberra 8715 ADC. Currently the 10x objective must be removed and the PMT-based tuning system must be run through the objective mount; a modular mount has been proposed that, once installed, will allow one-step switching between the 10x microscopy objective and the beam tuning system. Full characterization of the pinhole aperture and implementation of the tuning system are beyond the scope of this thesis, and will be considered in future work.

4.5 Experimental Control Systems

To attain the precision necessary for a charged-particle microbeam to control the number of particles traversing individually targeted cells, the software and physical components of the microbeam must be effectively integrated and coordinated through a manageable interface with the user.

The LABA control software, written in a proprietary language (Pyramid Technical Consultants, Waltham, MA) similar to C++ and running under the Windows NT operating system,[56] is responsible for controlling every aspect of the LABA microbeam, ranging from accelerator start-up and shutdown to manipulation of all beam-line components, including the subsystems of the endstation devoted specifically to cellular irradiation.

The control system has three general "properties":

- an interface within which parameters for the hardware can be both set and monitored routinely by the user
- the ability to input parameters necessary for specification of a particular cell irradiation experiment
- automated protection of the accelerator in the event of unexpected and unsafe increases in pressure or terminal voltage.

Controls specific to the various subsystems (Vacuum, Accelerator, Magnet/Deflector, Imaging, Imaging/Targeting) are divided into logical groups, with common functionality being grouped into distinct graphical user control interfaces. The Vacuum, Accel Control, and Facilities screens were covered in detail in **Chapter 3**, so the focus of this section will be on the "Acquire" and "Image" subsystem control screens.

4.5.1 Stage Movement/Positioning

As previously stated, a microbeam must be able to direct the beam to the target, or place the target in the path of the beam with a high degree of accuracy and precision. For the LABA Microbeam, the latter method was chosen as it simplifies the collimation system and associated hardware. The desired goal for the accuracy of stage motion is to be able to target a specific x/y coordinate within ± 3 μm of the desired positioning.

4.5.1.1 Physical System

The positioning stage for the LABA charged-particle microbeam is an X/Y stage mounted directly above the slit aperture (collimator). The 2-dimensional stage consists of a pair of Parker Zeta4 Drive Compumotors (5000 steps/revolution) coupled to precision Starrett micrometers (Starrett Model #261L, 0.001 inches/graduation; 25 graduations/revolution) that drive a precision x-y stage platform, the lattermost of which is shown in **Figures 4.28a** and **b**.

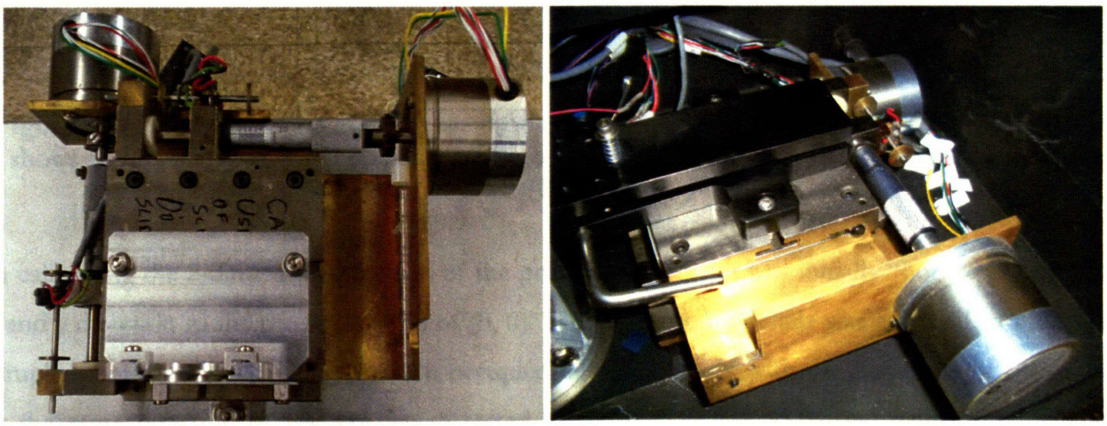

Figure 4.28 LABA Microbeam experimental stage system **a)** top view, **b)** placed within the light-tight box of the experimental endstation.

Based on the parameters of the Compumotors and the Starrett micrometers, the positioning stage is fundamentally limited to a certain step size.

$$\left(5000 steps/rev\right)\left(1 rev/25 grad\right)\left(1 grad/0.0001 in\right)\left(1 in/25.4 mm\right) \approx 7874\ steps/mm$$

Given the tolerances of the components, at 7874 steps/mm, the finest possible step size is ~0.2 μm. However, additional error can arise in a number of areas, including but not limited to the coupling of the compumotors to the micrometers, the coupling of the micrometers to the stage, and friction and/or mechanical errors in the stage motion.

In **Figure 4.29a** and **b**, the imaging screen used to verify the accuracy and precision of stage motion is shown. Using the graticle described in **Chapter 3**, **Section 3.1.1.2**, we can directly visualize the motion of the standard markings with the CCD camera system (to be described in more detail in **Section 4.5.2**), and calculate motion with an accuracy of < +/- 0.50 μm based on the pixel counts.

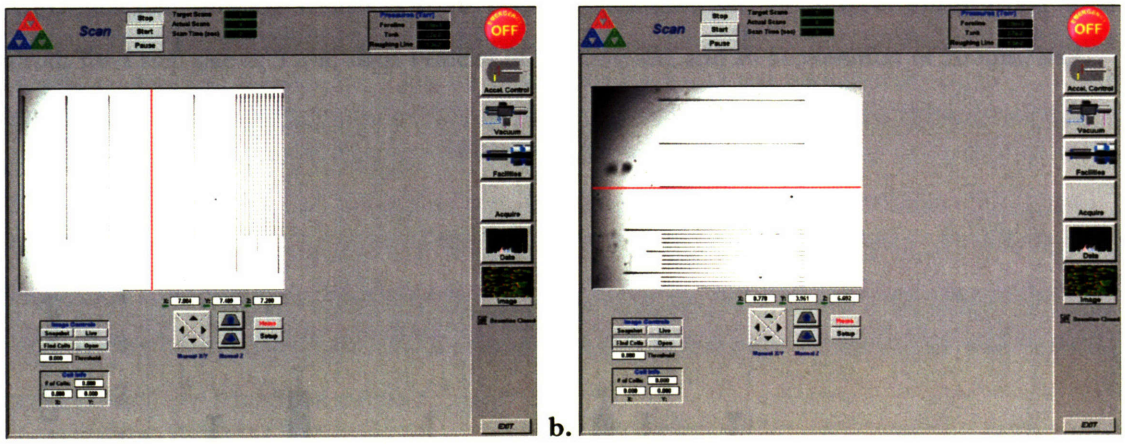

Figure 4.29 A screen capture of the image produced by the CCD camera on the CPU screen which shows the graticle scale, CPU readout and jog controls used during the calibration of the stage **a)** along the x-axis, **b)** along the y-axis.

In calibrating the 2-dimensional motion of the positioning stage, it was initially "homed" in both the x and y direction to the preset position of (0, 0). The microscope graticle was attached to the stage's sample mount arm in the same position occupied by the cell dish, with the alignment of the graticle in the same direction of the axis being tested. The graticle was visualized using the UV lamp, dichroic mirror, 10x objective, and CCD camera that will be described in full in **Section 4.5.2.1**. The image collected by the CCD camera was used to produce a live image on the CPU screen, as shown in **Figures 4.29a** and **b**. The stage was moved in both the x and y direction until the fine end of the

graticule scale was within the field of view of the CCD camera, which was previously determined to be approximately 630 μm x 467 μm, and brought into focus using the z-direction motor coupled to the 10x objective. Once in focus, an arbitrary 0.1 mm marking on the graticle scale was aligned with the edge of the CPU image.

For all stage motion verification experiments, the x and y coordinates of the stage indicated on the CPU screen were recorded at an arbitrary initial stage position. Using the computer jog controls, the stage was jogged in steps of a designated distance (generally 1 μm, 2 μm, 5 μm, and 10 μm) at a specified range of velocities (generally 0.1, 0.25, 0.50, and 1.0 mm/sec) and accelerations (generally 5.0, 10.0, and 20.0 mm/sec^2) along x or y axis (aligning the graticle to the observed axis as necessary) until the next 0.1 mm marking on the graticule scale was aligned with the edge of the CPU image, indicating on the graticle scale that the stage had moved 0.1 mm (100 μm). The CPU readout was recorded for the new stage position, which was 100 μm away from the previous recording. The stage was stepped in this manner, with readings taken every 100 μm, until the graticle indicated that the stage had moved a total distance of 2 mm. **Figures 4.30a** and **b** below show a typical measurement of CPU-indicated position deviation from position measured on the graticle image using these methods for a step size of 5 μm, stage velocity of 1.0 mm/sec, and an acceleration of 20 mm/sec^2.

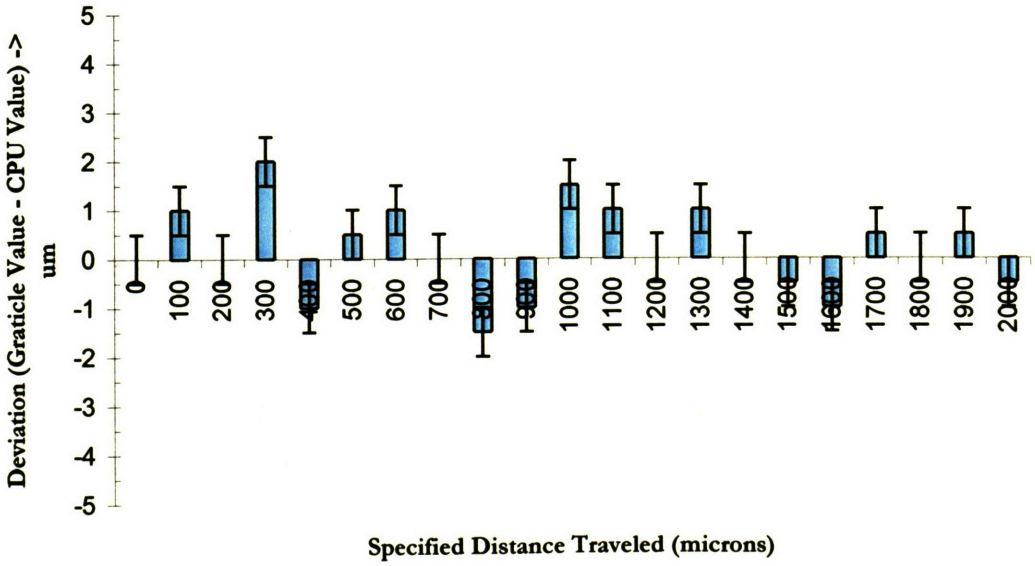

a.

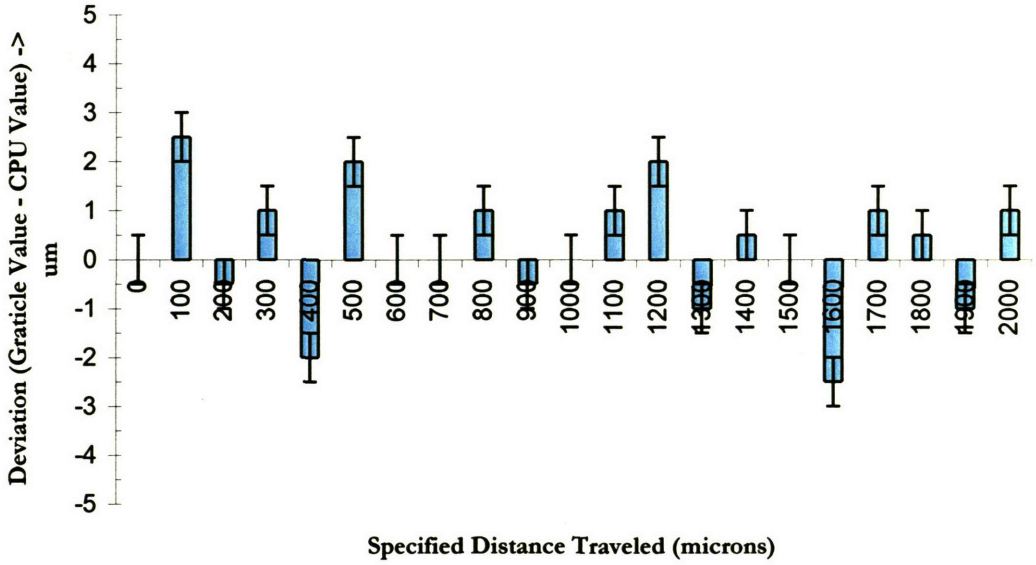

b.

Figure 4.30 a) X-Motion: Graph of CPU-indicated position deviation from position measured on the graticle image for a step size of 5 μm, velocity of 1.0 mm/sec, and acceleration of 20 mm/sec^2. Sum of mean deviation of 0.2 μm, standard deviation of 0.9 μm, and measurement error of 0.5 μm yield a total positional error of ± 1.6 μm with the stage moving in the x-direction; **b)** Y-Motion: Graph of CPU-indicated position deviation from position measured on the graticle image for a step of 5 μm, 1.0 mm/sec, 20 mm/sec^2. Sum of mean deviation of 0.2 μm, standard deviation of 1.3 μm, and measurement error of 0.5 μm yield a total positional error of ± 2.0 μm with the stage moving in the y-direction.

With a positional error of ± 1.6 μm in the x-direction and a positional error of ± 2.0 μm in the y-direction, the total radial positional error is ± 2.6 μm. Based on the total positional error of the stage system, it may be stated that the LABA Microbeam positioning stage can precisely and accurately target a specific x/y coordinate within ± 3 μm.

4.5.1.2 Stage Control, via the "Acquire" Screen

The "Acquire" control screen, shown in **Figure 4.31** with the ubiquitous "Common Border" removed (as described in **Chapter 3, Section 3.3**), allows the operator to set the parameters of a particular irradiation experiment, or "scan."

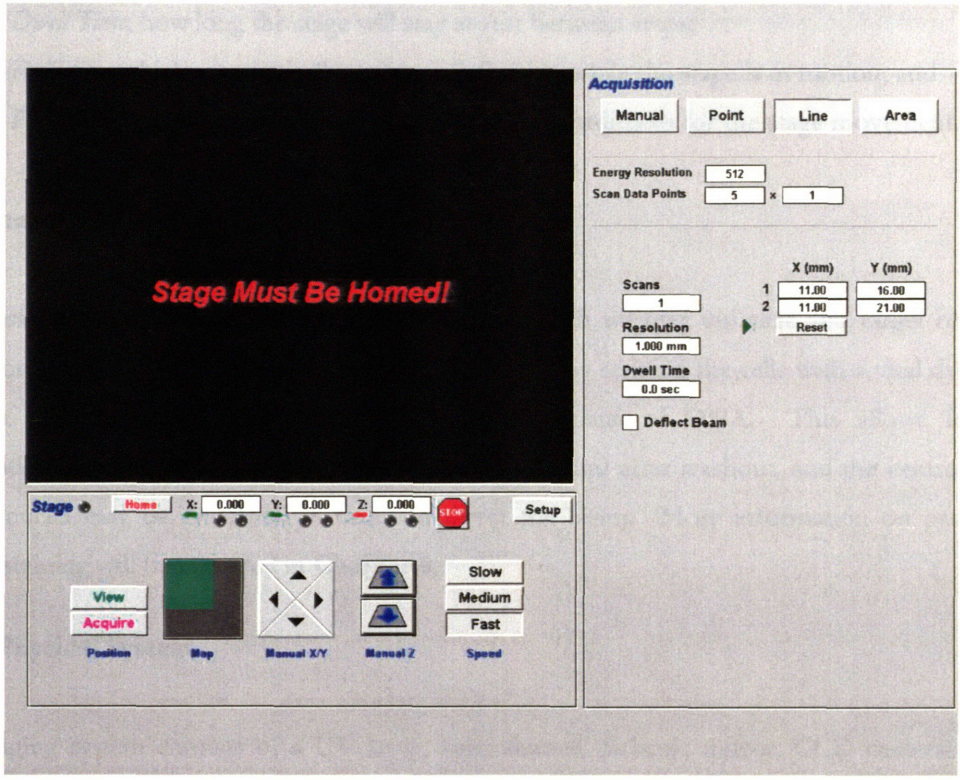

Figure 4.31 The "Acquire" control screen with "Common Border" removed.

Displayed in the upper left hand corner, the **Status Screen** shows a cursor during the course of a scan that indicates the relative position of the stage. When the stage is not in its "home" position following the completion of a scan, the program reminds the operator to return it prior to the initiation of a new scan. Directly below the **Status Screen** are the **Stage Movement** controls, that provide the operator with automated homing, manual X/Y stage motion control, manual Z control for the motorized focusing element tied to the microscope objective, speed control for the stage motion, and a general setup feature.

The **Acquisition Type** controls in the upper right hand corner allow the operator to limit the type of scan to specific types: *Manual*, which has the greatest degree of open parameters;

Point, which will only move the stage to a specific location defined by the operator;

Line, which will sweep the stage from one operator-specified point to another; and

Area, which will pan the stage repeatedly over an area, used for large automated tasks.

Below these controls are the **Scan Data** readbacks, that provide scan-specific data based on operator-defined parameters. The **Scan Parameters** in the lower right allow the operator to enter a number of parameters that define the behavior of a scan, specifically:

Resolution, the distance between each step movement of the stage;

Dwell Time, how long the stage will stay at rest between steps;

Deflection, which automatically turns on deflection while the stage is in motion; and

Position 1,2, which sets the initial and final X/Y coordinates for the stage movement.

4.5.2 Imaging/Targeting

A necessary feature of the endstation is a means by which we may visualize and target objects for irradiation. For nuclear irradiations, this is accomplished by staining the cells with a vital dye such as Hoechst 33258, which intercalates between the base pairs of DNA. This allows for direct visualization of nuclear DNA with relatively low background after washout, and the centroid of the stained nuclei may be calculated in order to direct the beam. More information on protein and nuclear staining will be provided in **Chapter 5**.

4.5.2.1 Physical System

The imaging system consists of a UV lamp, light shutter, dichroic mirror, CCD camera, and 10x objective on a motorized stage mounted over the biological target, shown in **Figure 4.32a** and **b**.

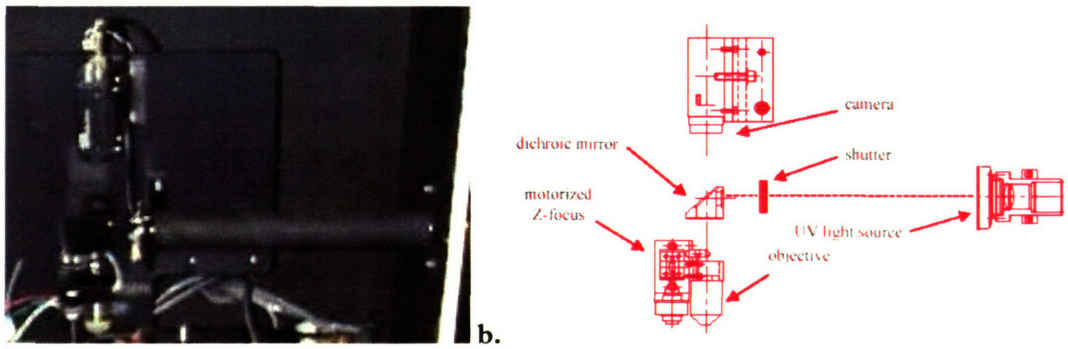

Figure 4.32 a) Assembly of optical arrangement in light-tight box, UV light source not pictured (outside of light-tight box). **b)** Diagram of optical arrangement without light-tight box.

The image is fed back to the central CPU-based control system, which displays the image and performs the processing required to calculate and register the coordinates of the targeted cells (**Figure 4.33**). This information is then used to guide the stage and positioning system (**Figure 4.31**).

4.5.2.2 Imaging Control, via the "Image" Screen

The "Imaging" control screen, shown in **Figure 4.33** with the "Common Border" removed,

provides the operator with a direct interface into the LABA Microbeam imaging system. Some of the imaging functions, such as cell targeting, are automated – however, the screen allows full manual control of all operations as well.

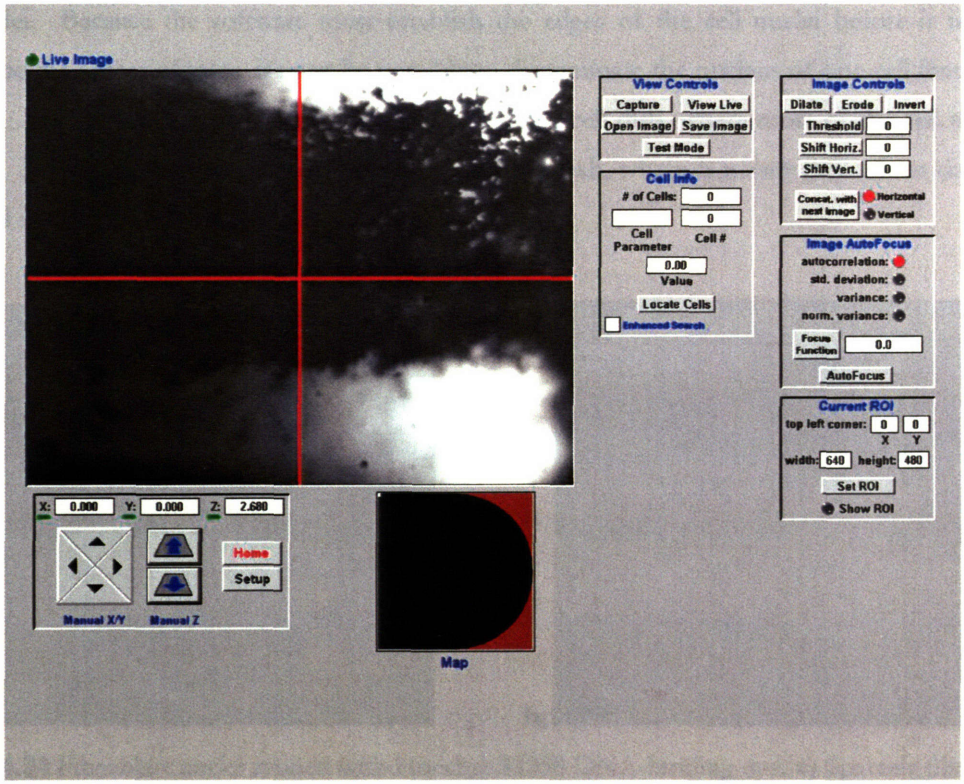

Figure 4.33 "Image" control screen with "Common Border" removed. The visualization window shows a view of the crossbar of the letter "T" in "MIT," written in black ink on regular paper.

Displayed in the upper left hand corner, the visualization window shows the image that is currently being captured by the CCD camera – if the camera is not acquiring data, a static image of the last image captured remains on the screen. The "Live Image" indicator light is on while the camera is actively capturing images. Directly below the visualization window is a set of **Stage Movement** controls, that provide the operator with readbacks of the current stage position, automated homing, manual X/Y stage motion control, manual Z control for the motorized focusing element tied to the microscope objective, and a general setup feature.

To the right of the visualization window are the **View Controls**, which set the imaging system on live or snapshot image capture modes. Below this is the **Cell Info** window, which allows the operator to designate a number of cells to locate and register. To the right of these two control sets

is a series of image manipulation tools, permitting the user to modify the edge-finding and threshold functions, the focus, and the size of the region of interest imaged.

Figures 4.34a and **b** show examples of the type of base images used to map out the centroids of the cell nuclei. Because the software must establish the edges of the cell nuclei before it is able to determine the center of mass, it must be possible to discriminate the nucleus of one cell from that of another. **Figure 4.34a** shows a relatively sparsely plated cell dish, where most of the cell nuclei are distinct. **Figure 4.34b** shows a very densely plated cell dish, where it is very difficult to distinguish once cell nuclei from the next.

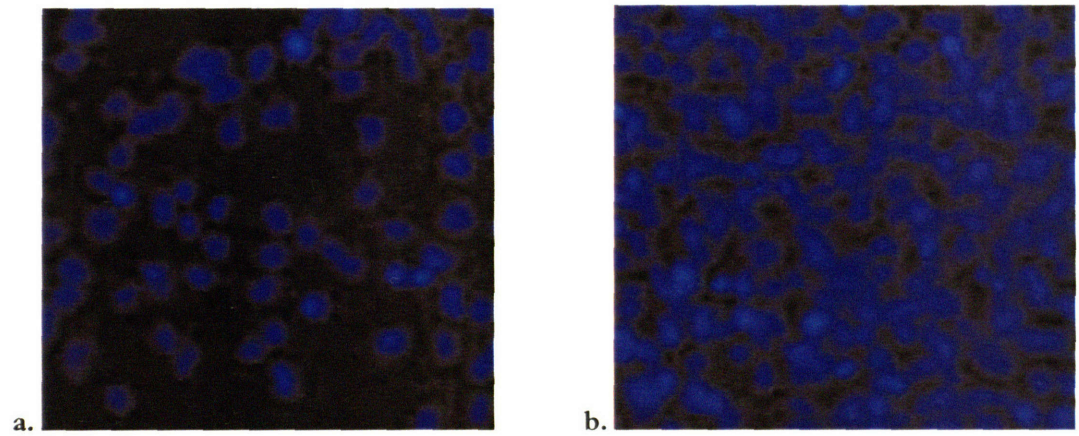

Figure 4.34 Fibroblast nuclei stained with Hoechst 33258 DNA-binding dye. **a)** Sparsely plated cells, **b)** Densely plated cells.

The software cannot currently discriminate well between cell nuclei in the latter case. If the software is not able to readily distinguish a nucleus, it rejects it and moves on to the next. The positions of each centroid will be logged to a file, and the x-y stage can be instructed to return to them sequentially or randomly over the entire dish or only over a selected region of interest. Full automation of the imaging and targeting system is beyond the scope of this thesis, and will be considered in future work.

4.6 Chapter Summary

In this chapter, the subsystems comprising the biological endstation were described and the experimental methodology used to characterize the operation of each system was discussed. In **Chapter 5**, the application of the LABA charged-particle microbeam to radiobiological investigations will be described.

5. Biological Applications of the LABA Microbeam

5.1. Background

Ever since the development of the first cyclotron by E.O. Lawrence at Berkeley and the resulting ability to accelerate heavy charged particles to energies sufficient to penetrate living tissue, physicists and biologists have been exploring their application to biological and medical research.[93] With the development and characterization of the charged-particle microslit complete, it is possible to investigate the response of cells to a subcellular distribution of radiation, delivered across a monolayer of cells with the LABA Microbeam.

It is hoped that this technique will shed further illumination on the radiation-induced bystander effect, by which irradiated cells appear to interact with other cells by currently unknown mechanisms to propagate the biological effects of radiation damage. (The radiation-induced bystander effect is discussed in greater detail in **Chapter 2.**) Such research provides an examination of the mechanisms by which low-level radiation may cause damage to populations of cells, which in turn may lead to pathological states in human tissues and organs. It is pertinent both to radiation protection, in which low doses of ionizing radiation on the order most often seen occupationally or by the general public may lead to increased risks of cancer or genomic instability, and to radiotherapeutic amounts of radiation, in which the interactions of radiation with cells in mixed environments may shed light on how to maximize the response of tumor tissue to radiation while reducing the damage to healthy tissues.

5.1.1 Radiobiological Assay Techniques

The radiation response chain is a complex and nonlinear pathway. As discussed in **Chapter 2**, the initial action of radiation on a biological system is chemical – the energy deposited by the radiation acts to break the bonds in DNA molecules, as well as to ionize water to produce free radicals that in turn cause further damage. An "injury signal" seems to be generated in response to this damage, setting in motion a cascade of biological reactions. Damage repair proteins are localized to the site(s), and the initial event is followed by a clean repair, mutation(s), or fixed damage that can kill the cell or impair its ability to reproduce.

The choice of biological assay techniques applied to the LABA Microbeam radiobiological studies was based heavily on the range of biological effects of interest – for example, one could look at fundamental **chemical effects** of radiation interaction with cellular material through the generation of reactive oxygen species such as peroxides, oxygen radicals, and superoxide anions; the **damage to the double-stranded DNA** (dsDNA) target of interest indicated by histone phosphorylation in proximity to a DNA double-strand break; or the aftereffects of such damage through the localization of **double-stranded DNA break repair** proteins. This is by no means an exhaustive list, but it covers the range of cause, effect, and consequence.

To assay each of these "steps" in the radiation response chain, the following assays were chosen:

1) Chemical effect: a compound known as 6-carboxy-2',7'-dichlorodihydrofluorescein diacetate, di(acetoxymethyl ester) (carboxy-H_2DCF-DA, Invitrogen Co., Carlsbad CA USA) dye may be used to label the production of reactive oxygen species (ROS, including oxygen radicals ($O^{\cdot-}$), hydroxyl radials ($OH^{\cdot}$), superoxide ions (O_2^{-}), and peroxides (H_2O_2)) from radiation interactions with intracellular water.[75] Carboxy-H_2DCF-DA is initially soluble in cell membranes, allowing it to permeate cells. Once in the cytoplasm, in the presence of reactive oxygen species, the carboxy-H_2DCF-DA molecule is cleaved, becoming both impermeant in cell membranes and fluorescent.[78] A diagram of the carboxy-H_2DCF-DA chemical process and an image produced using the ROS stain on a monolayer of charged-particle microslit-irradiated mouse fibroblast (MF) cells are shown in **Figures 5.1a** and **b**.

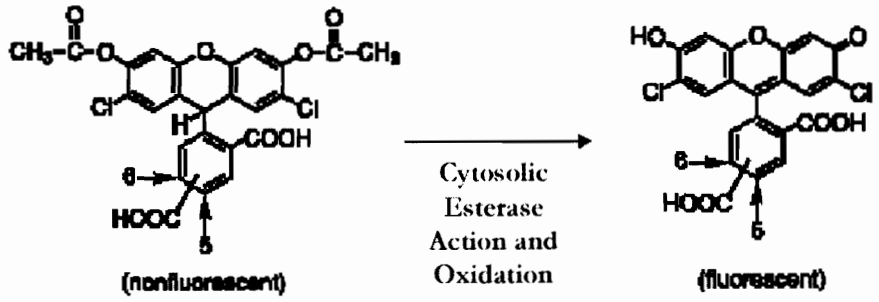

a.

b. 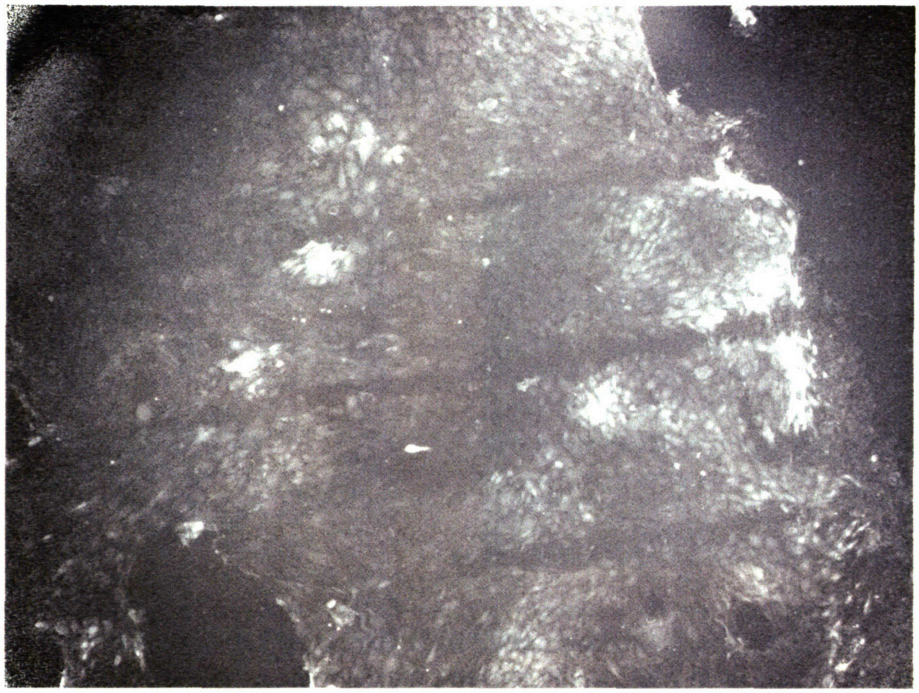

Figure 5.1 a) Conversion of carboxy-H_2DCFDA from non-fluorescent form to fluorescent form,[67] **b)** 200 Gy charged-particle microslit irradiation of mouse fibroblast (MF) cells pre-treated with carboxy-H_2DCF-DA, visualized immediately (1-3 min) after irradiation. (5x magnification, spacing between the dark lines = 500 μm, width of dark lines ~ 75 μm)

Because ROS have also been identified as signaling intermediates,[26] it is not possible to state that the ROS signal is confined to the initial interaction of radiation with water in the irradiated cells. Additionally, ROS have been implicated in a number of bystander studies,[49, 86] making their induction a good initial subject for LABA Microbeam studies. It is expected that both directly irradiated cells and those cells affected through radiation-induced bystander effect mechanisms will demonstrate some level of ROS induction after charged-particle microslit irradiation.

2) dsDNA damage: It has been noted that a certain structural protein identified as histone H2A.X becomes phosphorylated if in the proximity of a DNA double-strand break. This protein is a 14 kDa ubiquitous member of the H2A histone family that contains an evolutionarily conserved Serine/Glutamine motif at the protein C-terminus in eukaryotes.[85] Serine 139 within this motif becomes rapidly phosphorylated (on the order of milliseconds) in the presence of a DNA double-strand break to yield a form known as γ-H2A.X. Phosphorylation reaches half its maximum between 1-3 minutes after DNA damage occurs, and hundreds to several thousand molecules of γ-H2A.X are present per dsDNA break, providing a high degree of amplification.[87, 88, 89, 102] A diagram of the γ-H2A.X assay technique is provided in **Figure 5.2a**.

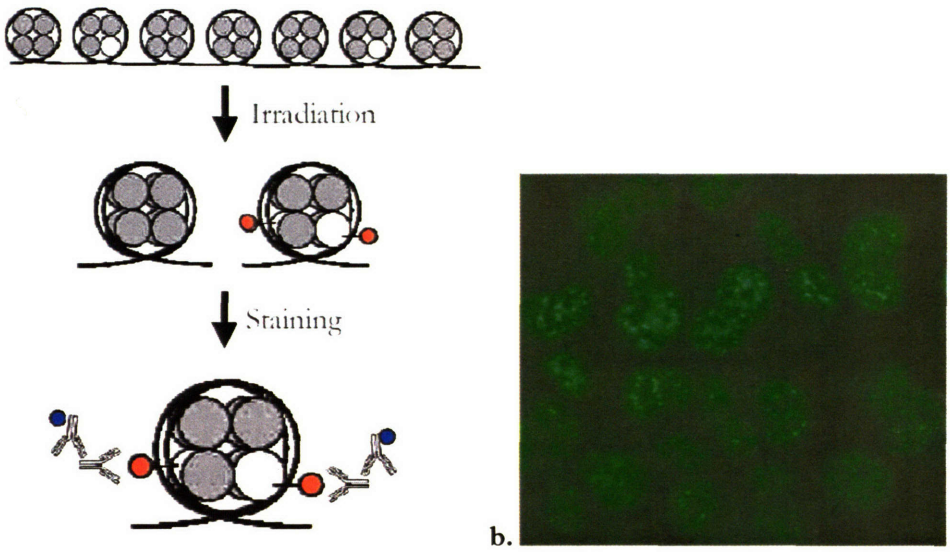

Figure 5.2 γ-H2A.X assay. **a)** At the top, intact native chromatin is shown with occasional H2A.X histone protein present (white circles) among other histone protein types (grey circles). In the middle, phosphorylated chromatin is shown in the presence of a dsDNA break (red circles). At the bottom, primary antibody is bound to the phosphorylated H2A.X (γ-H2A.X), and a secondary antibody covalently conjugated to a fluorophore (blue circles) is binding to the primary antibody; **b)** Expression of γ-H2A.X in 200 Gy charged-particle microslit irradiated NF cell nuclei (40x magnification, color adjusted).

Assaying for γ-H2A.X relies on an immunocytochemical technique using a mouse-generated antibody to the phosphorylated motif. This antibody is highly specific, detecting only phosphorylated histones at sites of double-strand DNA breaks.[85, 87, 88, 89, 96, 102]

3) DNA Damage Repair: Many proteins have been identified as having a role in the repair of radiation induced DNA damage. One of these, Mre-11 (of which hMre11 is the form found in humans), is an endonuclease of single-stranded DNA and an exonuclease of double-stranded DNA, facilitating DNA repair.[79] Mre11 is associated with the repair process known as Non-Homologous End Joining (NHEJ), which is the primary means by which mammalian cells may repair double strand DNA breaks. In this process, Mre11 acts as a 3' to 5' exonuclease - other proteins involved include XRCC4/5/6/7, Rad50 (which stimulates Mre11 exonuclease), and NBS1 (which interacts directly with both Rad50 and Mre11).[60] **Figures 5.3a** and **b** show an anti-hMRE11 fluorescent stain and a DAPI (DNA-specific stain) counterstain of the same normal fibroblast (NF) cell, during what appears to be a cell division.

a. 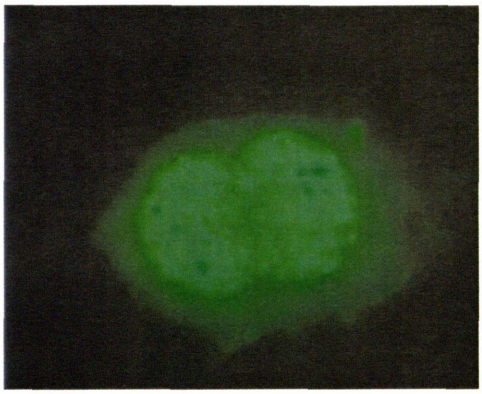 b. 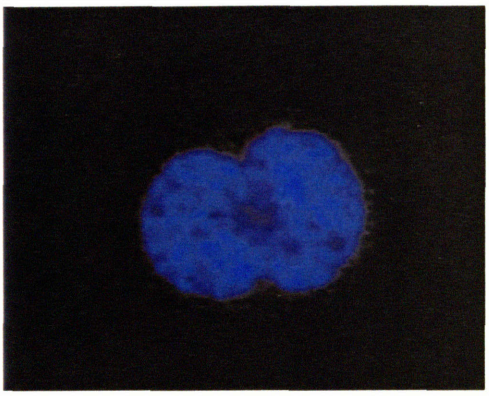

Figure 5.3 hMRE11-stained NF cells following 100 Gy "stripe" irradiation of cell dish. The cell shown was not directly irradiated, but was plated in the same dish as irradiated cells; **a)** anti-hMRE11 stain of an unirradiated NF cell, **b)** DAPI (DNA stain) counterstain of the same cell.

Assaying for hMre11 is also an immunocytochemical technique, using a rabbit-generated antibody to a conserved sequence in the protein structure. This allows visualization of localization of the hMre11 protein to the damage site.[76]

5.1.2 Other Radiobiological Stains

Several other stains were used to counterstain the cells for registration of the assay images against an image of the cell nuclei, or as a general assay of cell health.

1) Nuclear Imaging: A simple stain exists to highlight nuclear material – a vital dye known as Hoechst 33258 may be used to stain the DNA in the nuclei of the cells to be imaged.[32] The dye molecule, shown in **Figure 5.4a**, is specific for the A-T base pairs of DNA, but is not considered toxic (or to interfere with radiation response) at levels less than 5 μg/ml.[24,50] An image of Hoechst 33258-stained V79 cells is shown in **Figure 5.4b**.

a. 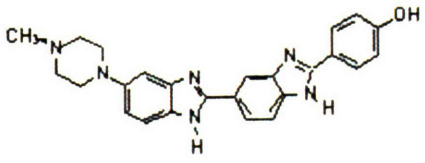 b. 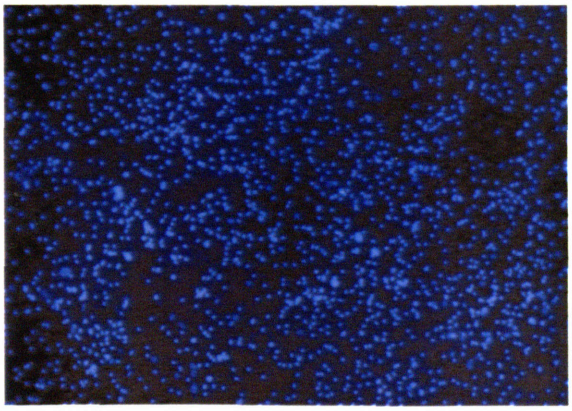

Figure 5.4 a) Hoechst 33258 molecule,[21,23] **b)** Hoechst 33258-stained V79 cells (50 nM concentration of the dye in normal growth medium, 5x magnification, color adjusted).

Counterstaining with Hoechst 33258 dye was done for two reasons; first, it provided a high-contrast image of cell nuclei suitable for analysis and targeting using the LABA Microbeam imaging system (see **Chapter 4, Section 4.5.2**), and second, comparing images of the highly-specific Hoechst 33258 nuclear stain to images produced using the two DNA repair- and damage-specific stains described above (anti-hMRE11 and anti-γ-H2A.X) allows for verification of co-localization with nuclear material.

2) Live/Dead Assay: The Live/Dead assay is a simple chemical stain assay that uses a combination of two molecules (**Figures 5.5a** and **b**) with dramatically different properties with respect to the integrity of the cell membrane.[20] This assay was used to determine relative cell health, and whether any particular manipulation of the cells was simply killing them outright.

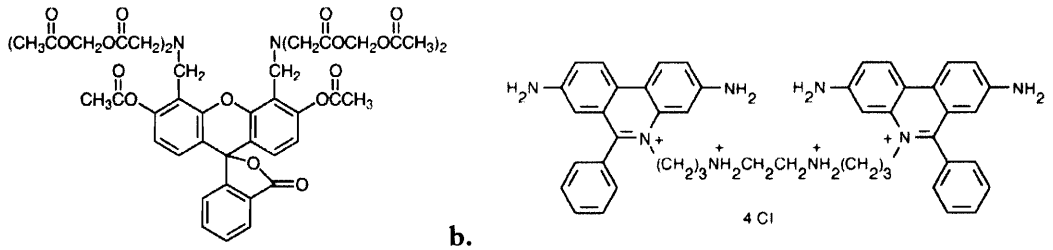

Figure 5.5 Live/Dead assay components.[66] **a)** Calcein-AM, **b)** Ethidium homodimer-1 (EthD-1).

The Calcein acetoxymethyl (AM) ester derivative of fluorescent Calcein (**Figure 5.5a**) is used for the imaging of live cells. The addition of the AM ester group results in an uncharged molecule that can easily permeate cell membranes. Once inside the cell, the lipophilic blocking groups are cleaved by nonspecific intracellular cytosolic esterases, resulting in a charged form of the compound that is relatively impermeable in cell membranes. Calcein AM is colorless and nonfluorescent until hydrolyzed, which results in the dye selectively staining the cytoplasm of intact cells. Target working concentrations are between 1 and 10 μM.[66]

Ethidium homodimer-1 (EthD-1, **Figure 5.5b**) is used for the imaging of dead and some forms of fatally damaged cells, the common characteristic being severe membrane damage. EthD-1 has a high-affinity for nucleic acids, and exhibits a red fluorescence when bound. It is specific for dead and dying cells in that it is only able to pass through their compromised membranes, and has a working concentration similar to that of Calcein AM.[66]

The intended purpose of using the Live/Dead assay (or its components) during the course of the initial LABA Microbeam experiments was to serve as a probe for membrane damage. For example, the ROS assay above requires an intact membrane to contain the fluorescent oxidized form of carboxy-H_2DCF-DA. The ethidium homodimer (EthD-1) can be used to verify if the cell membrane has been compromised.

5.2 Tissue Culture/Cell Dish Design

Cell lines cultured for experiments using the LABA Microbeam included Normal Human Fibroblast (NF) cells obtained from the Radiation Oncology Department at Massachusetts General Hospital (Boston, MA USA), Chinese Hamster Lung Fibroblast (V79) cells obtained from ATCC (Manassas, VA USA), and Mouse Fibroblast (MF) cells obtained from the Engleward Laboratory at the Massachusetts Institute of Technology (Cambridge, MA USA). All cell lines were maintained identically in Dulbecco's Modification of Eagle's Medium (DMEM) with 4.5 μg/ml glucose (Mediatech CellGro, Herndon, VA USA), supplemented with 10% fetal bovine serum (Sigma-Aldrich Co., St. Louis, MO USA), 10 μg/ml streptomycin and 10 μg/ml penicillin (Mediatech CellGro, Herndon, VA USA), and 10mM HEPES Buffer (Hyclone, Logan, UT USA).

Mammalian fibroblasts were chosen for the initial applications of the microbeam because they are relatively hardy, simple and inexpensive to culture, and possess nuclei of an easily targetable size (> 10 μm). **Figures 5.6a** and **b** show the shape of a V79 cell on Mylar and a histogram of their measured nuclear cross-sectional area.[24] Both the NF and MF cells were morphologically indistinguishable from and of equal or greater cross-sectional area than V79 cells by light microscopy, so they will be considered grossly morphologically similar for the purposes of the initial LABA microbeam studies. **Figure 5.6c** illustrates the variation in linear energy transfer (LET) of the protons delivered by the charged-particle microslit as they pass through the cell material, after the 750 keV proton beam has traversed the 1.4 μm mylar vacuum window, 5 μm scintillating plastic of the single-particle detection system, and the 1.4 μm mylar cell dish.

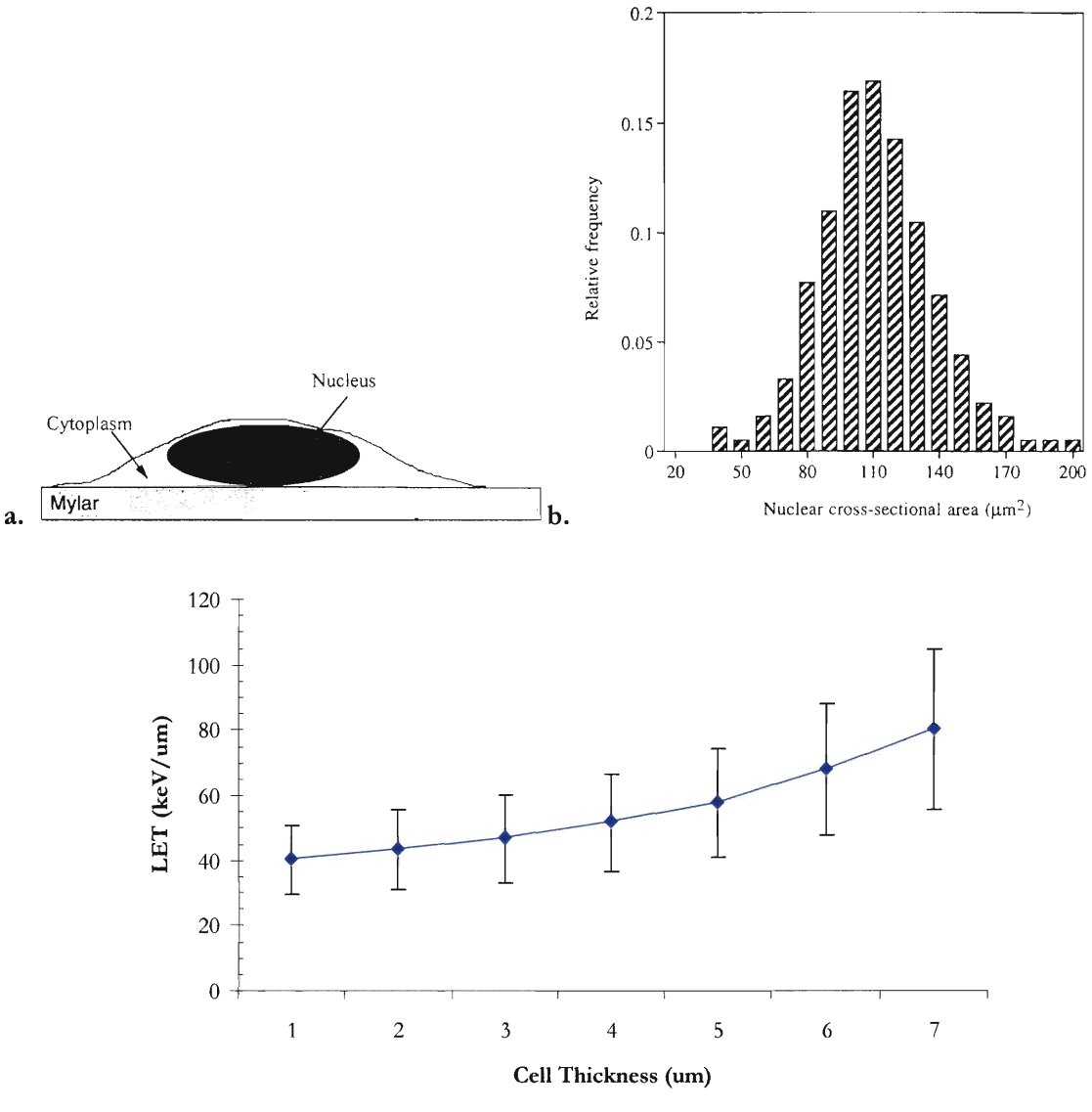

Figure 5.6 a) Diagram of V79 cell on Mylar (based on Pugliese 1997); **b)** Histogram of V79 nuclear cross-sectional area, mean is 106 μm², standard deviation of 27 μm²,[24] **c)** Plot of LET (keV/μm) vs. cell depth (μm) calculated using SRIM 2003, after the 750 keV proton beam has traversed the 1.4 μm mylar vacuum window, 5 μm scintillating plastic of the single-particle detection system, and the 1.4 μm mylar cell dish (residual proton beam energy prior to cellular material = 445.6 keV, standard deviation of 10.5 keV).

On average, V79 fibroblasts are about 6 μm thick,[99] which, as described in **Section 5.2**, is capable of being traversed by the 750 keV protons generated by the LABA Microbeam after passing through the Mylar of the vacuum window and the cell dish as well as the scintillating plastic of the particle detection system.

As mentioned in **Chapter 3**, the vertically aligned beam allows the irradiation of horizontally-placed cell dishes. This simplifies the irradiation process and allows the growth medium to remain on the

cells in a conformation that also allows the medium to be exposed to air (allowing oxygen to diffuse to the cells). As a result, long irradiations (~30 min or more) may be performed without adversely affecting the cells. The cell dish and irradiation configuration are shown in **Figure 5.7**. The plating surface is approximately 2 cm in diameter, with an effective plating area of ~ 285 mm^2 that allows for > $1.0x10^6$ mammalian fibroblast cells to be deposited in a confluent monolayer.

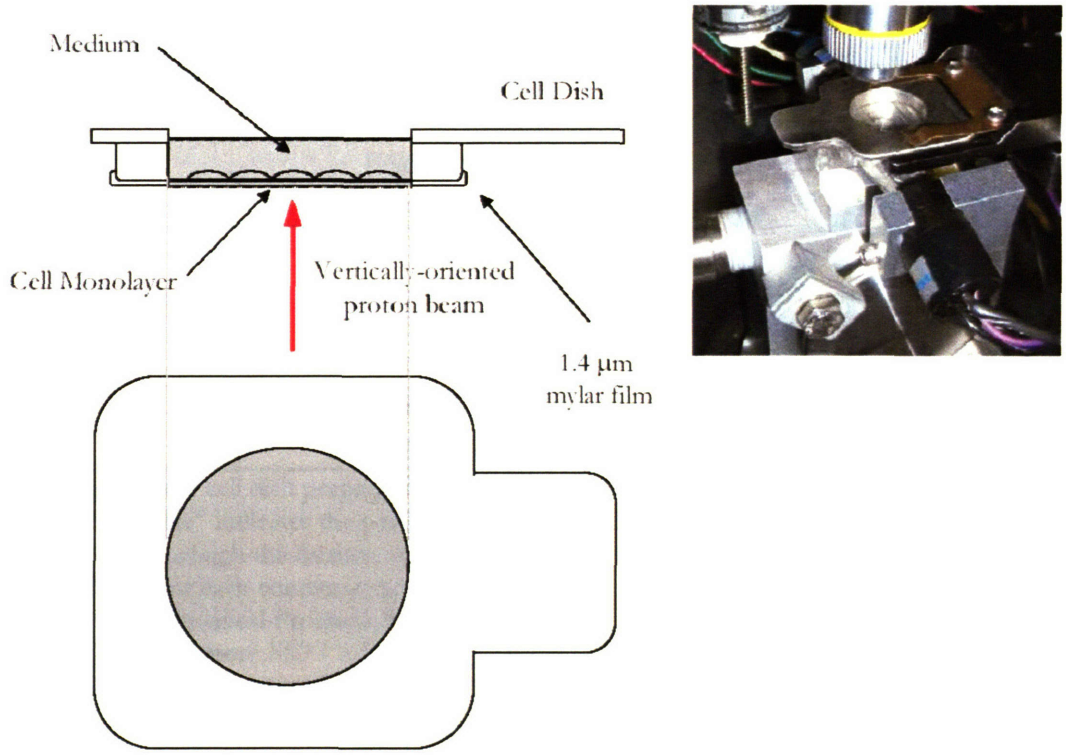

Figure 5.7 Vertical target irradiation configurations, cut away side view and physical placement in LABA Microbeam experimental endstation. Note that the cell monolayer is not to scale.

Irradiation dishes were prepared using a custom-made stainless-steel tray (Machine Technology, Beverly, MA USA), onto which either a 3.7 μm thick polypropylene film or a 1.4 μm thick Mylar film was affixed using 3M Spray Mount adhesive (3M, St. Paul, MN USA), as shown in **Figure 5.7**. A full description of the cell dish preparation is provided in **Appendix D, Section D.2**.

Adherence of the cells is a major issue with the custom cell dishes used in the LABA Microbeam. Standard tissue culture materials were too thick for the 750 keV protons produced by the LABA Microbeam accelerator to traverse with sufficient remaining energy to fully penetrate the target cells, so a number of very thin (< 4 μm thick) plastic films were examined. Unfortunately, mammalian fibroblasts do not adhere to these plastics well as they tend to carry a net neutral or positive charge,

and mammalian fibroblasts preferentially adhere to substances with a net negative charge. A number of products exist that can impart a net negative charge or other adherent properties to a surface, and several of these were tested with the custom cell dishes. The results are shown in **Table 5.1**, which provides the relative effectiveness of various cell treatments for the 3.7 μm thick polypropylene film and 1.4 μm thick Mylar film.

Dish Preparation	% Viable	Standard Deviation
3.7 μm polypropylene		
no treatment	6%	9%
Cell-Tak	23%	7%
FNC Coating Mix	19%	7%
Sigma Poly-l-lysine	45%	6%
1.4 μm Mylar		
no treatment	13%	N/D
Cell-Tak	31%	9%
FNC	36%	8%
Sigma Poly-l-lysine	56%	13%
EMS Poly-l-lysine	94%	7%

Table 5.1 Different cell dish preparations for 4 μm thick polypropylene film and 1.4 μm thick Mylar film. "% Viable" indicates the percentage of treated dishes in which the entire cell monolayer remained intact through the fixation step in the immunocytochemical staining process. The number of dishes for each condition ranged from 16 to 40. The treatments used were Cell-Tak (Collaborative Biomedical Products, Bedford, MA USA), FNC Coating Mix (Athena Environmental Sciences, Inc., Baltimore MD USA), Sigma poly-L-lysine (Sigma-Aldrich Co., St. Louis, MO USA), and Electron Microscopy Sciences (EMS) poly-l-lysine (Electron Microscopy Sciences, Fort Washington PA USA).

5.3 Charged-Particle Microslit Experiments

As shown in **Chapter 4**, the LABA charged-particle microslit was designed and characterized to deliver a radiation dose distribution of subnuclear width, such that the exposed area would be approximately 3-8 μm in width and 1 mm in length. By varying the duration of the cell exposure and/or the intensity of the charged-particle beam (primarily by varying the accelerator extraction voltage), a dose on the order of 1-2 Gy to hundreds of Gy is possible in a matter of seconds.

5.3.1 Experimental Design

The charged-particle microslit was originally designed as an alternative to the construction of a grid "mask," which was intended to provide a regularly repeating radiation delivery pattern in which a biological target would receive a varying degree of high proton dose and no proton dose. This

pattern was to be generated by alternating an attenuating material to block charged particles with voids to allow charged particles to freely pass through. However, construction of the grid soon proved to be too difficult in the case of the charged-particle beam produced by the LABA Microbeam accelerator, as a suitable rigid substrate could not be found that would support the attenuating material without completely attenuating the charged-particle beam itself.

The motivating idea behind grid construction was a 1998 Science paper by Nelms et al.,[76] in which a grid (shown in **Figure 5.8a**) was used to create a pattern of synchrotron-produced 1.34 keV x-rays in which the "void" zones of the grid received 100 Gy and the "attenuating" zones of the grid received 0.5 Gy. A subset of the results from such an irradiation performed using the x-ray grid is provided in **Figure 5.8b**, in which a grid-irradiated 37Lu fibroblast nucleus stained for hMRE11 (as explained in **Section 5.1.1**) and counterstained with DAPI (a nuclear binding dye) is shown. The merging of the hMRE11 and DAPI images demonstrated the localization of the DNA repair protein to the nucleus of the cell.

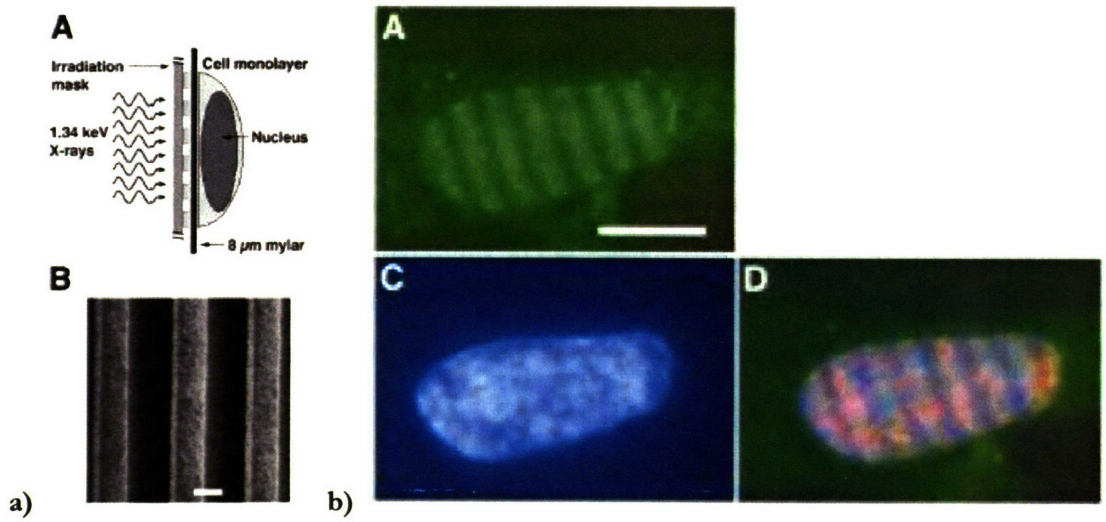

Figure 5.8 a) (A) Diagram of the Nelms et al.[76] partial volume irradiation scheme. Thickness of the Mylar surface (8 μm) is not drawn to scale. (B), scanning electron micrograph of irradiation mask. Bar, 1 μm; **b)** hMre11 stripes, 37Lu fibroblasts (**A**) hMre11 (**C**) DNA (DAPI) (**D**) Merged image of (A) to (C). Bar, 10 μm.[76]

The irradiation pattern deemed most suitable for radiobiological experiments using the charged-particle microslit is a "stripe"-style irradiation, in which the microslit is scanned lengthwise across the cell dish. The result of this irradiation is a dose distribution over the cells a few microns in width, and several mm in length. After treatment with a contrast agent such as an immunocytochemical stain or reactive dye, the effect of the radiation dose is more easily observable due to its magnitude

and shape. Also, the spatial distribution of secondary biological effects (such as the radiation induced bystander effect) may then be modeled as a 1-dimensional effect. The dose delivered to the cells was varied between 1 and 200 Gy.

Treatment with carboxy-H_2DCF-DA prior to irradiation allows visualization of the generation of reactive oxygen species (ROS), part of the initial cellular insult. Immunocytochemical treatment after the cells have been irradiated and fixed with anti-phosphorylated histone H2A.X (γ-H2A.X) allows for visualization of the approximate location of DNA double-strand breaks in chromosomal DNA, while treatment with anti-hMre11 allows visualization of one step in the non-homologous end-joining (NHEJ) DNA repair process.

5.3.2 Experimental Methods

5.3.2.1 Biological Preparation

Irradiation dishes were prepared as described in **Section 5.2** (**Figure 5.7**)/**Appendix D, Section D.2**. Prior to an irradiation experiment, exponentially growing cultured cells are trypsinized and resuspended in normal growth medium, and then plated on the prepared thin film/stainless-steel dishes such that the cells after adhesion would be 90-100% confluent. The cells were incubated in the stainless steel microbeam dishes protected by a plastic cell culture dish at 37°C for 8-12 hours. In almost all cases, cells were pre-treated with a 50 nM solution of Hoechst 33258 DNA-binding dye in relevant growth medium, incubated at 37°C for 30 min, and then washed 2x with 1X PBS at room temperature (22°C) (3 min/wash). After the cells were washed, relevant growth medium was then restored.

A variation that was used with some dish preparations was treatment with lindane. Lindane is a γ-isomer of hexachlorocyclohexane that functions as a gap junction intercellular communication (GJIC) blocker.[41] Gap junctions are specialized protein structures in cell membranes that create channels between cells, and GJIC is a means by which small molecules may pass between cells through these low-resistance channels. Lindane-susceptible GJIC has been previously implicated as a mediator of radiation-induced bystander damage,[4] and its use was intended to determine if GJIC-related mechanism(s) were involved in any observed biological effects.

Irradiations were performed at room temperature (22°C). Irradiations lasted 5-30 min, depending on area irradiated and total dose delivered. At times ranging from 10 minutes to 2 hours after

irradiation, cells were washed twice with 22°C 1X PBS (3 min/wash) and then fixed with 100% methanol on ice for 20 min.

5.3.2.2 Irradiation Methods

750 keV protons were generated using the 1.5 MeV charged-particle accelerator at the MIT LABA. Using the charged-particle microslit, radiation dose was delivered in 3 μm swaths over 5-10 mm lengths, such that multiple "stripes" were delivered over the area of the cell dish. Proton dose in the irradiated areas was initially approximately 200 Gy, while unirradiated areas received no dose. Later experiments were performed at progressively lower dose. Dose was calculated using LR115 film to determine proton fluence (for more information, refer to **Chapter 4, Section 4.4.3.1**) and the SRIM 2003 code was used to calculate the dose per proton.[94, 113]

It was expected that the results of the charged-particle microslit experiments would conform to the results obtained from the x-ray grid irradiations of 37Lu fibroblasts reported by Nelms et al.[76] (explained in detail in **Section 5.3.1**), in that the charged-particle microslit delivered a similar pattern of radiation to cells over a subnuclear width. However, by distributing the physical radiation dose in long, uniform strips of subnuclear width, it was intended that any resulting biological secondary effects would be more easily modeled as one-dimensional effects, simplifying the quantification of the results and eventual application to a radiation-induced secondary biological response model.

Background dose was determined by placing a calibrated μRem radiation meter (Bicron Micro-Rem Radiation Monitor, Saint-Gobain Crystals and Detectors, Paris France) within the experimental endstation during a charged-particle microslit irradiation, with the face of the detector directly above the cell dish. Ambient measurements (without power to the accelerator) in this position were generally ~10-15 μrem/hr, and typical background dose values in this position with the accelerator on and the collimated beam directed upon a cell dish ranged from 0.50-0.75 mrem/hr. Given that most stripe irradiations take < 5 min/dish, the conservative average background dose to a cell dish is approximately 42-63 μrem.

5.3.2.3 Biological Assay Techniques used on LABA Microbeam-irradiated Cells

ROS

The specific dye used for the chemical effect staining is 6-carboxy-2',7'- dichlorodihydrofluorescein diacetate, di(acetoxymethyl ester), or carboxy-H_2DCF-DA. (Invitrogen Co., Carlsbad CA USA)

Assaying for reactive oxygen species (ROS) production with carboxy-H_2DCF-DA is a simple process in which, during the pre-treatment Hoechst 33258 staining step described in **Section 5.3.2.1**, the cells are co-incubated with a solution of carboxy-H_2DCF-DA (50 nM) and Hoechst 33258 (50 nM) in normal growth medium at 37°C for 30 min, and washed 2x with 1X phosphate-buffered saline (PBS) at room temperature (22°C) (3 min/wash). Carboxy-H_2DCF-DA dye may also be added alone with the same incubation and washing steps. After the cells have been washed, relevant growth medium is then restored. The cells may be visualized immediately with no further manipulation after irradiation, before fixation.

Immunocytochemistry

Both the γ-H2A.X and Mre11 assays rely on immunocytochemical techniques using a mouse- or rabbit-generated antibody to a protein-specific amino acid sequence. These techniques require that the cells be fixed in methanol following irradiation, stabilized with a formaldehyde solution, and permeabilized with a detergent solution. To protect against non-specific binding of the primary and secondary antibody, the cells were treated with a blocking solution and incubated for 1 hour at 37°C.

After one wash, the cells were then incubated for 1 hour at 37°C with the primary antibody solution (either anti-hMre11 antibody (EMD Biosciences, CA USA) or anti-phosphorylated histone H2A.X antibody (Upstate USA Inc., Charlottesville VA USA), washed, and then incubated for another 30 min at 37°C with a secondary antibody with high specificity to the primary antibody and conjugated to a fluorophore (usually fluorescein isothiocyanate (FITC) or rhodamine). The cells may be visualized following the final washout of the secondary antibody solution.

All images of irradiated cells were captured using a SPOT charge-coupled device camera (Diagnostic Instruments, Sterling Heights, MI USA) mounted on a Zeiss Axioplan 2 epifluorescent microscope (Zeiss Inc., Oberkochen Germany). Images generated were processed using Microsoft Photo Editor and/or analyzed using MATLAB scripts. (See **Appendix E** for details on image analysis)

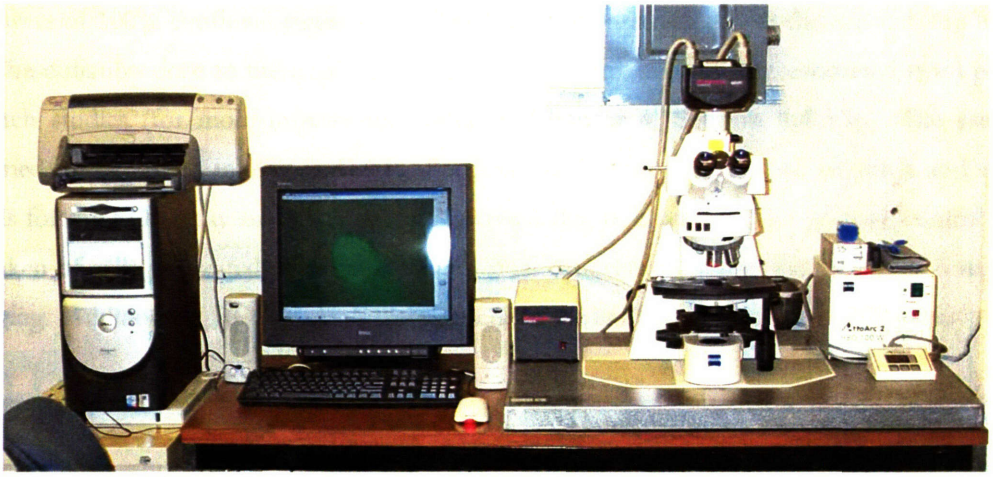

Figure 5.9 Imaging equipment. A Zeiss Axioplan 2 microscope connected to a 7 Megapixel SPOT Camera, images acquired by the computer on the left.

In all radiobiological assays, simple negative controls were performed in which dishes with confluent monolayers of mammalian fibroblast cells were placed in the experimental endstation (out of the path of the collimated charged-particle beam) and "sham-irradiated," such that they were subjected to conditions identical to irradiated cells (movement, handling, temperature variation, any background radiation dose, etc) with the exception of direct exposure to the collimated charged-particle beam. The negative control dishes were then visualized (in the case of ROS), or stained and visualized (in the case of γ-H2A.X and hMRE11). As discussed in **Section 5.3.2.2**, the background dose rate in the experimental endstation with the accelerator on and the collimated beam directed upon a cell dish results in a conservative average background dose to the cell dish of approximately 42-63 μRem. Observable induction of ROS, γ-H2A.X and/or hMRE11 was not expected from such a small dose, and none of the controls displayed any signal above background induction levels following sham irradiation. Where applicable, positive controls for each assay are described below in the relevant results section.

More details on the biological assay techniques used thus far in the LABA Microbeam are provided in **Appendix D**.

5.3.3 Results

5.3.3.1 Chemical Effect: ROS/carboxy-H_2DCF-DA Studies

A series of irradiations was performed looking specifically at induction of reactive oxygen species (ROS) activity. The irradiation pattern was a set of 3-4 ~5mm long "stripes," 500 μm apart, across

monolayers of 100% confluent mouse fibroblast (MF) cells pretreated with the carboxy-H_2DCF-DA dye. The radiation dose to the irradiated cells was approximately 200 Gy, estimated from previous track-etch studies (for more information, refer to **Chapter 4**, **Section 4.4.3.1**). The assay was performed as described in **Appendix D**, **Section D.3**. For comparison, negative and positive controls for the ROS assay are presented in **Figures 5.10a**, **b**, **c**, and **d**. The positive control images were taken of cells pretreated with H_2O_2 (0.05% final concentration) and incubated for 5 min prior to imaging. Additionally, ROS controls were generated for lindane-treated (lin+) V79 cells.

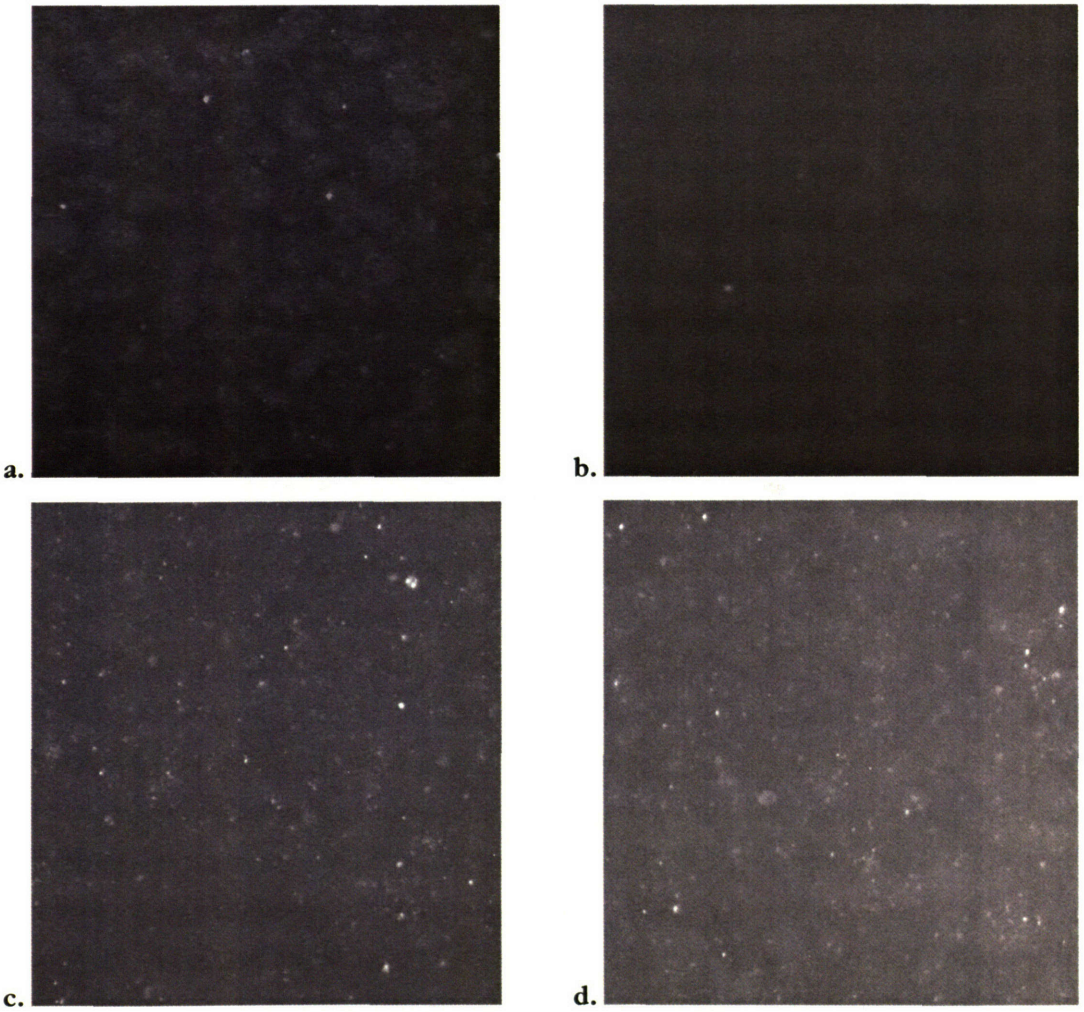

Figure 5.10 Negative and positive ROS controls for both lindane-treated (lin+) and untreated (lin-) V79 cells, pretreated with carboxy-H_2DCF-DA dye. Positive controls are pretreated with H_2O_2 (0.05% final concentration) and incubated for 5 min prior to imaging, **a)** lin- negative control, **b)** lin+ negative control, **c)** lin- positive control, **d)** lin+ positive control. (5x magnification)

The primary observation in the irradiated cells was the presence of the dark lines in the areas that were directly irradiated using the charged-particle microslit. (**Figures 5.11a** and **b**) Measurement of

the distance between them confirms that they are exactly 500 μm apart, which would refute the possibility that they are artifacts from an alternate event, and they were observed on multiple dishes.

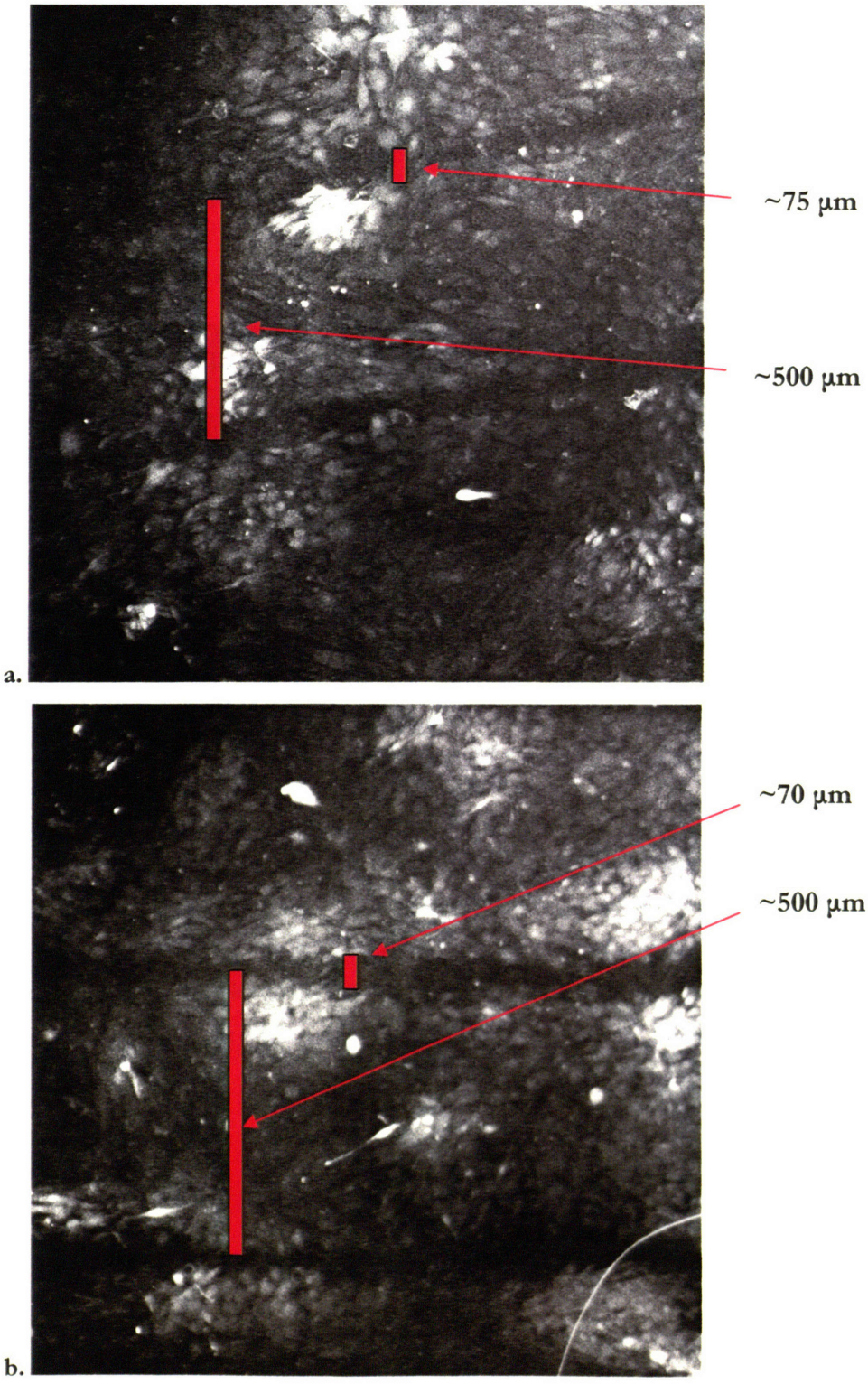

Figure 5.11 a) Irradiated MF, carboxy-H_2DCF-DA stain (5x magnification), **b)** Irradiated MF, carboxy-H_2DCF-DA stain (5x magnification) with scaling bars indicating the width of the "dark stripe" and the distance between "dark stripes."

The mechanism by which an inverse ROS signal would result from charged-particle irradiation is not known. One hypothesis is that the high dose (~200 Gy) delivered by the charged-particle microslit resulted in significant membrane damage, leading to increased permeability and ROS dye leakage. Comparison of the visible light image of the irradiated cells shown in **Figure 5.11a** revealed that the cell membranes were visibly altered following the irradiation. This comparison is shown in **Figures 5.12a** and **b**.

a. 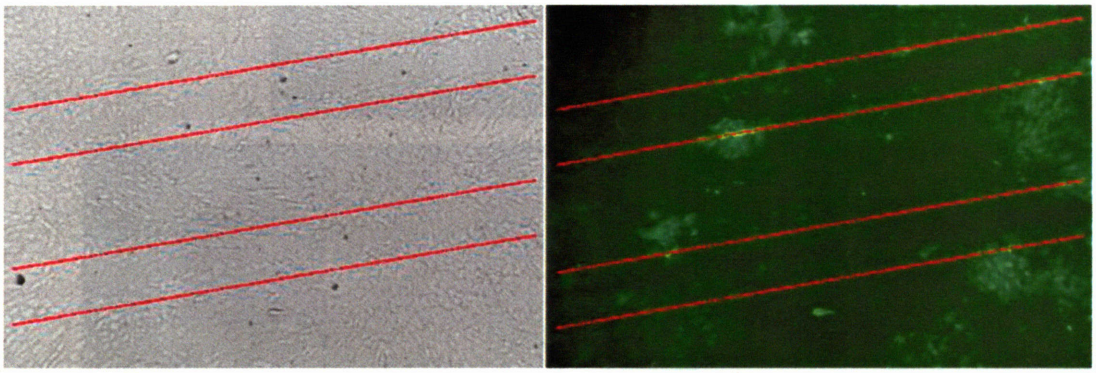 **b.**

Figure 5.12 a) Visible light microscopy detail of ~200 Gy charged-particle microslit irradiated, carboxy-H_2DCF-DA-stained MF cells, in which a loss of appreciable membrane structure can be observed, **b)** Registered ROS image. The width of this change equal to the width of the dark "stripe" observed in **Figure 5.11a**.

The second observation of interest was the presence of "bursts," or focal expression of ROS activity in small clusters of 10-20 cells. (**Figures 5.13a**, **b**, and **c**) These bursts appeared shortly after irradiation (~1-3 min) and developed from small clusters to large clusters over the course of their imaging (~10-20 min). The "burst" clusters appeared both in the immediate proximity of the dark "stripes" (within 1-2 cell widths) and at distances over 20 cell widths away from the irradiated sites.

a.

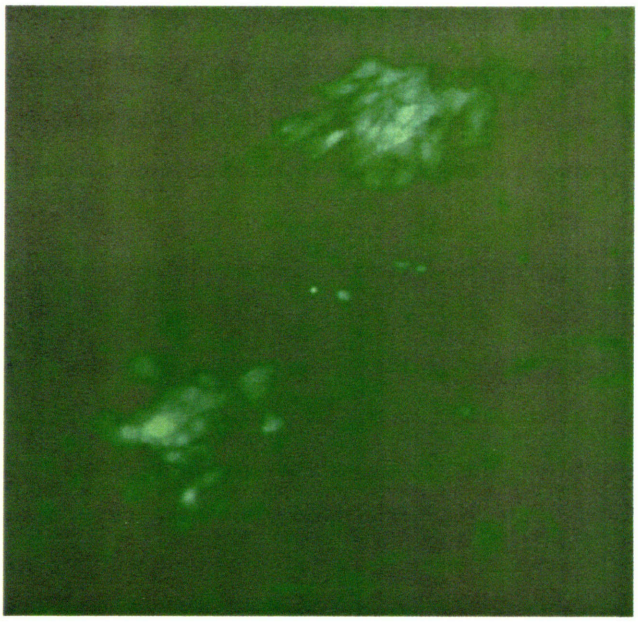

b.

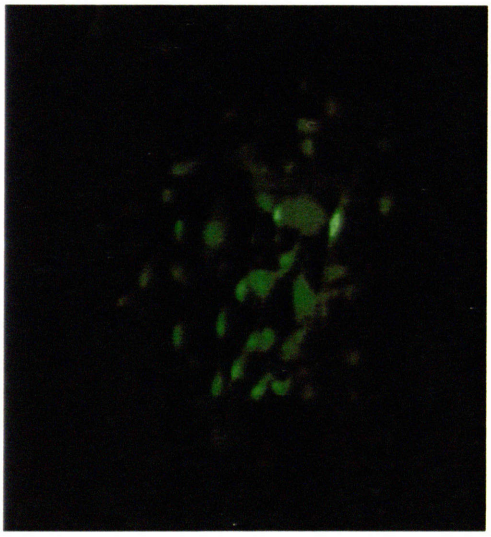

c.

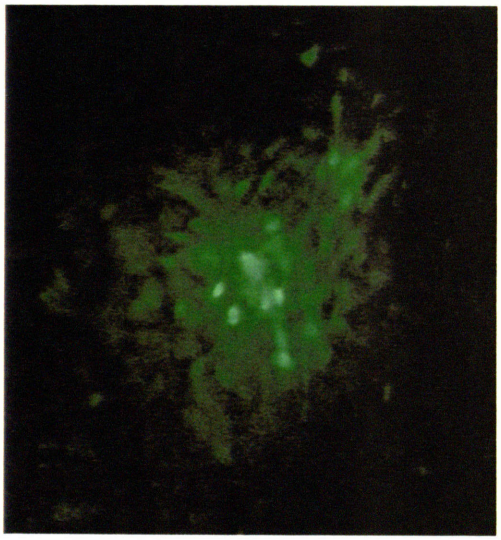

Figure 5.13 ROS "bursts" in irradiated cells pre-treated with carboxy-H_2DCF-DA. **a)** Closeup of "bursts" flanking either side of slit irradiation (within 1-2 cell widths) taken immediately after irradiation, (**b)** Closeup of "burst" ROS cluster distal to irradiation site (> 20 cell widths away), **v)** Closeup of "burst" ROS cluster distal to irradiation site. (> 20 cell widths away) taken ~3 min after irradiation. (cropped 10x magnification, all images color adjusted)

Comparison to the positive controls in **Figures 5.10c** and **b** reveals a marked difference in the appearance of the charged-particle microslit-irradiated cells. The ROS induction in the positive controls is diffuse with several focal points in individual cells, while the ROS induction in the "bursts" is very bright and manifests in clumps of 12-20 cells. The presence of "burst" expression of ROS activity, as denoted by the carboxy-H_2DCF-DA dye, suggests that one or more cells in a region experience an event that triggers a large amount of ROS activity within the insulted cell and the cells

in very close contact/proximity to it. It is interesting to note that treatment of the cells with lindane (50 nM suspension in normal growth medium) prior to irradiation appears to eliminate the induction of ROS "burst" clusters, resulting in only a diffuse expression of ROS as indicated by carboxy-H_2DCF-DA fluorescence comparable to the positive control shown in **Figure 5.10d**.

5.3.3.2 dsDNA Damage: anti γ-H2A.X Studies

A series of irradiations was performed looking specifically at the induction of γ-H2A.X. The irradiation pattern for **Figures 5.14-5.20** was a set of 3 ~5mm long "stripes," 500 μm apart, across a monolayer of 100% confluent normal human fibroblast (NF) cells, counterstained with Hoechst 33258 dye. The radiation dose to the first set of irradiated cells was approximately 200 Gy, estimated from previous track-etch studies (for more information, refer to **Chapter 4**, **Section 4.4.3.1**), and then progressively decreased to 1 Gy. Cells were incubated for 30-40 min following irradiation, washed two times with 1X phosphate-buffered saline (PBS) and then fixed in methanol on ice. The assay was performed as described in **Appendix D**, **Section D.4**.

Preliminary inspection of the 200 Gy charged-particle microslit-irradiated γ-H2A.X stained images (**Figures 5.14a** and **b**) shows a diffuse γ-H2A.X signal with a higher intensity along the regions that received dose "stripes." Again, measurement of the distance between "stripes" confirms that they are exactly 500 μm apart, which would refute the possibility that they are artifacts from an alternate event, and they were also observed on multiple dishes.

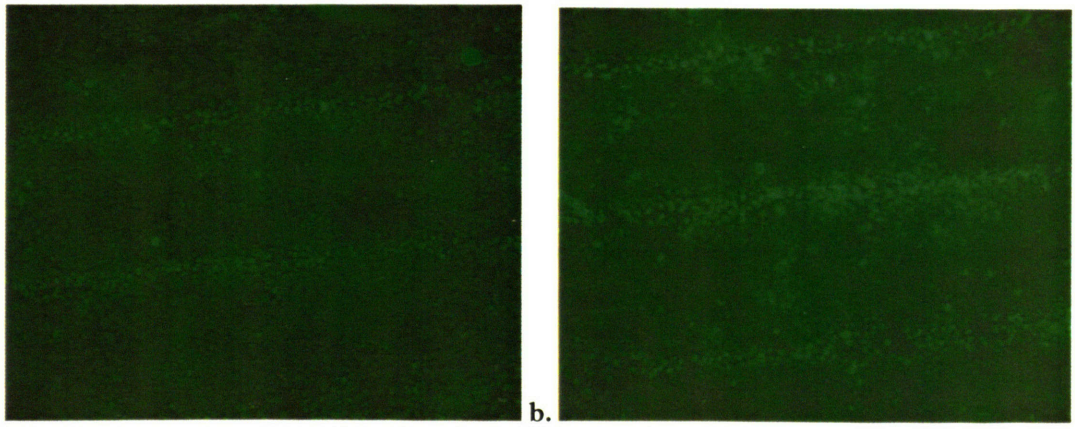

Figure 5.14 a) Irradiated NF, γ-H2A.X stain (5x magnification, color adjusted), **b)** Irradiated NF, γ-H2A.X stain (5x magnification, color adjusted).

Closer examination of the γ-H2A.X images shows that the nuclei within the directly irradiated regions show not only a greater intensity of staining, but a greater number of more intense foci (**Figures 5.15a** and **b**).

a. 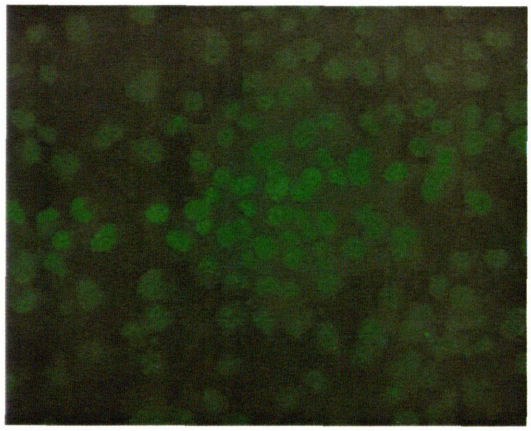 b. 

Figure 5.15 a) Directly irradiated NF, γ-H2A.X stain detail (40x magnification, color adjusted), **b)** Unirradiated NF (but in same dish as irradiated NF), γ-H2A.X stain detail (40x magnification, color adjusted).

Once the image was acquired with the microscope (in 8-bit grayscale TIFF format), a quantitative analysis of the γ-H2A.X images was performed using MATLAB (for details, see **Appendix E.2**), in which the following manipulations were performed:

1. Images were rotated so the fluorescent strip was aligned vertically
2. Images cropped to remove optical edge effects
3. Images were processed by a MATLAB script, which recorded the pixel intensity across the image in a direction perpendicular to the stripe and generated an intensity profile

Many such profiles were obtained for the stripe images produced at a particular dose, with or without lindane treatment (usually 20-40 per dish, or ~100 per dose point and lindane condition). The profiles were then averaged and the full-width half-maximum (FWHM) and standard deviation for the average intensity profile of the series was determined. An average intensity profile of the γ-H2A.X image in the direction of the irradiation "stripe" was also generated. This analysis is shown in **Figures 5.13** and **5.14**. (Corresponding to **Figures 5.11a** and **b**, respectively).

a.

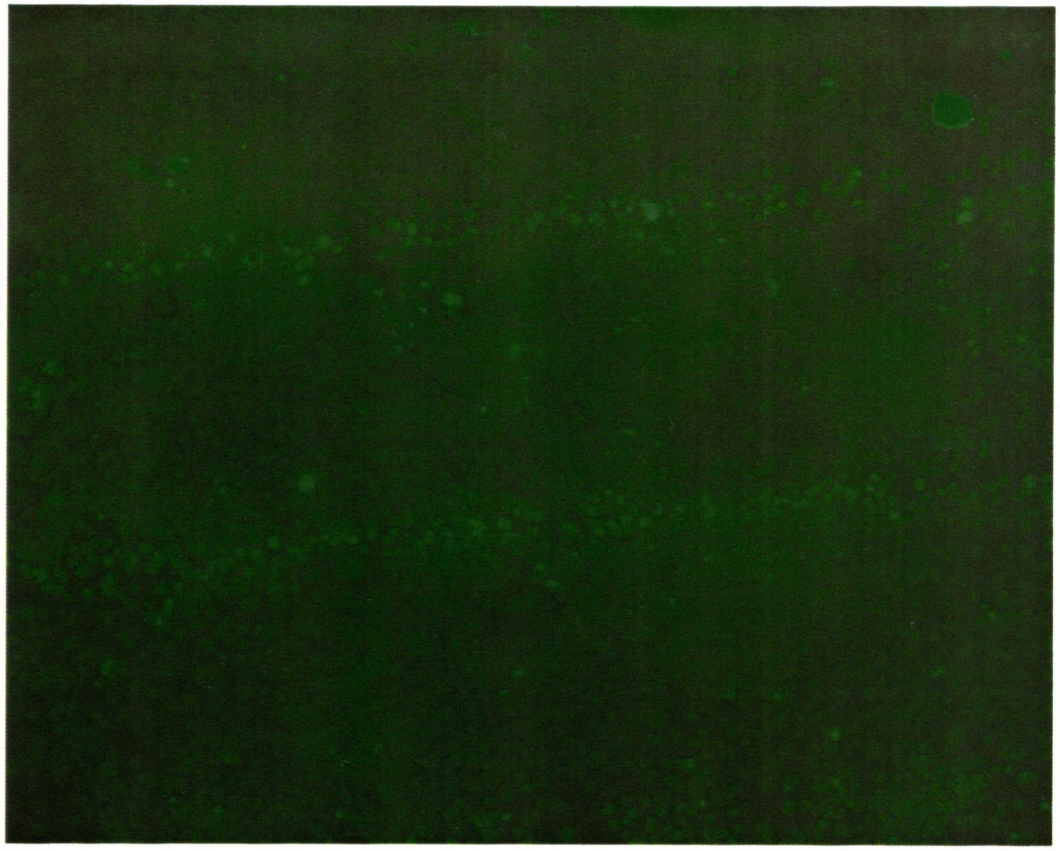

b.

c.

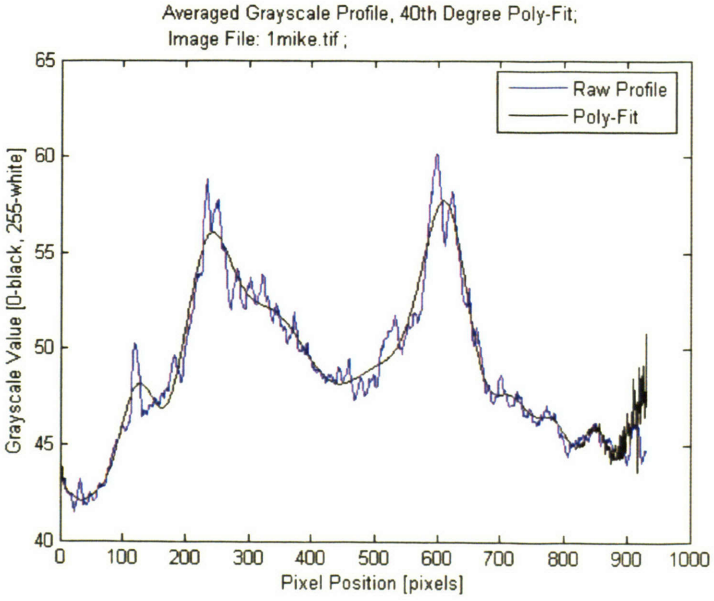

Figure 5.16 a) Color-adjusted raw image of irradiated cells, stained for γ-H2A.X, **b)** B&W aligned image for analysis, **c)** Vertically averaged intensity profile across the aligned image, with 40th degree polynomial curve fit. 1 pixel ~ 1.4 μm.

a.

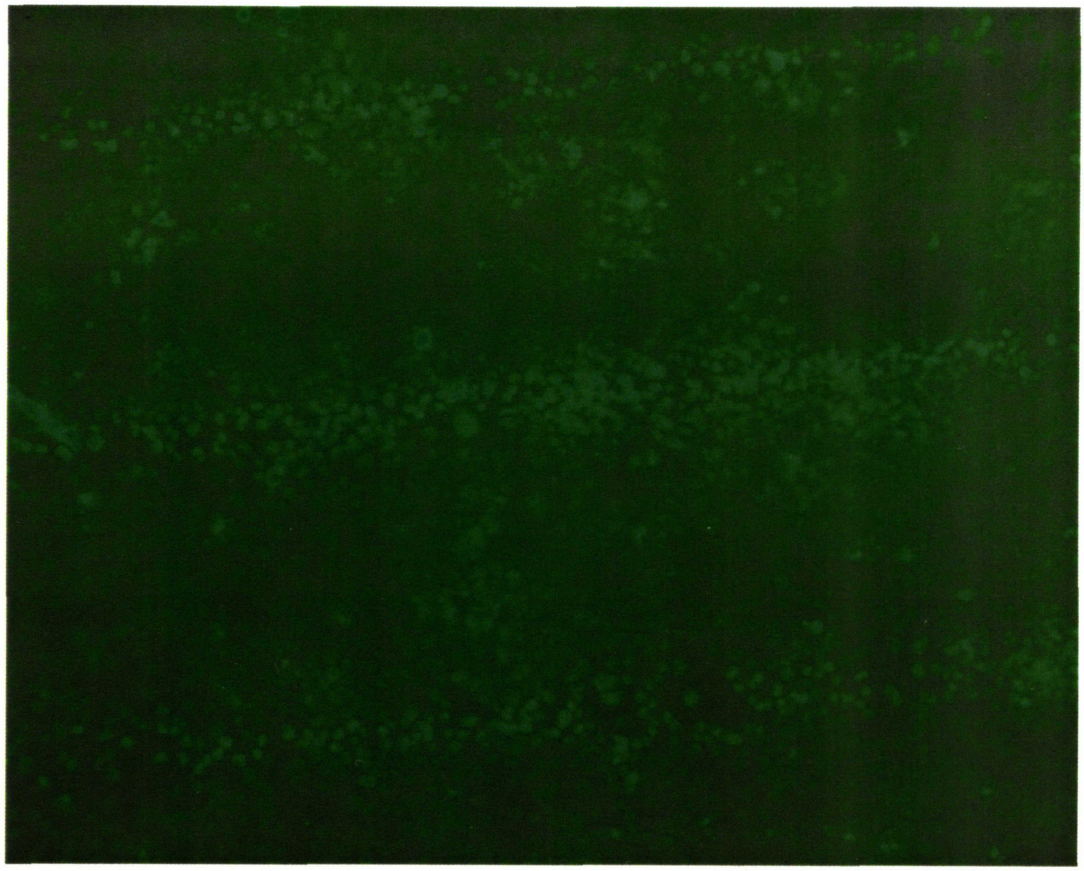

b.

c.

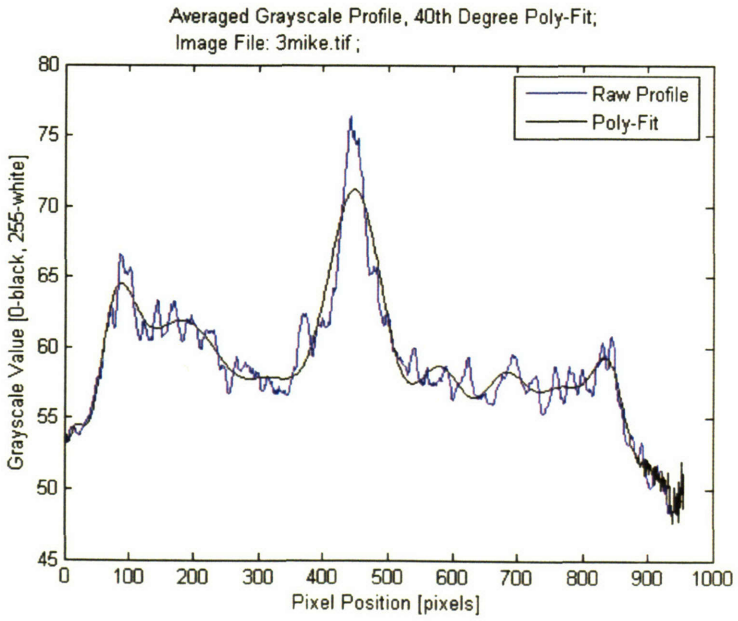

Figure 5.17 a) Color-adjusted raw image of irradiated cells, stained for γ-H2A.X. **b)** B&W aligned image for analysis, **c)** Vertically averaged intensity profile across the aligned image, with 40th degree polynomial curve fit. 1 pixel ~ 1.4 μm.

The width of the γ-H2A.X "stripes" were compared to a scaled intensity averaged image of a CR39 track-etch slit irradiation to demonstrate the relative widths of the "physical" and "biological" effects, as shown in **Figures 5.18** and **5.19** (corresponding to **Figures 5.16** and **5.17**, respectively).

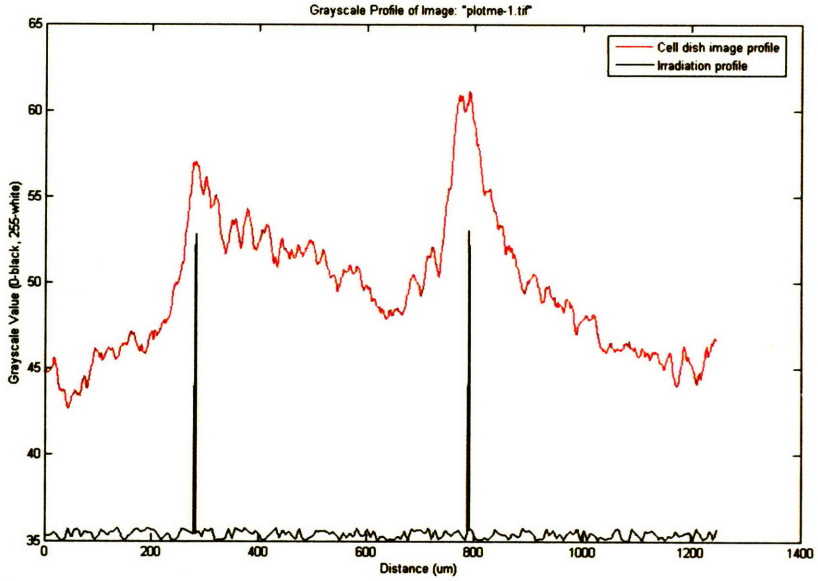

Figure 5.18 Plot of averaged γ-H2A.X profiles compared to the averaged CR39 profile (corresponds to **Figure 5.16a**).

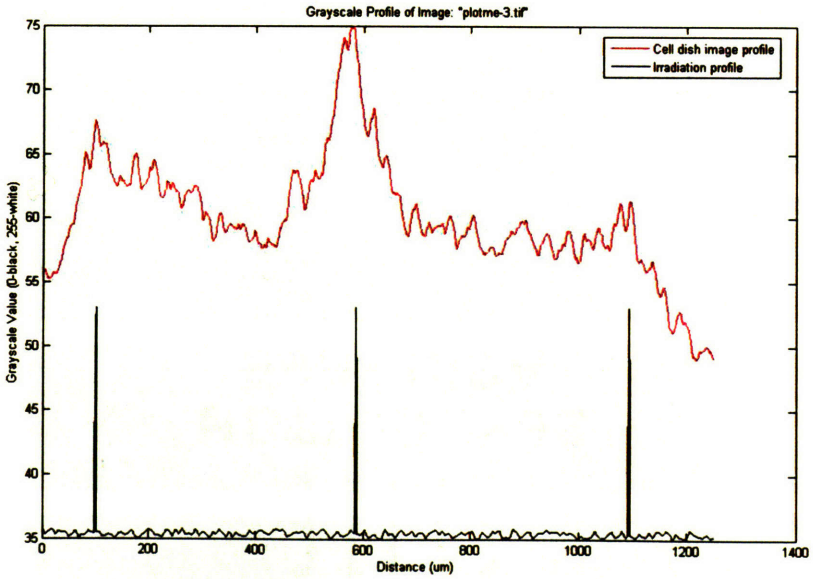

Figure 5.19 Plot of averaged γ-H2A.X profiles compared to the averaged CR39 profile (corresponds to **Figure 5.17a**).

The intensity average comparisons clearly show that the width of the biological effect of the ~200 Gy charged-particle microslit irradiation is significantly larger than the width of the actual physical distribution of radiation dose. As a rough estimate, the "full-width, half max" (FWHM) values of the right peak in **Figure 5.18** and the center peak in **Figure 5.19** are approximately 90 μm across, compared to the ~3 μm width of the image on the CR39 track-etch plastic.

An additional series of irradiations was performed looking specifically at variations in magnitude of induction of γ-H2A.X. The irradiation pattern was a set of 3 ~5mm long "stripes," 500 μm apart, across a monolayer of 100% confluent Chinese Hamster Lung Fibroblast (V79) cells. The radiation dose to the irradiated cells was performed at approximately 1-2, 10-20, and 60-80 Gy, estimated from previous track-etch studies (for more information, refer to **Chapter 4, Section 4.4.3.1**). Also, half of the irradiated cell dishes were treated with lindane (50 nM suspension in normal growth medium) to block gap junction intercellular communication (GJIC) in order to establish whether GJIC-based mechanism(s) were involved in the observed biological effect. An example series of images from one of these irradiations at 10-20 Gy and the corresponding averaged intensity profile of the anti-γ-H2A.X stain are shown in **Figures 5.20a** and **b**. These figures demonstrate the reproducibility of the unexpectedly wide profile of the γ-H2A.X signal with respect to the physical beam profile.

a.

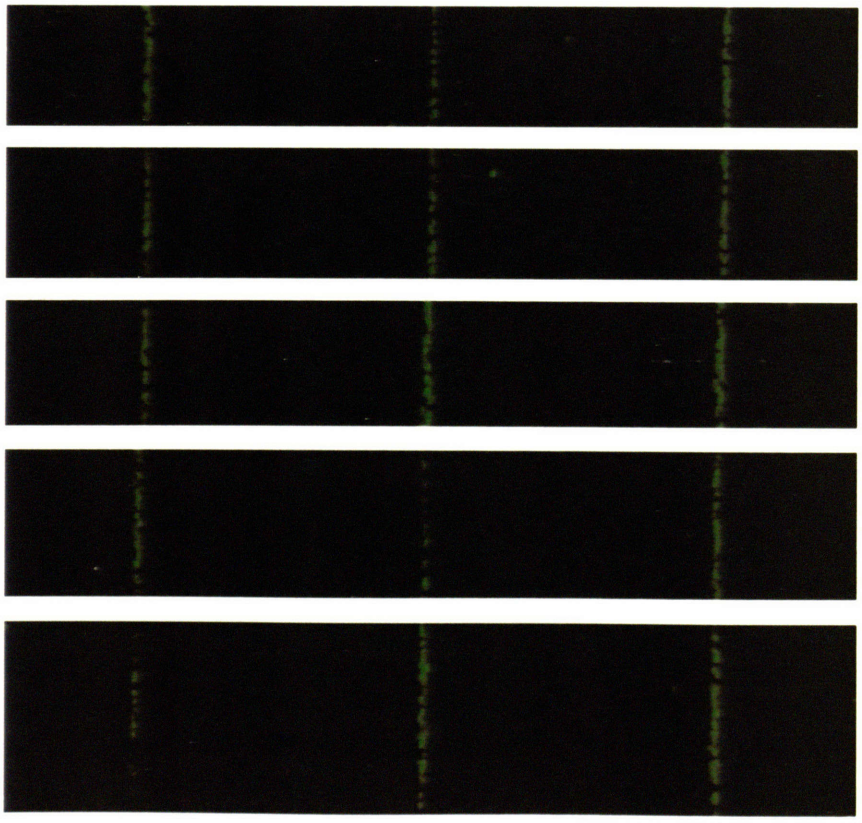

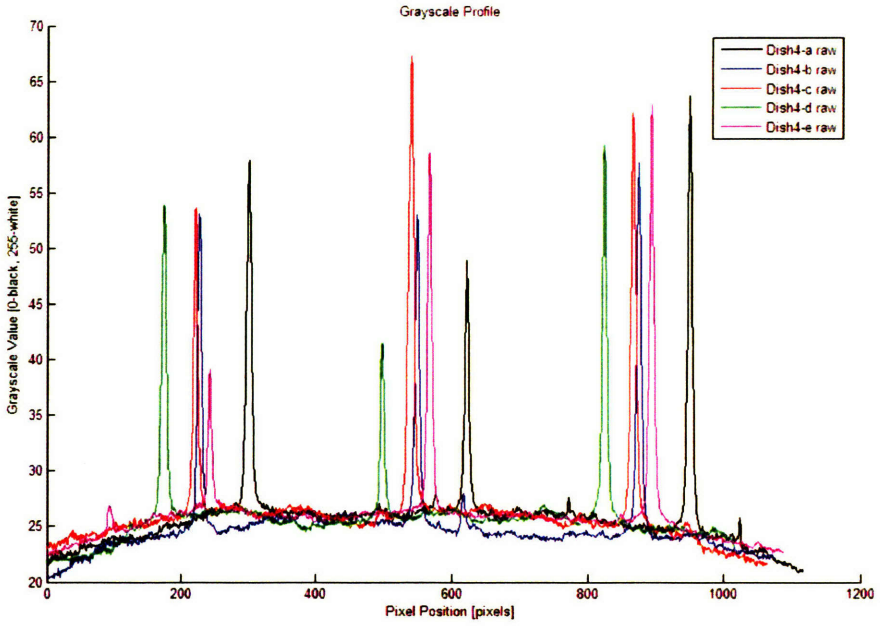

b.

Figure 5.20 a) Color-adjusted raw image slices of 10-20 Gy proton-irradiated V79 cells, stained for γ-H2A.X. **b)** Vertically averaged intensity profiles across the aligned image for each image slice. The individual γ-H2A.X peaks were intentionally offset to aid in visualization, and are not registered to other slices.

In **Figure 5.21**, averaged intensity profiles for the anti-γ-H2A.X stain for 1-2 Gy, 10-20 Gy, and 60-80 Gy charged-particle microslit V79 irradiations (with and without lindane treatment) are compared to the scaled image of the physical beam profile as measured using CR39 track-etch film.

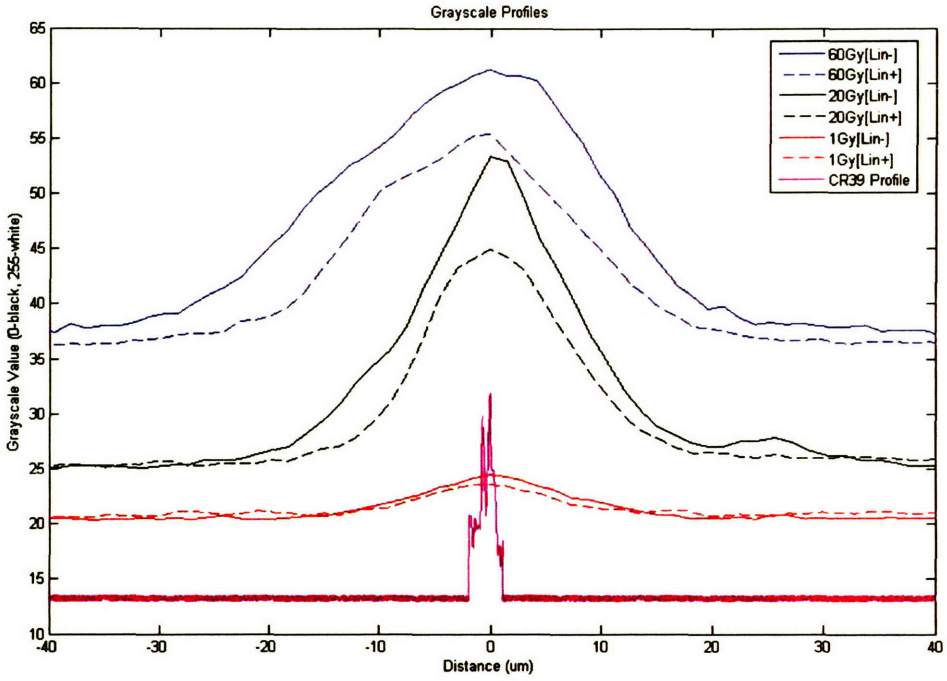

Figure 5.21 Vertically averaged intensity profiles across the charged-particle microslit-irradiated γ-H2A.X peak images, comparing the 1-2 Gy lindane(+/-) V79 irradiations, 10-20 Gy lindane(+/-) V79 irradiations, 60-80 Gy lindane(+/-)V79 irradiations, and a CR39 track-etch image

Averaged intensity profiles for each of the anti-γ-H2A.X stained irradiated V79 cell monolayers were used to compare the average full-width half-maximum (FWHM) of the γ-H2A.X peaks for the lindane-treated and untreated cells. **Table 5.2** shows the γ-H2A.X average peak FWHM for the irradiated V79 cells with respect to delivered dose from this experiment and the experiment described above (**Figures 5.13-5.16**), as well as the effect of lindane treatment.

Dose (Gy)	Lindane Treatment	FWHM (μm)	St. Dev. (μm)
200	-	~90	~10
60-80	-	52.7	6.5
60-80	+	49.5	4.9
10-20	-	23.8	0.9
10-20	+	20.5	0.3
1-2	-	14.9	2.1
1-2	+	12.2	1.7

Table 5.2 Comparison of γ-H2A.X average peak FWHM with respect to delivered dose and presence of lindane. All cells were V79 except for the 200 Gy series, which were NF cells.

While only a limited number of dose points has been investigated to date, there seems to be a correlation of radiation dose to the FWHM of the γ-H2A.X average peak. Additionally, treatment with a 50 nM concentration of lindane prior to irradiation seems to have a measurable effect on the width of the γ-H2A.X average intensity FWHM of the 10-20 Gy signal (over two standard deviations separation in both directions); however, there does not seem to be a statistically significant effect from lindane treatment on the FWHM of the γ-H2A.X average peak for the other V79 proton microslit irradiation dose points.

Figure 5.22 plots the FWHM of the γ-H2A.X-stained charged-particle microslit irradiated cell images vs. the physical dose delivered to the cells.

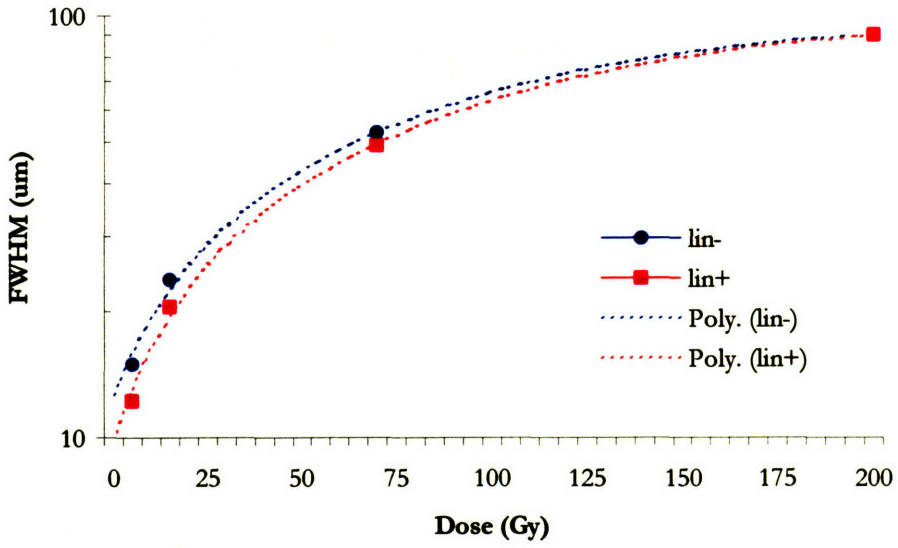

Figure 5.22 Plot of the FWHM of the γ-H2A.X-stained irradiated cell images vs. radiation dose delivered by the charged-particle microslit, with and without lindane treatment.

5.3.3.3 DNA Repair: anti-hMRE11 Studies

A series of irradiations was performed looking specifically at the localization of hMRE11 in response to charged-particle microslit irradiation. The irradiation pattern was chosen to be a set of 3 ~5mm long "stripes," 500 μm apart, across a monolayer of 100% confluent normal human fibroblast (NF) cells, counterstained with DAPI (a DNA-binding dye). The radiation dose to the irradiated cells was approximately 200 Gy, estimated from previous track-etch studies (for more information, refer to

Chapter 4, Section 4.4.3.1). The assay was performed as described in **Appendix D, Section D.5**. A possible charged-particle microslit-irradiated nucleus is shown in **Figure 5.23**.

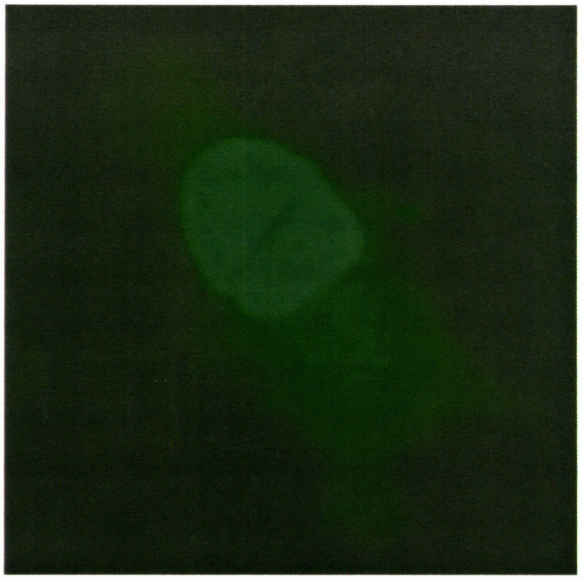

Figure 5.23 Charged-particle microslit-irradiated NF (~50 Gy), hMRE11 stain. (40x magnification, color adjusted)

The stripe across the center of the NF cell shown in **Figure 5.23** is believed to represent a heterogeneous subnuclear DNA repair response involving hMRE11. It certainly is different in character to the hMRE11 image of a mitotic cell shown in **Figure 5.3**, and while the distinct "stripe" across the middle does not conform to other biological processes, it does conform to the physical width of the charged-particle microslit beam profile.

This is the only assay of the three (ros, h2ax, mre11) that were chosen for initial charged-particle microslit irradiation studies that possibly corresponds to the Nelms et. al study[76] discussed in **Section 5.3.1**. However, as relatively little data have been generated at this point evaluating charged-particle microslit irradiations using the anti-hMRE11 stain, it cannot be said with certainty that the above image represents a directly irradiated cell; in addition, no significant bystander effects have yet been noted using anti-hMRE11 immunocytochemical techniques with LABA Microbeam-irradiated cells.

5.3.4 Discussion

Three separate radiobiological assays have been performed using the LABA Microbeam charged-particle microslit, and no two types of assay have generated completely consistent results. The first hypothesis is that this is merely a reflection of the complexity of the cellular response to radiation –

each assay examined a completely separate phase in the radiation response chain, and a wide range of signaling pathways and biological mediators has been implicated in each of these phases by other research groups. For example, many groups have observed hMRE11 foci in nuclei after irradiation, but only one paper has examined very high-contrast 'stripes' across nucleus resulting from 100 Gy soft x-ray irradiation, generated by a synchrotron source.[76]

It is of interest that the hMRE11 and γ-H2A.X stripes generated by the LABA Microbeam charged-particle microslit irradiations were of such variable contrast. High-dose irradiations, on the order of 200 Gy, resulted in very widespread induction of biological signal, particularly in the γ-H2A.X assay, while lower dose irradiations, on the order of 1-20 Gy, resulted in more defined induction of biological signal. A number of factors could be influencing this variation in observed response. For example, the hMRE11/γ-H2A.X localization may be highly dose, time, or LET-dependent; most likely, it is a combination of all three. The total irradiation dose administered by the LABA Microbeam for most of the described experiments was significantly higher than a standard radiotherapy treatment fraction (~2 Gy), which may have influenced the resulting biological effects. In addition, the irradiated cell monolayer fixation and staining protocols (timing and technique), as well as cell type, could have played a role in how the assays function. All of these variables are areas of continuing experimentation.

Of the issues that may be directly addressed, a purely physical flaw or miscalculation in the radiation delivery system could have come into play, where the actual aspect of the beam was significantly wider than predicted or previously measured. This is highly unlikely, as the observed difference between the physical beam profile and the induced radiobiological response was generally an order of magnitude or greater. This degree of beam widening could possibly be accounted for by the experimental geometry, but there would have to be a significant increase either in the intervening distance between the collimator and the target and/or in the amount of material traversed. SRIM calculations suggest that even a 0.5 mm air gap between the surface of the charged-particle microslit and the cell dish (possibly due to setup error on the part of the operator) would only result in an additional straggle of ~1.9 μm (radial straggle of 750 keV protons through 500 μm air, 1.4 μm Mylar, and 11 μm water), and additional intervening material that does not prevent the beam from interacting with the cells adds radial straggle on the order of 0.6 μm (radial straggle of 750keV protons through 1.4 μm Mylar, ~6 μm water, remainder through cell material). Re-verification of the charged-particle microslit beam profile was performed using either CR39 or LR115 track-etch film under the same conditions as the cell irradiations (usually at the end of the cell irradiation

experiment), and the beam profile was repeatedly demonstrated to be on the order of 3-5 μm in width.

The next possible issue was the possible effects of x-rays induced from the interaction of the 750 keV collimated proton beam with the material of the charged-particle microslit collimator substrate (stainless steel). This also seemed unlikely, as the diameter of the beam hitting the charged-particle microslit substrate was several mm, not tens of microns, so one would expect a much wider swath of induced γ-H2A.X expression on the irradiated cell monolayers than was observed in the experiments presented above. If induced x-rays are responsible for the wide "stripe" observed, examination of the proton-induced x-ray emission (PIXE) cross-sections for 750 keV protons on stainless steel suggested that a small yield of ~8 keV photons could be expected; the spectrum of the proton-induced radiation in the collimator material was examined accordingly. A very low dose rate was observed by placing a calibrated μRem radiation meter (Bicron Micro Rem, Saint-Gobain Crystals and Detectors, Paris France) within the experimental endstation during a charged-particle microslit irradiation, with the face of the detector directly above the cell dish. (See **Section 5.3.2.2**) The measured non-proton dose at this position during the irradiations was ~0.50-0.75 mrem/hour, and given that most cell dish irradiations are finished in less than 5 min, the total non-proton dose to the cell dish would be approximately 42-63 μRem. It was expected that this background dose rate was below the threshold for γ-H2A.X induction, and this factor was tested both by irradiating a piece of clinical radiographic film (Kodak T-MAT G/RA film) using a completely occluded slit (see **Chapter 4, Section 4.4.3.1**) and using the same occluded slit to irradiate a series of cell monolayers prepared as described in **Section 5.3.2.1**. It was expected that a completely occluded slit would not allow the transmission of any protons, but leave proton-induced x-ray emission unaffected. Although a small x-ray background from proton interactions with the stainless steel of the slit did indeed persist, in neither the film nor the sham-irradiated cells was a significant increase in signal observed (**Section 5.3.2.3**).

It was also suggested that background x-ray radiation from brehmsstrahlung during the acceleration process and/or excitation/de-excitation x-rays arising from the ion source could result in a significant x-ray dose contamination for the irradiated cells. This of course could not explain the observed "stripe" images; and ROS, γ-H2A.X, and hMRE11 staining of control dishes that were kept in the experimental endstation during charged-particle microslit irradiations but never directly exposed to the proton beam did not result in appreciable signal over background.

One assumption that was made with the initial LABA Microbeam charged-particle microslit radiobiological studies was that it would be best to start with three independent assays, each examining a completely separate phase in the radiation response chain. Because a wide range of signaling pathways and biological mediators have been implicated in each of these phases by other research groups, and because there may be no direct relation of one assay to the effect examined in one of the downstream assays, this may have actually complicated the examination of the cellular response to radiation. A refinement for future radiobiological assays would be to specifically compare two assays that take place in the same general phase of the cellular radiation response chain – for example, the localization of two independent dsDNA or ssDNA strand break repair proteins in response to a charged-particle microslit irradiation. Of course, the assays already developed should not be abandoned, as a wide range of variables still need to be explored.

It is possible that the results for the ROS and γ-H2A.X studies are not incompatible with the results from the Nelms et al x-ray grid irradiation study (**Section 5.3.1**).[76] ROS induction does not necessarily lead to dsDNA breaks, nor when dsDNA breaks result are they necessarily repaired by Non-Homologous End Joining (NHEJ) dsDNA repair (the form of repair in which hMRE11 is involved). The γ-H2A.X phosphorylation may also be due to double-strand break damage that is not repaired by NHEJ dsDNA repair; alternatively, it could be the result of an aberrant γ-H2A.X induction in the absence of an actual dsDNA break.

It is evident that the "radiobiological effective beam width," as measured by the spatial distribution of observed biological effects subsequent to irradiation, is significantly larger than the "physical beam width," as measured by the track-etch charged-particle microslit irradiation images. In several cases, most notably the ROS and γ-H2A.X assays, the biological effects of the radiation extended for many cell widths (> 40 μm), and demonstrated a dependence on the initial radiation dose delivered to the directly irradiated cells. Pre-treatment of a subset of the irradiated cells with the gap-junction intercellular communication (GJIC) blocker lindane additionally demonstrated that the mode of transmission of the ROS and γ-H2A.X-related biological effects is at least in part due to GJIC-mediated cellular interactions. Observations that a charged-particle beam with a "physical beam width" on the order of ~3 μm had significant induction of biological effects over a magnitude greater spatial range could signify a bystander effect that may play a role in radiotherapeutic dose control and treatment outcome.

5.4 Chapter Summary

In this **Chapter**, the design and construction of the biological target holder was described, and the methodology for performing a range of radiobiological studies was discussed. In **Chapter 6**, general conclusions about the LABA Microbeam will be presented, and the future work needed to improve upon the system so that it may meet its full potential as a standard research tool will be discussed.

Chapter 6. Conclusions and Future Work

The primary goal of this work, to develop an economical and compact charged-particle microbeam capable of delivering a dose distribution of subnuclear width, has been accomplished. The entire MIT LABA charged-particle microbeam, measuring less than 4 m and costing in its entirety < $2 million (in 2002 US dollars), may be placed in an existing room as the radiation background it creates is low enough that the operators may sit in the room while it is energized, thus saving on additional cost and space needs for radiation shielding. It utilizes a dedicated ion source, and may be put into operation from standby mode in as little as 10 minutes. As a simple, compact system capable of being operated with minimal trained personnel, the LABA Microbeam is a prototype for a general-purpose microbeam.

The charged particle microslit has been fully characterized and used to deliver a radiation pattern to a series of cell monolayers that have subsequently been assayed for direct and indirect chemical effects of irradiation, double-stranded DNA damage, and DNA repair protein localization. Data from these studies will contribute towards the characterization of the radiation-induced bystander effect. Analysis of the assays performed on microbeam-irradiated cells demonstrates that even though the physical radiation dose delivered by the LABA Microbeam is confined to a subnuclear width (< 5 μm), in several cases (the ROS and γ-H2A.X assays in particular) the biological effects of the radiation extend for many cell widths (> 40 μm), and show dependence on the initial radiation dose delivered to the directly irradiated cells. Additionally, pre-treatment of irradiated cells with the gap-junction intercellular communication (GJIC) blocker *lindane* has demonstrated the mode of transmission of two of these biologically-mediated secondary effects of radiation is at least in part due to GJIC-mediated cellular interactions.

While the LABA charged-particle microbeam is already a powerful research too, additional work will significantly expand its capabilities. As possibly the smallest microbeam in the world, the LABA Microbeam holds the greatest potential to serve as an economical research tool in smaller laboratories and hospital settings.

6.1 LABA Microbeam Design Improvements

6.1.1 Hardware Optimization

A root limitation of the LABA Microbeam is the terminal power supply/driver for the electrostatic accelerator itself. Although it was designed to accelerate singly-charged particles up to 1.5 MeV and doubly-charged particles up to 3.0 MeV, the driver becomes unstable and fails at energies over ~900 keV. The imposition of a large safety margin led to the choice of 750 keV as the standard beam energy for the accelerator, which limits the thickness of the scintillating plastic used in the single-particle detection system (and, as a result, the total light output of the plastic and the coincidence detection efficiency of the detection system), the range of materials that may be used in the cell dish, and the geometry of cells that can be irradiated.

While the charged-particle microbeam is capable of delivering radiation doses of hundreds of Gy with ease, for many clinically-relevant studies it is more important to be able to deliver dose on the order of 0.1-1 Gy; radiation protection studies would require an even lower dose range. Addition of a filter/delimiter/aperture near the exit of the accelerator, with or without defocusing the beam using the quadrupole triplet, may be useful in reducing the dose rate for lower dose applications of the charged-particle microslit.

Components in the LABA Microbeam experimental endstation that stand most in need of improvement include the pinhole aperture collimation system and the single-particle detection and counting system. The pinhole/capillary aperture was never wholly satisfactory, and issues with the penumbra generated by the charged-particle beam passing through the collimator need to be resolved. The single-particle counting system's highest attained counting efficiency was 98.5%, although 98.0% was a more typical value once the parameters were optimized. It is possible that using a higher energy beam and a thicker piece (or multiple stacked pieces) of scintillating plastic would improve the light output and possibly enhance this efficiency to the desired value of ~99%.

In the long term, while both the charged-particle microslit and the pinhole aperture collimation techniques are useful applications of the microbeam technique, the pinhole aperture is the more versatile of the two. While it is possible to replicate the radiation dose distribution of the microslit with the pinhole collimator by slowly sweeping the micron-scale spot along a cell monolayer, the microslit method will never be able to administer a point dose or target individual cells.

6.1.2 Automation

The application of the charged-particle microslit required only a limited range of automated features, all of which have already been integrated into the control software. For future large-scale or complex

irradiations, more automated features will have to be developed. Of primary concern is the nuclear targeting system, which needs to be able to recognize and accurately distinguish the centroid of every cell nucleus in the visual field, and be able to automatically position those centroids in the path of the beam for sequential irradiations. The operator should be able to specify a number of cells to be targeted (either all, a random percentage of the whole, or a specified subset) and an automated function would determine which subset of tracked cells will be targeted and hit with specified number of protons.

To make the LABA Microbeam a truly "turn-key" system, the startup process should be made a one-button affair. The current startup procedure, while relatively simple, requires the operator to follow a short series of procedures, punctuated with diagnostic checks to ensure the safety of the accelerator hardware. Consistent operation under well-maintained conditions would allow this process to be streamlined and automated.

6.1.3 Biological/Target

Several refinements could be made to the current cell dish configuration to improve its use in radiobiological studies – as stated above, the limitations on terminal voltage, and as such on the energy of the charged-particle beam, seriously restricts the thickness and choice of cell dish material. Several facets of the endstation and dish may contribute to deleterious effects on the cells. Two issues that may be resolved in the short term are the lack of temperature regulation and the optical geometry of the stainless steel dish. The addition of a low-power heating element to the endstation or to the dish itself (the entire dish could serve as a heating element, with proper regulation) could remove this confounding factor. Making the dish shallower would allow for easier visualization by microscopy (currently, the objectives come up against the walls of the dishes, which restricts the area of the dish that may be viewed). Larger surface area is another possibility, but the range of the x-y stage motion limits the total "range" that may be viewed.

In the long term, advanced cell culture and microenvironment control techniques could be integrated to provide a much more powerful research tool. For example, a microfluidic injection control system could be integrated with a more complex dish, creating a system that combines precise targeting of specific cells with an "*in-vivtro*"-style regulated microenvironment. Coupled with cell-patterning techniques to generate a tissue-like cellular architecture within the dish, this could allow for the culturing of a patient's tumor cells in an artificial tissue environment that closely mimics their own, permitting the radiation oncologist/radiation oncology physicists to accurately simulate a

radiotherapeutic treatment with or without complementary onco-pharmacological compounds. Experimental data from microbeam-based irradiation and analysis of tissue response to radiation and onco-pharmacological compounds could contribute to highly individualized (optimized) therapy designs for patients. This is an area in which the LABA Microbeam design is crucial, for only a small, relatively inexpensive microbeam available within a hospital environment could make this generalized application possible.

6.2 Radiobiological Modeling

One of the more ambitious long-term goals of the radiobiological assays performed using the LABA Microbeam is to gather data of a sufficiently rigorous and quantitative nature that accurate and precise cellular radiobiological response models may be developed. Using full dose-range studies, the biological effect of the soluble and directly transmitted (via GJIC, for example) biological mediators of the radiation-induced bystander effect can be elucidated, providing insight into the complex set of interactions that occurs within a cell and between cells after exposure to radiation.

Most radiodosimetric models focus solely on the direct radiation interaction, when the actual response of a tissue (a set of cells working towards a specific function, proximate to each other) seems to be due both to direct radiation insult and a set of biologically-mediated subreactions. For a cell hit by radiation, both of these interactions are evident. For a non-hit cell, only the biologically-mediated effects will be noted. Thus, a model that integrates these responses over a group of cells may serve as a significantly more accurate predictor of radiation response at the organismal level.

This begs the question: How does one separate out the radiological and biological effects of radiation? Microbeam techniques provide the answer. Consider the following example: in order to quantify effects of irradiation on every single cell in a system (where cells are contiguous, as in a tissue model), one first needs a case in which is only possible when every single cell in tissue system is hit by a precise number of particles, referred to as a "universal microbeam irradiation." Subsequent observation of a biological endpoint or range of endpoints then provides the sum damage (X_{tot}) for a tissue system for that endpoint(s).

Medium transfer experiments would then be performed, in which the medium from a series of "universial microbeam irradiation" irradiated cells is transferred to otherwise unmodified cell cultures, providing the contribution of soluble biologically-mediated factors towards the induction of the chosen biological endpoints ($X_{biological} = B_s+B_g$). Similar experiments using gap junction

intercellular communication (GJIC) blockers such as lindane can then be used to determine the relative contributions of GJIC-mediated (B_g) and diffusion-mediated (B_s) effects on damage expression (B_s vs B_s+B_g).

Universal microbeam irradiation experiments with GJIC-blockers would show the contribution of soluble factors and radiation to the induction of the chosen biological endpoint(s) ($X_{\text{radiation and soluble factors}} = X_{\text{radiation}} + B_s$).

The end result is a set of relations that can be used to simulate the complete response (X_{tot}) of a cell to specific initiating radiation dose via **Equation 6.1**:

$$X_{tot} = X_{\text{radiation}} + X_{\text{biological}} = X_{\text{radiation}} + B_s + B_g \qquad \textbf{Equation 6.1}$$

Where B_s = induced response from soluble factors

B_g = induced response from GJIC-mediated factors = $X_{tot} - X_{\text{radiation and soluble factors}}$

$X_{\text{biological}}$ = total biological-mediated induced response = $B_s + B_g$

$X_{\text{radiation}}$ = induced response from direct irradiation = $X_{tot} - X_{\text{biological}}$

$B_g = X_{tot} - X_{\text{radiation and soluble factors}}$

$X_{\text{radiation and soluble factors}} = X_{\text{radiation}} + B_s$

The equation for the total biological endpoint induction for a single cell as a function of initially administered radiation dose would then be:

$$X_{tot}(D) = X_{\text{radiation}}(D) + B_s(D) + B_g(D) \qquad \textbf{Equation 6.2}$$

For a cell, the summation with respect to endpoints is:

$$\sum_{endpoints} X_{tot}(D) = \sum_{endpoints} X_{\text{radiation}}(D) + B_s(D) + B_g(D) \qquad \textbf{Equation 6.3}$$

And for a system, the summation with respect to cells is:

$$\sum_{cells} \sum_{endpoints} X_{tot}(D) = \sum_{cells} \sum_{endpoints} X_{\text{radiation}}(D) + B_s(D) + B_g(D) \qquad \textbf{Equation 6.4}$$

The result may be used to model the net effect of a radiation exposure on a tissue system. While this is a daunting task that would require a vast number of experiments and would no doubt vary significantly by cell type and tissue microenvironment, the comprehensive understanding of the full range of radiobiological response to radiation it would impart would be highly beneficial both to basic science and clinical application.

Appendix A: Accelerator Control Systems and Interlocking

A.1 Control Systems

The LABA Microbeam Accelerator is controlled primarily by a graphical interface, which is written in a proprietary language developed by Pyramid Technical Consultants (Waltham, MA USA). This interface simplifies operation of the accelerator and the various subsystems, as well as providing a platform for the automation of specific tasks. At this level (leading up to but not including the experimental endstation), automation is responsible for a limited number of tasks, including: 1) emergency shutdown of all critical accelerator systems, 2) "soft" startup of the accelerator vacuum systems after a shutdown or power failure, 3) "priming" of the plasma to generate an accelerated beam, and 4) the tuning of the bending magnet current to the energy of the charged particles so that it produces the exact magnetic field required to direct the horizontal particle beam vertically through the beam collimator. These automated tasks will be described more fully in the sections specific to the applicable control system.

The three screens used in the basic operation of the LABA Microbeam Accelerator are the Vacuum Screen (**Figure A.2**), the Accelerator Control Screen (**Figure A.3**), and the Facilities Screen (**Figure A.4**). All screens have a common border that allows the operator to run experiments, monitor the integrity of the vacuum system, rapidly turn off critical systems, and switch between the various system interfaces. **Figure A.1** shows this common border with the variable interface removed.

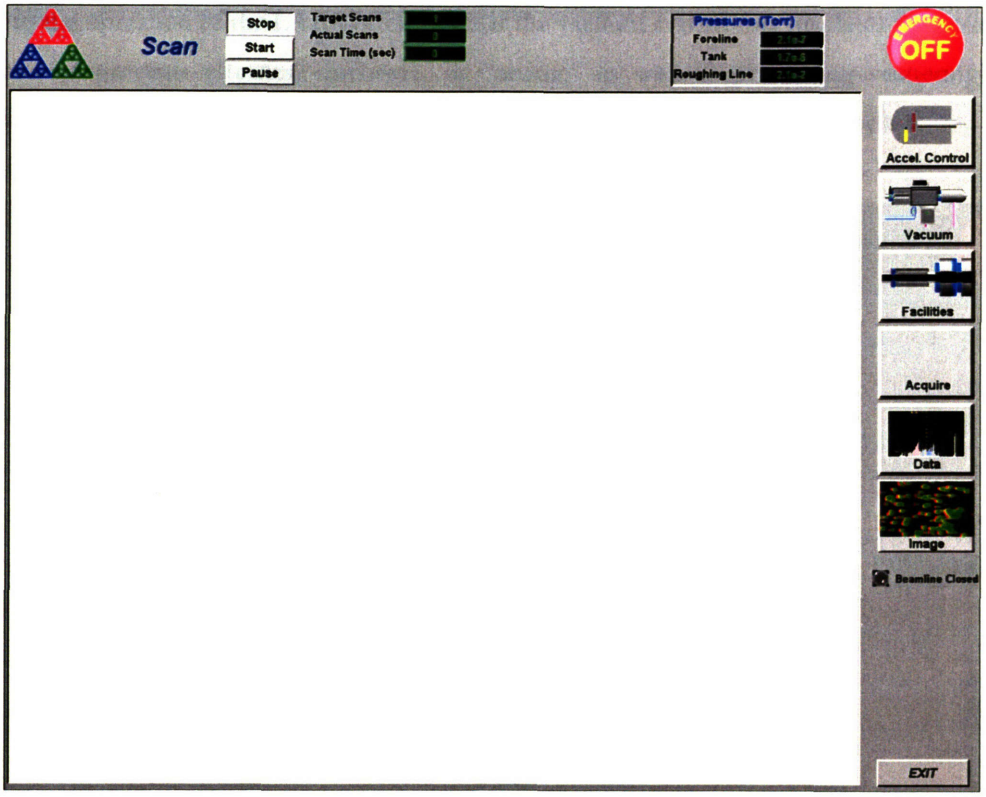

Figure A.1 The "Common Border," present on all graphical interface screens.

Description of "Common Border" executables and displays: (clockwise from the PTC symbol in the upper left corner)

Scan: These allow the operator to start, pause, and stop an experimental scan, as specified on the "Acquire" screen (to be explained in detail in Chapter 4). The displays indicate the number of scans performed and the total duration of an individual scan.

Pressures: Vacuum pressures in the foreline, tank, and roughing line indicate the integrity of the system.

Emergency Off: One of the automated subsystems that allows the operator to quickly and selectively turn off critical components and isolate vulnerable accelerator subsystems.

Screen Selection: Permits the operator to rapidly switch between control screens (Accelerator Control, Vacuum, Facilities, Acquire, Data, and Image).

Beamline Patency: Indicates whether an open path exists for delivery of accelerated particles to the experimental endstation.

Exit: Terminates the LABA Microbeam control program.

A.1.1 Vacuum Control

Crucial to the operation of the LABA Microbeam is the vacuum system that insulates the accelerating elements and prevents electrical discharge, or "arcing," as well as preventing scattering of the accelerated ions along the beamline. The Vacuum Screen is shown in **Figure A.2** below.

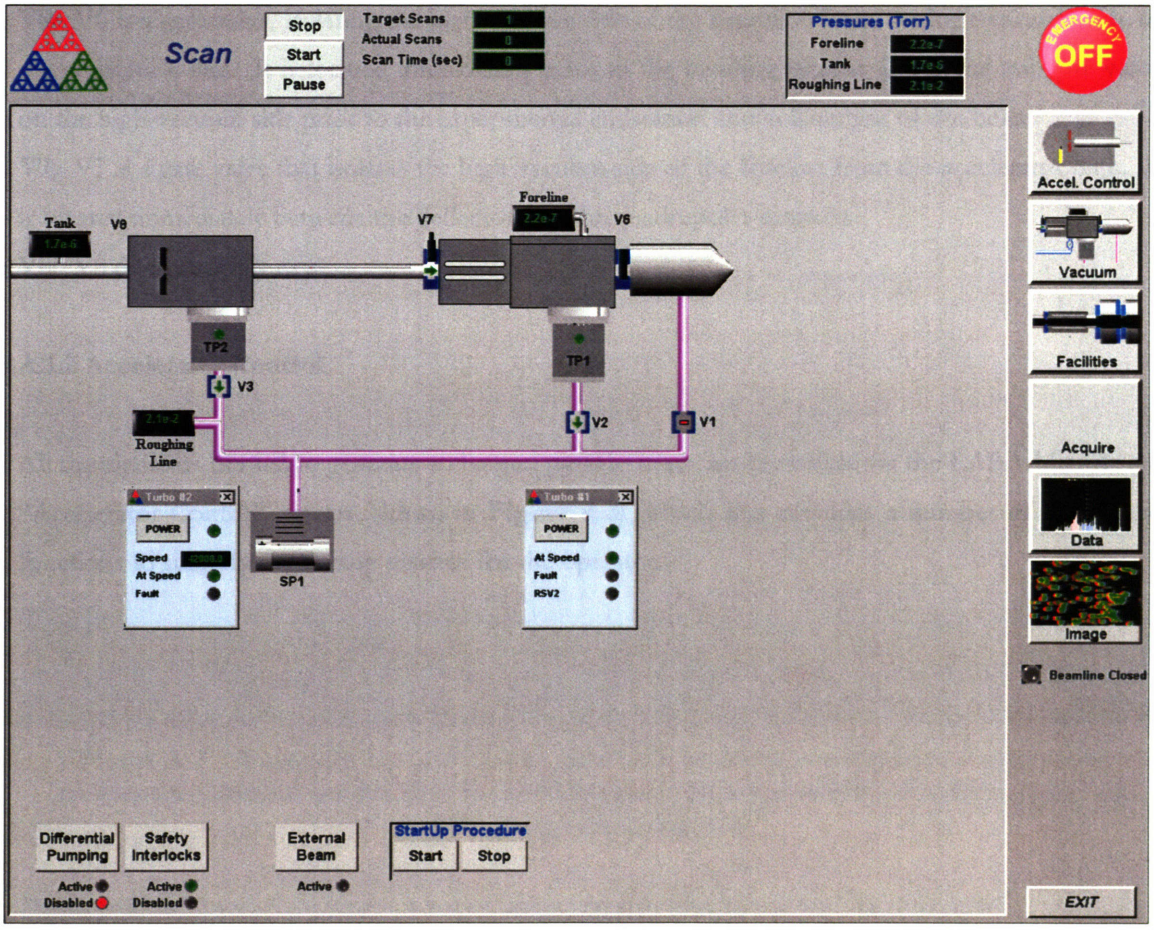

Figure A.2 The "Vacuum Screen" graphical interface, which allows the operator to control the LABA Microbeam vacuum subsystems and open/close the beamline.

Description of Vacuum Screen executables:

TP1: "Turbo #1" is a Varian V250 Turbopump, with an operating speed of 56 krpm. It provides high vacuum (on the order of 10^{-7} torr for a closed beamline, 10^{-5} torr with the microslit collimator in place on an open beamline, and 10^{-6} torr with the pinhole collimator in place on an open beamline) for the microbeam foreline. It is physically mounted after the deflectors and quadrupole magnets, between the V7 and V1 gate valves prior to the bending magnet.

TP2: "Turbo #2" is a Varian V550, with an operating speed of 42 krpm. It provides high vacuum (on the order of 10^{-7} torr for a closed beamline and 10^{-6} torr while generating beam) for the microbeam accelerator tank. It is located immediately at the exit of the accelerator tank.

V1: V1 is a gate valve, isolating the endstation low-vacuum line from the general roughing line.

V2: V2 is a gate valve, isolating the low-vacuum side of TP1 from the general roughing line.

V3: V3 is a gate valve, isolating the low-vacuum side of TP2 from the general roughing line.

V4, V5: V4 and V5 are test valves that are not used as part of normal operation.

V6: V6 is a gate valve, isolating the high-vacuum side of the beamline from the high-vacuum side of the endstation line. It is located immediately prior to the bending magnet and is the last gate valve on the high-vacuum side prior to the experimental endstation and collimation of the beam.

V7: V7 is a gate valve that isolates the high-vacuum side of the foreline from the accelerator tank. It is located immediately between the deflector and the quadrupoles magnets.

V8: V8 does not truly exist.

A.1.2 Accelerator Control

All the elements needed to generate a charged-particle beam are accessible via the LABA Microbeam "Accelerator Control" screen (shown in **Figure A.3**), which also provides a number of automated functions to simplify the startup process for the operator.

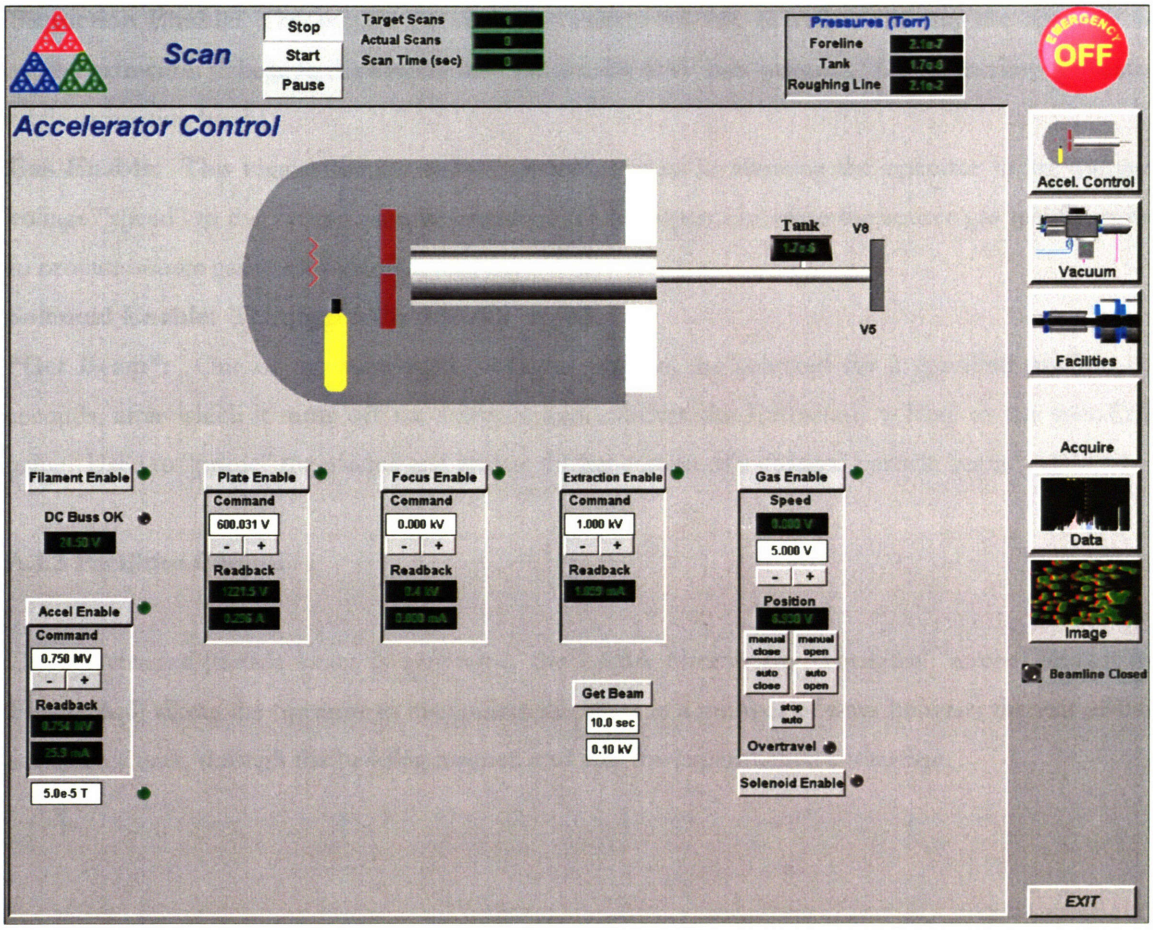

Figure A.3 "Accelerator Control" Screen, which allows the user to regulate the accelerator components: terminal voltage, filament, oscillator plate, focusing element, extraction probe, gas valve, and priming solenoid.

Description of Accelerator Control Screen executables: (clockwise from "Accel Enable")

Accel Enable: This toggles the terminal voltage on/off, as well as allowing the operator to set the terminal voltage to the desired amount (usually 0.750 MeV).

DC Buss OK: This indicates whether sufficient voltage is provided by step-down from the terminal voltage to run the systems inside the accelerator. The readback provides the voltage generated by stepdown – safe values range from 12-30V.

Filament Enable: This simply toggles the filament on and off.

Plate Enable: This toggles the plate voltage on/off, as well as allowing the operator to set the plate voltage to the desired amount (usually 600V).

Focus Enable: This toggles the focus voltage on/off, as well as allowing the operator to set the focus voltage to the desired amount (usually 6 kV).

Extraction Enable: This toggles the extraction voltage on/off, as well as allowing the operator to set the extraction voltage to the desired amount (usually 5 kV for "priming," 0.5 kV during operation while generating beam).

Gas Enable: This toggles the gas voltage on/off, as well as allowing the operator to set the gas voltage "speed" to the desired amount (usually 5 V) and open and close the source gas needle valve to provide source gas to ionize and accelerate.

Solenoid Enable: This toggles the solenoid on/off.

"Get Beam": One of the automated functions, triggers the solenoid for a specified number of seconds, after which it turns off the solenoid and switches the Extraction voltage to the specified value. Used to "prime" the plasma and initiate the generation of a charged-particle beam.

A.1.3 Facilities Control

Once a charged-particle beam is generated, the LABA Microbeam "Facilities" screen (shown in **Figure A.4**) allows the operator to manipulate the beam in a number of ways between the exit of the accelerator tank, through the bending magnet, and into the experimental endstation.

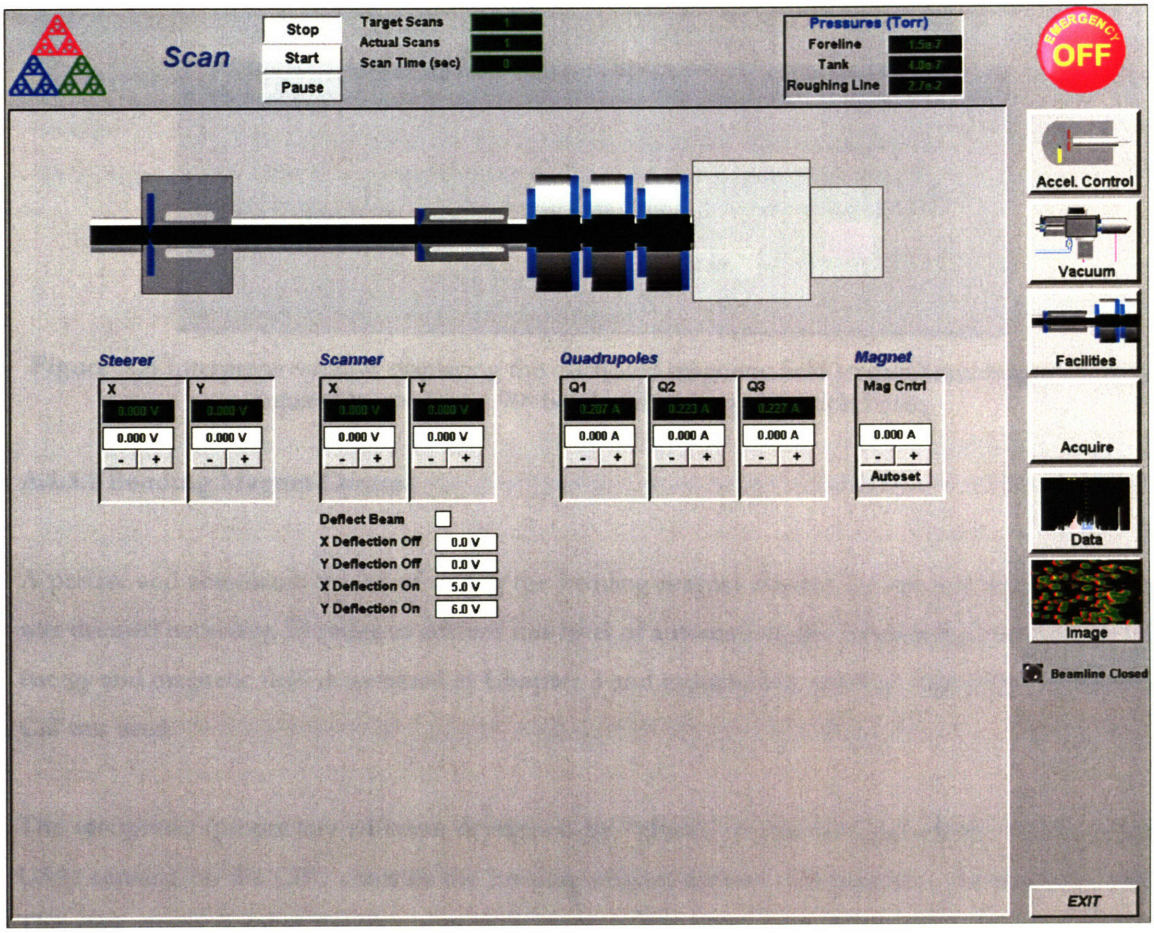

Figure A.4 The "Facilities Screen" graphical interface, which allows the operator to control the LABA Microbeam beamline subsystems and deflect the beam.

Description of Facilities Screen executables: (left to right)

Steerer (X and Y): Not used.

Scanner (X and Y): These allow the deflection of the beam in two dimensions perpendicular to the beamline. The presets specifically allow the operator to define "resting" and "active" deflection during the course of an irradiation – these presets are engaged while the experimental stage (to be described in detail in Chapter 4) is in motion, and disengaged when the stage is at rest.

Quadrupoles: These control the current applied to the magnets in the quadrupole triplet, and allow the operator to alter the beam profile to varying degrees.

Magnet: This sets the current applied to the bending magnet that turns the horizontal beam into a vertical beam, directed into the experimental endstation. The "autoset" button automatically sets the bending magnet current to the value required for the kinetic energy of the accelerated particles (which, in turn, is a function of the terminal voltage set on the "Accelerator Control" screen). The popup screen is shown in **Figure A.5.**

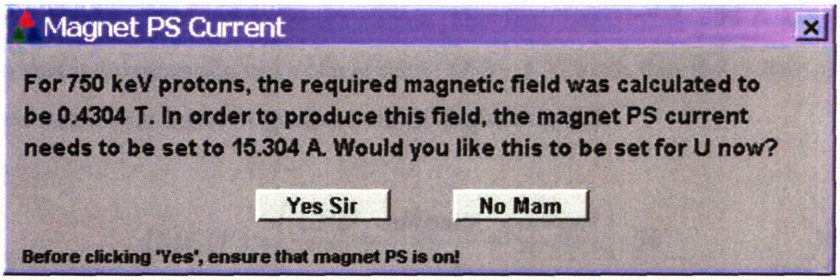

Figure A.5 Interpreter window displaying the calculated magnetic field strength and magnet current required to produce a 90^0 bend in the charged-particle beam.

A.1.3.1 Bending Magnet Control

A precise and automated means of tuning the bending magnet current for specific proton energies was deemed necessary. In order to achieve this level of automation, the relationship between proton energy and magnetic field determined in **Chapter 3** and explained in detail in **Appendix C, Section C.2** was used.

The interpreter (proprietary software developed by Pyramid Technical Consultants, Waltham MA USA) running on the CPU controls the bending magnet current that generates the magnetic field. The user enters a value for the magnet current at the CPU, and this input value is internally converted to a voltage ranging from 0 to 5 volts by a Digital-to-Analog converter (DAC). This output voltage is then scaled down by a voltage divider, which consists of a 15 Ohm resistor in series with an 820 Ohm resistor. This scaled-down voltage is then placed across the programming inputs (0-100 mV) of an Electronic Measurements Inc. EMS Power Supply Model EMS 150-33 (0-150 VDC, 0-33 ADC), which is attached in series to the terminals of the bending magnet.

Editing the appropriate line in the file that controls the variable associated with the bending magnet ('Loop1.tab') can alter the scaling applied by the interpreter to the user-input magnet current. Figure 1 displays the information originally defined in the 'Loop1.tab' file for the magnet current (i.e., c_Mag_I), which is used in the conversion that determines the output voltage of the DAC.

```
I/O   c_Mag_I   ANALOG   C6   U   LINEAR      0 25  0 25        // 0 to 5V
```

Figure A.6 Scaling information, in the 'Loop1.tab' file, used to translate the CPU input for magnet current into a DAC output voltage.

Of particular significance in Figure 1 is the number sequence '0 25 0 25'. Each pair of numbers corresponds to a range of magnet current values. The first range of 0 - 25 A is translated by the interpreter so that it corresponds to a voltage range of 0 – 5 V, such that the output voltage from the DAC is related to the user-input magnet current by **Equation A.1**:

$$DAC(V) = \left(\frac{CPU\_magnet\_current}{25} \right) \cdot 5V \qquad \textbf{Equation A.1}$$

The second range of 0 – 25 A in **Figure A.6** Above refers to the range of values that the user may input for the magnet current. Values below 0 A or above 25 A will not be accepted as valid user input. It should also be noted here that the scaling factors in 'Loop1.tab' file for 'c_Mag_I' were originally '0 25 0 25'. These values were then changed to '0 29.9 0 25' , to account for the correction factor included in **Equation 3.10** in Chapter 3.

The voltage output from the DAC is fed into the aforementioned voltage divider (VD), a 15 Ohm and a 820 Ohm resistor in series, which divides the DAC output voltage by a factor of approx. 56 (i.e., (15 + 820) / 15). This divided voltage is then applied across the programming terminals of the magnet power supply. For the bending magnet power supply, the programming range is 0 – 100 mV for the current range of 0 – 33 A. Thus, **Equation A.2** relates the power supply input voltage to the power supply current output.

$$PS\_output\_current(A) = \left(\frac{input\_voltage}{100mV} \right) \cdot 33A \qquad \textbf{Equation A.2}$$

This output current is then applied to the bending magnet to produce the required magnetic field. The current output from the magnet power supply can be related back to the user-input CPU magnet current by combining both **Equations A.1** and **A.2** to produce **Equation A.3**.

$$PS\_output\_current(A) = \left(\frac{\frac{CPU\_magnet\_current}{25A} \cdot 5V \cdot \frac{1000mV}{1V}}{100mV \cdot \frac{15+820}{15}} \right) \cdot 33A \qquad \textbf{Equation A.3}$$

The calculation of CPU magnet current shown by **Equation A.3** was coded into the interpreter to complete the aforementioned automation. When the 'AutoSet' button is pressed, the user is

presented with a pop-up window similar to the one shown in **Figure A.6** above. If the user so wishes, the interpreter will then step the CPU magnet current up until the calculated magnet current is reached. If the user chooses no, then no action is taken.

A.1.4 Stage Control, via the "Acquire" Screen

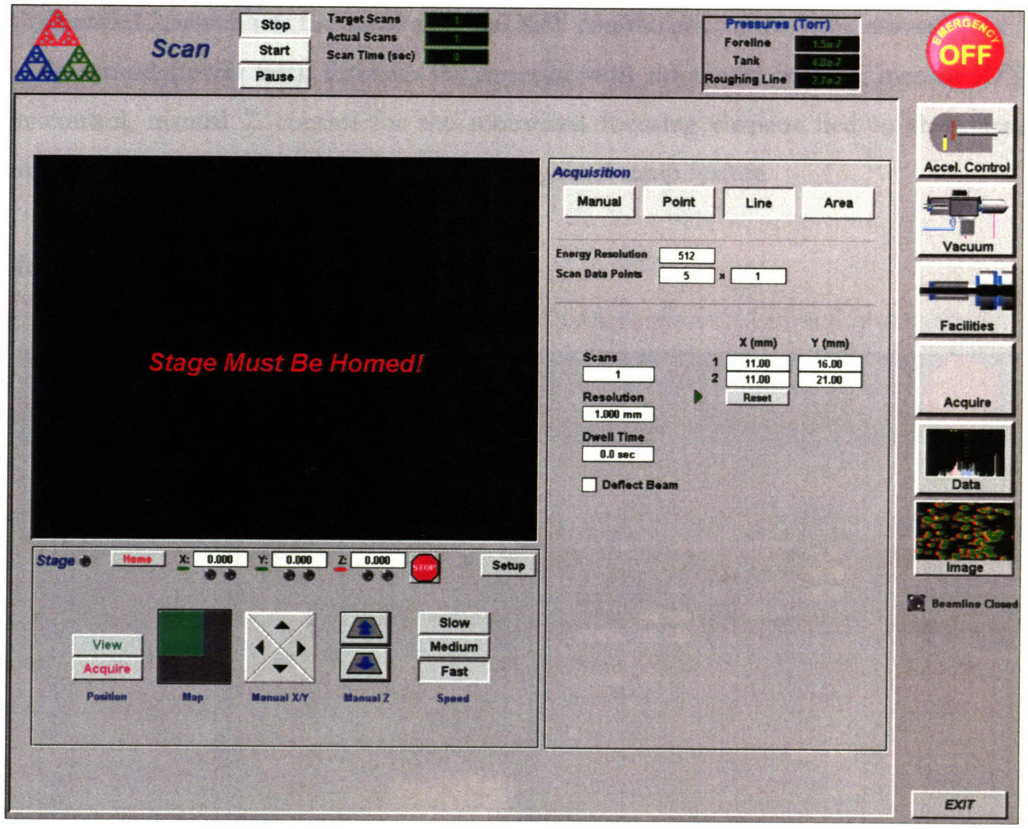

Figure A.7 "Acquire" control screen.

Description of Acquire Screen executables: (clockwise from "Stage Must Be Homed")

Status Screen (upper left): Shows a cursor during the course of a scan that indicates the relative position of the stage. When the stage is not in its "home" position following the completion of a scan, the program reminds the operator to return it prior to the initiation of a new scan.

Acquisition Type (upper right): The **Acquisition Type** controls in the upper right hand corner allow the operator to limit the type of scan to specific types: *Manual*, which has the greatest degree of open parameters;

Point, which will only move the stage to a specific location defined by the operator;

Line, which will sweep the stage from one operator-specified point to another; and

Area, which will pan the stage repeatedly over an area, used for large automated tasks.

Scan Data (middle right): Provides scan-specific data based on operator-defined parameters.

Scan Parameters (lower right): The **Scan Parameters** in the lower right **a**llow the operator to enter a number of parameters that define the behavior of a scan, specifically:

Resolution, the distance between each step movement of the stage;

Dwell Time, how long the stage will stay at rest between steps;

Deflection, which automatically turns on deflection while the stage is in motion; and

Position 1,2, which sets the initial and final X/Y coordinates for the stage movement.

Stage Movement (lower left): Provides the operator with automated homing, manual X/Y stage motion control, manual Z control for the motorized focusing element tied to the microscope objective, speed control for the stage motion, and a general setup feature.

A.1.5 Imaging Control, via the "Image" Screen

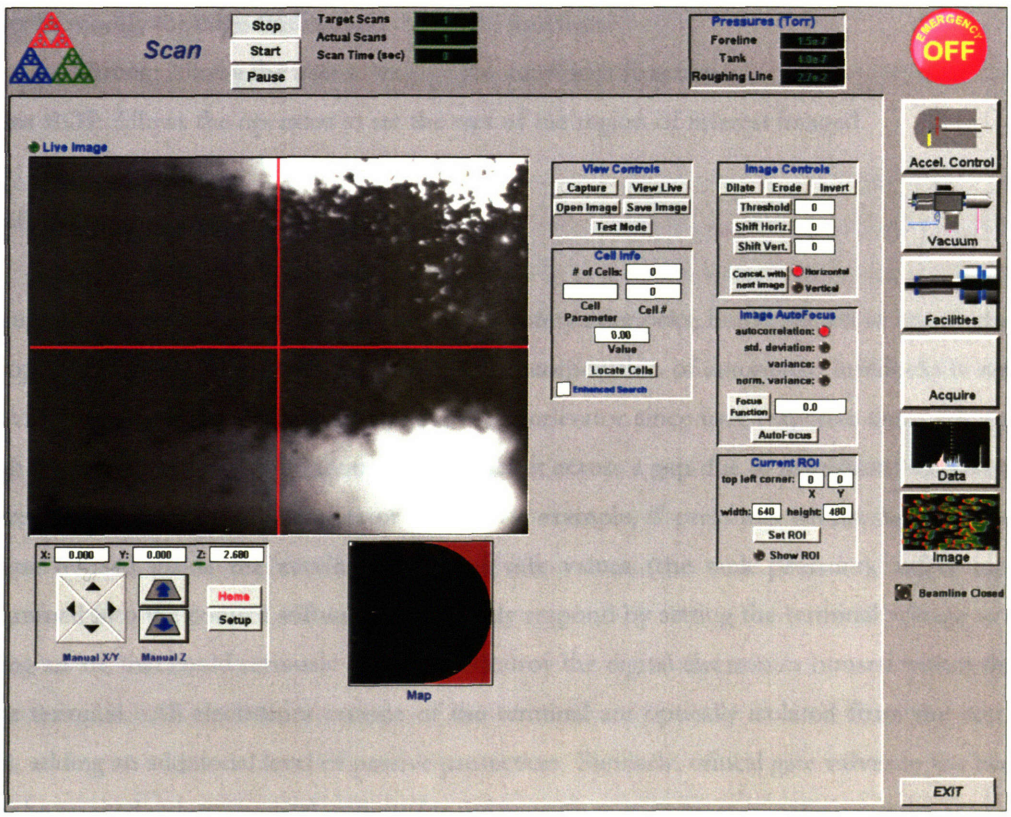

Figure A.8 "Image" control screen.

Description of Image Screen executables: (left to right from "Live Image")

Visualization Screen (upper left): The visualization window shows the image that is currently being captured by the CCD camera – if the camera is not acquiring data, a static image of the last

image captured remains on the screen. The "Live Image" indicator light is on while the camera is actively capturing images.

Stage Movement: Directly below the visualization window are a set of **Stage Movement** controls, that provide the operator with readbacks of the current stage position, automated homing, manual X/Y stage motion control, manual Z control for the motorized focusing element tied to the microscope objective, a general setup feature.

Map: below the visualization window and to the right of the **Stage Movement** controls, depicts the location of the beam with respect to a virtual image of the entire dish.

View Controls: To the right of the visualization window are the **View Controls**, which set the imaging system on live or snapshot image capture modes.

Cell Info: Below **View Controls** are the **Cell Info** controls, which allow the operator to designate a number of cells to locate and register.

Image Controls: To the right of **View Controls** are a series of image manipulation tools, permitting the user to modify the edge-finding and threshold functions

Image Autofocus: Allows the user to engage the autofocus function.

Current ROI: Allows the operator to set the size of the region of interest imaged.

A.2 Safety Interlocks

Underneath the graphical interface is a network of safety interlocks, implemented to ensure the safety of components within the high-voltage terminal. Incorporation of automated interlocks is necessary to provide a sufficient level of protection for the accelerator since user response times are not rapid enough to prevent catastrophic "arcing" (short circuit across a gap due to insulation breakdown) due to increased pressures in the accelerator tank. For example, if pressures within the portion of the beamline housed inside the accelerator exceed safe values (the tank pressure), safety interlocks programmed into the control software immediately respond by setting the terminal voltage to 0, thus avoiding an arc that could seriously damage or destroy the digital electronics housed within the high-voltage terminal. All electronics outside of the terminal are optically isolated from the rest of the system, adding an additional level of passive protection. Similarly, critical gate valves in the beam line cannot be opened unless required settings for the vacuum pumps meet specific conditions.

A.2.1 Electronic Interlocks (Integrated into the Control System)

A number of software interlocks have been developed to protect the accelerator against an uninformed user or to prevent a transient operating change from damaging the accelerator.

On "Accelerator Control" screen:

1) "Accel Enable," which allows the user to adjust the terminal voltage, cannot be activated or increased above zero value if the pressure value in the Tank exceeds the user specified pressure fault value. If the measured Tank pressure exceeds that value during operation, the terminal value is immediately set to "zero" and deactivated.

2) Any decrease in terminal voltage can be made, but increases in terminal voltage may only be performed incrementally, so as not to overload the power supply.

3) The usual value for Tank threshold pressure is 5x10-5 torr – more stringent values may be set, but as it is not safe to run at values above 5x10-5 torr a warning message will be shown (error message: "Error! Number is too large. Tank thresh. press. must be <= 5E-5 T."). Any change will also result in an alert of "Warning. Tank threshold pressure has been changed."

4) The AutoOpen function on the "Gas Enable" controls is interlocked to cut out if gas pressure in the Tank exceeds 1x10-6 torr. When it cuts out, the warning message "Tank pressure has exceeded 1E-6 Torr. Suspending AutoOpen..." is displayed.

On "Vacuum" screen:

The Vacuum system for the LABA microbeam is the most extensively interlocked, as in many cases a single valve manipulation could create a very unsafe operating state.

1) **V1 valve:** V1 may always be changed to "closed," however, in order to open it Differential Pumping must be enabled and V2 and V3 must be closed.

2) **V2 valve:** V2 may always be changed to "closed," however, in order to be opened the pressure in the roughing line must be less than 1.2 torr.

3) **V3 valve:** V3 may always be changed to "closed," however, in order to be opened the pressure in the roughing line must be less than 0.5 torr.

4) **V6 valve:** V6 may always be changed to "closed," however, in order to be opened, turbopump 1 must be on, V7 must be closed (to prevent sudden pressure load going back to Tank), V2 must be open (or else resulting backpressure may damage turbopump). Apparently turning Differential Pumping on will open it on the .prg file, but I haven't seen that (perhaps it is just a requirement)

5) **V7 valve:** V7 may always be changed to "closed," however, in order to be opened the pressure in the foreline must be less than 2.0x10-3 torr.

On "Facilities" screen:

The only software interlocks implemented at this level pertain to the controls for the bending magnet power supply. As sudden increases in current may damage the bending magnet coils (due to the threat of significant inductive heating) any increase in current made in small incremental steps.

A.2.2 Physical Interlocks

In addition to the range of interlocks integrated directly into the control system, a number of physical interlocks have been added to protect the accelerator and bending magnet hardware.

The accelerator terminal power supply, located outside of the accelerator vessel, consists of a high voltage driver and a generating voltage meter (GVM). The GVM checks the high voltage driver voltage against the voltage specified by the operator, which would otherwise steadily increase. As precise voltage control is necessary for the intended experimental applications of the microbeam, and excessively high voltages (>900 kV for the LABA Microbeam Accelerator) could damage the accelerator terminal electronics and the high voltage driver, the driver power supply is interlocked to a fuse box that will not allow it to be turned on without the GVM activated to modulate it. The fuse box is located underneath the accelerator tank, as shown in **Figure A.9**.

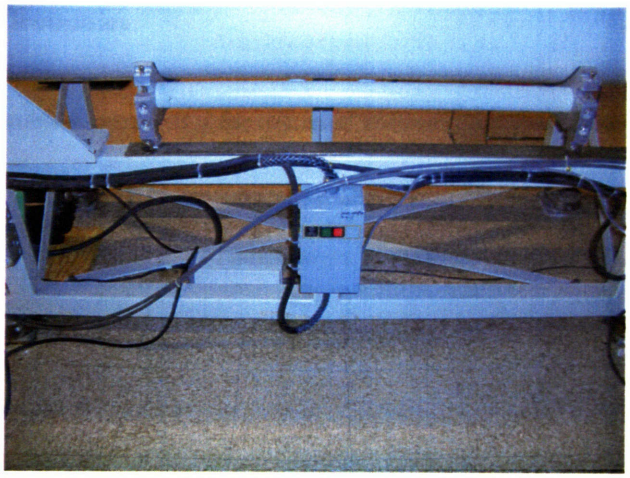

Figure A.9 Fuse box that prevents terminal power supply from being activated without the GVM voltage regulator engaged.

The bending magnet power supply is passively interlocked in by its voltage regulation and by a fuse system. Voltage regulation is performed by a circuit that prevents the control voltage from the OptoElectronics (capable of ranging from 0-5V) to exceed a voltage of 50 mV to the control inputs of the bending magnet power supply. This prevents the power supply from applying excessive current to the magnetic coils of the bending magnet. Additionally, because excessive current can cause heating in the magnetic coils sufficient to overwhelm the cooling system, the circuit is tied to a 30A fuse.

Appendix B. LABA Electronics

A range of NIM-compatible electronics were available for use in LABA Microbeam applications.

Component Type	Model
Detectors	2 Hamamatsu R7400U series photomultiplier (PMT) tubes using a Bicron BC-400 scintillating plastic 1 Silicon Surface Barrier (SSB) Detector
Preamplifer	2 Hamamatsu C5781 Socket Assemblies, attached to a +/- 15 V power supply 1 Ortec 142IH Preamplifier
High Voltage Power Supply	2 Canberra 3105 HV power supplies (1-5000 V) 1 big Harshaw NV-25A HV power supply (0-2000 V) 1 small Canberra 3102 HV power supply (1-1000 V)
Amplifier	1 Ortec 471 Spectroscopy Amplifier 1 Aptec 6300 Spectroscopy Amplifier 1 Ortec 575 Amplifier 1 Canberra 816 Amplifier
TCSA	2 Canberra 2037A Edge/Crossover Timing Single Channel Analyzers 1 Ortec 553 TSCA
TAC	1 Ortec 566 Time-to-Amplitude Converter
Coincidence Analyzer	1 Canberra 2040 Coincidence Analyzer
Counter	1 Ortec 770 Counter
Computer Interface	1 Canberra 8715ADC

Table B.1 Electronics used in the LABA Microbeam.

Detectors (Scintillating Material): For use with the PMT-based detectors, the scintillating material is an organic plastic with a well-characterized energy to light conversion. In the case of Bicron BC-400, the rise time is ~0.9 nS and the decay time is ~ 2.4 nS.

Preamplifier: The output of the photomultiplier tube (PMT) is a charge pulse proportional to the number of detected light particles generated by the scintillating material in response to the energy deposited by the incident particles. The preamplifier is used to convert this charge pulse to a voltage pulse using a capacitor (V = Q/C). The pulse rise time is dependent upon the scintillation decay time (Bicron BC-400, ~2.4 nS) and on the collection and transit time characteristics of the PMT for scintillation detectors; for the SSB detector it is more specifically dependent on the rise time in the semiconductor.

Amplifier: The amplifier amplifies the pulse height, and may be used for shaping the pulse to optimize energy or time resolution.

Single Channel Analyzer (SCA): The SCA produces a logic output pulse indicating the presence of a linear input pulse within the range determined by the "lower E" and "upper E" settings (differential mode) or merely exceeding the "lower E" setting (integral mode). The logic output pulse generated by the SCA retains a definite time relationship to the measured input linear pulse.

Time to Amplitude Converter (TAC): This instrument utilizes the fast negative logic outputs of the SCAs as inputs. The TAC output is proportional to the time interval between the start input (from one SCA) and the stop input (from the other SCA). If these two signals are unrelated to each other, the time difference between them can take on any value and the TAC output can be any pulse height. All true coincident events bear a specific temporal relationship, generating a specific pulse height on the TAC output. This pulse height may be used to identify all true coincident events. Additionally, the width of the TAC pulse-height distribution indicates the time resolution of the system.

Coincidence Analyzer (CA): The CA produces a logic output pulse when leading edges of all of the enabled logic inputs occur within the set resolving time defined by the CA. The output signal may be registered on a Counter or output directly to an ADC in order to be displayed on a CPU.

Counter: A simple scalar that counts the number of logic pulses received from an SCA.

Multi-Channel Analyzer (MCA) - The MCA sorts individual pulses into bins (channels) according to their pulse height. The voltage span of the output (0 to 5 V) is divided into 8192 energy bins of equal width, and an input signal is displayed as an energy spectrum with the number of counts at each energy subdivision sorted into the relevant bin. Calibration to a known source is required to determine the energy per channel. Once this is known, the width of relevant peaks may be used to measure of the energy resolution of the system.

Appendix C. Calculations for Deflector and Bending Magnet

C.1 Deflector Calculations

The following is a supplement for the description of the deflector characterization in **Chapter 3**, **Section 3.2.1.2**. The LABA Microbeam deflectors are each ~0.15 m in length, the diameter of the beam tube is ~0.012 m, and the total distance between the deflector and the beginning of the bending magnet is ~1 m. The direction of the beam is defined as "z," and "x" and "y" are defined as the horizontal transverse and vertical transverse directions, respectively. This arrangement is shown in **Figure C.1**.

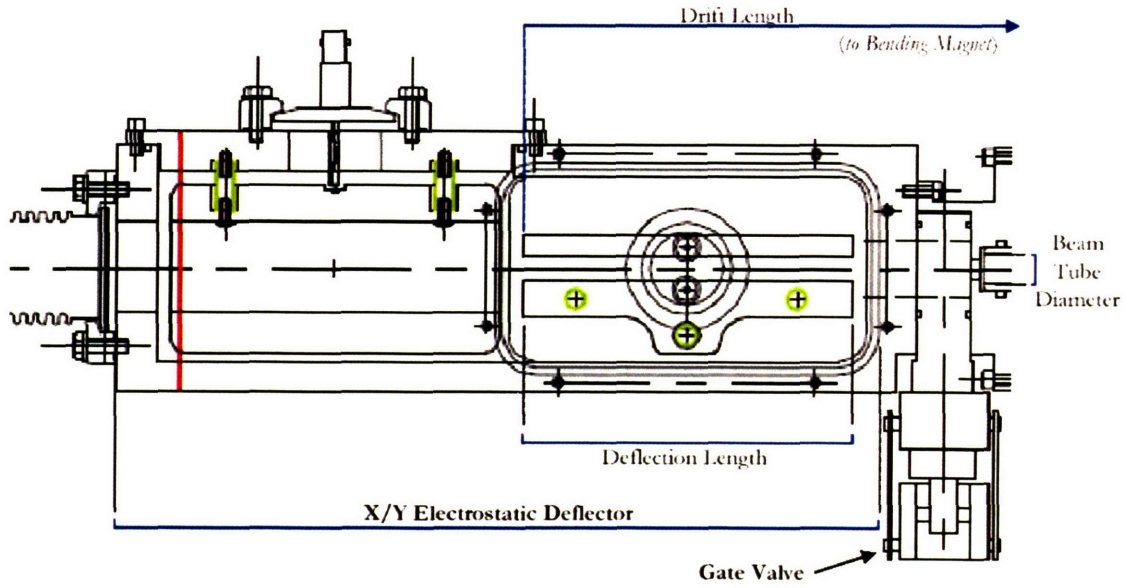

Figure C.1 A diagrammatic representation of the LABA x/y electrostatic deflector. The beam tube diameter and deflection length are labeled. (*Courtesy Andrew Dart, Pyramid Technical Consultants*)

Following the methods of Larson at the Brookhaven National Laboratory,[55] a reasonable estimate for the y-displacement necessary to "dump" the charged-particle beam on the beam tube wall prior to entering the bending magnet based on the geometry of the LABA Microbeam beamline would be $y_{deflect}$ = 0.006 m at 1 m, placing the termination of the beam beyond the quadrupole triplet and before the bending magnet. Moreover, the beam should be deflected vertically "up," which results in the bending magnet "overdeflecting" the beam, rather than creating a situation where the bending magnet may accidentally compensate for the electrostatic deflection and "undeflect" the beam. The deflection in the y-direction, $y_{deflect}$, is given by **Equation C.1**:

$$y_{deflect} = \alpha\left[\frac{\ell}{2} + z\right] \qquad \textbf{Equation C.1}$$

where α = deflection angle (steradians)

ℓ = length of deflection field (~0.15 m)

z = drift length before terminating (~1.0 m)

Solving for α yields **Equation C.2**:

$$\alpha = \frac{y_{deflect}}{\left[\frac{\ell}{2} + z\right]} = \frac{0.006}{\left[\frac{0.15}{2} + 1.0\right]} \approx 5.6mrad \qquad \textbf{Equation C.2}$$

Electrostatic deflection in a given direction is produced when the charged-particle beam interacts with an electric field *E*. Defining the orientation of the beamline as "z," and "x" and "y" as the horizontal transverse and vertical transverse directions, respectively, let:

E_y = electric field in the vertical (y) direction

v_y = vertical component of particle velocity

Then the rate of change in particle momentum may be described by **Equation C.3**:

$$\frac{dp_y}{dt} = eE_y \qquad \textbf{Equation C.3}$$

where $e = q_p$ = charge of a proton (1.6022×10^{-19} C).

Assuming that the vertical transverse component of the particle momentum prior to entering the deflector is negligible and integrating **Equation C.3** with respect to time yields **Equation C.4**:

$$p_y = \int eE_y dt = eE_y t \quad (\text{where } p_{y0} = 0) \qquad \textbf{Equation C.4}$$

The vertical transverse component of the particle may also be defined in terms of the particle mass and velocity by **Equation C.5**:

$$p_y = m_p v_y \qquad \textbf{Equation C.5}$$

Where m_p = mass of a proton (1.6726×10^{-27} kg)

Combining **Equations C.4** and **C.5** yields **Equation C.6**:

$$v_y = \frac{e}{m} E_y t \qquad \textbf{Equation C.6}$$

Integrating v_y over time for a relativistic particle yields **Equation C.7**:

$$y = \int v_y dt = \frac{eE_y}{m_0 \gamma} \int t dt = \frac{eE_y}{m_0 \gamma} \frac{t^2}{2} \qquad \textbf{Equation C.7}$$

and for a relativistic particle,

$$t = \frac{\ell}{\beta c}, \text{ so } t^2 = \frac{\ell^2}{\beta^2 c^2} \qquad \textbf{Equation C.8}$$

Substituting **Equation C.8** into **Equation C.7** results in **Equation C.9,**

$$y = \frac{e}{m_0} \frac{E_y}{2\gamma} \frac{\ell^2}{\beta^2 c^2} \qquad \textbf{Equation C.9}$$

Given that

$$\alpha = \left[\frac{2y}{\ell} \right] \qquad \textbf{Equation C.10}$$

for small angles α, defining y as $y_{deflect}$ and inserting **Equation C.9** into **Equation C.10** results in **Equation C.11,**

$$\alpha = \frac{e}{\gamma m_0 \beta^2 c^2} E_y \ell \qquad \textbf{Equation C.11}$$

For 750 KeV protons,

$$\frac{e}{\gamma m_0 \beta^2 c^2} = \frac{1.6x10^{-19}}{(1.0008)(1.6726x10^{-27})(0.03998)^2(2.998x10^8)^2} = 6.65x10^{-7}$$

$$\alpha = 6.65x10^{-7} E_y \lambda$$

$$E_y = \frac{\alpha}{6.65x10^{-7}\lambda} \qquad \textbf{Equation C.12}$$

$$E_y = \frac{5.6x10^{-3}}{6.65x10^{-7}(0.15)} = 5.6x10^4 \, V/m = 560 \, V/cm$$

For a 1.2 cm plate gap,

$$V = E_y d = (560)(1.2) = 670V \qquad \textbf{Equation C.13}$$

A general equation for the deflector voltage required to completely deflect the charged-particle beam generated by the LABA Microbeam accelerator is given in **Equation C.14**:

$$V = E_y d = \frac{\alpha \gamma m_0 \beta^2 c^2}{e\lambda} d \qquad \textbf{Equation C.14}$$

A plot of the relationship between the particle energy and the deflection voltage required to completely terminate the beam is provided in **Figure C.2.**

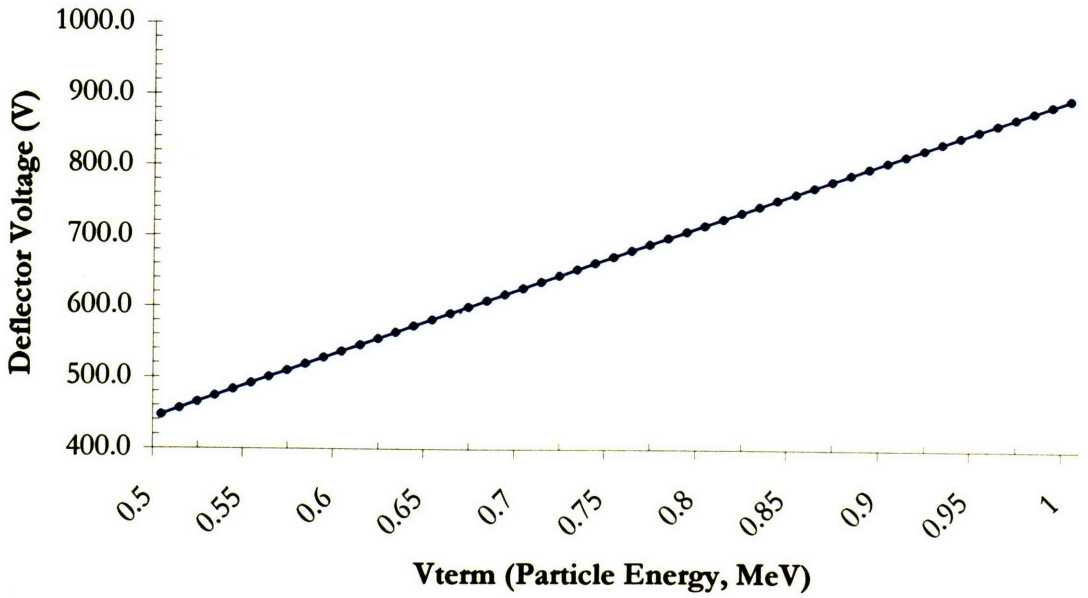

Figure C.2 The relationship between the particle energy and the deflection voltage required to completely terminate the beam using the LABA Microbeam deflection system.

C.2 Bending Magnet Calculations

The following is a supplement for the description of the bending magnet characterization in **Chapter 3, Section 3.2.3.2.** In order to characterize the bending magnet, a relationship between proton energy and magnetic field was needed. **Equations C.15 – C.23** were used to arrive at the required relationship, **Equation C.24**. **Equation C.15** first defines the Lorentzian force, F_L, experienced by a charged particle moving in the magnetic field of strength B.

$$F_L = qv \times B = qvB \qquad \textbf{Equation C.15}$$

where q = magnitude of particle charge (Coulombs)

v = component of particle velocity perpendicular to magnetic field (m/s)

B = magnetic field (Tesla)

For circular motion, v x B simplifies to the product vB. Applying Newton's First Law of Motion to this particle results in **Equation C.16**.

$$F_L = ma = m\frac{v^2}{r} \qquad \textbf{Equation C.16}$$

where m = particle mass (kg)

a = particle acceleration (m/s^2) = v^2/r for uniform circular motion

v = tangential velocity of particle (m/s)

r = radius of curvature (m)

If **Equation C.15** is then equated with **Equation C.16**, **Equation C.17** may be written:

$$qvB = m\frac{v^2}{r} \qquad \textbf{Equation C.17}$$

Solving for momentum results in **Equation C.18**:

$$qBr = mv = p \qquad \textbf{Equation C.18}$$

where p = particle's momentum (kg•m/s)

The kinetic energy of a non-relativistic particle can be written in the form of **Equation C.19**:

$$E_k = \frac{1}{2}mv^2 \qquad \textbf{Equation C.19}$$

Again, solving for momentum of the particle in terms of kinetic energy results in **Equation C.20**:

$$p = mv = \sqrt{2mE_k} \qquad \textbf{Equation C.20}$$

where E_k = kinetic energy of the particle (J)

If **Equation C.20** is equated with **Equation C.18**, the magnetic field required to produce circular motion can be written in terms of the particle's kinetic energy.

$$B = \frac{1}{rq}\sqrt{2mE_k} \qquad \textbf{Equation C.21}$$

Expanding E_k in **Equation C.21** with respect to the accelerated protons produced by the LABA accelerator results in **Equation C.22**:

$$B = \frac{1}{Rq_p}\sqrt{2m_p q_p V_{term}} \qquad \textbf{Equation C.22}$$

where R= radius of curvature of bending magnet (0.280 m)

q_p = charge of a proton (1.6022 x 10^{-19} C)

m_p = mass of a proton (1.6726 x 10^{-27} kg)

V_{term} = accelerator terminal voltage (V)

Equation C.22 provides a relationship between magnetic field strength and the kinetic energy of the proton. However, missing is a factor relating the bending magnet current to the strength of the resulting magnetic field. A plot of magnet current vs. central magnetic field, as displayed in **Figure C.3,** supplies this last relationship. From the figure, a slope of 0.2812 kG/A can be inferred. Thus, the needed relationship between magnet current and magnetic field is calculated to be 35.56 A/Tesla. Combining this value with **Equation C.22** results in the relationship between proton energy and magnet current shown in **Equation C.23**:

$$BendingMagnetCurrent(A) = \left(\frac{1}{Rq_p} \sqrt{2m_p q_p V_{term}} \right) \cdot 35.56 \, {}^{A}/_{Tesla} \qquad \textbf{Equation C.23}$$

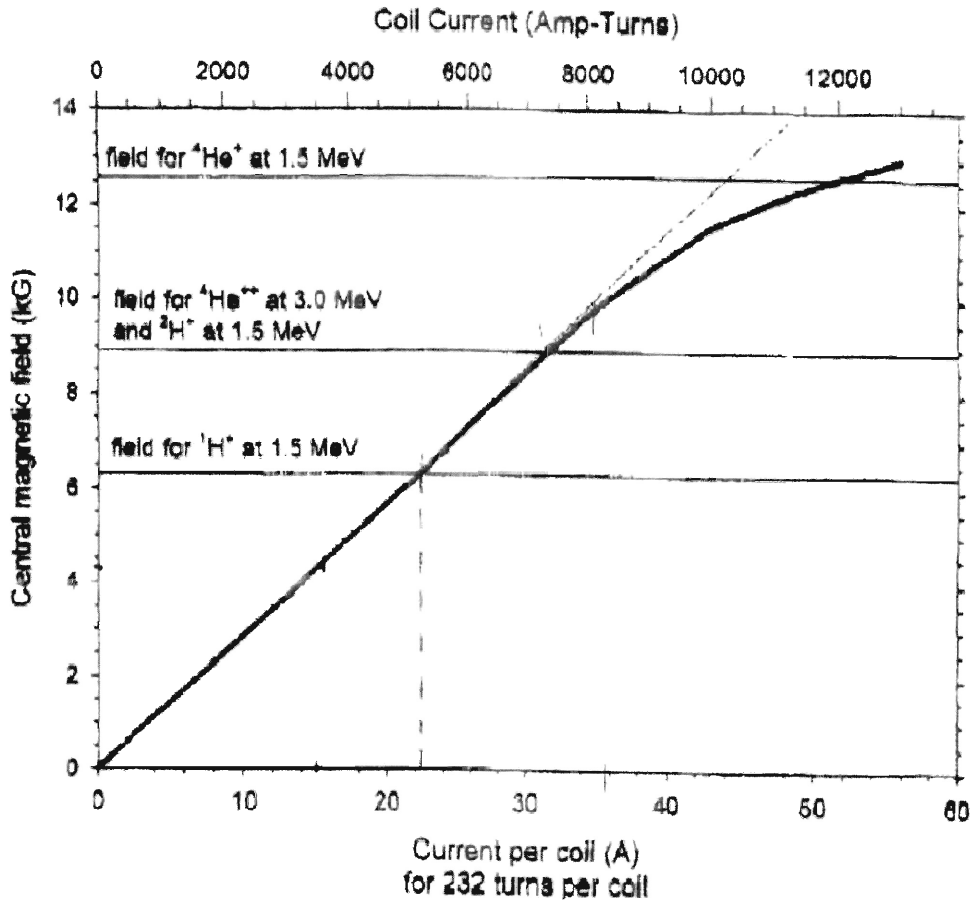

Figure C.3 Relationship between magnet current and the resulting magnetic field (provided by Pyramid Technical Consultants)

Using this relationship, experimental characterization of the bending magnet subsystem (composed of the bending magnet itself, the bending magnet power supply, and the control system) was then performed by a series of experiments in which protons of various energies were passed through the bending magnet, and the magnet current was adjusted via the CPU until the proton beam was centered on the quartz window placed in the target position within the experimental endstation. The setup for quartz window irradiation was shown above in **Chapter 3, Section 3.1.1.2, Figure 3.8**, and Figures **C.4a** and **b** below show the irradiation of the quartz window with the beam properly centered.

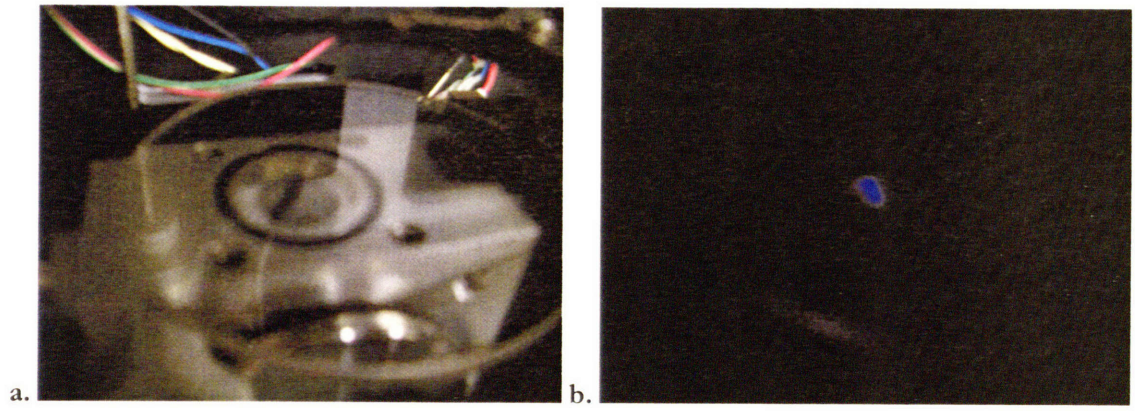

Figures C.4 a) Closeup view of the quartz window with room lights on, **b)** Image of the centered beamspot on the quartz window with the room lights off.

Once the beam was centered on the quartz window, thus indicating that the correct magnetic field had been produced, the CPU magnet current was recorded for that proton energy along with the voltage applied across the programming terminals of the magnet power supply. The measured programming voltages were used to calculate the actual bending magnet currents, which were compared to those requested by the CPU. The results of this experiment are displayed graphically in **Figure C.5**. The magnetic field, and thus the magnet current, should vary as (proton energy)$^{1/2}$. Therefore, the relationship in **Figure C.5** only appears linear due to the small range of proton energies plotted.

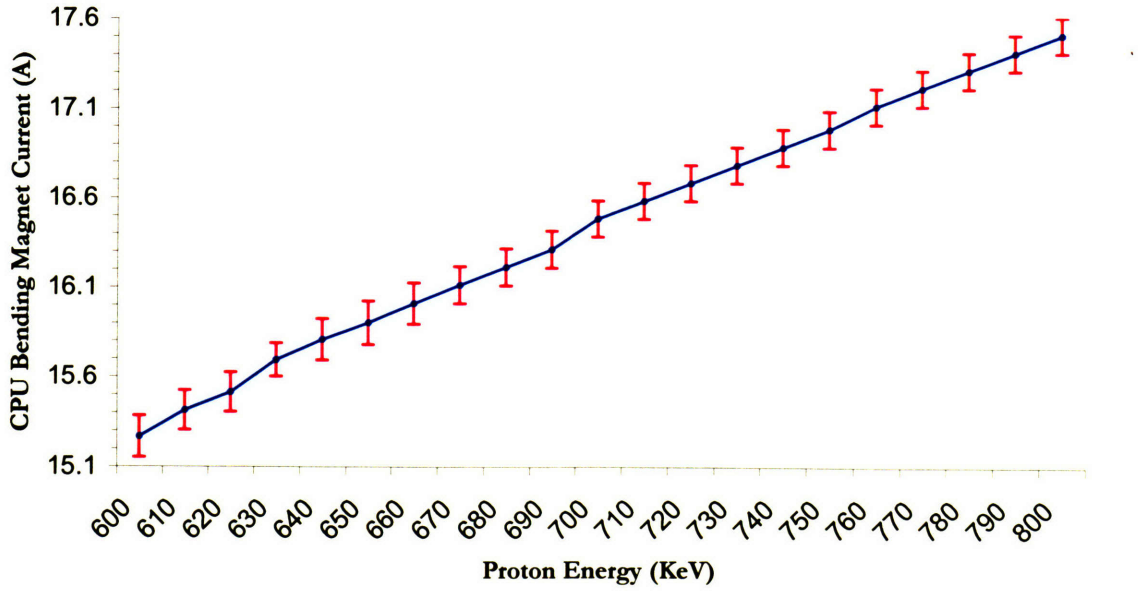

Figure C.5 Plot of bending magnet current vs. proton energy required for a 90° bend (verified by quartz window irradiation). Error bars represent the standard deviation of three sets of experimental measurements.

Magnet currents calculated by **Equation C.23** were compared to the experimental magnet currents that produced a beam spot on the quartz window, and a correction ratio of 1.061 was calculated for 750 keV protons and could be a result of a number of different sources of error (possibly the 35.57 A/Tesla slope determined from **Figure C.3**). The 1.061 correction ratio at 750 keV appears consistent over the range of proton energies most likely to be used for radiobiological studies, so it was incorporated into **Equation C.23** to correct the calculated magnet currents. **Equation C.24** is the result (37.74 A/Tesla = 35.57 A/Tesla * 1.061).

$$BendingMagnetCurrent(A) = \left(\frac{1}{Rq_p} \sqrt{2 m_p q_p V_{term}} \right) \cdot 37.74 \, {}^{A}\!/_{Tesla} \qquad \textbf{Equation C.24}$$

Appendix D. Biological Protocols

D.1 Tissue Culture

Wherever "normal growth medium" is referred to, the standard formula used for cells cultured for use with the LABA Microbeam is Dulbecco's Modification of Eagle's Medium (DMEM) with 4.5 μg/ml glucose (Mediatech CellGro, Herndon, VA USA), supplemented with 10% fetal bovine serum (FBS) (Sigma-Aldrich Co., St. Louis, MO USA), 10 μg/ml streptomycin and 10 μg/ml penicillin (Mediatech CellGro, Herndon, VA USA), and 10mM HEPES Buffer (Hyclone, Logan, UT USA).

D.2. Cell Dish Preparation and Cell Plating

Cell dish preparation:

1. The stainless steel dishes machined by Machine Technology (Beverly, MA USA) were cleaned thoroughly with hot (60°C) 200 proof ethanol.
2. The bottom surfaces of the stainless steel dishes were sprayed with 3M SprayMount adhesive (Type 6065; 3M, St. Paul MN USA), allowed to dry for about 30 seconds, and then pressed on 1.4 um mylar.
3. After 30 seconds, the extraneous mylar was cut away with a scalpel, and the glued mylar was smoothed and stretched taut against the stainless steel dish.
4. The stainless steel dishes were placed in small plastic cell culture dishes and sterilized with UV for a minimum of 2 hours.
5. 0.5 ml of a 0.01% solution of poly-l-lysine (Electron Microscopy Sciences, Fort Washington PA USA) in 1X phosphate-buffered saline (PBS) was added to each dish, and the treated stainless steel dishes were incubated for 30 min at 37°C.
6. The 0.01% poly-l-lysine solution was then aspirated, and the dishes were dried at room temperature for 2 hours.
7. Treated dishes were then stored at 4°C overnight (they may be stored for up to 1 week).
8. Prior to plating cells on the treated dishes, they are warmed to 37°C.

Cell plating:

1. Cells are trypsinized and resuspended in normal growth medium
2. 0.1 ml of cell suspension is added to each dish.

3. Dishes are incubated for 8-12 hours.
4. Medium is aspirated, and new medium is added (with or without Hoechst 33258 and/or DCHF)
    a. If Hoechst 33258 and/or DCHF are added (generally to a final operating concentration of 50 nM), incubate for 30 min at 37^{0}C, then wash 2x with 1X PBS and add new medium.
    b. If lindane is to be added, (generally to a final operating concentration of 50 nM), incubate for 30 min at 37^{0}C prior to irradiation.
5. Irradiate as desired.

D.3 Reactive Oxygen Species Assay

The compound known as 6-carboxy-2',7'-dichlorodihydrofluorescein diacetate, di(acetoxymethyl ester) (carboxy-H_2DCF-DA) may be used to label the production of reactive oxygen species (oxygen radicals, superoxide ions, and peroxides, for example).

D.3.1 Reagents

6-carboxy-2',7'-dichlorodihydrofluorescein diacetate, di(acetoxymethyl ester) (Invitrogen Co., Carlsbad CA USA; Molecular Probes Catalog #C2938)
Dimethyl Sulfoxide (DMSO), (ATCC Manassas VA USA; Catalog #4-X)
Normal growth medium (LABA)

D.3.2 Methodology

Aliquot ROS dye into smaller glass vials w/ rubber stoppers (makes 300 µl of concentrated ROS dye solution in DMSO):

1. Add 1.5 ml of anhydrous DMSO to 5 mg (MW 675.43) of C2938 to tube.
2. Vortex thoroughly.
3. Aliquot 150 µl of the resulting ROS dye solution into each of 10 glass vials.
4. Add an additional 105 µl of anyhydrous DMSO to each vial. Place a rubber stopper on each vial.

Removing oxygen from vial:

5. Attach needle to argon source.
6. Insert one needle into the rubber stopper for ventilation.
7. Insert argon stream into vial for ~30 seconds.

8. Remove the needle, and wrap the stopper in parafilm.
9. Place vials into secondary jar, fill jar with argon, and then wrap jar with parafilm.
10. Store at -20^{0}C.

Using ROS dye:

11. Dilute 300 µl of ROS dye in 9.7 ml of normal growth medium to make 74 µM solution.
12. Remove medium from cells and wash the cells 1x with 1X PBS.
13. Dilute the ROS dye in normal growth medium to a final concentation of 5 µM.
14. Add 1 ml of of 5 µM ROS dye solution to each well.
15. Incubate at 37^{0}C for 30 min.
16. Aspirate dye solution and wash 2x with 1X PBS.
17. Add 0.5-1.0 ml normal growth medium to wells.

D.4 Phosphorylation of Histone H2A.X Assay

The chromosomal structural protein identified as histone H2A.X becomes phosphorylated if in the proximity of a DNA double-strand break. This protein is a 14 kDa ubiquitous member of the H2A histone family that contains an evolutionarily conserved Serine/Glutamine motif at the protein C-terminus in eukaryotes. Serine 139 within this motif becomes rapidly phosphorylated (on the order of milliseconds) in the presence of a DNA double-strand break to yield a form known as γ-H2A.X, which may be detected using standard immunocytochemical techniques.

D.4.1 Reagents

100% Methanol

1% Formaldehyde in TBS: For each dish dilute 300 µl 37% formaldehyde solution (formalin) in 1ml 1X TBS. This solution must be prepared fresh. Discard unused portion following assay completion.

1X TBS: Dilute 2.5 ml 20X tris-buffered saline (TBS) (Upstate Catalog #20-190) with 47.5 ml sterile water to create a working solution of 1X TBS. Store at room temperature.

1X TBS/T (Wash Buffer): Dilute 125 µl 20% Tween.-20 (v/v) (Upstate Catalog #20-246) in 600 ml 1X TBS to create a working solution of 1X TBS with 0.05% Tween.-20 (v/v). Store at room temperature.

Blocking Buffer: For each dish dilute 1 ml 10% BSA in TBS (Upstate Catalog #20-191B) with 2.3 ml of 1X TBS to make a working solution of 3% BSA in TBS. This solution is stable for several days at 4°C. Discard unused portion following assay completion.

Primary Antibody Solution: Prepare 0.5 ml/dish of 7.5 µg/ml of Primary Antibody by diluting 3.75 µl/dish anti-phospho histone H2A.X (Upstate Catalog #05-636) in 0.5 ml/dish Blocking Buffer. Vortex the solution to ensure antibody is evenly diluted in the solution. Discard unused portion following assay completion. Store at 4°C.

Secondary Antibody Solution (Fluorescein): Prepare 0.5 ml/dish of 7.5 µg/ml of Primary Antibody by diluting 3.75 µl/dish of Goat Anti-Mouse IgG Fluorescein Conjugate (Upstate Catalog #12-506) in 0.5 ml Blocking Buffer. Vortex the solution to ensure antibody is evenly diluted in the solution. Discard unused portion following assay completion. Store at 4°C.

D.4.2 Methodology

Fixation: Fixing of the cells should be done as soon as the irradiation is completed, or depending on the desired time point of damage resolution.

1. Aspirate media from the dishes, leaving approximately 10 µl of media. Avoid touching the bottom of the dish and/or removing/disturbing cells.
2. Wash 2x with 1x PBS at room temperature.
3. Immerse in 100% methanol on ice for 20 minutes.
4. Aspirate excess methanol and store at 4°C if not staining immediately.
5. If staining immediately, add 500 µl/dish of 1% formaldehyde in TBS. Add solution slowly to ensure cells are not dislodged from the dishes. Let stand for 5 minutes at room temperature.
6. Aspirate formaldehyde solution and add 500 µl/dish Wash Buffer. Let stand for 1 minute at room temperature.
7. Aspirate wash buffer.
8. Add 500 µl/dish Blocking Agent (3% BSA in TBS) and incubate for 1 hour at 37°C or overnight at 4°C.

Addition of Primary and Secondary Antibodies:

1. Aspirate blocking agent.
2. Rinse the dishes once with 500 µl/dish of Wash Buffer.
3. Aspirate Wash Buffer.
4. Add 250 µl/dish of Primary Antibody Solution and incubate for 1 hour at 37°C.

5. Aspirate Primary Antibody.
6. Rinse the dishes once with 500 µl/dish of Wash Buffer.
7. Aspirate Wash Buffer.
8. Wash cells 3-5 times with 500 µl/dish Wash Buffer for ~3 minutes each with gentle agitation. Aspirate Wash Buffer in between washes.
9. Add 250 µl/dish of Secondary Antibody solution and incubate for 1 hour at room temperature or 30 min at 37^{0}C.

Fluorescence Detection:

1. Aspirate Secondary Antibody solution.
2. Rinse dishes once with 500 µl/dish Wash Buffer.
3. Aspirate Wash Buffer.
4. Wash dishes 3-5 times with 500 µl/dish Wash Buffer for ~3 minutes with gentle agitation. Aspirate Wash Buffer after each wash.
5. Image. (refer to **Appendix E, Section E.2.1**)
6. Seal slides and store at 4^{0}C.

D.5 Localization of DNA Damage Repair Protein hMre11 Assay

Mre-11 (of which hMre11 is the form found in humans), is one of many proteins that have been identified as having a role in the repair of radiation induced DNA damage. Specifically, Mre11 is an endonuclease of single-stranded DNA and an exonuclease of double-stranded DNA, facilitating DNA repair. Mre11 is associated with the repair process known as Non-Homologous End Joining (NHEJ), which is the primary means by which mammalian cells may repair double strand DNA breaks. In this process, Mre11's 3' to 5' exonuclease is utilized - other proteins involved include XRCC4/5/6/7, Rad50 (which stimulates Mre11 exonuclease), and NBS1 (which interacts directly with both Rad50 and Mre11).

D.5.1 Reagents

Triton (permeabilization) Buffer: using distilled water as a base, prepare a solution of 0.5% Triton X-100, 50 mM NaCl (GFW 58.4), 3 mM $MgCl_2$ (GFW 95.2), 20 mM HEPES Buffer, 300 µM Sucrose (GFW 342.3); final pH = 7.4.

Blocking Solution: prepare a solution of 10% fetal bovine serum (FBS) in 1X PBS or 2% bovine serum albumin (BSA) in 1X PBS.

Wash Buffer: prepare a 5% FBS, 0.1% Triton X-100 in a base of 1X PBS.

Primary (anti hMre11) Antibody Solution: prepare a 35 µl hMre11/ml solution (EMD Biosciences, CA USA; Catalog #PC388) with 1% BSA and 0.1% Triton X-100 in a base of 1X PBS.

Secondary (FITC-conjugate) Antibody Solution: prepare a solution of Goat Anti-Rabbit IgG, H & L Chain Specific antibody in 1:80 or 1:60 Ab/suspension ratio - usu. 15 µl Ab for 900 µl suspenstion (EMD Biosciences, Catalog #401311), with 5% FBS and 0.1% Triton X-100 in a base of 1X PBS.

D.5.2 Methodology

Fixation:

1. Wash 2x with 1x PBS, room temperature.
2. Immerse in 100% methanol on ice for 20 minutes.
3. Aspirate excess methanol and store at 4^0C.

Staining:

1. Permeabilize cells for 5min on ice w/ Triton Buffer.
2. Rinse 2x with 1x PBS on ice.
3. Incubate in blocking solution for 1 h at room temperature, or 30min at 37^0C.
4. Rinse 2x with 1x PBS on ice.
5. Incubate cells with hMre11 buffer for >2h at 37^0C.
6. Wash 3x for 5 min each with wash buffer.
7. Incubate with secondary (FITC-conjugate) antibody for 40min at 37^0C.
8. Wash 3-5x for 5min with 1X PBS.
9. Image. (refer to **Appendix E, Section E.2.1**)
10. Seal slides and store at 4^0C.

D.6 Live/Dead Assay

This is a binary chemical stain technique that uses a combination of Calcein acetoxymethyl (Calcein AM) and Ethidium homodimer-1. (Invitrogen Co., Carlsbad CA USA) Calcein AM is absorbed into

cells, cleaved by cytosolic esterases, and then becomes epifluorescent; the Ethidium homodimer is only able to permeate dead cells, where it concentrates and binds to DNA, becoming fluorescent. Thus, the Calcein AM stain is highly specific for living cells, while the Ethidium homodimer is highly specific for dead cells.

D.6.1 Reagents

LIVE/DEAD Viability/Cytotoxicity Kit
(Invitrogen Co., Carlsbad CA USA; Molecular Probes Catalog #L3224)

or

Calcein acetoxymethyl (AM), 1mg/ml 1mM solution in anhydrous DMSO (a/e 494/517 nm) (Invitrogen Co., Carlsbad CA USA; Molecular Probes Catalog #C3099)
Ethidium homodimer-1, 1 mg (a/e 528/617 nm) (Invitrogen Co., Carlsbad CA USA; Molecular Probes Catalog #E1169)

D.6.2 Methodology

If you buy the Invitrogen kit, simply use the directions provided. Otherwise, general use protocols for Calcein AM and Ethidium homodimer staining follow:

Calcein AM Dye preparation:

1. Aliquot 10 ul of 1 mM Calcein AM solution into 10 ml normal growth medium to make 1 uM Calcein AM solution.

Cell preparation:

1. Culture cells in confluent or subconfluent monolayer.
2. Aspirate cell medium and wash w/ 1x PBS.

Cell Treatment/Assay:

1. Add 500 ul of 1uM Calcein AM solution to washed cell culture dish.
2. Incubate treated cells for 30min at 37C.
3. Image. (refer to **Appendix E, Section E.2.1**)
4. Irradiate as needed for experiment.
5. Image. (refer to **Appendix E, Section E.2.1**)

Ethidium Dye preparation:

1. Mix 35 μg of Ethidium homodimer-1 into 10 ml normal growth medium to make 1 μM Ethidium solution in medium.

Cell preparation:

1. Culture cells in concluent or subconfluent monolayer.
2. Aspirate cell medium and wash w/ 1x PBS.

Cell Treatment/Assay:

1. Add 500 ul of 1 μM Ethidium solution to washed cell culture dish.
2. Incubate treated cells for 30 min at 37^0C.
3. Image. (refer to **Appendix E, Section E.2.1**)
4. Irradiate as needed for experiment.
5. Image. (refer to **Appendix E, Section E.2.1**)

Appendix E. Image Analysis

E.1 Microsoft Photo Editor Image Manipulation and Measurement Techniques

Microsoft Photo Editor was used for several minor adjustments to acquired images, primarily rotation, cropping, and color adjustments. In the lattermost case, color adjustment was a simple subtraction process in which an image of a "green" stain was stripped of its red and blue components, while an image of a "blue" stain was stripped of its red and green components.

Exact Pixel to Micron conversion values were determined by measuring the pixel distances between like points on the graticle standard, and applying the resulting pixel:micron ratio to biological assay images taken under identical magnification conditions

E.2 MATLAB Image Processing Techniques

E.2.1 Image Acquisition and Processing

This process assumes that epifluorescent images are acquired using a SPOT camera and a Zeiss Axioplan 2 microscope, using the UV light source at 50% intensity. All exposure times and gain values should be kept identical (generally a 200 msec exposure with a gain of 2). While the full-chip image dimensions are 1600 pixels (width) by 1200 pixels (height), cropping 100-150 pixels from each side makes it significantly easier to focus the image in UV light. Additionally, this correction will minimize optical aberrations that result in darkening at the image corners. Both the "Flatfield Correction" and the "Chip Defect Correction" options provided in the SPOT software are also used for image acquisition.

The image processing using MATLAB for a charged-particle microslit irradiation is as follows:

4. Acquire an image with the microscope (in 8-bit grayscale TIFF format)
5. Rotate images so the fluorescent strip is vertical
6. Crop the image so we're left with the fluorescent band
7. Run the MATLAB script that will read the image and generate the image profile

The MATLAB script processing scheme is to convert the 8-bit grayscale TIFF image into a matrix where each pixel is an entry a grayscale value ranging from 0 [black] to 255 [white]. The script scans

the image, converts it into a matrix value, averages the grayscale values of each column of pixels in the matrix, and then plots the average values.

E.2.2 Primary Modules

The basic image post-processing module is image_processing.m. This function loads the TIFF file, converts it into a grayscale value matrix, and then averages the column values in the matrix. The output of this function is number stream that is equivalent to the average pixel intensity profile of the image. The number of entries of this vector equals to the width (in pixels) of the analyzed image. (more details in the commented header of the script)

image_processing.m:

```
function img_profile=image_processing(filename)
% 'img_profile' is the grayscale profile of the image that is processed
% 'filename' is the name of the file where the grayscale image is
% this function will average the grayscale pixel values along the vertical
% the result will be a one-dimensional vector - the profile of the image
%
% Note: grayscale TIF images are a matrix with each pixel
% being an entry from 0[black] to 255[white]. This function will
% only process 8bit grayscale TIF images

% Check if the given file exists
fid=0;
[fid,message]=fopen(filename,'r');
if fid==-1
   disp(message);
end
fclose(fid);

% read the image and the make:
% IMG - the grayscale values matrix
% map - the image map, a three column matrix (not of interest to us)

[IMG, map]=imread(filename);

% find the dimensions of the image
[img_height, img_width]=size(IMG);

% take the average of each column to create the profile
for i=1:img_width
    img_profile(i)=mean(IMG(:,i));
end

% this is the end of the file
```

The next module is poly_fit.m. It takes the average pixel intensity profile (the output of "image_processing.m") and makes a polynomial fit to the data. For most complex images, MATLAB will give the warning message: "Polynomial is badly conditioned. Remove repeated data points or ...".

The user specifies at the beginning what degree polynomial to fit the data to. For a single fluorescent stripe induced by charged-particle microslit irradiation, a degree polynomial value ranging from 5-10 will result in a relatively accurate fit. However, if more than one stripe is present in the image, a 40th or 60th degree polynomial fitting will most likely be necessary. (more details in the commented header of the script)

poly_fit.m:

```
function [polynom, coeff]=poly_fit(data_set, degree);
% this function performs polynomial fitting of a data set
% the function will find a polynomial of 'degree' (integer number)
% 'polynom' is the evaluated polynom at every pixel/point of the set
% 'coeff' is the set of coefficients that describe the polynomial, MATLAB way

% find the size of the data set
N=length(data_set);

% fit a polynomial of 'degree' to the data set
coeff=polyfit(1:N, data_set,degree);

% evaluate the polynomial at every point (i.e. pixel in the image)
polynom=polyval(coeff,1:N);

% this is the end of the function
```

The MATLAB script single_profile.m uses the previous two modules ("image_processing.m" and "poly_fit.m") to plot both the profile of an image and its polynomial fit. The script will ask for the filename (file has to be in the same folder as the script) and the polynomial degree for fitting. It is useful for a quick analysis of the image and highlighting general features. To run the script requires the user to place the files image_processing.m, poly_fit.m, single_profile.m, and the aligned and cropped TIFF image for analysis in the same folder. Running MATLAB in that folder, the user enters "single_profile" in the MATLAB window to run the script. The script will ask for the filename and the polynomial degree. (more details in the commented header of the script)

single_profile.m:

```
% This script analyzes a single image profile


% set the fitting polynomial degree, 5-9 are good values
poly_degree=40;

% get the filename first
filename=input('Enter the image filename: ','s');
poly_degree=input('Enter the degree of polynomial for fitting: ');
%filename='img1.tif';
```

```
% process the images and get their raw profile
profile=image_processing(filename);

% get the fitting polynomials
[poly,coeff]=poly_fit(profile, poly_degree);

h1=figure;
plot(profile,'b');
hold on;
plot(poly,'k');
hold off;
legend('Raw Profile','Poly-Fit');
ylabel('Grayscale Value [0-black, 255-white]');
xlabel('Pixel Position [pixels]');
title(['Averaged Grayscale Profile, ',num2str(poly_degree),'th Degree Poly-Fit;
',',\newline Image File: ',filename,' ;'])

% retrieve the width as a function of height from the top of the curve
% [h,w]=width_analysis(poly,60,500,100);

% change the direction of the vectors to make the plot unerstandable
% plot the width of the curve as a function of distance from the peak
% also change the vertical coordinate (height) so measurements start from
% the peak
%
% M=length(h);
% for i=1:M
%     h_flip(i)=h(M-i+1);
%     w_flip(i)=w(M-i+1);
% end
%
% % adjust the vertical coordinate
% top=h(M);
% h_flip=-(h_flip-top);
%
% h2=figure;
% plot(h_flip,w_flip,'b');
% legend('Width');
% ylabel('Curve Width [pixels]');
% xlabel('Distance from the curve peak [pixels]');
% title(['Polynomial fit curve width as a function of distance from the peak,
',num2str(poly_degree),'th Degree Poly-Fit; ','\newline',filename,';']);
```

References

1. "Extended Abstracts: Proceedings of the 4th International Workshop: Microbeam Probes of Cellular Radiation Response," *Radiation Research* **153**:220–238 (2000).
2. "Extended Abstracts: Proceedings of the 5th International Workshop: Microbeam Probes of Cellular Radiation Response," *Radiation Research* **158**:365–385 (2002).
3. "Extended Abstracts: Proceedings of the 6th International Workshop/12th L. H. Gray Workshop: Microbeam Probes of Cellular Radiation Response," *Radiation Research* **161**:87–119 (2004).
4. E.I. **Azzam**, S.M. deToledo, T. Gooding, J.B. Little, "Intercellular communication is involved in the bystander regulation of gene expression in human cells exposed to very low fluences of alpha particles," *Radiation Research* **150:**497-504 (1998).
5. R. **Barillon**, M. Fromm, A. Chambaudet, H. Marah, A. Sabir, "Track Etch Velocity Study in a Radon Detector (LR 115, Cellulose Nitrate)," *Radiation Measurements* **28(1-6):**619-628 (1997).
6. K. **Baverstock**, "Radiation-induced genomic instability: a paradigm-breaking phenomenon and its relevance to environmentally induced cancer," *Mutation Research* **454**:89-109 (2000).
7. Berkeley University Advanced Light Source (ALS) website, http://www-als.lbl.gov.
8. A. **Bishayee**, D.V. Rao, R.W. Howell, "Evidence for pronounced bystander effects caused by nonuniform distributions of radioactivity using a novel three-dimensional tissue culture model," *Radiation Research* **152:**88-97 (1999).
9. A. **Bishayee**, H.Z. Hill, D. Stein, D.V. Rao, R.W. Howell, "Free radical-initiated and gap junction-mediated bystander effect due to nonuniform distribution of incorporated radioactivity in a three-dimensional tissue culture model," *Radiation Research* **155:**335-344 (2001).
10. R.P. **Boisseau**, "SBIR Phase II Application: Atmospheric Proton Microprobe for Trace Element Analysis," Phase I Grant #GM47206-01, Internal Copy (August 15th 1994).
11. L.A **Braby**, "Microbeam studies of the sensitivity of structures within living cells," *Scanning Microscopy*, **6:**167-175 (1992).
12. D.J. **Brenner**, R. Doll, D.T. Goodhead, E.J. Hall, C.E. Land, J.B. Little, J.H. Lubin, D.L. Preston, R.J. Preston, J.S. Puskin, E. Ron, R.K. Sachs, J.M. Samet, R.B. Setlow, and M. Zaider, "Cancer risks attributable to low doses of ionizing radiation: Assessing what we really know," *PNAS* **100(24):**13761-13766 (2003).
13. T. **Butz**, R-H. Flagmeyer, J. Heitmann, D. N. Jamieson, G. J. F. Legge, D. Lehmann, U. Reibetanz, T. Reinert, A. Saint, J. Zhu, "The Leipzig high-energy ion nanoprobe: A report on first results," *Nucl. Instrum. Methods Phys. Res. B* **161–163**:323–327 (2000).
14. Canberra, http://www.canberra.com/literature/basic_principles/timing.htm.
15. B.G. **Cartwright**, E.K. Shirk, P.B. Price, "A nuclear-track-recording polymer of unique sensitivity and resolution," *Nuclear Instruments and Methods* **153(2-3):**457-60 (1978).
16. R.M. **Cassou**, E.V. Benton, "Properties and applications of CR39 polymeric nuclear track detector," *Nuclear Track Detection* **2(3):**173-179 (1978).
17. R. **Cherubini**, M. Conzato, G. Galeazzi, S. Gerardi, "Light-ion microcollimated beam facility for single-ion, single mammalian cell irradiation studies at LNL-INFN," *Radiation Research* **158**: 371–372 (2002).
18. J.D. **Cockroft**, E.T.S. Walton, "Experiments with High Velocity Positive Ions," *Proceedings of the Royal Society of London. Series A, Containing Papers of a Mathematical and Physical* Character **129(811):**477-489 (1930).
19. J.D. **Cockroft**, E.T.S. Walton, "Experiments with High Velocity Positive Ions (I) Further Developments in the Method of Obtaining High Velocity Positive Ions," *Proceedings of the Royal Society of London. Series A, Containing Papers of a Mathematical and Physical* Character **136(830):**619-630 (1932).
20. P. **Decherchi**, P. Cochard, P. Gauthier, "Dual Staining Assessment of Schwann Cell Viability within Whole Peripheral Nerves using Calcein-AM and Ethidium Homodimer," *Journal of*

Neuroscientific Methods **71(2)**:205-13 (1997).
21. J.M **Dixon**, M. Taniguchi, J.S. Lindsey, "PhotochemCAD 2: A Refined Program with Accompanying Spectral Databases for Photochemical Calculations," *Photochemistry and Photobiology* **81**:212-213 (2005).
22. Dosirad, http://pro.wanadoo.fr/dosirad/Notice%20LR115-A.html, Villa Parc Le Chêne, 77185 Lognes, France.
23. H. **Du**, R.-C.A. Fuh, J. Li, A. Corkan, J.S. Lindsey, "PhotochemCAD: a computer-aided design and research tool in photochemistry," *Photochemistry and Photobiology* **68**:141-142 (1998).
24. M. **Durante**, G.F. Grossi, M. Pugliese, G. Gialanella, "Nuclear Track Detectors in Cellular Radiation Biology," *Radiation Measurements* **26(2):**179-186 (1996).
25. A.D. **Dymnikov**, D.J. Brenner, G. Johnson, G. Randers-Pehrson, "Theoretical Study of a Short Electrostatic Lens for the Columbia Ion Microprobe," *Review of Scientific Instruments*, **71(4):**1646-1650 (2000)
26. T. **Finkel**, "Oxygen radicals and signaling," *Current Opinion in Cell Biology* **10(2)**:248–253. (1998).
27. B.E. **Fischer**, "Single-particle techniques," *Nuclear Instruments and Methods in Physics Research*, **B54:**401-406 (1991).
28. B. E. **Fischer**, "The heavy-ion microprobe at GSI—used for single ion micromechanics," *Nucl. Instrum. Methods B* **30**:284-288 (1988).
29. R.L. **Fleischer**, P.B. Price, R.M. Walker, E.L. Hubbard, "Track Registration in Various Solid-State Nuclear Track Detectors," *Physical Review* **133:**A1443 (1964).
30. R.L. **Fleischer**, P.B. Price, R.M. Walker, Nuclear Tracks in Solids, University of California Press, Berkeley (1975).
31. M. **Folkard**, K.M. Prise, B. Vojnovic, H.C. Newman, M.J. Roper, K.J. Hollis, B.D. Michael, "Conventional and microbeam studies using low-energy charged particles relevant to risk assessment and the mechanisms of radiation action," *Radiation Protection Dosimetry,* **61:**215-218 (1995).
32. M. **Folkard**, B. Vojnovic, K.M. Prise, A.G. Bowey, R.J. Locke, G. Schettino, B.D. Michael, "A charged-particle microbeam: I. Development of an experimental system for targeting cells individually with counted particles," *International Journal of Radiation Biology*, **72(4):**375-385 (1997).
33. M. **Folkard**, B. Vojnovic, K.J. Hollis, A.G. Bowey, S.J. Watts, G. Schettino, K.M. Prise, B.D. Michael, "A charged-particle microbeam: II. A single-particle micro-collimation and detection system," *International Journal of Radiation Biology*, **72(4):**387-395 (1997).
34. C.R. **Geard**, D.J. Brenner, G. Randers-Pehrson, S.A. Marino, "Single-particle irradiation of mammalian cells at the Radiological Research Accelerator Facility: induction of chromosomal changes," *Nuclear Instruments and Methods*, **B54:**411-415 (1991).
35. C.R. **Geard**, G. Randers-Pehrson, S.A. Marino, G. Jenkins-Baker, T. Hei, E.J. Hall, D.J. Brenner, "Intra- and intercellular responses after cell-site specific microbeam irradiation" *Radiation Research* **153**:233 (2000).
36. A.M. **Giusti**, M. Raimondi, G. Ravagnan, O. Sapora, T. Parasassi, "Human cell membrane oxidative damage induced by single and fractionated doses of ionizing radiation: a fluorescence spectroscopy study," *International Journal Of Radiation Biology* **74(5)**:595-605 (1998).
37. D.T. **Goodhead**, "Initial events in the cellular effects of ionizing radiations: clustered damage in DNA," *International Journal of Radiation Biology* **65(1)**:7-17 (1994).
38. Gray Cancer Institute Website: http://www.graylab.ac.uk/research/rad_science.htm
39. P.F. **Green**, A.G. Ramli, S.R. Hashemi-Hazhad, S.A.R. Al-Najjar, C.M. Ooi, F. Abu-Jarad, R.K. Bull, S.A. Durrani, "On the optimization of etching conditions for CR39 and other plastic track detectors," *Nuclear Tracks, Methods, Instruments and Applications*, **5(4):**351 (1981).
40. K.D. **Greif**, H.J. Brede, U. Giesena, D. Frankenberg, "The PTB Focused Microbeam for High- and Low-LET Radiation," *Radiation Research*, 6th Workshop *Radiation Research* **161**:89-90 (2004).
41. X. **Guan**, W.J. Bonney, R.J. Ruch, "Changes in Gap Junction Permeability, Gap Junction Number, and Connexin43 Expression in Lindane-Treated Rat Liver Epithelial Cells," *Toxicology and Applied Pharmacology* **130**:79-86 (1995).

42. E.J. **Hall**, Radiobiology for the Radiologist, J.B. Lipincott Company, Philadelphia (1994).
43. E.J. **Hall**, "The Bystander Effect," *Health Physics* **85(1):**31-35 (2003).
44. A. **Hauptner**, G. Dollinger, G. Datzmann, H-J. Korner, R. Krucken, P. Reichart, "The Munich Microprobe Setup for Single-Ion Irradiation of Cells," *Radiation Research* **161**:98 (2004).
45. R.G. **Herb**, "The Pelletron Accelerator," *IEEE Transactions on Nuclear Science* **18(3)**:71-75 (1971).
46. R.G. **Herb**, "Pelletron Accelerators for Very High Voltage", *Nuclear Instruments and Methods* **122**:267-276 (1974).
47. S. **Hu**, Y. Wu and B. Chen, "The research of a single-particle equipment." *Nucl. Tech.* **25**:741–744 (2002).
48. **ICRP**, "Human Respiratory Tract Model for Radiological Protection. A Report of a Task Force Group of the International Commission on Radiological Protection," *Ann. ICRP* **24**:1-482 (1994).
49. R. **Iyer**, B.E. Lehnert, "Factors Underlying the Cell Growth-Related Bystander Responses to α Particles" *Cancer Research* **60**:1290–1298 (2000).
50. K.F. **Jorgenson**, J.H. van de Sande, C.C. Lin, "The use of base pair specific DNA binding agents as affinity labels for the study of mammalian chromosomes," *Chromosoma* **68(4)**:287-302 (1978).
51. A.I. **Kassis**, "In vivo validation of the bystander effect," *Hum Exp Toxicol.* **23(2)**:71-3 (2004).
52. R. **Klinkowstein**, R. **Shefer**, (Newton Scientific, Inc.), personal communications.
53. G.F. **Knoll**, Radiation Detection and Measurement (2nd Ed.), John Wiley & Sons, New York; pp. 698-703 (1989).
54. Y. **Kobayashi**, M. Taguchi, H. Watanabe, "Use of a collimated heavy ion microbeam for irradiating cells individually," *Radiation Research* **153**:228–229 (2000).
55. R.A. **Larson**, *AGS DIVISION TECHNICAL NOTE* **No. 61**, Brookhaven National Laboratory Accelerator Department, June 20, 1969.
56. R. **Ledoux**, B. **Nett** (Pyramid Technical Consultants), personal communications.
57. L. **Li**, A. Sharipo, E. Chaves-Olarte, M.G. Masucci, V. Levitsky, M. Thelestam, T. Frisan, "The Haemophilus ducreyi cytolethal distending toxin activates sensors of DNA damage and repair complexes in proliferating and non-proliferating cells," Cell. Microbiol. **4**:87-99 (2002).
58. J.B. **Little**, "Radiation Carcinogenesis," *Carcinogenesis* **21**:397-404 (2000).
59. F.M. **Lyng**, C.B. Seymour, C. Mothersill, "Initiation of apoptosis in cells exposed to medium from the progeny of irradiated cells: a possible mechanism for "bystander" induced instability?" *Radiation Research* **157:**365–370 (2002).
60. R.S. **Maser**, K.J. Monsen, B.E. Nelms, J.H.J. Petrini, "hMre11 and hRad50 nuclear foci are induced during the normal cellular response to DNA double-strand breaks," *Mol. Cel. Biol.* **17**, 6087-6096 (1997).
61. W.L. **McLaughlin**, M. Al Sheikhly, D.F. Lewis, A. Kovacx, L, Wojnarovits, "Radiochromic solid-state polymerization reaction," *Irradiation Of Polymers ACS Symposium Series* **620**:152-166 (1996).
62. N.F. **Metting**, A.M. Koehler, H. Nagasawa, J.M. Nelson, J.B. Little, "Design of a Benchtop Alpha Particle Irradiator," *Health Physics* **68(5):**710-715 (1995).
63. B.D. **Michael**, M. Folkard, K.M. Prise, "Meeting report: Microbeam probes of cellular radiation response, 4th L.H. Gray Workshop, 8–10 July 1993," *Int. J. Radiat. Biol.* **65**:503–508 (1994).
64. C. **Michelet**, P. Moretto, P. Barberet, A. Balana, R.K. Dutta, P. Aguer, "A focused microbeam for targeting cells with counted multiple particles," *Radiation Research* **158**:370–371 (2002).
65. R.C. **Miller**, G. Randers-Pehrson, C.R. Geard, E.J. Hall, D.J. Brenner, "The Oncogenic Transforming Potential of the Passage of Single Alpha Particles Through Mammalian Cell Nuclei," *Proceedings of the National Academy of Sciences* **96**:19-22 (1999).
66. Molecular Probes, Invitrogen Detection Technologies Product Information "Acetoxymethyl (AM) and Acetate Esters," (2002).
67. Molecular Probes, Invitrogen Detection Technologies Product Information, "Reactive Oxygen Species (ROS) Detection Reagents," (2004).
68. P. **Moretto**, C. Michelet, A. Balana, P. Barberet, W. Przybylowicz, J.P. Slabbert, V. Prozesky, C.

Pineda, G. Brut, G. Laurent, F.Lhoste, "Development of a single ion irradiation system at CENBG for applications in radiation biology," *Nucl. Instrum. Methods B* **181**:104–109 (2001).
69. C. **Mothersill**, C.B. Seymour, "Medium from irradiated human epithelial cells but not human fibroblasts reduces the clonogenic survival of unirradiated cells: Possible evidence of a 'bystander effect'," *Int J Radiat Biol* **71:**421–427 (1997).
70. C. **Mothersill**, C.B. Seymour, "Survival of human epithelial cells irradiated with cobalt 60 as microcolonies or single cells," *Int J Radiat Biol* **72:**597–606 (1997).
71. C. **Mothersill**, C.B. Seymour, "Cell-cell contact during gamma irradiation is not required to induce bystander effects in normal human keratinocytes: Evidence for release during irradiation of a signal controlling survival in the medium," *Radiation Research* **149:**256–262 (1998).
72. C. **Mothersill**, C.B. Seymour, "Review: radiation-induced bystander effects: past history and future perspectives," *Radiation Research* **155:**759–767 (2001).
73. C. **Mothersill**, E.G. Wright, D.M. Rea, D. Murphy, S. Lorimore, C.B. Seymour, K. O'Malley, "Individual variation in the production of a bystander effect by radiation in normal human urothelium," *Carcinogenesis* **22:**1465–1471 (2001).
74. H. **Nagasawa**, J.B. Little, "Induction of sister chromatid exchange by extremely low doses of α-particles," *Cancer Research*, **52:**6394-6396 (1992).
75. P.K. **Narayanan**, E.H. Goodwin, B.E. Lehnert, "Alpha particles initiate biological production of superoxide anions and hydrogen peroxide in human cells," *Cancer Research* **57(18)**: 3963-3971 (1997).
76. B.E. **Nelms**, R.S. Maser, J.F. MacKay, M.G. Lagally, J.H.J. Petrini, "In Situ Visualization of DNA Double-Strand Break Repair in Human Fibroblasts, *Science* **280:**590-592 (1998).
77. J.M. **O'Meara**, R.P. Boisseau, A. Dart, R.J. Ledoux, W.P. Nett, J.C. Yanch, "Single-Particle Detection for the MIT Charged-Particle Microbeam," *Radiation Research* **158**:372–373 (2002).
78. M.P. **Oksvold**, E. Skarpen, J. Widerberg, H.S. Huitfeldt, "Fluorescent Histochemical Techniques for Analysis of Intracellular Signaling," *The Journal of Histochemistry and Cytochemistry* **50(3)**:289–303 (2002).
79. J.H.J. **Petrini**, M.E. Walsh, C. DiMare, X.-N. Chen, J.R. Korenberg, D.T. Weaver, "Isolation and Characterization of the human MRE11 homologue," *Genomics* **29**, 80-86 (1995).
80. K.M. **Prise**, O.V. Belyakov, M. Folkard, B.D. Michael, "Studies of the bystander effects in human fibroblasts using a charged particle microbeam," *International Journal of Radiation Biology* **74:**793-798 (1998).
81. K.M. **Prise**, M. Folkard, B.D. Michael, "The Use of Microbeams in Radiation Biology: An Overview," *Proceedings of the 11th ICRR Meeting* Dublin, July 18-23 (1999).
82. G. **Randers-Pehrson**, C.R. Geard, G. Johnson, D.J. Brenner, "Technical Characteristics of the Columbia University Single-Ion Microbeam," *Radiation Research,* **153:**221-223 (2000).
83. G. **Randers-Pehrson**, C.R. Geard, C.D. Johnson, C.D. Elliston, D.J. Brenner, "The Columbia University single-ion microbeam," *Radiation Research* **156:**210–214 (2001).
84. Columbia University, RARAF Microbeam Website, http://www.raraf.org/microbeam.htm.
85. C. **Redon**, D.R. Pilch, E.P. Rogakou, O. Sedelnikova, K. Newrock, W.M. Bonner, "Histone H2A variants H2AX and H2AZ," *Curr. Opin. Genet. Dev.* **12**:162-169, (2002).
86. K. **Reznikov**, L. Kolesnikova, A. Pramanik, K. Tan-No, I. Gileva, T. Yakovleva, R. Rigler, L. Terenius, G. Bakalkin, "Clustering of apoptotic cells via bystander killing by peroxides," *The FASEB Journal* **14**:1754-1764 (2000).
87. E. P. **Rogakou**, D. R. Pilch, A. H. Orr, V.S. Ivanova, W. M. Bonner, "DNA double-stranded breaks induce histone H2AX phosphorylation on serine 139," *J. Biol. Chem.* **273**, 5858-5868 (1998).
88. E.P. **Rogakou**, C. Boon, C. Redon, C., W.M. Bonner, "Megabase chromatin domains involved in DNA double-strand breaks in vivo," *J. Cell Biol.* **146**:905-916 (1999).
89. E.P. **Rogakou**, W. Nieves-Neira, C. Boon, Y. Pommier, W.M. Bonner, "Initiation of DNA fragmentation during apoptosis induces phosphorylation of H2AX histone at serine 139," *J. Biol. Chem.* **275**:9390-9395 (2000).

90. S.G. **Sawant**, G. Randers-Pehrson, C.R. Geard, D.J. Brenner, E.J. Hall, "The bystander effect in radiation oncogenesis: I. Transformation in C3H10T1/2 cells in vitro can be initiated in the unirradiated neighbors of irradiated cells," *Radiation Research* **155:**397–401 (2001).
91. S.G. **Sawant**, W. Zheng, K.M. Hopkins, G. Randers-Pehrson, H.B. Lieberman, E.J. Hall, "The radiation-induced bystander effect for clonogenic survival," *Radiation Research* **157:**361–364 (2002).
92. G. **Schettino**, M. Folkard, B. Vojnovic, A.G. Michette, D. Stekel, S.J. Pfauntsch, K.M. Prise, B.D. Michael, "The Ultrasoft X-Ray Microbeam: A Subcellular Probe of Radiation Response," *Radiation Research,* **153:**223-225 (2000).
93. L.D. **Skarsgard**, "Radiobiology with heavy charged particles: a historical review," *Physica Medica* **XIV(1):**1-19 (1998).
94. SRIM 2003 Code Information, http://srim.org/SRIM/SRIM2003.html.
95. B.M. **Sutherland**, P.V. Bennett, O. Sidorkina, J. Laval, "Clustered DNA damages induced in isolated DNA and in human cells by low doses of ionizing radiation," *Proceedings of the National Academy of Sciences* **97(1)**:103-108 (2000).
96. H. **Talasz**, W. Helliger, B. Sarg, P.L. Debbage, B. Puschendorf, H. Lindner, "Hyperphosphorylation of histone H2A.X and dephosphorylation of histone H1 subtypes in the course of apoptosis," Cell Death Differ. **9**:27-39 (2002).
97. Texas A&M University Special Microbeam Utilization Research Facility (SMURF), http://microbeam.tamu.edu/index.shtml.
98. W.P. **Thorpe**, M. Toner, R.M. Ezzell, R.G. Tompkins, M.L. Yarmush, "Dynamics of Photoinduced Cell Plasma Membrane Injury," *Biophysical Journal* **68:**2198-2206 (1995).
99. K.M.S. **Townsend**, A. Stretch, D.L. Stevens, D.T. Goodhead, "Thickness Measurements on V79-4 Cells: A Comparison between Laser Scanning Confocal Microscopy and Electron Microscopy," *International Journal of Radiation Biology* **58(3)**:499-508 (1990).
100. Tsukuba University Website, http://tsukuba.ac.jp.
101. R.B. **Uretz**, R.E. Zirkle, W. Bloom, "Irradiation of Parts of Individual Cells II. Effects of an Ultaviolet Microbeam Focused on Parts of Chromosomes," *Science (New Series)*, **120(3110):**197-199 (1954).
102. I.M. **Ward**, J. Chen, "Histone H2AX is phosphorylated in an ATR-dependent manner in response to replicational stress," *J. Biol. Chem.* **276**:47759-47762 (2001).
103. J.F. **Ward**, "The complexity of DNA damage: relevance to biological consequences," *International Journal of Radiation Biology* **66(5)**:427-432 (1994).
104. F. **Watt**, G. Grime, Principles and Applications of High Energy Ion Microbeams, Bristol, (1987).
105. R.R. **Wilson**, "Radiological use of fast protons," *Radiology* **47:**487-491 (1946).
106. L.-J. **Wu**, G. Randers-Pehrson, A. Xu, C.A. Waldren, C.R. Geard, Z.L. Yu, T.K. Hei, "Targeted Cytoplasmic Irradiation Induces Mutations in Mammalian Cells," *Proceedings of the National Academy of Sciences* **96:**4959-4964 (1999).
107. L.Y. **Xue**, N.J. Butler, G.M. Makrigiorgos, S.J. Adelstein, A.I. Kassis, "Bystander Effect Produced by Radiolabeled Tumor Cells *in Vivo*," *Proceedings of the National Academy of Sciences* **99(21):**13765-13770 (2002).
108. H. **Yamaguchi**, Y. Sato, H. Imaseki, N. Yasuda, T. Hamano, Y. Furusawa, M. Suzuki, T. Ishikawa, T. Mori, K. Matsumoto, M. Yukawa and F. Soga, "Single Particle Irradiation System to Cell (SPICE) at NIRS," *Radiation Research* **161**:94-95 (2004).
109. J.C. **Yanch**, (MIT Laboratory for Accelerator Beam Applications) personal communications.
110. H. **Zhou**, G. Randers-Pehrson, C.A. Waldren, D. Vannais, E.J. Hall, T.K. Hei, "Induction of a bystander mutagenic effect of alpha particles in mammalian cells," *PNAS* **97:**2099–2104 (2000).
111. H. **Zhou**, M. Suzuki, G. Randers-Pehrson, D. Vannais, G. Chen, J.E. Trosko, C.A. Waldren, T.K. Hei, "Radiation risk to low fluences of alpha particles may be greater than we thought," *PNAS* **98:**14410–14415 (2001).
112. H. **Zhou**, G. Randers-Pehrson, M. Suzuki, C.A. Waldren, T.K. Hei, "Genotoxic damage in non-irradiated cells: Contribution from the bystander effect," *Radiation Protection Dosimetry* **99:**227–232

(2002).
113. J. F. **Ziegler**, J. P. Biersack and U. Littmark, The Stopping and Range of Ions in Solids, Pergamon Press, New York, (1985).
114. R.E. **Zirkle**, "Biological Effectiveness of alpha particles as a function of ion concentration produced in their paths," *American Journal of Cancer* **28**:558-567 (1935).
115. R.E. **Zirkle**, "The Particle Physics Approach to Biology," *The Scientific Monthly*, **64(3):**213-217 (1947).
116. R.E. **Zirkle**, W. Bloom, "Irradiation of Parts of Individual Cells," *Science (New Series)*, **117(3045):**487-493 (1953).